Quantum-Engineered Germanium for Spin-Based Quantum Computing

Tosato, A.

DOI
10.4233/uuid:305eb39a-9a78-400e-bbfb-c161b4e4aac2

Publication date
2025

Document Version
Final published version

Citation (APA)
Tosato, A. (2025). *Quantum-Engineered Germanium for Spin-Based Quantum Computing*. [Dissertation (TU Delft), Delft University of Technology]. https://doi.org/10.4233/uuid:305eb39a-9a78-400e-bbfb-c161b4e4aac2

Important note
To cite this publication, please use the final published version (if applicable).
Please check the document version above.

Quantum-Engineered Germanium for Spin-Based Quantum Computing

Alberto Tosato

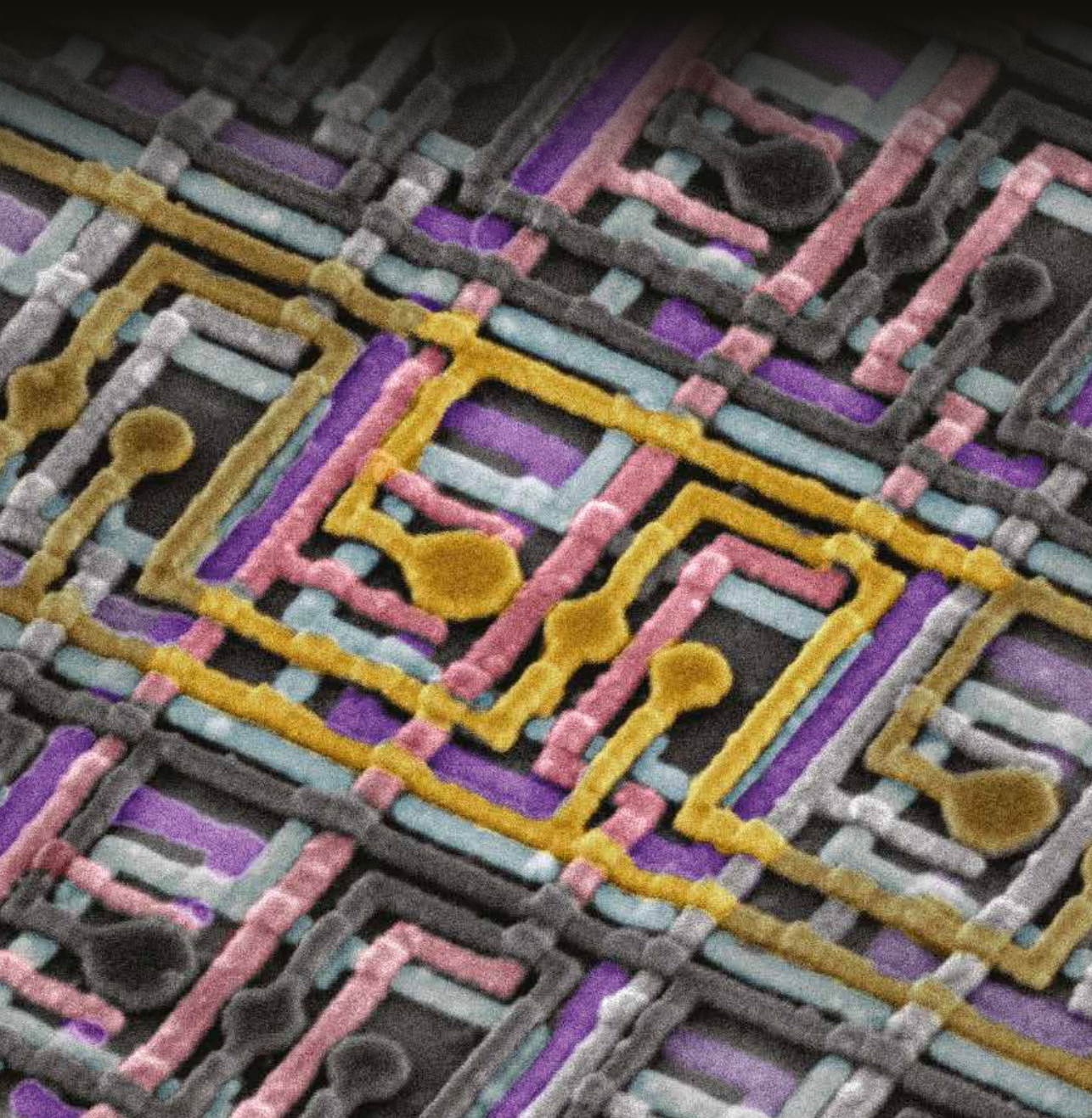

QUANTUM-ENGINEERED GERMANIUM FOR SPIN-BASED QUANTUM COMPUTING

QUANTUM-ENGINEERED GERMANIUM FOR SPIN-BASED QUANTUM COMPUTING

Dissertation

for the purpose of obtaining the degree of doctor
at Delft University of Technology
by the authority of the Rector Magnificus, prof. dr. ir. T.H.J.J. van der Hagen,
chair of the Board for Doctorates
to be defended publicly on
Wednesday, 17 September, 2025 at 17:30

by

Alberto TOSATO

Master of Science in Materials Science
Augsburg University, Germany,
Born in Padova, Italy.

This dissertation has been approved by the promotors.

Composition of the doctoral committee:

Rector Magnificus	Chairperson
Dr. G. Scappucci	Delft University of Technology, promotor
Dr. ir. M. Veldhorst	Delft University of Technology, promotor
Independent members:	
Prof.dr.ir. L.M.K. Vandersypen	Delft University of Technology
Dr. M.T. Wimmer	Delft University of Technology
Dr. E. Greplová	Delft University of Technology
Prof.dr. G. Katsaros	ISTA, Austria
Dr. S. De Franceschi	CEA, France
Reserve member:	
Prof. dr. ir. R. Hanson	Delft University of Technology

Keywords: Germanium quantum wells, bilayer systems, semiconductor-superconductor hybrids, quantum dots, spin-qubits

Printed by: Gildeprint

Front: False-colored scanning electron microscopy image of the QARPET device presented in Chapter 10. Credit to Karina Hudson for the SEM image and to Federico Poggiali for the coloring.

ISBN 978-94-6496-459-2

An electronic version of this dissertation is available at
http://repository.tudelft.nl/.

CONTENTS

1

INTRODUCTION

The pursuit of quantum computers is driven by their potential to solve certain computational problems exponentially faster than classical computers. In particular, quantum computers could revolutionize fields like cryptography through Shor's algorithm for factoring large numbers [1], optimize complex logistics and financial modeling through quantum optimization algorithms [2], and enable the simulation of quantum mechanical systems [3, 4], a task that becomes exponentially complex on classical computers. This latter capability could accelerate the discovery of new materials, catalysts, and drugs by allowing scientists to accurately model molecular and chemical interactions at the quantum level [5, 6].

While today's most powerful supercomputers struggle with these problems, quantum computers take advantage of quantum mechanical phenomena like superposition and entanglement to process information in fundamentally different ways. For example, where a classical computer with n bits can only be in one of 2^n states at a time, a quantum computer with n qubits can be in a quantum superposition of all 2^n states. This inherent parallelism, enables quantum algorithms that can solve certain problems with dramatically fewer steps than their classical counterparts. However, harnessing this computational advantage requires overcoming significant challenges in building and controlling quantum systems while protecting their fragile quantum states.

Since Feynman's seminal proposal for quantum computation in 1981 [3], several qubit platforms have been investigated, including superconducting quantum circuits [7], quantum dots in semiconductors [8], nitrogen-vacancy centers in diamond [9], topological superconductors [10] and trapped ions [11]. The journey from theoretical proposals to practical quantum computation devices has proven challenging, as quantum operation on qubits must be executed with exceptional precision and speed to outpace decoherence, the loss of quantum information due to interactions with the environment surrounding the qubit. [12, 13].

While an ideally isolated qubit would maintain its quantum state indefinitely, practical quantum computation requires qubits to interact with each other and the external world for operations and measurements. Quantum error correction enables reliable

computation even in the presence of quantum errors, by encoding the information of a single logical qubit across multiple physical qubits [14, 15]. However, implementing error correction at scale requires a platform capable of supporting millions of physical qubits with high coherence times and operation fidelities. [15, 16, 17].

In the past decade much of the effort towards a chip with quantum processing power has focused on operation (qubit initialization, readout, single and two-qubits gates and gate speed), quality (qubit coherence, uniformity and gate fidelities), and architecture (qubits connectivity, layout and integration with classical electronics). Combined advances in these three areas are essential for building a scalable quantum processor that integrates a large number of high-quality qubits in a scalable architecture.

Among the several candidates for building a quantum computer, semiconductor quantum dot spin qubits stand out for their similarity to the classical transistors [18]. Quantum dots can be fabricated using well-established semiconductor processing techniques and can integrate with existing CMOS technology [19]. Their small footprint, typically on the order of 30–100 nanometers, offers compelling advantages for scalability and integration with classical control electronics. In quantum dots, charge is confined using gate electrodes to trap and manipulate individual charges much like traditional transistors. However, the quantum operation regime of quantum dots introduces new challenges. Unlike classical transistors that operate with thousands of electrons, quantum dots must precisely control individual electrons or holes, maintaining quantum coherence and enabling high-fidelity operations.

Initial research focused on quantum dots in III-V semiconductor heterostructures due to their compelling high carrier mobility (a proxy for the uniformity of the potential landscape in a 2D carrier gas), and low effective mass, which translates to a larger energy spacing in quantum dots. However, in these materials, the intrinsic nuclear spin of the host crystal couples to the qubit significantly reducing its coherence [20, 21]. A shift to group IV semiconductors, which can be isotopically purified to zero nuclear spin, was driven by the need for less noisy materials to host spin qubits. Silicon-Metal Oxide Semiconductor (Si-MOS) and Si/SiGe heterostructures represent the most widely adopted semiconductor spin-qubit material platform in both the academic and industrial environment. Due to separation from the defects at the Si-oxide interface, Si quantum wells in Si/SiGe heterostructures present less disorder compared to Si-MOS where electrons are accumulated directly at the Si-oxide interface [22].

Recently, Ge/SiGe planar heterostructures [23] have emerged as a promising candidate for hosting hole spin qubits. The low disorder achieved in these structures makes it easy to confine single holes in quantum dots and the low effective mass reduces the lithographic constraint of the devices, increasing the fabrication yield. Further, the strong spin-orbit coupling enables all-electrical qubit control eliminating the needs for micro magnet or strip-lines resulting in simpler and more scalable devices. Finally, thanks to the Fermi-level pinning of several metals to the valence band of Ge, it is possible to create transparent contacts including superconductor-semiconductor contacts, which can provide avenues for long-range coupling of spin qubits and information transfer between different qubit types.

At the start of this Ph.D. work, the first Ge quantum dots and hole spin qubits in planar germanium heterostructures were reported, showing the formation of gate-controlled

hole quantum dots [24], demonstration of fast two-qubit logic [25] and single-shot readout [26]. In addition, first demonstrations of superconducting aluminum contacts to planar germanium quantum devices was reported [27, 28]. Building on this foundation, my Ph.D. research focused on expanding the germanium quantum toolbox in several directions. On the one hand, I contributed to designing, investigating, and validating different flavors of Ge/SiGe heterostructures through systematic cycles of optimization and validation. On the other hand, I ventured into novel directions: Ge bilayers to support vertically stacked quantum dots, Ge superconductor-semiconductor hybrid devices based on a superconducting germanide for exploring monolithic superconductor-semiconductor quantum circuits, and a quantum dots crossbar array for statistical characterization of qubits at scale. The results and insights gained expand the foundations for future development of scalable quantum processors in Ge, while also highlighting the remaining challenges that must be addressed as the field continues to advance.

1.1. THESIS OUTLINE

The thesis is organized as follows.

Chapter 2 Introduces the theoretical concepts necessary to describe the physics of holes in Ge/SiGe heterostructures, of superconductor-semiconductor hybrid systems, and the basics of hole spin qubits in quantum dots.

Chapter 3 provides an overview of the experimental methods relevant to the results presented in this thesis. I present numerical techniques for the simulations I performed of charges in semiconductors with an applied electric field (Scrödinger-Poisson) and of charge stability diagrams in a two quantum dot system (Fermi-Hubbard). Then I present details of the crystal growth of Ge/SiGe heterostructures along with the structural characterizations used in this thesis. Further, I present the fabrication techniques used for the different devices I fabricated for the work in this thesis. Finally, I present the relevant cryogenic setups I operated along with the measurement techniques commonly used to characterize the devices.

Chapter 4 presents the effective mass experimental dependence on the carrier density in strained Ge/$Si_{0.2}Ge_{0.8}$ heterostructures wells, confirming the prediction of a light effective mass in compressively strained Germanium quantum wells, and shows the dependence of the percolation density and mobility for different quantum well depths.

Chapter 5 shows classical and quantum transport on a lightly strained Ge quantum well, achieved by growth on a $Si_{0.1}Ge_{0.9}$ strain-relaxed buffer. The purpose of this study was to induce a stronger HH-LH mixing compared to the Ge/$Si_{0.2}Ge_{0.8}$ heterostructures, study the effect on effective mass and g-factor, and to reduce disorder by reducing the lattice mismatch between the QW and the substrate.

Chapter 6 presents the characterization of a Ge/$Si_{0.2}Ge_{0.8}$ heterostructure which is grown starting from a Ge wafer (as opposed to the mainstream approach of starting from a Si substrate) yielding to a substantial reduction of disorder because of the smaller lattice mismatch between substrate and quantum well.

Chapter 7 describes experiments in which we expand our 2D Ge/SiGe system to the third dimension by developing a high-mobility hole bilayer in a germanium double quantum well. This system provides a platform for building 3D lattices of quantum dots, and possibly a suitable testbed for exotic phenomena such as exciton condensation

in the quantum Hall regime and counterflow superconductivity in solid state devices at accessible temperatures.

Chapter 8 demonstrates the operation of a vertical gate defined quantum dot in a Ge double quantum well system, where the charge state of the two quantum dots can be controlled via electrostatic gates on the top of the heterostructure. Vertically coupled quantum dots represent a crucial step toward three-dimensional quantum lattices of quantum dots which may enable novel functionalities, such as integrated charge sensing, coherent spin shuttling between layers, and the potential for new qubit implementations like vertical singlet-triplet qubits. Moreover, these structures open up new opportunities for analog quantum simulation of exotic physics like exciton condensation and artificial superconductivity, which would be difficult to achieve in single-layer systems.

Chapter 9 introduces a novel superconductor-semiconductor interface between high-mobility planar germanium and platinum-germanosilicide (PtSiGe). Creating hybrid quantum systems that combine spin qubits with superconducting elements requires a hard superconducting gap (meaning with no quasi particle states within the gap), a persistent challenge in the field. We achieve this through a thermally-activated reaction between platinum and Ge/SiGe that creates an oxide-free, low-disorder interface. Through measurements of quantum point contacts and Josephson junctions, we demonstrate both near-unity contact transparency and a clean superconducting gap, marking an important step toward monolithic quantum circuits that combine the advantages of both spin and superconducting systems.

Chapter 10 presents an innovative crossbar array architecture for measuring Ge spin qubits at scale with a minimal number of connection lines. We perform charge characterization of several devices in this array, and demonstrate single qubit operations for one unit tile in the array.

Finally, **Chapter 11** discusses future directions and concludes this thesis.

BIBLIOGRAPHY

[1] P. W. Shor. "Algorithms for quantum computation: discrete logarithms and factoring". In: *Proceedings 35th annual symposium on foundations of computer science*. Ieee. 1994, pp. 124–134.

[2] E. Farhi, J. Goldstone, and S. Gutmann. "A quantum approximate optimization algorithm". In: *arXiv preprint arXiv:1411.4028* (2014).

[3] R. P. Feynman. "Simulating physics with computers". In: *International Journal of Theoretical Physics* 21 (6-7 June 1982), pp. 467–488. ISSN: 0020-7748.

[4] S. Lloyd. "Universal quantum simulators". In: *Science* 273.5278 (1996), pp. 1073–1078.

[5] A. Aspuru-Guzik, A. D. Dutoi, P. J. Love, and M. Head-Gordon. "Simulated quantum computation of molecular energies". In: *Science* 309.5741 (2005), pp. 1704–1707.

[6] Y. Cao, J. Romero, J. P. Olson, M. Degroote, P. D. Johnson, M. Kieferová, I. D. Kivlichan, T. Menke, B. Peropadre, N. P. Sawaya, et al. "Quantum chemistry in the age of quantum computing". In: *Chemical reviews* 119.19 (2019), pp. 10856–10915.

[7] Y. Nakamura, Y. A. Pashkin, and J. Tsai. "Coherent control of macroscopic quantum states in a single-Cooper-pair box". In: *nature* 398.6730 (1999), pp. 786–788.

[8] D. Loss and D. P. DiVincenzo. "Quantum computation with quantum dots". In: *Physical Review A* 57.1 (1998), p. 120.

[9] A. Gruber, A. Drabenstedt, C. Tietz, L. Fleury, J. Wrachtrup, and C. v. Borczyskowski. "Scanning confocal optical microscopy and magnetic resonance on single defect centers". In: *Science* 276.5321 (1997), pp. 2012–2014.

[10] A. Y. Kitaev. "Unpaired Majorana fermions in quantum wires". In: *Physics-uspekhi* 44.10S (2001), p. 131.

[11] J. I. Cirac and P. Zoller. "Quantum computations with cold trapped ions". In: *Physical review letters* 74.20 (1995), p. 4091.

[12] D. P. DiVincenzo. "The Physical Implementation of Quantum Computation". In: *Fortschritte der Physik* 48 (9-11 Sept. 2000), pp. 771–783. ISSN: 00158208.

[13] J. Preskill. "Quantum Computing in the NISQ era and beyond". In: *arXiv:1801.00862* (Jan. 2018).

[14] P. W. Shor. "Scheme for reducing decoherence in quantum computer memory". In: *Physical review A* 52.4 (1995), R2493.

[15] A. G. Fowler, M. Mariantoni, J. M. Martinis, and A. N. Cleland. "Surface codes: Towards practical large-scale quantum computation". In: *Physical Review A - Atomic, Molecular, and Optical Physics* 86 (3 Sept. 2012). ISSN: 10502947.

[16] D. Wecker, B. Bauer, B. K. Clark, M. B. Hastings, and M. Troyer. “Gate-count estimates for performing quantum chemistry on small quantum computers”. In: *Physical Review A* 90.2 (2014), p. 022305.

[17] B. M. Terhal. “Quantum error correction for quantum memories”. In: *Reviews of Modern Physics* 87.2 (2015), pp. 307–346.

[18] L. M. Vandersypen and M. A. Eriksson. “Quantum computing with semiconductor spins”. In: *Physics Today* 72 (8 Aug. 2019), pp. 38–45. ISSN: 00319228.

[19] A. M. J. Zwerver, T. Krähenmann, T. F. Watson, L. Lampert, H. C. George, R. Pillarisetty, S. A. Bojarski, P. Amin, S. V. Amitonov, J. M. Boter, R. Caudillo, D. Correas-Serrano, J. P. Dehollain, G. Droulers, E. M. Henry, R. Kotlyar, M. Lodari, F. Lüthi, D. J. Michalak, B. K. Mueller, S. Neyens, J. Roberts, N. Samkharadze, G. Zheng, O. K. Zietz, G. Scappucci, M. Veldhorst, L. M. K. Vandersypen, and J. S. Clarke. “Qubits made by advanced semiconductor manufacturing”. In: ().

[20] I. Merkulov, A. L. Efros, and M. Rosen. “Electron spin relaxation by nuclei in semiconductor quantum dots”. In: *Physical review B* 65.20 (2002), p. 205309.

[21] J. Taylor, J. Petta, A. Johnson, A. Yacoby, C. Marcus, and M. Lukin. “Relaxation, dephasing, and quantum control of electron spins in double quantum dots”. In: *Physical Review B—Condensed Matter and Materials Physics* 76.3 (2007), p. 035315.

[22] G. Scappucci, P. Taylor, J. Williams, T. Ginley, and S. Law. “Crystalline materials for quantum computing: Semiconductor heterostructures and topological insulators exemplars”. In: *MRS Bulletin* 46.7 (2021), pp. 596–606.

[23] G. Scappucci, C. Kloeffel, F. A. Zwanenburg, D. Loss, M. Myronov, J.-J. Zhang, S. De Franceschi, G. Katsaros, and M. Veldhorst. “The germanium quantum information route”. en. In: *Nature Reviews Materials* 6.10 (Oct. 2021), pp. 926–943. ISSN: 2058-8437.

[24] N. W. Hendrickx, D. P. Franke, A. Sammak, M. Kouwenhoven, D. Sabbagh, L. Yeoh, R. Li, M. L. V. Tagliaferri, M. Virgilio, G. Capellini, G. Scappucci, and M. Veldhorst. “Gate-controlled quantum dots and superconductivity in planar germanium”. En. In: *Nature Communications* 9.1 (July 2018), p. 2835. ISSN: 2041-1723.

[25] N. Hendrickx, D. Franke, A. Sammak, G. Scappucci, and M. Veldhorst. “Fast two-qubit logic with holes in germanium”. In: *arXiv preprint arXiv:1904.11443* (2019).

[26] N. W. Hendrickx, W. I. L. Lawrie, L. Petit, A. Sammak, G. Scappucci, and M. Veldhorst. “A single-hole spin qubit”. en. In: *Nature Communications* 11.1 (July 2020), p. 3478. ISSN: 2041-1723.

[27] N. W. Hendrickx, M. L. V. Tagliaferri, M. Kouwenhoven, R. Li, D. P. Franke, A. Sammak, A. Brinkman, G. Scappucci, and M. Veldhorst. “Ballistic supercurrent discretization and micrometer-long Josephson coupling in germanium”. In: *Phys. Rev. B* 99.7 (Feb. 2019), p. 075435.

[28] F. Vigneau, R. Mizokuchi, D. C. Zanuz, X. Huang, S. Tan, R. Maurand, S. Frolov, A. Sammak, G. Scappucci, F. Lefloch, and S. De Franceschi. “Germanium Quantum-Well Josephson Field-Effect Transistors and Interferometers”. In: *Nano Lett.* 19.2 (Feb. 2019), pp. 1023–1027. ISSN: 1530-6984.

2

GERMANIUM QUANTUM TECHNOLOGY

2.1. GE/SIGE HETEROSTRUCTURES

Si and Ge share the same zincblende crystal structure with a lattice constant of a_{Si} = 0.5431nm a_{Ge} = 0.5658nm respectively. The epitaxial growth of strained Ge/SiGe heterostructure provides a compelling material platform for exploring the physical properties of quantum confined holes. Layers of Ge and SiGe can be stacked to provide a potential landscape which confines holes in the z-direction, while the biaxial strain in the x and y direction can be used to tune the physical properties of the confined carriers.

2.1.1. BAND STRUCTURE OF STRAINED GE QUANTUM WELLS

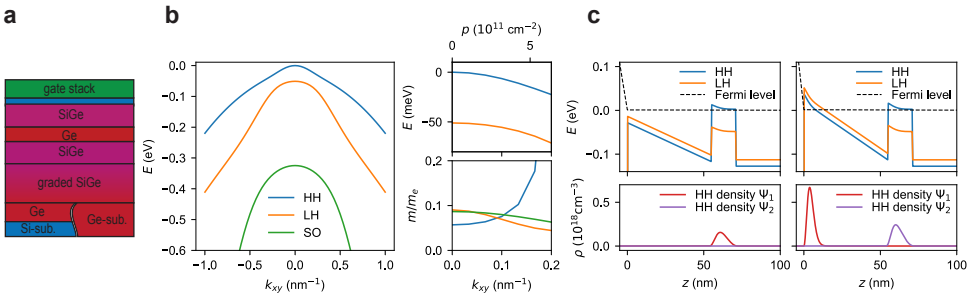

Figure 2.1: a) Schematics of a Ge/SiGe heterostructure. **b)** Band structure for a tensile strained Ge QW of a Ge $Si_{0.2}Ge_{0.8}$ heterostructure calculated with 6-band k.p, the inset on the top right shows a zoom in around the Γ point ($k_{xy} = 0$) and the one at the bottom right shows the calculated effective mass for the different bands. **c** 1D Schrödinger-Poisson simulation of a Ge/$Si_{0.2}Ge_{0.8}$ QW with a 55 nm SiGe spacer. An electric field is applied from a top gate separated from 30 nm of Al_2O_3 from the SiGe spacer. The HH and LH band edges are plotted as a function of z (opposite to the growth direction of the heterostructure) for a small and a larger electric field (left and right panel respectively). The bottom panels show the hole density for the first two energy states.

Ge valence band electrons (holes) are situated in p-orbitals and a 6 fold degeneracy is expected (from quantum numbers $l = 1$ and $s = 1/2$). However due to spin orbit the angular momentum **L** and the spin **S** are coupled and therefore the total angular momentum $\mathbf{L} = \mathbf{S} + \mathbf{J}$ characterizes the electron states. At the top of the valence band the six fold degeneracy spits into 4-fold degenerate states corresponding to j=3/2 and 2-fold degenerate states corresponding to j=1/2 [1] and at the Γ point they are separated by the spin-orbit gap Δ_0.

The 4-fold degenerate states at the top of the valence band can be described with the Luttinger-Kohn Hamiltonian. These states further split depending on the projections of **J** on **k** into the heavy hole band (HH) with $m_j = \pm 3/2$ and the light hole band (LH) with $m_j = \pm 1/2$.

Ge/SiGe heterostructures 2.1a can be used to confine holes in a Ge quantum well thanks to the band offset which results from the different band-gaps of Ge and SiGe. The Ge-SiGe interface of these heterostructures brakes the Ge crystal symmetry resulting in a splitting of the HH and LH bands and inverting the masses of these two bands at the Γ point. At the Γ point therefore the HH mass $m_{HH} = \frac{m_0}{\gamma_1+\gamma_s} = 0.055$ is lighter than the LH mass $m_{LH} = \frac{m_0}{\gamma_1-\gamma_s} = 0.125$ where the Luttinger parameters for Ge are for Ge, $\gamma_1 \approx 13$ and $\gamma_s \approx 5$ [1], meaning that HH and LH sub-bands have reversed characters for the in-plane motion. When epitaxially grown, the Ge in the quantum well is compressively strained in the xy direction, this biaxial strain further increases the HH-LH splitting. Figure 2.1b shows the valence-band of a strained Ge quantum well in a $Ge/Si_{0.2}Ge_{0.8}$ heterostructure. At the Γ point the HH effective mass is $\sim 0.05 m_0$, for larger k-vectors the HH mass increases while the LH mass decreases and at k_{xy} ~0.09 nm^{-1} which corresponds to a hole density of ~1.3 10^{11} cm^{-2} the HH and LH masses cross.

Holes can be accumulated in the quantum well by applying an electric field in the z-direction, which tilts the valence band till the top of the HH band in the Ge quantum well region crosses the Fermi energy. Figure 2.1c shows the HH and LH bands and the resulting hole density upon the application of an electric field (from left to right the intensity of the electric field is increased). An increase in electric field results in an increase in hole density in the quantum well region, until the HH band at the SiGe-oxide interface crosses the Fermi level and forms a triangular well filled with holes at that interface (Fig. 2.1c right panel). From there onward a further increase in electric field results in an increase in hole density in the triangular well, leaving the density in the quantum well relatively unchanged.

The HH-LH splitting observed in the SiGe region in the simulation of Figure 2.1c arises from the residual tensile strain which is typical in heterostructures with a SiGe virtual substrate. This is due to the difference in thermal contraction coefficients of Si and Ge [2] from the growth temperature and only affects Ge/SiGe heterostructures grown on Si wafers.

2.1.2. CLASSICAL AND QUANTUM TRANSPORT METRICS IN 2D SYSTEMS

The transport properties of carriers confined in two-dimensional (2D) systems are a crucial tool to the development of quantum materials, offering insight on bandstructure properties, and information about disorder and impurities in the system. A transport experiment is typically performed with a Hall-bar device which it easy to fabricate

and quick to measure, thereby providing a rapid feedback to material stack design and growth. Some of the common metrics that can be extracted by such a device include the carrier effective mass (m^*), which accounts for the periodic electric potential of atoms in the crystal, this quantity is crucial in the design of the confinement potential for quantum dots as it determines the quantized levels energy spacing. The effective g-factor (g^*) which determines the energy levels splitting under a magnetic field. The carrier mobility (μ) at different carrier density (n) which gives insights on the uniformity of the potential landscape and the various scattering sources, and the quantum lifetime (τ_q) which is a good proxy for the quantum system quality.

Classical transport of a 2D electron/hole gas can be described by the following conductivity equation:

$$\boldsymbol{\sigma} = \begin{pmatrix} \sigma_{xx} & \sigma_{xy} \\ -\sigma_{xy} & \sigma_{xx} \end{pmatrix} = \frac{\sigma_0}{1+\omega_c^2\tau^2} \begin{pmatrix} 1 & -\omega_c\tau \\ \omega_c\tau & 1 \end{pmatrix} \tag{2.1}$$

with $\sigma_0 = ne^2\tau/m$ being the normal Drude conductivity, and $\omega_c = eB/m$ the cyclotron energy.

The resistivity is then defined as the inverse of the conductivity

$$\boldsymbol{\rho} = \begin{pmatrix} \rho_{xx} & \rho_{xy} \\ -\rho_{xy} & \rho_{xx} \end{pmatrix} = \boldsymbol{\sigma}^{-1} = \frac{1}{\sigma_0} \begin{pmatrix} 1 & \omega_c\tau \\ -\omega_c\tau & 1 \end{pmatrix} \tag{2.2}$$

The off-diagonal elements of resistivity matrix depend only on the density, and are therefore independent on the scattering time and the effective mass. Therefore measuring the transversal resistance R_{xy} gives directly access to the density (in cm^{-1}):

$$n = \left(\frac{dR_{xy}}{dB} e 10^4 \right)^{-1} \tag{2.3}$$

The mobility $\mu = v_d/E$ is defined as drift velocity (v_d) of the charge carriers per unit electric field (E) from the Drude formula we can derive $\sigma = ne\mu$ which enables us to calculate the mobility given the density and the longitudinal resistivity at zero magnetic field (ρ_0):

$$\mu = \left(ne\rho_0\right)^{-1} \tag{2.4}$$

From the mobility then one can calculate the transport lifetime $\tau_{tr} = \mu m^*/e$ and the mean free path $l_{mfp} = \hbar(2\pi n)^{1/2}\mu/e$.

A quantum mechanical treatment of free particles moving in a magnetic field requires to solve the following Hamiltonian

$$H = \frac{1}{2m}\left(\mathbf{p} + e\mathbf{A}\right)^2 \tag{2.5}$$

with $\mathbf{p}$ being the canonical momentum, and $\mathbf{A}$ being the gauge potential such that $\nabla \times \mathbf{A} = B\hat{\mathbf{z}}$. This Hamiltonian yields the following energy states:

$$E_n = \hbar\omega_c\left(n + \frac{1}{2}\right) \quad n \in \mathbb{N} \tag{2.6}$$

From which we learn that the energy levels of an electron (or hole) system in a magnetic field are quantized and equally spaced from each other with an energy separation proportional to the magnetic field. These levels are know as Landau levels.

The integer quantum Hall effect is a consequence of this quantization, and results in plateaus in the ρ_{xy} and vanishing of the ρ_{xx} for magnetic field values corresponding to

$$B = \frac{2\pi\hbar n}{\nu e} = \frac{n}{\nu}\Phi_0 \quad \nu \in \mathbb{Z} \tag{2.7}$$

On the ρ_{xy} plateaus the resistivity takes the value

$$\rho_{xy} = \frac{2\pi\hbar}{e^2}\frac{1}{\nu} \tag{2.8}$$

Peak mobility is often quoted as a metric for comparing the quality of 2D charge systems. Mobility itself however depends on the carrier density and on the effective mass m^*, which in the case of Ge/SiGe quantum wells, can vary even within the same sample depending on the density (k-vector) (Fig. 2.1). The transport time which $\tau_t = \mu m^*/e$ is independent of the mass, and therefore would be a more suitable metric for comparing 2D systems at the same carrier density. However, for 2D systems, mobility in general is not a good proxy for quality since the scattering events used to compute this metric are weighted by the scattering angle $1 - cos\theta_{kk'}$ [3], which makes forward scattering events (scattering with small angle θ) poorly captured by τ_t. A more suitable proxy for quality of a 2D system is the quantum lifetime τ_q. In a model which consider only remote and background impurities, with a 2D-density n_R of remote charged impurities at a distance d_R from the 2D electron/hole gas and a 2D-density n_B of background charge impurities, the two characteristic times are described by the following equation:

$$\frac{1}{\tau_{t,q}} = \frac{2\pi}{\hbar}\left(\frac{2\pi e^2}{\kappa}\right)^2 \int \frac{d^2k'}{(2\pi)^2}) \frac{\delta(E_k - E_{k'}}{q_{TF} + |k-k'|^2} f_{t,q}(\theta) \times \{n_e^{-2|k-k'|d_R} + n_B\}, \tag{2.9}$$

where the only difference between τ_t and τ_q is the factor $f_t(\theta) = 1 - cos\theta_{kk'}$ and $f_q(\theta) = 1$. In the limit $2k_F d_R \gg 1$ one can write an analytical solution to the integral

$$\tau_t^{-1} = A_t^{(R)} n_R/(2k_F d_R)^3 + A_t^{(B)} n_B, \tag{2.10}$$

$$\tau_q^{-1} = A_q^{(R)} n_R/(2k_F d_R) + A_q^{(B)} n_B, \tag{2.11}$$

where A is a prefactor [3]. If the condition

$$2k_F d_R \ll n_R/n_B \ll (2k_F d_R)^3 \tag{2.12}$$

is satisfied the transport lifetime (mobility) is controlled by background impurities while the quantum lifetime or quality (quantum mobility) is controlled by the remote impurities, giving rise to a mobility/quality dichotomy.

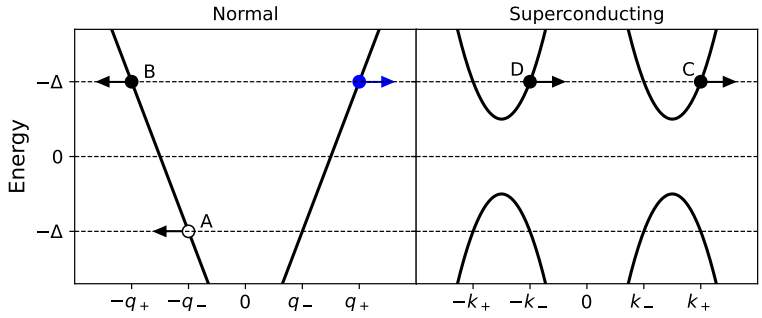

Figure 2.2: Schematic diagram of energy vs momentum at the normal-superconducting interface for an electron incident to an NS interface (blue dot), along with the transmitted and reflected particles resulting from different mechanisms. Open and closed circles denote electrons receptively. The arrows represent the group velocity. The blue circle represents the impinging electron to the NS interface. Note: in the BTK theory the dispersion relation for a metal around the Fermi energy is approximated with a straight line.

2.2. HYBRID SUPERCONDUTOR-SEMICONDUCTOR SYSTEMS

2.2.1. TRANSPORT IN NS JUNCTION

Transport through a superconducting-normal interface with a delta barrier of strength Z in between is described by the BTK model [4]. An electron with energy $E > \Delta$, incident on a NS interface, can undergo through different processes described in Figure **??** and for each process a probability is defined. B is the probability that the electron is elastically reflected into a state with opposite momentum. C is the probability of transmission through the NS interface into a quasi-particle state with the same wave vector at the same side of the Fermi surface. D is the probability of transmission to a state with same group velocity but at the opposite side Fermi surface. And finally, A is the probability of Andreev reflection as a hole on the opposite side of the Fermi surface, this process involves the transfer of a pair across the interface with charge $2e$. In the Andreev reflection process the hole is generated as far below the chemical potential as much as the incident electron was above, this condition ensures energy conservation. Note that for energy conservation the sum of the probabilities $A(E)+B(E)+C(E)+D(E)=1$, and for energies below the gap $E<\Delta$ there can be no transmitted quasiparticles, so that $C=D=0$.

The current through an NS interface is given by

$$I_{NS} = 2N(0)e v_F \mathscr{A} \int_{-\infty}^{\infty} \left[f(E-eV) - f(E) \right] \left[1 + A(E) - B(E) \right] dE \tag{2.13}$$

with $N(0)$ being the density of state of the metal, v the fermi velocity, $\mathscr{A}$ is an effective-neck cross-sectional area, and f the Fermi-Dirac distribution. Figure 2.3a shows the differential conductance calculated from the current from the equation above, as a function of the applied voltage bias for different transparencies for a single mode. For low transparencies the in gap conductance is strongly suppressed, while for high transparencies the ingap conductance doubles owing to the Andreev reflection process which effectively transports 2 electrons at the time.

When $T=0$ the quantity $[1+A(eV)-B(eV)]$ is proportional to the differential con-

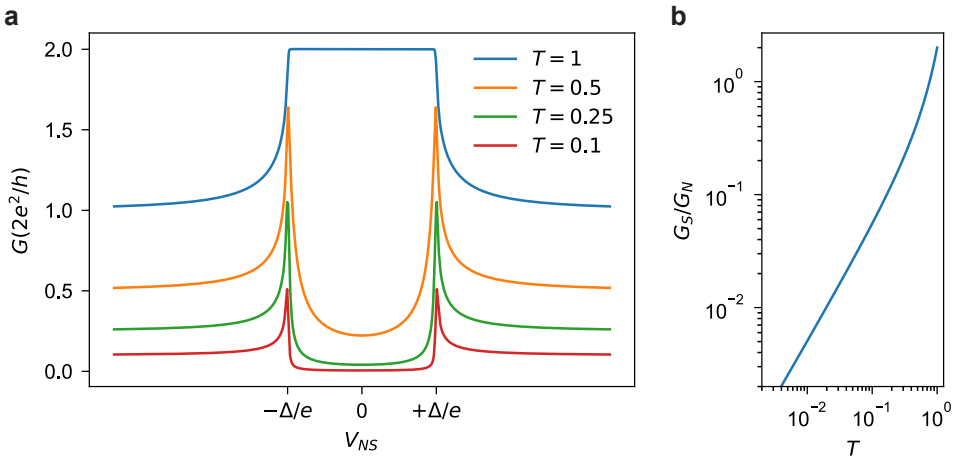

Figure 2.3: **a)** Simulated differential conductance across an NS junction as a function of the bias voltage (V_{NS} for different transparencies T. **b)** Simulated zero-bias conductance ratio G_S/G_N vs transparency T.

ductance $G = dI/dV$:

$$G(V_{NS}) = \frac{2e^2}{h}(1 + A(eV_{NS}) - B(eV_{NS})) \tag{2.14}$$

with V_{NS} being the bias applied across the junction. For perfect transmission ($T = 1$, $Z = 0$) the conductance exhibit a plateau at $4e^2/h$ inside the gap, which indicates the the incident electrons are perfectly Andreev reflected. For small transmission (strong barrier Z»1) the in-gap conductance is strongly suppressed compared to the out of gap conductance. Conductance through a single channel at zero bias (G_S) is well described by the Beenakker formula [5]

$$G_S = \frac{2e^2}{h}\frac{2T^2}{(2-T)^2} \tag{2.15}$$

Single channel conductance for a metal-metal junction is $G_N = \frac{2e^2}{h}T$, this is also the conductance expected for a NS junction when the applied bias is much larger than the gap $V_{NS} \gg \Delta$

$$G_S/G_N = \frac{2e^2}{h}\frac{2T}{(2-T)^2} \tag{2.16}$$

The ratio in-gap to out-of-gap conductance (plotted in Figure 2.3) is commonly used to asses the quality of the superconducting gap. A good fit with the BTK model or the Beenakker model ensures the absence of quasi-particle states within the gap which may arise from disorder or impurities at the NS interface. In the absence of in gap states we call the superconducting gap a hard gap. We note that a two-orders of magnitude suppression of in-gap conductance compared to the out-of-gap conductance is consistent with a hard gap only when the out-of-gap conductance is $G_N \sim 0.02$.

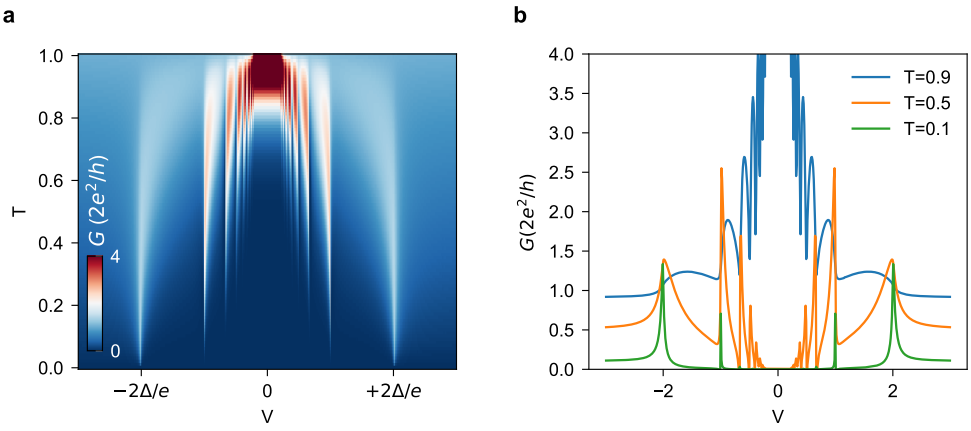

Figure 2.4: **a)** Simulated differential conductance through a SNS junction for different bias voltages V and different transparencies computed numerically using the scattering approach [6]. **b)** Linecuts from panel a.

2.2.2. TRANSPORT IN SNS JUNCTION

Supercurrent transport in an superconducting-normal-superconducting (SNS) junction is mediated by Andreev reflection processes. When a SNS junction is biased and the bias and the bias is $eV < 2\Delta$ with Δ being the superconducting gap, single particle transport is not allowed as there are no direct states to tunnel to. However charge can still be transported via multiple Andreev reflection processes. In a MAR process of order $n = 1$ a single Andreev reflection occurs: an electron from the valence band of the left superconductor is Andreev reflected on the right NS interface and the hole is injected back in the valence band of the left superconductor. A MAR process of order $n = 2$ involves two Andreev reflections, first a hole is Andreev reflected from the incident electron on the right NS interface, this hole then is incident on the left NS interface but has energy within the superconducting gap of the left superconductor, so an electron is Andreev reflected from the left NS interface and finally injected in the conduction band of the right superconductor. This effectively transports a cooper pair and one electron from the left superconductor to the right superconductor. This MARs processes give rise to conductance peaks at specific bias voltages, if the superconducting gap of the left and right superconductor is the same, then conductance peaks are observed at $2\Delta/ne$ with n being the order of the MAR process. For normal regions with transmission of the N section $T < 1$ the contribution of the n-th order MAR is reduced by T^n, therefore observing larger order MARs implies a higher transparency of the SNS junction.

2.2.3. JOSEPHSON JUNCTIONS AND SQUIDS

A Josephson junction (JJ) consist of two superconducting electrodes connected by a weak link. This weak link can be an insulating layer (as initially proposed by Josephson), a normal layer, or a constriction in the superconductor. Transport through a Josephson junction is described by the Josephson equations

$$I = I_c \sin \Delta\varphi, \tag{2.17}$$

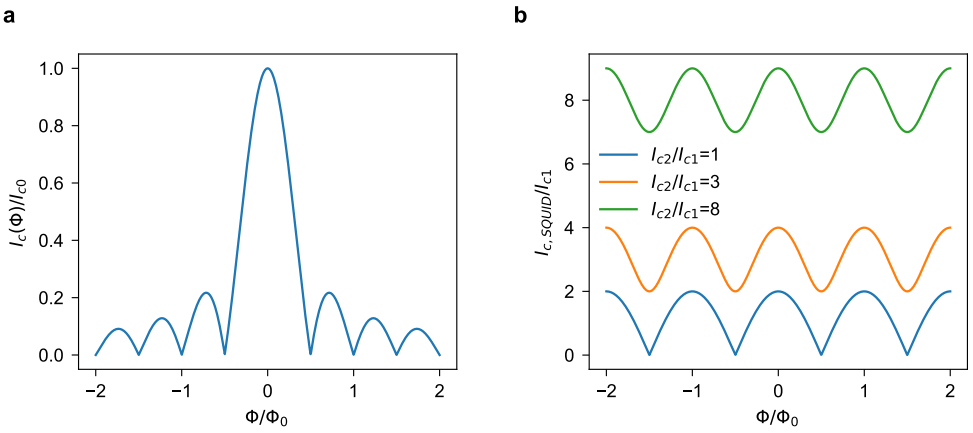

Figure 2.5: **a)** Critical current of a Josephson junction as a function of magnetic flux through the junction, also referred to as Fraunhofer patter. **b)** SQUID critical current I_c vs magnetic flux through the SQUID Φ for different ratios of the critical current of the two separate junctions of the squid I_{c2}/I_{c1}

where $\Delta\varphi$ is the difference in the phase of the Ginzburg-Landau wavefunction in the two electrodes, and I_c is the critical current of the junction.

$$\frac{d\varphi}{dt} = \frac{2e}{\hbar}V \tag{2.18}$$

Which indicate that an alternating current results from applying a bias (V) to the junction.

When a rectangular Josepshon junction is placed in a magnetic field (B) an interference pattern is observed (Fig. 2.5a), which is described by:

$$I_c(B) = I_{c,0}\left|\frac{\sin(\pi\Phi/\Phi_0)}{(\pi\Phi/\Phi_0)}\right| \tag{2.19}$$

with $I_{c,0}$ the critical current at zero field, and Φ_0 the flux quantum, and $\Phi = B_\perp A$ is the quantum flux through the junction area A (the effective area is typically larger than the geometric area due to the flux focusing effect from the superconducting leads).

A DC SQUID consist of two JJs connected in parallel and connected by a superconducting loop. The supercurrent through this device is:

$$I_{SQUID} = I_{c1}\sin(\varphi_1) + I_{c2}\sin(\varphi_2) \tag{2.20}$$

where φ_1 and φ_2 are the phase differences across each junction. These are related to the magnetic flux Φ through the superconducting loop by:

$$\varphi_1 - \varphi_2 = 2\pi\frac{\Phi}{\Phi_0} \tag{2.21}$$

From the last two equation one can calculate the critical current for the SQUID:

$$I_{c,SQUID} = \sqrt{I_{c1}^2 + I_{c2}^2 + 2I_{c1}I_{c2}\cos\left(2\pi\frac{\Phi}{\Phi_0}\right)} \tag{2.22}$$

Figure 2.5 shows the SQUID critical current vs flux for different ratios I_{c2}/I_{c1}.

Measurements of SQUIDs are used as a common experimental method to investigate the current phase relation (CPR) of a Josephson junction. This is possible if the critical current of the junction under investigation is much smaller than the other junction ($I_{c1} \ll I_{c2}$). In these conditions the magnetic flux modulates the phase difference of the junction with smaller critical current, while on the other junction it remains relatively constant.

2.2.4. PROXIMITY EFFECT

The BTK model assumes a step-like superconducting pair potential at the NS interface. In reality the cooper pairs can leak into the normal conductor where, although there is no strong enough electron-phonon interaction to overcome Coulomb repulsion, they can maintain phase coherence for a certain time, before it is destroyed by scattering events. The phase coherence decay in the normal part of the NS junction decays exponentially with characteristic coherence length ξ_N. One can distinguish to cases for which the coherence lenght can be described analytically. The clean case where the scattering length is much larger than the coherence length ($l_e \gg \xi_e$):

$$\xi_N^c = \frac{\hbar v_F}{2\pi k_B T} = \frac{\hbar^2\sqrt{2\pi}}{2\pi m^* k_B T}\sqrt{n} \tag{2.23}$$

and the dirty limit where $l_e \gg \xi_e$ which results in

$$\xi_N^d = \sqrt{\frac{\hbar D_n}{2\pi k_B T}} = \sqrt{\frac{\hbar^3}{2m^* e k_B T}}\sqrt{\mu n} \tag{2.24}$$

In the dirty limit the coherence length depends in the square root of the density and mobility of the normal region.

2.3. HOLE SPIN QUBITS IN QUANTUM DOTS

Ge/SiGe heterostructures allow to define a confining potential for holes in the z direction. In these structures, single charges can be confined by patterning electrostatics gates on top of the heterostructures, therefore providing an electrical mean for shaping the lateral electrostatic potential. The spin of a single electron or hole in a magnetic field can then be used as a physical system to implement a qubit.

2.3.1. ELECTROSTATICALLY DEFINED QUANTUM DOTS

With the confinement in the z-direction provided by the band alignment of the different layers of the heterostructure, the confinement in the x- and y-directions can be achieved by shaping the potential landscape by patterning metal electrodes and applying an electrical potential. Since the Ge QW populates with holes upon application of a negative potential, it is sufficient to use a circular metal electrode (plunger gate) biased to a negative potential to confine a quantum dot. In practice, to control the tunnel coupling with neighboring dots or with Ohmic contacts and to screen the electric field of the lead to the plunger gate, smaller barrier electrodes often surround the plunger gate. These barrier

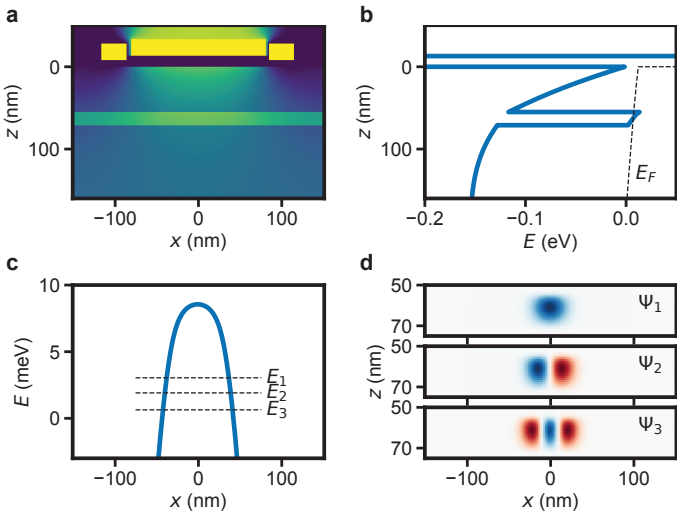

Figure 2.6: 2D Schrödinger-Poisson simulation of a quantum dot device in a $Ge/Si_{0.2}Ge_{0.8}$ heterostructure with a 55 nm SiGe spacer and a 16 nm QW. Two barrier gates (30 nm diameter) and a plunger gate (180 nm diameter) are position on top of the heterostructure separated by 5 and 10 nm of Al_2O_3 respectively. **a)** colorplot of the HH band edge with a negative potential applied to the barrier and the plunger gate. **b)** line-cut of the HH band edge in panel a at $x = 0$ along with the Fermi energy E_F. **c)** line-cut of the HH band edge in panel a at $z = 60$ (within the QW region) along with the first three energy levels. **d** wavefunction amplitudes of the first three states.

and screening gates can be grounded if their purpose is just to screen an electrode or are biased positively or negatively to shape the confinement potential or to tune the tunnel coupling.

Figure 2.6 a shows the potential landscape calculated from a 2D Schrödinger-Poisson simulation of a $Ge/Si_{0.2}Ge_{0.8}$ quantum well with a plunger gate and a barrier gate on each side. Linecuts of the potential landscape along the x and z directions are presented in panels b and c respectively. Panel b shows for $x = 0$, that the edge of the HH band rapidly decays moving away from the surface, unlike a Hall-bar device where the potential decays linearly due to the infinitely large gate size. This poses a limit on how far the quantum well can be positioned from the surface before states become available for holes in the SiGe spacer. Panel c shows the harmonic like potential potential of the HH band-edge in a line-cut along the x axis taken at the center of the QW, along with the first three energy states. We note that the position of the first energy state is pushed to lower energies due to the sharp QW confinement in the z-direction. Since in a real system it is desirable to obtain the dot at the center of the plunger and to minimize the risk of creating spurious dots, it is crucial that the first energy level lies below the potential fluctuations of the HH band edge that arise from disorder in the material stack. To achieve this, one can shrink the QW width or the plunger gate diameter to create a stronger confinement potential. Panel d shows the wavefunction amplitude for the first three energy states.

2.3.2. QUBIT CONTROL AND READOUT

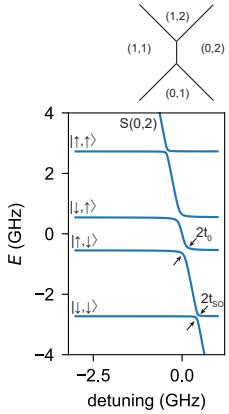

Figure 2.7: Energy diagram of a double quantum dot, along with the charge stability diagram aligned with the detuning axis. The spin orbit interaction term (t_so) enables a coupling between S(0,2) and the parallel spin states. The inter-dot tunneling coupling term (t_0) enables coupling between the S(0,2) and the antiparallel spin states. The detuning is set to 0 at the inter-dot line between (1,1) and (0,2).

If we consider the 6 lowest energy states of a double quantum dot system and write the Hamiltonian in the two spin basis $\{|2,0\rangle, |0,2\rangle, |\uparrow,\uparrow\rangle, |\downarrow,\uparrow\rangle, |\uparrow,\downarrow\rangle, |\downarrow,\downarrow\rangle\}$:

$$H = \begin{pmatrix} U-\epsilon & 0 & -t_{\mathrm{SO},y}+it_{\mathrm{SO},x} & t_0-it_{\mathrm{SO},z} & -t_0-it_{\mathrm{SO},z} & -t_{\mathrm{SO},y}-it_{\mathrm{SO},x} \\ 0 & U+\epsilon & -t_{\mathrm{SO},y}+it_{\mathrm{SO},x} & t_0+it_{\mathrm{SO},z} & -t_0+it_{\mathrm{SO},z} & -t_{\mathrm{SO},y}+it_{\mathrm{SO},x} \\ -t_{\mathrm{SO},y}-it_{\mathrm{SO},x} & -t_{\mathrm{SO},y}-it_{\mathrm{SO},x} & E_Z & \delta E_Z/2 & 0 & 0 \\ t_0+it_{\mathrm{SO},z} & t_0-it_{\mathrm{SO},z} & \delta E_Z/2 & 0 & -\delta E_Z/2 & 0 \\ -t_0+it_{\mathrm{SO},z} & -t_0-it_{\mathrm{SO},z} & 0 & -\delta E_Z/2 & 0 & -E_Z \\ -t_{\mathrm{SO},y}+it_{\mathrm{SO},x} & -t_{\mathrm{SO},y}-it_{\mathrm{SO},x} & 0 & 0 & -E_Z & 0 \end{pmatrix} \tag{2.25}$$

with t_0 being the inter-dot tunnel coupling and $\vec{t} = \{t_{so,x}, t_{so,y}, t_{so,z}\}$ the spin-orbit interaction which enables spin-flip tunneling. From performing perturbation theory we can define an analytical relation of the exchange energy J_0 as a function of detuning ϵ:

$$J_0 = \frac{4Ut_0^2}{U^2-\epsilon^2} \tag{2.26}$$

Initialization. The spins can be initialized by adiabatically (slowly) pulsing from the (0,2) to the center of the (1,1) charge region.

Single qubit gates. The full single qubit Hilbert space can be accessed by applying a microwave pulse which results into a effective magnetic field orthogonal to the direction of B to the qubit resonant to the Zeeman splitting $E_Z = g^*\mu_B B$. The length of the pulse determines the angle of spin rotation, while the phase of the microwaves determines the direction of the rotation axis. Together they allow to access any point in the Bloch sphere.

Two qubit gates. Two qubit gates can be implemented via the exchange interaction (J_0). The strength of J_0 is typically controlled by either varying the detuning (to increase the exchange,, one can pulse the detuningtoward the anti-crossings) or by varying the tunnel coupling (exchange increases when tunnel coupling is increased),

Read-out. The magnetic moment of an electron or hole spin is very small and therefore hard to measure directly. To overcome this limitation, one can use spin-to-charge conversion. A common way to achieve spin-to-charge conversion is to use the Pauli spin blockade readout mechanism. This technique involves two tunnel coupled quantum dots in a finite magnetic field. The detuning of the double quantum dot system is adiabatically pulsed from the (1,1) charge region to the (0,2) charge region, the lowest laying antiparallel state is the only state which can adiabatically get to the S(0,2), while the remaining three states are blocked in the T(1,1) until due to spin relaxation eventually decays the system into the S(0,2) ground state.

BIBLIOGRAPHY

[1] R. Winkler, S. Papadakis, E. De Poortere, and M. Shayegan. *Spin-orbit coupling in two-dimensional electron and hole systems*. Vol. 41. Springer, 2003.

[2] A. Sammak, D. Sabbagh, N. W. Hendrickx, M. Lodari, B. P. Wuetz, A. Tosato, L. Yeoh, M. Bollani, M. Virgilio, M. A. Schubert, P. Zaumseil, G. Capellini, M. Veldhorst, and G. Scappucci. "Shallow and Undoped Germanium Quantum Wells: A Playground for Spin and Hybrid Quantum Technology". en. In: *Advanced Functional Materials* 29.14 (2019), p. 1807613. ISSN: 1616-3028.

[3] S. Das Sarma and E. H. Hwang. "Mobility versus quality in two-dimensional semiconductor structures". In: *PHYSICAL REVIEW B* 90 (2014), p. 35425.

[4] G. E. Blonder, M. Tinkham, and T. M. Klapwijk. "Transition from metallic to tunneling regimes in superconducting microconstrictions: Excess current, charge imbalance, and supercurrent conversion". In: *Physical Review B* 25.7 (1982), pp. 4515–4532. ISSN: 01631829.

[5] C. W. J. Beenakker. "Quantum transport in semiconductor-superconductor microjunctions". In: *PHYSICAL REVIEW B* 46 (1992), pp. 15–1992.

[6] D. Averin and A. Bardas. "ac Josephson effect in a single quantum channel". In: *Physical Review Letters* 75.9 (1995), pp. 1831–1834. ISSN: 00319007.

3

METHODS

3.1. BANDSTRUCTURE DESIGN AND SIMULATIONS

3.1.1. SCHRÖDINGER-POISSON

The self consistent Schrödinger-Poisson equation is key tool to design new heterostructures and devices as it allows to simulate charge carriers in quantum-confined systems upon the application of electrical potentials. Initially I developed a python based code to perform 1D simulations which allows to simulate confinement of carriers in 2D, then we moved to a commercial tool (Nextnano) which provides also support for 2D and 3D simulations.

The simulation process consists in iteratively solving the Poisson and Schcrödinger equations. First the Poisson equation is solved

$$-\nabla \cdot (\epsilon \nabla V) = \rho \tag{3.1}$$

where V is the electrical potential, ϵ is the permittivity and ρ the spatial charge density.

Second, the potential energy $U = qV$ is added to the band edge energy profile of the heterostructure and plugged in the Schcrödinger equation, then the latter is solved with a numerical model. For this we used a matrix solutions of the discretised Schrödinger equation

$$\frac{-h^2}{2m^*}\frac{\partial^2}{\partial z^2}\psi(z) + U(z)\psi(z) = E\psi(z) \tag{3.2}$$

Using the finite-difference on the second derivitive and taking a small δz such that the approximation is good, then:

$$a_i\phi_{i-1} + b_i\phi_i + c_i + \phi_{i+1} = E\phi_i \tag{3.3}$$

with

$$a_{i+1} = c_i = \frac{\hbar^2}{2m^*(\delta z)^2} \quad \text{and} \quad b_i = \frac{\hbar^2}{m^*)(\delta z)^2} + V_i \tag{3.4}$$

where each index i denotes a sample of the wavefunction such that $\phi_0 = \phi(0)$, $\phi_1 = \delta_z$) and so on. Taking the standard boundary condition $\phi_0 = \phi_{N+1} = 0$ eq. 3.3 can be expressed at each point using a system of equations which can be represented in matrix form:

$$\mathrm{H}\psi = E\psi \tag{3.5}$$

with H being the coefficient matrix:

$$\mathrm{H} = \begin{pmatrix} b_1 & c_1 & 0 & \cdots & 0 \\ a_2 & b_2 & c_2 & \cdots & 0 \\ 0 & \ddots & \ddots & \ddots & \vdots \\ \vdots & & a_{N-1} & b_{N-1} & c_{N-1} \\ 0 & \cdots & 0 & a_N & b_N \end{pmatrix} \tag{3.6}$$

The solution of this eigenvalue problem yields to the wavefunction and respective energies of the system.

Third the electron/hole density profile is calculated from the weighted sum of the probability densities

$$\eta_{\mathrm{tot}}(z) = \sum_i N_i |\Psi_i|^2 \tag{3.7}$$

where the the weight N_i is given by integrating the Fermi-Dirac distribution for the energy level E_i.

Finally, the so obtained charge density is plugged back into the Poisson equation (step 1) and the steps are repeated until convergence.

3.1.2. FERMI HUBBARD

To perform simulations of the charge stability diagram of two tunnel coupled quantum dots we use the Fermi-Hubbard model:

$$H = H_\mu + H_t + H_U + H_J \tag{3.8}$$

The first term describes the chemical potential energy

$$H_\mu = -\sum_{i\sigma} \mu_i n_{i\sigma} \tag{3.9}$$

the second term describes the tunnel coupling

$$H_t = -\sum_\sigma (t^\dagger_{c_{1\sigma}} c_{2\sigma} + h.c.) \tag{3.10}$$

the third term consists of the Coulomb repulsion

$$H_U = U_1 n_{1\uparrow} n_{1\downarrow} + U_2 n_{2\uparrow} n_{2\downarrow} + U_{12}(n_{1\uparrow} n_{2\downarrow} + n_{1\downarrow} n_{2\uparrow}) + (U_{12} - J_e)(n_{1\uparrow} n_{2\uparrow} + n_{1\downarrow} n_{2\downarrow}), \tag{3.11}$$

Solving the spinless part of this Hamiltonian and obtaining the transition lines corresponding to the interdot and reservoir transitions. This was particularly useful to interpret the results obtained for the vertical quantum dots in the Ge bilayer system (Chapter 8)

3.2. CRYSTAL GROWTH

The different heterostructures presented in this thesis are grown starting from a Si or a Ge substrate. First, a SiGe strain relaxed buffer (SRB) is grown, in order to produce a "virtual" substrate with the desired chemical composition and lattice constant. The chemical composition of the top layer of the SRB sets the band offset between the quantum well and the adjacent SiGe layers, this band offset arises from both the difference in bandgap between SiGe and Ge (Ge has the smaller bandgap) and the strain, determined by the lattice mismatch between Ge and SiGe. Second the active region of the heterostructure is grown this typically comprises a SiGe layer with composition that matches the top of the SRB, the Ge quantum well and another SiGe layer with the same composition. This same structure can be extended to multiple quantum wells interleaved with a layer of SiGe. Finally, the heterostructure is terminated by a Si cap which will form natural oxide when exposed to air.

A crucial aspect of the growth process is to manage strain relaxation in the SiGe SRB. The build up of strain originates from growing epitaxial layers with different chemical composition of Si and Ge, which have different lattice constant. The mechanism that allows for lattice relaxation is the addition of misfit dislocations in the crystal lattice, these dislocations extend in the <110> direction but get blocked when crossing each-other in the same plane, and generate a threading dislocation, which typically extends along the 111 planes. The pile-up of misfit dislocations in the SRB generates strain fluctuations in the substrate and in the quantum well. Such strain fluctuations give rise to the typical cross-hatch pattern visible with an optical microscope on the surface of the heterostructure. The threading dislocations can reach the surface of the heterostructure, inducing defects in the quantum well, and can be visualized at the microscope after a HCl etching process.

Overall, the Ge/SiGe heterostructures described in this thesis comprise the following parts:

1. substrate: Si or Ge wafer, this sets the lattice mismatch that the following SiGe SRB needs to accommodate.
2. SiGe strain relaxed buffer (SRB): comprising a graded and a uniform composition layer, it serves the purpose of engineering the lattice parameter of the subsequent quantum well.
3. Ge quantum well: is grown pseudomorphic to the SiGe SRB, therefore it has the same lattice parameter, which is mismatched to the substrate wafer.
4. SiGe barrier: is lattice matched to the QW and the SRB and serves the purpose to separate the QW from the dielectric interface
5. Cap: provides a better interface for subsequent processing.

3.2.1. EPITAXIAL DEPOSITION PROCESS

The Ge/SiGe heterostructures are grown at the Else Kooi Laboratories (EKL) of TU Delft via reduced-pressure chemical vapor deposition (RP-CVD) in an industrial reactor (ASMI Epsilon 2000). The substrate used for growing the heterostructures in this thesis is either

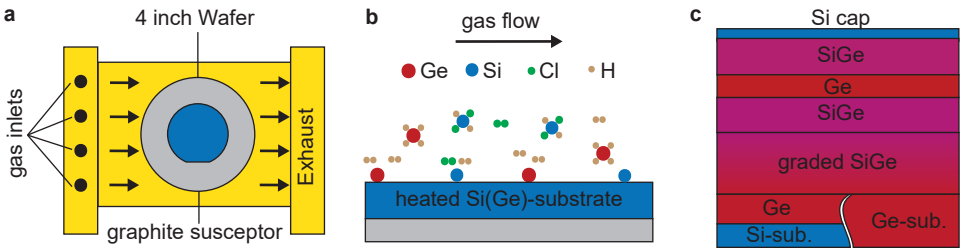

Figure 3.1: **Epitaxial Growth: a)** Schematics of the RP-CVD used to grow Ge/SiGe heterostructures. **b)** schematics of the wafer with the precursor gases reacting during growth. **c)**. Schematics of a Ge/SiGe heterostructure grown starting from either a Si or a Ge wafer.

a Si(001) or a Ge(001) wafer (diameter of 100 mm), to explore the influence of a different lattice mismatch that the SRB needs to accommodate onto the structural and electrical properties of the heterostructure. A schematic of the RP-CVD reactor is shown in Figure 3.1a, in the reactor chamber a selection of precursor gases flow along with the hydrogen carrier gas into the quartz chamber were the wafer is located on top of a graphite susceptor plate. The wafer is heated from from radiant heat supplied by lamp arrays on top and below the quartz chamber. We use germane and dichlorosilane as precursors to grow germanium and silicon which on the heated substrate undergo to the following reactions $SiH_2Cl_2 \rightarrow Si + H_2 + Cl_2$, $GeH_4 \rightarrow Ge + 2H_2$, yielding to an epitaxial deposition of Ge and Si (Fig. 3.1b).

Starting from a Si substrate, after a cleaning step, we grow a 420 C seed layer, after which we grow high T epitaxial Ge at 625 C and repeat this sequence 5 times. Then we anneal at 800 C. This process reduces the amount of threading dislocations to 1×10^6 cm^2 This is followed by a higher temperature (625 °C) relaxed Ge layer . The temperature is then increased to 800 °C to grow the graded $Si_{1-x}Ge_x$ layer where the chemical composition of the SiGe alloys (x) varies from 1 to the desired chemical composition (typically 0.8-0.9). The main reason to increase the temperature in this layer is to boost the growth rate given that the thickness of this layer is approximately 1 µm. These layers all together constitute the strain relaxed buffer (SRB).

Starting from a Ge substrate, after a cleaning step, we grow directly the 800 °C graded $Si_{1-x}Ge_x$ layer where the Ge concentration in the SiGe alloy (x) varies from 1 to the desired chemical composition. This forms the SRB.

Finally we grow the layers which define the quantum well: a constant composition layer of SiGe (matching the chemical composition of the top of the SRB), one or more Ge quantum wells, and a final layer of SiGe. The lower growth temperature of these layers (500 °C) is chosen as a trade-off between having a low background concentration of contaminants (lower oxygen content at higher temperatures) and sharp interfaces, whilst avoiding strain relaxation [1], in the proximity of the quantum well.

3.2.2. STRUCTURAL CHARACTERIZATION

We use a wide set of material characterization techniques to investigate the structural properties of the grown heterostructures and to inspect the fabricated devices. Some

of these analysis are outsourced to trusted companies to have reproducible results and baselines. The following list comprises the set of techniques commonly used to provide feedback to our material stack and fabrication, and that were key to the advancement presented in this thesis.

- Secondary ion mass spectroscopy (SIMS): We use the SIMS technique to assess the thickness, composition and isotopic concentration of the different layers which comprise the heterostructure.
- X-ray diffraction (XRD): The XRD technique provides us with insights on the lattice parameter of the semiconductor layers at the top of the heterostructure.
- Raman spectroscopy: allows to map the strain of the top most layer of the heterostructure in the planar direction.
- Tunneling electron microscopy (TEM): provides us with a clear picture of the cross-section of the heterostructure, from which we typically extract the thickness of the different layers and sharpness of the interfaces. It can be combined with energy discursive x-ray spectroscopy (EDX) or electron energy loss spectroscopy (EELS) to also provide respectively qualitative and quantitative information on the chemical composition. Further it allows to visualize defects and specifically dislocations.
- AFM: Atomic force microscopy is an essential feedback tool for fabrication, as it allows to non-destructively analyze the development of the resist after each lithographic step and the morphology of each layer of the device. It also allows to investigate the surface of the heterostructure, allowing to map roughness, strain fluctuations, and pits which may arise from contaminations.
- Optical inspection: at the naked eye, the reflectivity of a wafer correlates to the cristallinity, while the color provides insights on the composition of the top layers of the heterostructure, or on the different depth or thickness of the quantum well. With the microscope one can observe the cross-hatch pattern, which stems from the pile-up of misfit dislocations in the SRB, and correlates with the strain fluctuations in the heterostructure. Along with an HCl etching process in the growth chamber, the optical microscope also allows for quantifying the number of threading dislocations.

3.3. DEVICE FABRICATION

During my thesis I fabricated several devices, Figure 3.2a shows the most relevant ones. Hall-bar devices (a) were instrumental for the development and understanding of new heterostructures, e.g. bilayers, lowering the strain in the QW or switching from Si to Ge wafers (see results in chapters 4-7). Normal-superconductor QPCs and normal-superconductor-normal QPC devices, SQUID devices and superconductor-semiconductor arrays (b) were used for studying the superconductor-semiconductor systems in Ge (chapter 9). Quantum dots devices (c) were used for studying holes occupation of vertically stacked quantum dots (chapter 8 and charge noise in ref. [2]. A crossbar array of accumulation and barrier gates (d) was fabricated to map threshold voltages across a chip and where crucial

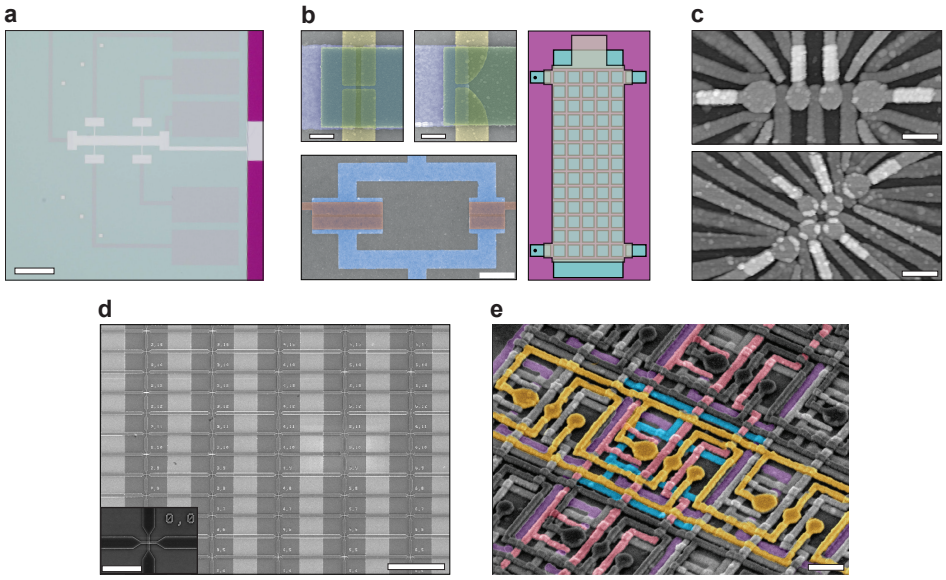

Figure 3.2: **Selection of devices I fabricated: a)** Optical image of a Hall-bar device (scale-bar corresponds to 20 µm). **b** The top two panels show SEM images of a SNS and a NS qpc (scale-bars corresponds to 300 nm). Bottom panel shows an SEM image of a SQUID device (scale-bar corresponds to 1 µm). Right panel shows schematics of a Hall-bar shaped device comprising an array of superconducting islands (light blue). **c)** AFM images of a two-dots device with two sensors (top), and a four-dots device with two sensors (bottom). Scale-bars corresponds to 100 nm. **d)** SEM image of a crossbar array where each unit cell comprises an horizontal accumulation gate crossed by a vertical barrier gate (scale-bar corresponds to 100 µm and 2 µm in the inset). **e** False colored SEM image of a QARPET device: a crossbar array with 529 unit cells where each unit cell comprises two quantum dots and a sensor (scale-bar corresponds to 325 nm).

to developing the fabrication techniques and skills necessary for more complex crossbar architecture. And finally, a qubit-array research-platform for engineering and testing (QARPET), a crossbar array of hosting over a thousand potential spin qubits with an interconnect compatible with modern dilution refrigerators (e).

The devices in this thesis are fabricated using a lift-off based multi-layer fabrication process. Starting from a 4 inch wafer, we dice the wafer in 20x20mm coupons. Each coupon typically contains 9 4x4mm cells which are diced into chips when the multi-layer fabrication is completed. For all devices in this thesis the first layer consist of alignment markers. These are typically made with a thick layer of Ti/Pt (3 nm if Ti and 50 nm or more of Pt), which thanks to the Pt high Z number is well suited for the SEM detection system of the e-beam lithography machine. The second layer we deposit is a thick insulating layer of Si_3N_4 which is positioned under the gate bonding pads, this ensures that when bonding a wire to a gate bonding pad no electrical short is created between the gate electrode and the quantum well.

3.3.1. HETEROSTRUCTURE FIELD EFFECT TRANSISTOR

Heterostructure field effect transistors consist of two layers, one for the ohmic contacts and one for the gate. These layers are typically patterned using a laser writer given their macroscopic size. First we pattern the ohmic layer and after resist development we perform a 15 s dip in buffer oxide etch to remove, within the ohmic contact, the thin Si oxide layer which caps the heterostructure. Then we deposit via e-beam evaporation 15-60nm of Pt, depending on the depth of the quantum well we are intending to contact. We anneal the Pt into the heterostructure either for 30 minutes at 300 °C in the ALD machine (next step) or at 400 °C for 15 min in the rapid thermal annealer in argon atmosphere. Both methods provide a sufficient thermal budget to promote the diffusion of Pt into the heterostructure. We then deposit via atomic layer deposition at 300 C a 30 nm thick layer of Al_2O_3 to insulate the ohmic layer from the gate layer. Finally, proceed with patterning and depositing 3 nm of Ti and 17 nm of Pd.

3.3.2. HYBRID SUPERCONDUCTOR-SEMICONDUCTOR DEVICES

Our approach to fabricating superconducting contacts for hybrid devices is to deposit a metal on top of the heterostructure and anneal it to form a metal-germanosilicide. The annealing process provides energy for a solid state reaction between the metal and the Si and Ge where the Pt diffuses into the SiGe and Si and Ge diffuse into metal. The fabrication of the superconducting PtGeSi contacts proceeds similarly to the fabrication of ohmic contacts, etching the Si cap, and depositing 15 nm of Pt via e-beam evaporation. We preform annealing in a rapid thermal annealer (the heat is provided by a infrared light source) in argon gas to ensure a non reactive environment. Then we deposit alternating layers of Al_2O_3 and TiPd gates which are used to define the shape of the electrostatical potential in the quantum well.

3.3.3. QUANTUM DOTS AND CROSSBAR ARRAYS

The fabrication process for quantum dots and crossbar arrays is similar to that for hybrid devices. Although the width of the ohmic contacts is rather small ~50 nm the Pt annealing recipe used for superconducting devices works well also to form small ohmic contacts close to the device. An important aspect of the fabrication of tightly packed gate layers (like in the case of crossbars) is to add additional topography to ease liftoff of enclosed areas, this can be done by patterning dummy squares and avoiding continuous long parallel electrode lines at sub-micron distance. We perform the liftoff of critical layers in a 40 C bath of AR600-74 with substantial sonication power for 1 h, with the coupon facing downwards to avoid particle deposition on the coupon.

3.4. CRYOGENIC SETUP AND MEASUREMENTS

During my Ph.D. I used different low-temperature systems to investigate the electrical properties of the devices.

3.4.1. DIPSTICK

This system allows to dip devices in liquid He at 4 K. It offers a fast way to characterize transport through devices and assess whether all gates are modulating the potential

landscape in the quantum well as desired. For Hallbar shaped devices one can apply an out of plane magnetic field, measure classical Hall effect through the device and calculate mobility, density, and capacitance of the device. This offers preliminary information on the quality of the heterostructure, stability of the device, and offers insights in possible flaws in the fabrication process. For Ge quantum dots the temperature is not sufficiently low compared to the charging energy and therefore a dipstick measurement only allows to verify the current flow through the sensor or a series of quantum dots and have a qualitative estimation of lever arm for the different gates.

3.4.2. VARIABLE TEMPERATURE INSERT (VTI)

The Variable Temperature Insert (VTI) is used for temperature sweeps, providing precise temperature control up to 10 K. This capability is particularly useful for measuring Germanium (Ge), where the lower effective mass results in increased energy level spacing. This enables to perform measurement in a temperature range relevant for extracting an estimate of the effective mass.

3.4.3. DILUTION REFRIGERATOR

For the electrical characterization of the devices, I used both wet dilution refrigerators (Leiden cryogenics, Oxford Kelvinox 300) and modern dry fridges (Oxford bottom loader, Bluefors LD-400). These systems allow to reach mK temperatures thanks to the cooling power provided by the separation of ^{3}He and ^{4}He phases. At temperatures below 870 mK the mixture of ^{3}He and ^{4}He undergoes to a spontaneous phase transition into a ^{3}He rich phase and a dilute phase with 6.6% concentration of ^{3}He. The ^{3}He is circulated in the system by taking it out from the ^{3}He-rich phase and pumping it back into the diluted phase. The cooling power is provided by the negative enthalpy of ^{3}He when passing from the diluted to the concentrated phase.

BIBLIOGRAPHY

[1] A. Sammak, D. Sabbagh, N. W. Hendrickx, M. Lodari, B. Paquelet Wuetz, A. Tosato, L. Yeoh, M. Bollani, M. Virgilio, M. A. Schubert, P. Zaumseil, G. Capellini, M. Veldhorst, and G. Scappucci. "Shallow and Undoped Germanium Quantum Wells: A Playground for Spin and Hybrid Quantum Technology". In: *Advanced Functional Materials* 29.14 (2019), p. 1807613. ISSN: 1616301X.

[2] L. E. Stehouwer, C. X. Yu, B. van Straaten, A. Tosato, V. John, D. D. Esposti, A. Elsayed, D. Costa, S. D. Oosterhout, N. W. Hendrickx, et al. "Exploiting epitaxial strained germanium for scaling low noise spin qubits at the micron-scale". In: *arXiv preprint arXiv:2411.11526* (2024).

4

LIGHT EFFECTIVE HOLE MASS IN UNDOPED GE/SIGE QUANTUM WELLS

One of the key properties of compressively strained germanium quantum wells is the predicted low effective mass of holes arising from strain and confinement along the 001 directions. In this work we study the dependence of the hole effective mass on the density in top-gated field effect transistors by positioning the strained buried Ge channel at different depths of 12 and 44 nm from the surface. We confirm the theoretically predicted dependence of increasing mass with density and by extrapolation we find an effective mass of $\sim 0.05 m_e$ *at zero density, the lightest effective mass for a planar platform that demonstrated spin qubits in quantum dots. The low effective mass and low disorder in this system allow for larger electrostatically defined quantum dots compared to Silicon, easing the fabrication process and the electrostatic control in the few holes regime.*

This work was originally published as:
M. Lodari, A. Tosato, D. Sabbagh, M. A. Schubert, G. Capellini, A. Sammak, M. Veldhorst, G. Scappucci, Light effective hole mass in undoped Ge/SiGe quantum wells. Physical Review B, 100(4), 041304 (2019).

4.1. INTRODUCTION

Holes are rapidly emerging as a promising candidate for semiconductor quantum computing.[1, 2, 3] In particular, holes in germanium (Ge) bear favorable properties for quantum operation, such as strong spin-orbit coupling enabling electric driving without the need of microscopic objects,[2, 3] large excited state splitting energies to isolate the qubit states,[4] and ohmic contacts to virtually all metals for hybrid superconducting-semiconducting research[5, 6, 7, 8, 9]. Furthermore, undoped planar Ge quantum wells with hole mobilities $\mu > 5 \times 10^5$ cm^2/Vs were recently developed[10] and shown to support quantum dots[11, 12] and single and two qubit logic,[3] providing scope to scale up the number of qubits.

Holes in strained Ge/SiGe quantum wells have the attractive property of a light effective mass parallel to the Ge well interface.[13, 14, 4] This property is highly desirable for spin qubits since it provides large energy level spacing in quantum dots, allowing to relax lithographic fabrication requirements and enhance tunnel rates. The light effective hole mass is due to the compressive strain in the quantum well, which splits the heavy hole and light hole bands and induces a mass inversion, i.e. the topmost band develops a lighter mass than the lower-lying band.[14] An effective hole mass of $0.05m_e$ was recently predicted[4] for Ge/$Si_{1-x}Ge_x$ heterostructures with alloy concentrations $x \sim 0.75$, corresponding to strain levels accessible experimentally.

Previous studies in modulation doped Ge/SiGe heterostructures showed, indeed, a very light effective mass of $0.055m_e$,[15] measured in Hall-bar devices aligned with the <110> crystallographic direction and further reduced to $0.035m_e$ for the <100> direction. The nonparabolicity effects of the valence bands[16, 17, 18, 19] tend to increase the effective mass, with smaller values expected at lower hole densities p due to the decreasing of the associated Fermi vector.

Modulation doping, however, exhibits impurities that are a source for charge noise, disorder, gate leakage, and device instability at low temperature.[20] Therefore, undoped Ge/SiGe quantum wells are preferable for quantum dot fabrication.[11] The transport properties of undoped Ge/SiGe quantum wells are relatively unexplored and effective mass measurements have shown so far conflicting results. In Ref. [21] a rather large effective mass of $0.105m_e$ was reported at a low density of 1×10^{11} cm^{-2}. Furthermore, no clear dependence of the effective mass with density could be extracted in the investigated range from $\sim 0.6 \times 10^{11}$ cm^{-2} to $\sim 1.4 \times 10^{11}$ cm^{-2}. In Ref. [22, 12], instead, a lighter mass was reported with a nearly constant value of $0.08m_e$ over the measured density range ($\sim 1-4 \times 10^{11}$ cm^{-2}).

In this Letter we reconcile experiments with theoretical expectations and provide evidence that the effective hole mass in low-disorder undoped Ge/SiGe decreases towards lower densities. We measure a minimum effective mass value of $0.061m_e$ at a density of 2.2×10^{11} cm^{-2}, which extrapolates to $(0.048 \pm 0.006)m_e$ at zero density. This makes strained Ge/SiGe the planar platform with the lightest effective mass for spin qubit devices.

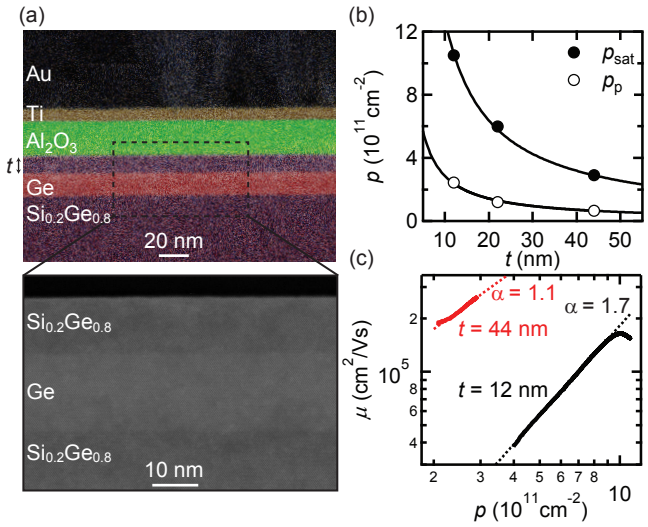

Figure 4.1: (a) STEM-EDX and TEM of a Ge/SiGe heterostructure field effect transistor with the quantum well positioned 12 nm under the gate stack. (b) Saturation p_{sat} and percolation density p_p as a function of the position of the quantum well t. Curves are fits to a $\sim 1/t$ dependence. Data for $t = 22$ nm are extracted from Ref [10]. (c) Density-dependent mobility $\mu(p)$ and power law fit.

4.2. STRUCTURAL AND ELECTRICAL CHARACTERIZATION

The undoped Ge/SiGe heterostructures are grown by reduced-pressure chemical vapor deposition and comprise a $Si_{0.2}Ge_{0.8}$ virtual substrate, a 16-nm-thick Ge quantum well (in-plane compressive strain of -0.63%) and a $Si_{0.2}Ge_{0.8}$ barrier. Two heterostructures of different barrier thickness are considered (t = 12, 44 nm). Hall-bar shaped heterostructure field effect transistors (H-FET) are fabricated aligned along the <110> direction using a low-thermal budget process which features platinum-germanosilicide ohmic contacts and an Al_2O_3/Ti/Au gate stack. Magnetotransport characterization of the devices is performed at temperature $T = 1.7 - 10$ K using standard four-probe low-frequency lock-in techniques.[1] A negative bias applied to the gate induces a two-dimensional hole gas and controls the carrier density in the quantum well. Details of the heterostructure growth, device fabrication and operation, and magnetotransport measurements are reported in Ref. [10].

Figure 4.1(a) shows scanning transmission electron microscopy with energy dispersive X-ray (STEM-EDX) analysis of the shallow Ge quantum well (t = 12 nm) under the gate stack. These images highlight the overall quality of the strained Ge H-FET. A uniform quantum well of constant thickness is obtained, and sharp interfaces are observed between the quantum well and the barrier and between the barrier and the dielectric layer.

The position of the quantum well determines the range of accessible density p in these Ge H-FETs. At a given t, the density range extends from the percolation threshold

1

density p_p (Fig. 4.1(b), open circles) to the saturation density p_{sat} (Fig. 4.1(b) , solid circles). Saturation of carriers in the quantum well is achieved at high gate bias when the Fermi level aligns with the valence band edge at the dielectric/SiGe interface.[23] We observe a $p_{sat} \sim 1/t$ dependence, as expected from Poisson's equation, indicating that charges in the system are in the equilibrium state.[24] The percolation threshold density represents the critical density for establishing metallic conduction in the channel. This is extracted by fitting the density-dependent conductivity in the low density regime to percolation theory,[25, 26] as applied in Ref. [10] to Ge H-FETs. We observe a $\sim 1/t$ dependence, expected for long-range scattering from remote impurities at the dielectric/semiconductor interface.[27, 28]

Figure 4.1(c) shows the density-dependent mobility μ at $T = 1.7$ K. The observed power law dependence $\mu \sim p^{\alpha}$ is characterized by an exponent α of 1.6 and 1.1 in the shallow (black line, $t = 12$ nm) and deeper quantum well (red line, $t = 44$ nm), respectively. The α values indicate that the mobility is limited by scattering from the dielectric/semiconductor interface, as previously observed in Si/SiGe and Ge/SiGe H-FETs.[29, 30, 24, 10] Despite the close proximity to the dielectric interface, the shallower quantum well has a remarkable peak mobility of 1.64×10^5 cm^2/Vs at $p = 1.05 \times 10^{12}$ cm^{-2}, 2.4× larger than previous reports for quantum wells positioned at a similar distance from the surface.[24] At higher density the mobility starts to drop, possibly due to occupation of the second subband or to different scattering mechanisms becoming dominant. The deeper quantum well ($t = 44$ nm) has a higher mobility of 2.6×10^5 cm^2/Vs at a much lower density of 2.9×10^{11} cm^{-2}, as expected due to the larger separation from the scattering impurities. We therefore find, by using Ge H-FETs with different t, that high values of mobility are achieved over a large range of density, making these devices well suited for Shubnikov-de Haas (SdH) measurements of the density-dependent effective mass.

4.3. LANDAU FAN DIAGRAM

In Fig. 4.2(a) we show a Landau fan diagram for the shallow quantum well ($t = 12$ nm). This is obtained by plotting the oscillatory component of the magnetoresistivity $\Delta\rho_{xx}/\rho_0 = (\rho_{xx}(B) - \rho_0)/\rho_0$ at $T = 1.7$ K as a function of out-of-plane magnetic field B and carrier density p, obtained from the low-field Hall data. Shubnikov-de Haas oscillations fan out towards higher field and density, with Zeeman spin splitting visible at odd filling factors ν. Temperature dependence of the oscillation amplitudes are shown in Fig. 4.2(b) and (c) after a polynomial background subtraction. Fig. 4.2(b) shows the cross-section of the fan diagram at fixed density, obtained by keeping the gate voltage constant while sweeping the magnetic field. Alternatively, the density is swept at a fixed magnetic field (Fig. 4.2(c)). Both data sets allow the estimate of the effective mass with a better insight into the dependence on B and p. The effective mass m^* is obtained by fitting the thermal damping of the SdH oscillations by using the expression[31]

$$\frac{\Delta\rho/\rho_0(T)}{\Delta\rho/\rho_0(T_0)} = \frac{T\sinh(\beta T_0)}{T_0\sinh(\beta T)}, \tag{4.1}$$

where $\beta = \dfrac{2\pi k_B m^*}{\hbar e B}$, k_B is the Boltzmann constant, $\hbar$ is the Plank constant, e is the electron charge and $T_0 = 1.7$ K is the coldest temperature at which the oscillations were mea-

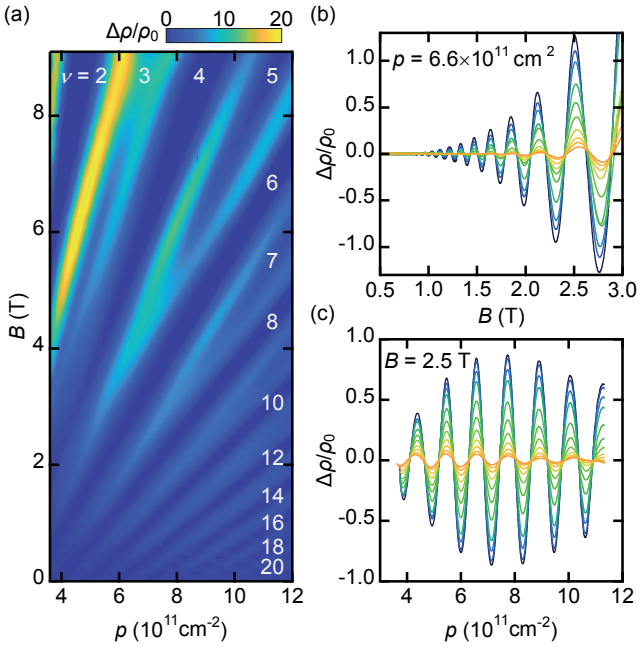

Figure 4.2: (a) Fan diagram at $T = 1.7$ K showing the magnetoresistance normalized to the zero field value $\Delta\rho_{xx}/\rho_0$ as a function of B and p for the sample with $t = 12$ nm. Filling factors ν assigned from quantum Hall effect are indicated. (b) $\Delta\rho_{xx}/\rho_0$ as a function of B. The data was taken at a fixed density $p = 6.6 \times 10^{11}$ cm^{-2}. Different colors correspond to different temperatures from 1.7 K (dark blue) to 10 K (orange). (c) $\Delta\rho_{xx}/\rho_0$ as a function of p. The data was taken at a fixed magnetic field $B = 2.5$ T. Different colors correspond to different temperatures from 1.7 K (dark blue) to 10 K (orange). Data in (b) and (c) are plotted after polynomial background subtraction to take into account for non-oscillatory components of the magnetoresistance, likely arising from bandstructure semi-classical effects and/or hole-hole interactions. The polynomial background is fitted by using the low field resistivity before onset of the SdH oscillations and the oscillation nodes. These are found by averaging adjacent SdH oscillations maxima and minima.

sured.

4.4. DENSITY AND FIELD DEPENDENCE OF THE EFFECTIVE MASS

In Fig. 4.3(a) experimental data and theoretical fitting are shown for different densities at a fixed magnetic field $B = 2.5$ T. The resulting m^* values are reported in units of the electron mass as a function of the correspondent density p in Fig. 4.3(b) for both quantum wells. We observe a strong increasing mass with density, which nearly doubles over the range of investigated densities. The magnetic field dependence of the mass (Fig. 4.3(c)) is rather weak in the investigated range ($B \leq 4$ T), which is limited to SdH oscillations before Zeeman splitting. From a phenomenological linear fit of the density-dependent effective mass in Fig.3(b) we extrapolate an effective mass of $(0.048 \pm 0.006) m_e$ at zero density. This value is in agreement with the predicted theoretical value calculated from the density of states at the Γ point,[4] reconciling theory and experiments This value is in agreement with the predicted theoretical value calculated from the density of states at

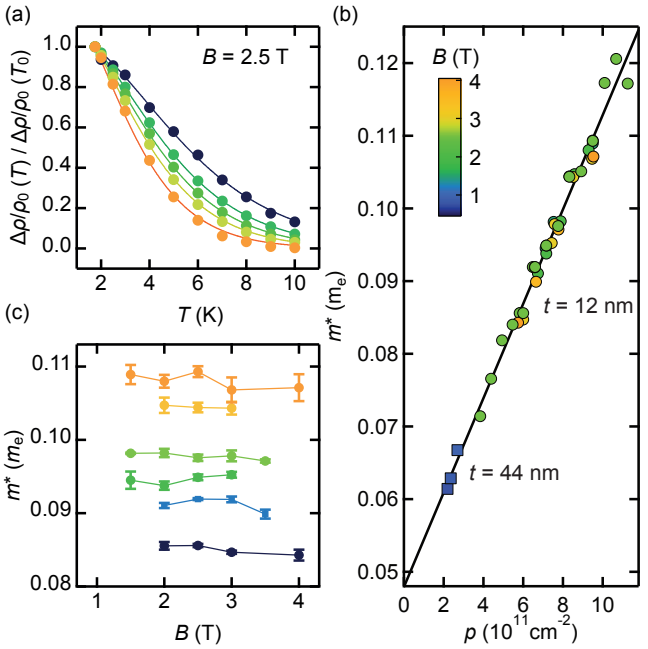

Figure 4.3: $\Delta\rho_{xx}/\rho_0$ (solid circles) as a function of T, normalized at $\Delta\rho_{xx}/\rho_0(T_0)$, with $T_0 = 1.7$ K. The data was taken at a fixed magnetic field $B = 2.5$ T. Different colors correspond to increasing densities from 3.84×10^{11} cm^{-2} (dark blue) to 10.66×10^{11} cm^{-2} (orange). Lines are theoretical fits used to extract m^* as a function of density. (b) Density dependent m^* and linear extrapolation to zero density. The data at $t = 44$ nm was obtained by sweeping the magnetic field at a fixed density, while those at $t = 12$ nm were obtained by sweeping the density at fixed magnetic field. Different colors correspond to different magnetic fields (see legend). (c) Effective mass m^* as a function of magnetic field B. Different colors correspond to increasing densities from $\sim 5.8 \times 10^{11}$ cm^{-2} (dark blue) to $\sim 9.5 \times 10^{11}$ cm^{-2} (orange). For clarity, lines join experimental points taken at the same density.

the Γ point,[4] reconciling theory and experiments.

4.5. DISCUSSION

In summary, we have measured the effective hole mass over a large range of densities in high-mobility undoped Ge/SiGe quantum wells. The obtained values ($0.061 m_e$), extrapolated to ($0.048 \pm 0.006) m_e$ at zero density, are the lightest effective mass reported for a planar platform that demonstrated spin qubits in quantum dots. These results position planar germanium as a promising material towards the development of spin and hybrid quantum technologies.

BIBLIOGRAPHY

[1] R. Maurand, X. Jehl, D. Kotekar-Patil, A. Corna, H. Bohuslavskyi, R. Laviéville, L. Hutin, S. Barraud, M. Vinet, M. Sanquer, and S. De Franceschi. "A CMOS silicon spin qubit". en. In: *Nature Communications* 7 (Nov. 2016), p. 13575. ISSN: 2041-1723.

[2] H. Watzinger, J. Kukučka, L. Vukušić, F. Gao, T. Wang, F. Schäffler, J.-J. Zhang, and G. Katsaros. "A germanium hole spin qubit". In: *Nature communications* 9.1 (2018), p. 3902.

[3] N. Hendrickx, D. Franke, A. Sammak, G. Scappucci, and M. Veldhorst. "Fast two-qubit logic with holes in germanium". In: *arXiv preprint arXiv:1904.11443* (2019).

[4] L. A. Terrazos, E. Marcellina, S. N. Coppersmith, M. Friesen, A. R. Hamilton, X. Hu, B. Koiller, A. L. Saraiva, D. Culcer, and R. B. Capaz. "Qubits Based on Hole Quantum Dots in Strained Ge". In: *arXiv:1803.10320 [cond-mat]* (Mar. 2018). arXiv: 1803.10320.

[5] A. Dimoulas, P. Tsipas, A. Sotiropoulos, and E. K. Evangelou. "Fermi-level pinning and charge neutrality level in germanium". In: *Appl. Phys. Lett.* 89.25 (Dec. 2006), p. 252110. ISSN: 0003-6951.

[6] G. Katsaros, P. Spathis, M. Stoffel, F. Fournel, M. Mongillo, V. Bouchiat, F. Lefloch, A. Rastelli, O. G. Schmidt, and S. D. Franceschi. "Hybrid superconductor–semiconductor devices made from self-assembled SiGe nanocrystals on silicon". In: *Nat. Nanotech.* 5.6 (June 2010), pp. 458–464. ISSN: 1748-3395.

[7] N. W. Hendrickx, M. L. V. Tagliaferri, M. Kouwenhoven, R. Li, D. P. Franke, A. Sammak, A. Brinkman, G. Scappucci, and M. Veldhorst. "Ballistic supercurrent discretization and micrometer-long Josephson coupling in germanium". In: *Phys. Rev. B* 99.7 (Feb. 2019), p. 075435.

[8] F. Vigneau, R. Mizokuchi, D. C. Zanuz, X. Huang, S. Tan, R. Maurand, S. Frolov, A. Sammak, G. Scappucci, F. Lefloch, and S. De Franceschi. "Germanium Quantum-Well Josephson Field-Effect Transistors and Interferometers". In: *Nano Lett.* 19.2 (Feb. 2019), pp. 1023–1027. ISSN: 1530-6984.

[9] J. Xiang, A. Vidan, M. Tinkham, R. M. Westervelt, and C. M. Lieber. "Ge/Si nanowire mesoscopic Josephson junctions". In: *Nature nanotechnology* 1.3 (2006), p. 208.

[10] A. Sammak, D. Sabbagh, N. W. Hendrickx, M. Lodari, B. P. Wuetz, A. Tosato, L. Yeoh, M. Bollani, M. Virgilio, M. A. Schubert, P. Zaumseil, G. Capellini, M. Veldhorst, and G. Scappucci. "Shallow and Undoped Germanium Quantum Wells: A Playground for Spin and Hybrid Quantum Technology". en. In: *Advanced Functional Materials* 29.14 (2019), p. 1807613. ISSN: 1616-3028.

[11] N. W. Hendrickx, D. P. Franke, A. Sammak, M. Kouwenhoven, D. Sabbagh, L. Yeoh, R. Li, M. L. V. Tagliaferri, M. Virgilio, G. Capellini, G. Scappucci, and M. Veldhorst. "Gate-controlled quantum dots and superconductivity in planar germanium". En. In: *Nature Communications* 9.1 (July 2018), p. 2835. ISSN: 2041-1723.

[12] W. J. Hardy, C. T. Harris, Y.-H. Su, Y. Chuang, J. Moussa, L. N. Maurer, J.-Y. Li, T.-M. Lu, and D. R. Luhman. "Single and double hole quantum dots in strained Ge/SiGe quantum wells". en. In: *Nanotechnology* 30.21 (Mar. 2019), p. 215202. ISSN: 0957-4484.

[13] R. Winkler, M. Merkler, T. Darnhofer, and U. Rössler. "Theory for the cyclotron resonance of holes in strained asymmetric Ge-SiGe quantum wells". In: *Physical Review B* 53.16 (1996), p. 10858.

[14] F. Schäffler. "High-mobility Si and Ge structures". In: *Semiconductor Science and Technology* 12.12 (1997), p. 1515.

[15] C. Morrison and M. Myronov. "Electronic transport anisotropy of 2D carriers in biaxial compressive strained germanium". In: *Applied Physics Letters* 111.19 (2017), p. 192103.

[16] T. Irisawa, M. Myronov, O. Mironov, E. Parker, K. Nakagawa, M. Murata, S. Koh, and Y. Shiraki. "Hole density dependence of effective mass, mobility and transport time in strained Ge channel modulation-doped heterostructures". In: *Applied physics letters* 82.9 (2003), pp. 1425–1427.

[17] B. Rößner, G. Isella, and H. v. Känel. "Effective mass in remotely doped Ge quantum wells". In: *Applied physics letters* 82.5 (2003), pp. 754–756.

[18] K. Sawano, Y. Kunishi, Y. Shiraki, K. Toyama, T. Okamoto, N. Usami, and K. Nakagawa. "Magnetotransport properties of Ge channels with extremely high compressive strain". In: *Applied physics letters* 89.16 (2006), p. 162103.

[19] B. Rössner, H. von Känel, D. Chrastina, G. Isella, and B. Batlogg. "Effective mass measurement: the influence of hole band nonparabolicity in SiGe/Ge quantum wells". In: *Semiconductor science and technology* 22.1 (2006), S191.

[20] M. G. Borselli, K. Eng, E. T. Croke, B. M. Maune, B. Huang, R. S. Ross, A. A. Kiselev, P. W. Deelman, I. Alvarado-Rodriguez, A. E. Schmitz, et al. "Pauli spin blockade in undoped Si/SiGe two-electron double quantum dots". In: *Applied Physics Letters* 99.6 (2011), p. 063109.

[21] D. Laroche, S.-H. Huang, Y. Chuang, J.-Y. Li, C. W. Liu, and T. M. Lu. "Magnetotransport analysis of an ultra-low-density two-dimensional hole gas in an undoped strained Ge/SiGe heterostructure". In: *Appl. Phys. Lett.* 108.23 (June 2016), p. 233504. ISSN: 0003-6951.

[22] W. J. Hardy, C. Harris, Y.-H. Su, Y. Chuang, J. Moussa, L. Maurer, J.-Y. Li, T.-M. Lu, and D. R. Luhman. "Single and Double Hole Quantum Dots in Strained Ge/SiGe Quantum Wells". In: *arXiv preprint arXiv:1808.07077v1* (2018).

[23] T. Lu, C.-H. Lee, S.-H. Huang, D. Tsui, and C. Liu. "Upper limit of two-dimensional electron density in enhancement-mode Si/SiGe heterostructure field-effect transistors". In: *Applied Physics Letters* 99.15 (2011), p. 153510.

[24] Y.-H. Su, Y. Chuang, C.-Y. Liu, J.-Y. Li, and T.-M. Lu. “Effects of surface tunneling of two-dimensional hole gases in undoped Ge/GeSi heterostructures”. In: *Phys. Rev. Materials* 1.4 (Sept. 2017), p. 044601.

[25] L. A. Tracy, E. Hwang, K. Eng, G. Ten Eyck, E. Nordberg, K. Childs, M. S. Carroll, M. P. Lilly, and S. D. Sarma. “Observation of percolation-induced two-dimensional metal-insulator transition in a Si MOSFET”. In: *Physical Review B* 79.23 (2009), p. 235307.

[26] J.-S. Kim, A. M. Tyryshkin, and S. A. Lyon. “Annealing shallow Si/SiO2 interface traps in electron-beam irradiated high-mobility metal-oxide-silicon transistors”. In: *Applied Physics Letters* 110.12 (2017), p. 123505.

[27] A. Gold. “Metal-insulator transition in Al x Ga 1- x As/GaAs heterostructures with large spacer width”. In: *Physical Review B* 44.16 (1991), p. 8818.

[28] A. Gold. “Metal–insulator transition in Si/SiGe heterostructures: mobility, spin polarization and Dingle temperature”. In: *Semiconductor Science and Technology* 26.4 (2011), p. 045017.

[29] D. Laroche, S.-H. Huang, E. Nielsen, Y. Chuang, J.-Y. Li, C.-W. Liu, and T.-M. Lu. “Scattering mechanisms in shallow undoped Si/SiGe quantum wells”. In: *AIP Advances* 5.10 (2015), p. 107106.

[30] X. Mi, T. Hazard, C. Payette, K. Wang, D. Zajac, J. Cady, and J. Petta. “Magnetotransport studies of mobility limiting mechanisms in undoped Si/SiGe heterostructures”. In: *Physical Review B* 92.3 (2015), p. 035304.

[31] W. De Lange, F. Blom, and J. Wolter. “Effective electron mass in GaAs/AlxGa1-xAs heterostructures under hydrostatic pressure”. In: *Semiconductor science and technology* 8.3 (1993), p. 341.

5

LIGHTLY-STRAINED GERMANIUM QUANTUM WELLS WITH HOLE MOBILITY EXCEEDING ONE MILLION

Strain is a crucial design parameter of Ge/SiGe heterostructures. On one hand, strain in the quantum well enables tuning of the system's band structure and associated properties such as effective mass, g-factor and spin orbit. On the other hand such quantum wells are grown coherently on SiGe strained relaxed buffers, where strain becomes a source of structural defects and variability and it needs to be carefully managed to ensure a uniform potential landscape in the active region of the heterostructure. In this work we demonstrate that a lightly-strained germanium channel ($\varepsilon_{//} = -0.41\%$) in an undoped Ge/$Si_{0.1}Ge_{0.9}$ heterostructure field effect transistor supports a 2D hole gas with mobility in excess of 1×10^6 cm^2/Vs and percolation density less than 5×10^{10} cm^{-2}. This low disorder 2D hole system shows tunable fractional quantum Hall effect at low density and low magnetic field. The low-disorder and small effective mass ($0.068m_e$) defines lightly-strained germanium as a basis to tune the strength of the spin-orbit coupling for fast and coherent quantum hardware.

This work was originally published as:
M. Lodari, O. Kong, M. Rendell, A. Tosato, A. Sammak, M. Veldhorst, A. R. Hamilton, G. Scappucci, Lightly strained germanium quantum wells with hole mobility exceeding one million. Applied Physics Letters 120, 12 (2022).

5.1. INTRODUCTION

Quantum confined holes in germanium are emerging as a compelling platform for quantum information processing because of several favorable properties.[1] The light hole effective mass ($\sim 0.05 m_e$ at zero density)[2] and the absence of valley degeneracy[3, 4] give rise to large orbital splittings in quantum dots.[5] The intrinsic sizable and tunable spin-orbit coupling (SOC)[6, 7] enables all-electrical fast qubit driving.[8, 9, 10, 11] Furthermore, the capability to host superconducting pairing correlations[12, 13, 14] is promising for the co-integration of spin-qubits with superconductors in hybrid architectures for spin–spin long-distance entanglement and quantum information transfer between different qubit types.[15, 16, 17, 18, 19, 20, 21]

Planar Ge/SiGe heterostructures are promising for scaling up to large quantum processors due to their compatibility with advanced semiconductor manufacturing.[22] The low-disorder in planar Ge quantum wells[23] enabled the demonstration of a four-qubit quantum processor based on hole spins in a two-by-two array of quantum dots.[24] These heterostructures featured a $Si_{0.2}Ge_{0.8}$ strain-relaxed buffer (SRB), resulting in quantum wells with compressive strain $\varepsilon_{//} = -0.63\%$.[25] Alternatively, higher strained Ge ($\varepsilon_{//} = -1.18\,\%$) on $Si_{0.25}Ge_{0.75}$ SRBs enabled singlet-triplet spin qubits.[26] Lightly-strained Ge/SiGe heterostructures are unexplored and could offer potentially larger SOC because of the reduced energy splitting between heavy-holes (HH) and light holes (LH),[27] which is ≈ 17 meV for Ge/$Si_{0.1}Ge_{0.9}$ compared to ≈ 51 meV for Ge/$Si_{0.2}Ge_{0.8}$, respectively.[4, 3] As such, lightly-strained Ge is interesting for exploring faster spin-qubit driving and for topological devices. In this letter we demonstrate that lightly-strained Ge quantum wells in undoped Ge/$Si_{0.1}Ge_{0.9}$ support a two-dimensional hole gas (2DHG) with low disorder at low density, a prerequisite for further exploration of lightly-strained Ge quantum devices.

5.2. STRAIN CHARACTERIZATION AND CLASSICAL TRANSPORT

We grow the Ge/SiGe heterostructure by reduced-pressure chemical vapor deposition on a Si(001) wafer and then we fabricate Hall-bar shaped heterostructure field effect transistors (H-FETs) with the same process as in Refs. [25, 2, 23]. Here, a 16 nm strained Ge (sGe) quantum well (QW) is positioned between two strain-relaxed layers of $Si_{0.1}Ge_{0.9}$, at a depth of 66 nm [schematics in Fig. 5.1(a)].[1] Applying a negative DC bias to the accumulation gate V_g induces a 2DHG at the Ge/$Si_{0.1}Ge_{0.9}$ interface. The density in the 2DHG p is increased above the percolation density p_p by making V_g more negative. We use standard four-probe low-frequency lock-in techniques for mobility-density and magnetotransport characterization at $T = 1.7$ K and 70 mK, with excitation source-drain bias of 1 mV and 100 µeV, respectively. We do not measure gate to drain current leakage over the range of applied V_g. Figure 5.1(b) shows the Raman spectra measured with a 633 nm red laser to determine the strain in the Ge QW. Comparing Ge/$Si_{0.1}Ge_{0.9}$ (red) to a control Ge/$Si_{0.2}Ge_{0.8}$ (black), we observe the Raman peak from the Ge-Ge vibration mode (sGe) in the QW appearing at a lower Raman shift. Conversely, the Raman peak from the SiGe layer is appearing at a higher Raman shift. These observations are consistent with the QW in Ge/$Si_{0.1}Ge_{0.9}$ being less strained due to a Ge-richer SiGe SRB.[28] From

[1] The chemical composition of the layers is measured by secondary ion mass spectroscopy

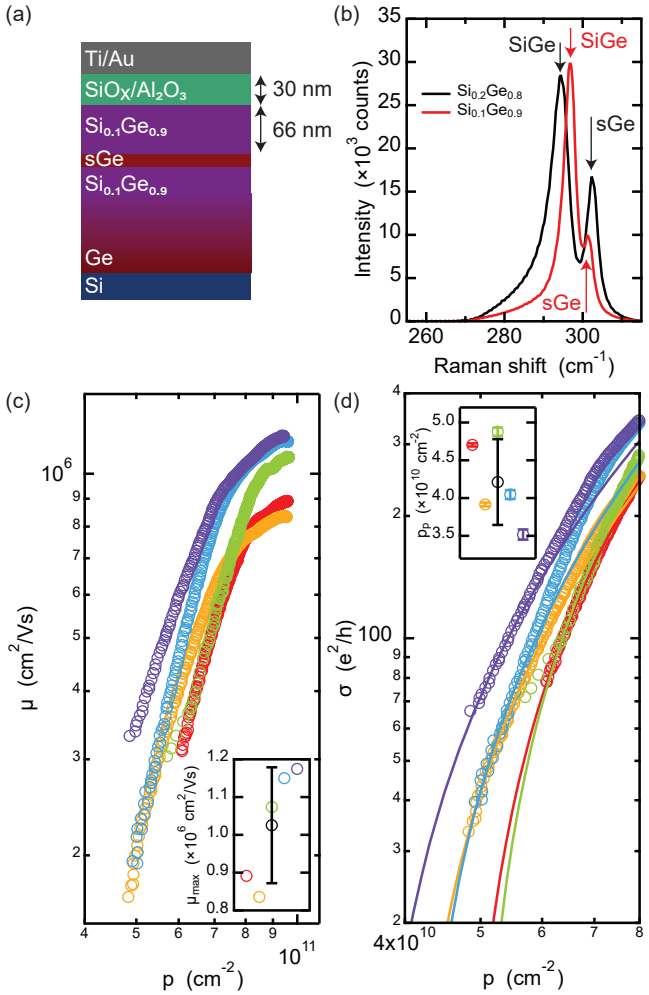

Figure 5.1: (a) Schematic of a Ge/SiGe heterostructure field effect transistor. The strained Ge QW (sGe) is grown with the same lattice parameter to a $Si_{0.1}Ge_{0.9}$ SRB obtained by reverse grading, and it is separated from the native-SiO_x/Al_2O_3 dielectric and from the Ti/Au metallic gate stack by a 66 nm thick $Si_{0.1}Ge_{0.9}$ layer. (b) Intensity spectra as a function of Raman shift from a $Ge/Si_{0.2}Ge_{0.8}$ (black) and $Ge/Si_{0.1}Ge_{0.9}$ (red) heterostructures. (c) Mobility μ as a function of density p at $T = 1.7$ K from five Hall bar devices from the same wafer. The inset shows the maximum mobility μ_{max} from all the devices and average value ± standard deviation (black). (d) Conductivity σ_{xx} as a function of density p (circles) and fit to percolation theory in the low density regime (solid lines). The inset shows the percolation density p_p from all the devices and average value ± standard deviation (black).

the position of the Raman shift (301.7 cm^{-1}), we estimate a light compressive strain of $\varepsilon_{//} = -0.41\%$ for the QW in $Ge/Si_{0.1}Ge_{0.9}$. This is significantly lower than in Refs. [25, 26].

Moving on to electrical characterisation, we operate the H-FET as following. We turn on the device at $V_g \sim -0.4$ V and sweep V_g to larger negative voltages ($V_g \approx -9$ V) to saturate the traps at the semiconductor/dielectric interface via charge tunneling from the

quantum well, similarly to what observed in shallow $Ge/Si_{0.2}Ge_{0.8}$ H-FETs.[25] At these large gate voltages, the density reaches saturation (p_{sat}) when the Fermi level crosses the surface quantum well at the $Si_{0.1}SiGe_{0.9}$/dielectric interface,[29] thereby screening the electric field at the sGe QW.[30] Fig. 5.1(c) shows the mobility μ as a function of Hall density p from five H-FETs fabricated on a 2×2 cm^2 coupon from the center of the 100 mm wafer and measured at $T = 1.7$ K. The mobility increases steeply with p due to the increasing screening of scattering from remote charged impurities.[31, 32, 30] At higher density ($p \geq 7 \times 10^{10}$ cm^{-2}), short range scattering from impurities within and/or in proximity of the quantum well becomes the mobility-limiting scattering mechanism.[30] We observe a maximum mobility μ_{max} in the range of $0.8 - 1.2 \times 10^6$ cm^2/Vs for p_{sat} in the range of $9.43 - 9.64 \times 10^{10}$ cm^{-2} over the five investigated H-FETs. The inset in Fig. 5.1(c) shows a box plot of μ_{max} across the devices, with an average value of $(1.03 \pm 0.15) \times 10^6$ cm^2/Vs (black), setting a benchmark for holes in buried channel transistors. Crucially, such high mobility is measured at very low density below $p = 1 \times 10^{11}$ cm^{-2}, a significant improvement compared to previous studies in Ge/SiGe.[25, 23]

5

Beyond μ_{max}, p_p is a key metric for characterizing the disorder potential landscape at low density, the regime relevant for quantum dot qubits. Figure 5.1(d) shows the conductivity σ_{xx} (circles) as a function of density p for all the investigated devices and their fit to percolation theory (lines) $\sigma \sim (p - p_p)^{1.31}$, where the exponent 1.31 is fixed for 2D systems.[33] p_p ranges from 3.5 to 4.8×10^{10} cm^{-2}. Figure 5.1(d) inset shows a box plot of the percolation density p_p across the devices with an average value of $p_p = (4.2 \pm 0.6) \times 10^{10}$ cm^{-2} (black). We take these values as an upper bound for p_p, since we observed smaller values of p_p [$(1.76 \pm 0.04) \times 10^{10}$ cm^{-2} at $T = 70$ mK] if the range of applied gate voltage is restricted to small voltages above the turn-on threshold.

5.3. MAGNETOTRANSPORT AND LANDAU FAN DIAGRAM

Since $Ge/S_{0.1}Ge_{0.9}$ is characterized by such low level of disorder, we further explored the quantum transport proprieties of the 2DHG at 70 mK. Figure 5.2(a) shows the longitudinal resistivity ρ_{xx} (black) and transverse Hall resistivity ρ_{xy} (red) as a function of perpendicular magnetic field B up to 0.75 T and at a Hall density of 7.2×10^{10} cm^{-2} and $\mu = 8.1 \times 10^5$ cm^2/Vs. We observe clear Shubnikov–de Haas (SdH) resistivity oscillations above 80 mT. The onset for resolving the spin-degeneracy by Zeeman splitting is 0.17 T and ρ_{xx} minima reach zero already at 0.5 T. We do not observe beatings in the SdH oscillations associated with increased Rashba spin-splitting. We speculate that such beatings are more likely to be visible at higher densities, that require the quantum well to be closer to the dielectric interface.[2]

Fig. 5.3(b) shows the SdH oscillations at higher magnetic fields: strong minima are developed for filling factors ν with integer and fractional values. Clear plateaus are visible in ρ_{xy} for $\nu = 2/3$ and $1/3$, where correspondingly ρ_{xx} vanishes. Such high quality fractional quantum Hall effect (FQHE) has previously only been reported holes in modulation-doped systems at higher carrier density and, hence, at larger magnetic fields.[34, 35, 36] Here, in undoped heterostructure, we use the top-gate to follow the evolution of FQHE states down to low density, providing avenues for studying the underlying physics.

The color map in Fig. 5.3(a), measured at $T = 70$ mK, shows ρ_{xx} (normalized to the

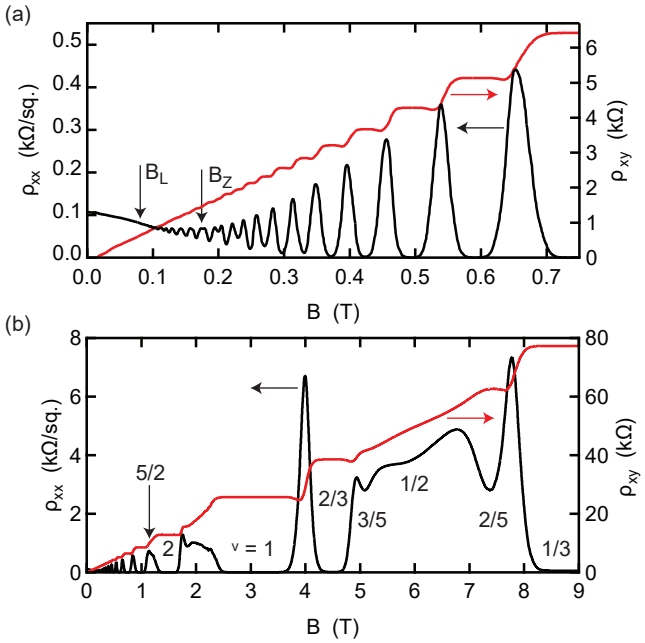

Figure 5.2: Longitudinal resistivity ρ_{xx} (black) and transverse Hall resistivity ρ_{xy} (red) as a function of perpendicular magnetic field B at 70 mK, at a density of $p = 7.2 \times 10^{10}$ cm^{-2} and mobility $\mu = 8.1 \times 10^5$ cm^2/Vs. (a) Low-field Shubnikov-de Haas oscillations from $B = 0$ to 0.75 T, and (b) in a expanded magnetic field range from $B = 0$ to 9 T. Onset of Landau levels (B_L) and Zeeman splitting (B_Z) are reported. Integer and fractional Landau levels labels are reported.

value $\rho_{xx,0}$ at zero magnetic field) as a function of magnetic field B and Hall density p in the range of $4.1 - 7.1 \times 10^{10}$ cm^{-2}. Yellow and blue regions in the color map correspond to peaks and dips in the normalized ρ_{xx}, highlighting the density-dependent evolution of integer and fractional filling factors. All filling factors fan out towards higher magnetic field and density, and fractional filling factors are well resolved across the full investigated range of density and magnetic field. Three line cuts from the color map are shown in Fig. 5.3(b–d), at decreasing density $p = 7.1$ (blue), 5.9 (green), and 4.2×10^{10} cm^{-2} (red), respectively. We observe that the minima associated with fractional ν become shallower as the density is decreased, possibly because of increased level broadening by unscreened disorder and because of weaker Coulomb interactions and correlation effects.[35, 36] We also observe the distance between the onset of Shubnikov-de Haas oscillations (B_L) and Zeeman splitting (B_Z) reducing from Fig. 5.3(b) to Fig. 5.3(c). In Fig. 5.3(d), B_L and B_Z have crossed, meaning that at $p = 4.2 \times 10^{10}$ cm^{-2} the Zeeman gap is larger than the cyclotron gap and therefore the spin susceptibility $(g^* m^*)/m_e \geq 1$,[37] where m^* is the effective mass and g^* the effective g-factor out of plane. Indeed, from thermal activation measurement (Supplementary Material) we estimate $m^* = (0.068 \pm 0.001) m_e$ and $g^* = 13.95 \pm 0.18$ at a density of 5.8×10^{10} cm^{-2}, corresponding to a spin susceptibility of ≈ 1. We note that similar values of m^* and g^* were reported in Ge/$Si_{0.2}Ge_{0.8}$[2,

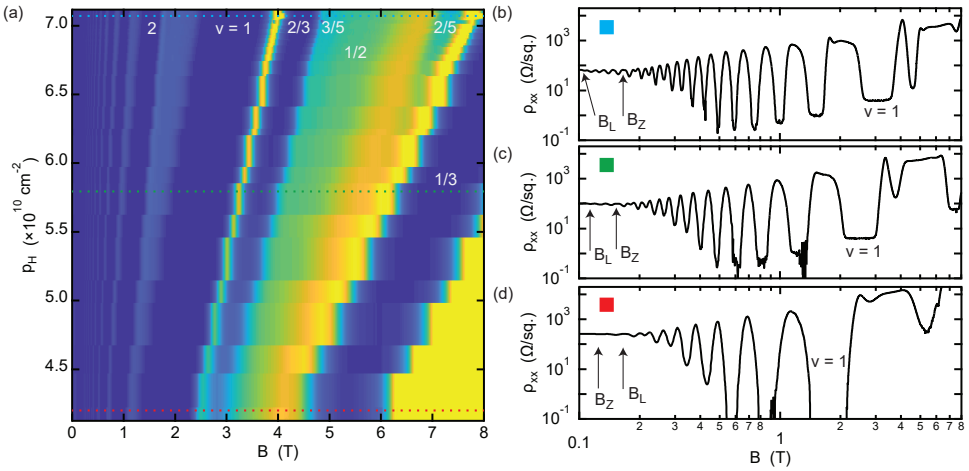

Figure 5.3: (a) Normalized longitudinal resistivity $\rho_{xx}/\rho_{xx,0}$ as a function of magnetic field B and Hall density p at $T = 70$ mK. Labels of integer and fractional ν assigned from the quantum Hall effect are reported. Amplitude color scale: 0 to 60. Dashed lines correspondent to the line cuts ρ_{xx} vs. B at different densities are reported for (b) $p = 7.1$, (c) 5.9, and (d) 4.2×10^{10} cm^{-2}. Labels of Landau levels (B_L) and Zeeman splitting (B_Z) onset are reported.

5] albeit at much higher density, pointing to higher HH-LH intermixing in the lightly strained quantum wells at lower density, as expected from theory.[3]

5.4. DISCUSSION

In conclusion, we demonstrated a lightly-strained Ge/SiGe heterostrucure supporting a 2DHG with mobility in excess of one million and low percolation density (less than 5×10^{10} cm^{-2}). Such low disorder enables measurement of FQHE at tunable low density and low magnetic fields. To mitigate the effect of traps at the interface and to suppress tunneling from the quantum well to the surface, we speculate that lightly-strained Ge channels could be positioned deeper compared to more strained channels[29, 23] because of the smaller band offset (≈ 66 meV Ge/$Si_{0.2}Ge_{0.9}$ vs. ≈ 130 meV in Ge/$Si_{0.2}Ge_{0.8}$). Further measurements in quantum dots, where confinement increases the HH-LH mixing, will help to elucidate the effect of reduced strain on the spin-orbit coupling in the system. The demonstration that holes can be defined in QWs with varying strain provides avenues to explore the opportunities in the germanium quantum information route.

5.5. SUPPLEMENTARY INFORMATION

We extrapolate the effective g^* factor and the effective mass m^* from the temperature-dependent decay of the longitudinal resistivity ρ_{xx} at different filling factors $\nu = ph/eB_\nu$, where h is the Planck constant, e is the electron charge, and B_ν is the magnetic field at integer values of ν. Figure 5.4 shows the Shubnikov-de Haas oscillations as a function of ν measured at a density of $p = 5.8 \times 10^{10}$ cm^{-2} in the temperature range from $T =$ 68 mK to 1.2 K. Filling factors $\nu = 2$ is resolved at a magnetic field $B \sim 1.2$ T, and both

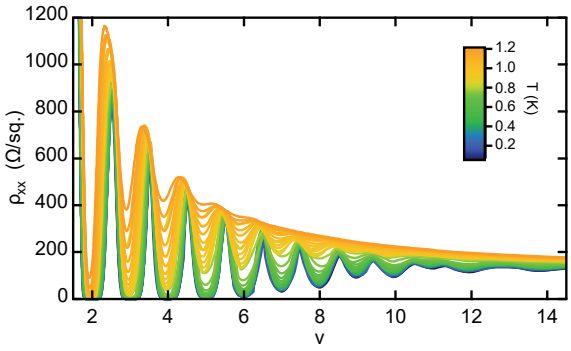

Figure 5.4: Temperature dependent longitudinal resistivity ρ_{xx} as a function of filling factor ν in the temperature range from $T = 68$ mK (blue) to 1.2 K (orange).

even and odd filling factors are resolved up to $\nu = 26$ and 15 at lower field at the coldest temperature, respectively.

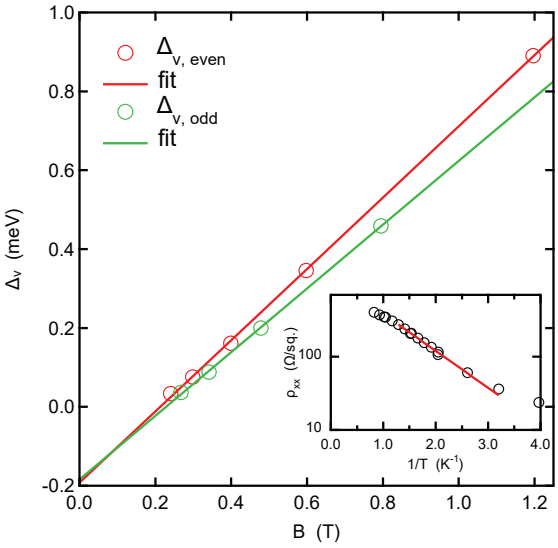

Figure 5.5: Activation energy gap Δ_ν as a function of magnetic field B for even (red) and odd (green) filling factors ν, along with linear fits. The inset shows the Arrhenius plot The inset shows the Arrhenius plot and fit to extract Δ_ν for $\nu = 5$.

The activation energy gap Δ_ν of each filling factor can be obtained from the thermally activated dependence of the SdH oscillation minimum for a given filling factor, as reported in the Arrhenius plot of the $ln(\rho_{xx,\nu})$ vs. $1/T$ (black circles, inset Fig. 5.5). Following the Boltzmann statistics, the longitudinal magnetoresistance of a specific minima can be described via the relation $ln(\rho_{xx,\nu}) \propto -\Delta_\nu/(2k_BT)$, where k_B is the Boltzmann constant. The activation energy of the filling factors Δ_ν can be extrapolated from the slope of a linear fit (red).

Since the even and odd filling factors corresponds to the cyclotron frequency and the Zeeman splitting, respectively, and a linear relation links activation energy Δ_ν and the magnetic field B_ν at which each ν occur, the effective mass m^* and the effective g^* can be extrapolated from a linear fit of the $\Delta_\nu(B_\nu)$ dependence. Figure 5.5 shows the extrapolated activation energy Δ_ν as a function of magnetic field B for all the investigated even and odd filling factors (red and green, respectively). The effective g^* can be extrapolated from the slope of a linear fit $\Delta_{\nu,odd} = g^*\mu_B B$ (green line), where μ_B is the Bohr magnetron. Once the g^* is know, then the effective mass m^* can be obtained from the slope of the linear fit $\Delta_{\nu,even} = \hbar eB/m^* - g^*\mu_B B$ (red line).
For a density of $p = 0.58 \times 10^{10}$ cm^{-2}, we found an effective g^* factor of 13.95 ± 0.18 and an effective mass m^* of 0.068 ± 0.001.

BIBLIOGRAPHY

[1] G. Scappucci, C. Kloeffel, F. A. Zwanenburg, D. Loss, M. Myronov, J.-J. Zhang, S. De Franceschi, G. Katsaros, and M. Veldhorst. "The germanium quantum information route". In: *Nature Reviews Materials* 6.10 (2021), pp. 926–943. ISSN: 2058-8437.

[2] M. Lodari, A. Tosato, D. Sabbagh, M. A. Schubert, G. Capellini, A. Sammak, M. Veldhorst, and G. Scappucci. "Light effective hole mass in undoped Ge/SiGe quantum wells". In: *Physical Review B* 100.4 (July 2019), p. 041304.

[3] L. A. Terrazos, E. Marcellina, Z. Wang, S. N. Coppersmith, M. Friesen, A. R. Hamilton, X. Hu, B. Koiller, A. L. Saraiva, D. Culcer, and R. B. Capaz. "Theory of hole-spin qubits in strained germanium quantum dots". In: *Phys. Rev. B* 103 (12 Mar. 2021), p. 125201.

[4] P. Del Vecchio, M. Lodari, A. Sammak, G. Scappucci, and O. Moutanabbir. "Vanishing Zeeman energy in a two-dimensional hole gas". In: *Phys. Rev. B* 102 (11 Sept. 2020), p. 115304.

[5] N. W. Hendrickx, D. P. Franke, A. Sammak, M. Kouwenhoven, D. Sabbagh, L. Yeoh, R. Li, M. L. Tagliaferri, M. Virgilio, G. Capellini, G. Scappucci, and M. Veldhorst. "Gate-controlled quantum dots and superconductivity in planar germanium". In: *Nature Communications* 9.1 (2018), pp. 1–7. ISSN: 20411723. arXiv: 1801.08869.

[6] F. N. M. Froning, M. J. Rančić, B. Hetényi, S. Bosco, M. K. Rehmann, A. Li, E. P. A. M. Bakkers, F. A. Zwanenburg, D. Loss, D. M. Zumbühl, and F. R. Braakman. "Strong spin-orbit interaction and g-factor renormalization of hole spins in Ge/Si nanowire quantum dots". In: *Physical Review Research* 3.1 (Jan. 2021), p. 013081.

[7] S. Bosco, M. Benito, C. Adelsberger, and D. Loss. "Squeezed hole spin qubits in Ge quantum dots with ultrafast gates at low power". In: *Physical Review B* 104.11 (Sept. 2021), p. 115425.

[8] H. Watzinger, J. Kukučka, L. Vukušić, F. Gao, T. Wang, F. Schäffler, J.-J. Zhang, and G. Katsaros. "A germanium hole spin qubit". En. In: *Nature Communications* 9.1 (Sept. 2018), p. 3902. ISSN: 2041-1723.

[9] N. W. Hendrickx, D. P. Franke, A. Sammak, G. Scappucci, and M. Veldhorst. "Fast two-qubit logic with holes in germanium". In: *Nature* 577.7791 (2020), pp. 487–491. ISSN: 14764687. arXiv: 1904.11443.

[10] F. N. M. Froning, L. C. Camenzind, O. A. H. van der Molen, A. Li, E. P. A. M. Bakkers, D. M. Zumbühl, and F. R. Braakman. "Ultrafast hole spin qubit with gate-tunable spin–orbit switch functionality". en. In: *Nature Nanotechnology* 16.3 (Mar. 2021), pp. 308–312. ISSN: 1748-3395.

[11] K. Wang, G. Xu, F. Gao, H. Liu, R.-L. Ma, X. Zhang, Z. Wang, G. Cao, T. Wang, J.-J. Zhang, D. Culcer, X. Hu, H.-W. Jiang, H.-O. Li, G.-C. Guo, and G.-P. Guo. "Ultrafast coherent control of a hole spin qubit in a germanium quantum dot". In: *Nature Communications* 13.1 (Dec. 2022). arXiv: 2006.12340, p. 206. ISSN: 2041-1723.

[12] R. Mizokuchi, R. Maurand, F. Vigneau, M. Myronov, and S. De Franceschi. "Ballistic One-Dimensional Holes with Strong g-Factor Anisotropy in Germanium". In: *Nano Letters* 18.8 (Aug. 2018), pp. 4861–4865. ISSN: 1530-6984.

[13] N. W. Hendrickx, M. L. V. Tagliaferri, M. Kouwenhoven, R. Li, D. P. Franke, A. Sammak, A. Brinkman, G. Scappucci, and M. Veldhorst. "Ballistic supercurrent discretization and micrometer-long Josephson coupling in germanium". In: *Phys. Rev. B* 99 (7 Feb. 2019), p. 075435.

[14] K. Aggarwal, A. Hofmann, D. Jirovec, I. Prieto, A. Sammak, M. Botifoll, S. Martí-Sánchez, M. Veldhorst, J. Arbiol, G. Scappucci, J. Danon, and G. Katsaros. "Enhancement of proximity-induced superconductivity in a planar Ge hole gas". In: *Phys. Rev. Research* 3 (2 Apr. 2021), p. L022005.

[15] M.-S. Choi, C. Bruder, and D. Loss. "Spin-dependent Josephson current through double quantum dots and measurement of entangled electron states". In: *Physical Review B* 62.20 (Nov. 2000), pp. 13569–13572.

[16] X. Hu, Y.-x. Liu, and F. Nori. "Strong coupling of a spin qubit to a superconducting stripline cavity". In: *Physical Review B* 86.3 (July 2012), p. 035314.

[17] M. Leijnse and K. Flensberg. "Hybrid topological-spin qubit systems for two-qubit-spin gates". In: *Physical Review B* 86.10 (Sept. 2012), p. 104511.

[18] M. Leijnse and K. Flensberg. "Coupling Spin Qubits via Superconductors". In: *Physical Review Letters* 111.6 (Aug. 2013), p. 060501.

[19] F. Hassler, G. Catelani, and H. Bluhm. "Exchange interaction of two spin qubits mediated by a superconductor". In: *Physical Review B* 92.23 (Dec. 2015), p. 235401.

[20] S. Hoffman, C. Schrade, J. Klinovaja, and D. Loss. "Universal quantum computation with hybrid spin-Majorana qubits". In: *Physical Review B* 94.4 (July 2016), p. 045316.

[21] M. J. Rančić, S. Hoffman, C. Schrade, J. Klinovaja, and D. Loss. "Entangling spins in double quantum dots and Majorana bound states". In: *Physical Review B* 99.16 (Apr. 2019), p. 165306.

[22] R. Pillarisetty. "Academic and industry research progress in germanium nanodevices". In: *Nature* 479.7373 (2011), pp. 324–328. ISSN: 1476-4687.

[23] M. Lodari, N. W. Hendrickx, W. I. L. Lawrie, T.-K. Hsiao, L. M. K. Vandersypen, A. Sammak, M. Veldhorst, and G. Scappucci. "Low percolation density and charge noise with holes in germanium". In: *Materials for Quantum Technology* 1.1 (2021), p. 011002. ISSN: 23318422. arXiv: 2007.06328.

[24] N. W. Hendrickx, W. I. L. Lawrie, M. Russ, F. van Riggelen, S. L. de Snoo, R. N. Schouten, A. Sammak, G. Scappucci, and M. Veldhorst. "A four-qubit germanium quantum processor". In: *Nature* 591.7851 (2021), pp. 580–585. ISSN: 1476-4687.

[25] A. Sammak, D. Sabbagh, N. W. Hendrickx, M. Lodari, B. Paquelet Wuetz, A. Tosato, L. R. Yeoh, M. Bollani, M. Virgilio, M. A. Schubert, P. Zaumseil, G. Capellini, M. Veldhorst, and G. Scappucci. "Shallow and Undoped Germanium Quantum Wells: A Playground for Spin and Hybrid Quantum Technology". In: *Advanced Functional Materials* 29.14 (2019), pp. 1–8. ISSN: 16163028.

[26] D. Jirovec, A. Hofmann, A. Ballabio, P. M. Mutter, G. Tavani, M. Botifoll, A. Crippa, J. Kukucka, O. Sagi, F. Martins, J. Saez-Mollejo, I. Prieto, M. Borovkov, J. Arbiol, D. Chrastina, G. Isella, and G. Katsaros. "A singlet-triplet hole spin qubit in planar Ge". In: *Nature Materials* 20.8 (2021), pp. 1106–1112. ISSN: 1476-4660.

[27] R. Moriya, K. Sawano, Y. Hoshi, S. Masubuchi, Y. Shiraki, A. Wild, C. Neumann, G. Abstreiter, D. Bougeard, T. Koga, and T. Machida. "Cubic Rashba Spin-Orbit Interaction of a Two-Dimensional Hole Gas in a Strained-Ge-SiGe Quantum Well". In: *Phys. Rev. Lett.* 113.8 (Aug. 2014), p. 086601.

[28] F. Pezzoli, E. Bonera, E. Grilli, M. Guzzi, S. Sanguinetti, D. Chrastina, G. Isella, H. Von Känel, E. Wintersberger, J. Stangl, and G. Bauer. "Phonon strain shift coefficients in Si1-x Gex alloys". In: *Journal of Applied Physics* 103.9 (2008). ISSN: 00218979.

[29] Y.-H. Su, Y. Chuang, C.-Y. Liu, J.-Y. Li, and T.-M. Lu. "Effects of surface tunneling of two-dimensional hole gases in undoped Ge/GeSi heterostructures". In: *Phys. Rev. Materials* 1 (4 Sept. 2017), p. 044601.

[30] D. Laroche, S. H. Huang, Y. Chuang, J. Y. Li, C. W. Liu, and T. M. Lu. "Magnetotransport analysis of an ultra-low-density two-dimensional hole gas in an undoped strained Ge/SiGe heterostructure". In: *Applied Physics Letters* 108.23 (2016). ISSN: 00036951.

[31] D. Monroe. "Comparison of mobility-limiting mechanisms in high-mobility Si1-xGex heterostructures". In: *Journal of Vacuum Science & Technology B: Microelectronics and Nanometer Structures* 11.4 (1993), p. 1731. ISSN: 0734211X.

[32] A. Gold. "Mobility and metal-insulator transition of the two-dimensional electron gas in SiGe/Si/SiGe quantum wells". In: *Journal of Applied Physics* 108.6 (2010). ISSN: 00218979.

[33] L. A. Tracy, E. H. Hwang, K. Eng, G. A. Ten Eyck, E. P. Nordberg, K. Childs, M. S. Carroll, M. P. Lilly, and S. Das Sarma. "Observation of percolation-induced two-dimensional metal-insulator transition in a Si MOSFET". In: *Physical Review B - Condensed Matter and Materials Physics* 79.23 (2009), pp. 1–6. ISSN: 10980121.

[34] Q. Shi, M. A. Zudov, C. Morrison, and M. Myronov. "Spinless composite fermions in an ultrahigh-quality strained Ge quantum well". In: *Phys. Rev. B* 91 (24 June 2015), p. 241303.

[35] O. A. Mironov, N. d'Ambrumenil, A. Dobbie, D. R. Leadley, A. V. Suslov, and E. Green. "Fractional Quantum Hall States in a Ge Quantum Well". In: *Phys. Rev. Lett.* 116 (17 Apr. 2016), p. 176802.

[36] I. B. Berkutov, V. V. Andrievskii, Y. A. Kolesnichenko, and O. A. Mironov. “Quantum effects in a germanium quantum well with ultrahigh mobility of charge carrier”. In: *Low Temperature Physics* 45.11 (2019), pp. 1202–1208.

[37] T. M. Lu, L. A. Tracy, D. Laroche, S.-H. Huang, Y. Chuang, Y.-H. Su, J.-Y. Li, and C. W. Liu. “Density-controlled quantum Hall ferromagnetic transition in a two-dimensional hole system”. en. In: *Scientific Reports* 7.1 (June 2017), p. 2468. ISSN: 2045-2322.

6

GERMANIUM WAFERS FOR STRAINED QUANTUM WELLS WITH LOW DISORDER

A crucial requirement for building scalable quantum systems in Ge/SiGe heterostructures is achieving a remarkably uniform active region. However, the presence of structural defects and strain fluctuations can severely undermine this uniformity. In this work we address these issues and improve the uniformity of the active region by adopting a novel approach: growing Ge/SiGe heterostructures on 100 mm Ge wafers. The use of Ge wafers as substrates for epitaxy enables high-quality Ge-rich SiGe strain-relaxed buffers with a threading dislocation density of $(6 \pm 1) \times 10^5$ cm^{-2}*, nearly an order of magnitude improvement compared to control strain-relaxed buffers on Si wafers. The associated reduction in short-range scattering allows for a drastic improvement of the disorder properties of the two-dimensional hole gas, measured in several Ge/SiGe heterostructure field-effect transistors. We measure an average low percolation density of* $(1.22 \pm 0.03) \times 10^{10}$ cm^{-2}*, and an average maximum mobility of* $(3.4 \pm 0.1) \times 10^6$ $\mathrm{cm}^2/\mathrm{Vs}$ *and quantum mobility of* $(8.4 \pm 0.5) \times 10^4$ $\mathrm{cm}^2/\mathrm{Vs}$ *when the hole density in the quantum well is saturated to* $(1.65 \pm 0.02) \times 10^{11}$ cm^{-2}*. We anticipate immediate application of these heterostructures for next-generation, higher-performance Ge spin-qubits and their integration into larger quantum processors.*

This work was originally published as:
L. E. A. Stehouwer, A. Tosato, D. d. Esposti, D. Costa, M. Veldhorst, A. Sammak, G. Scappucci, Germanium wafers for strained quantum wells with low disorder, Applied Physics Letters, 123, 9 (2023).

6.1. INTRODUCTION

Strained germanium quantum wells in silicon-germanium heterostructures (Ge/SiGe) have become the leading platform for quantum computation with hole spin qubits.[1] Single-hole spin qubits and singlet-triplet qubits can be universally controlled,[2, 3, 4] four-qubit logic has been executed,[5] and quantum dot systems have been scaled to crossbar arrays comprising 16 quantum dots.[6] Furthermore, the demonstration of a hard superconducting gap in Ge[7] motivates the pursuit of coherent coupling of high fidelity Ge spin qubits using crossed Andreev reflection for achieving two-qubit gates over micrometer distances.[8, 9] While single-spin qubits have been operated with fidelity as high as 99.99%,[10] and rudimentary error correction circuits have been executed,[11] quantum coherence limits the operation of larger systems. Although Ge can be isotopically enriched to remove dephasing due to hyperfine interaction,[12] which can also be achieved by strong confinement,[13] hole spin qubits are highly sensitive to charge noise, strain fluctuations, and other types of disorder that can affect the spin-orbit interactions.[14, 15, 16, 17] In addition to optimizing the semiconductor-dielectric interface in qubit devices, further improving the crystalline quality of strained quantum wells[18] appears as a key step to obtain a quieter environment for Ge quantum dots.

In the absence of suitable SiGe wafers for high-quality and uniform epitaxy, strained Ge quantum wells are commonly deposited on $Si_{1-x}Ge_x$ strain-relaxed buffers (SRBs) with high Ge composition ($x \approx 0.7-0.8$).[1] Starting epitaxy from a Si wafer, Ge-rich SiGe SRBs are obtained by composition grading either in a forward-graded process[19] or in a reverse-graded process after the deposition of a thick strain-relaxed Ge layer.[20, 21] In both cases, the large lattice mismatch between the Si substrate and the Ge-rich SiGe SRB causes a dense misfit dislocation network, with associated threading dislocations that propagate through the quantum well. Moreover, such misfit dislocation network drives significant local strain fluctuations inside the Ge quantum well,[22], thus challenging the scalability of semiconductor qubits. In Ge/SiGe heterostructures used to host qubits, the threading dislocation density (TDD) is in the range $\approx 10^6 - 10^7$ cm^{-2}.[21, 3] It is not surprising that Si/SiGe heterostructures have smaller TDD ($\approx 10^5$ cm^{-2}) because the Si-rich SiGe SRBs have less lattice mismatch to the Si substrate due to the smaller Ge composition ($x \approx 0.2-0.3$). In this Letter we depart from Si wafers and investigate Ge/SiGe heterostructures grown directly on Ge wafers, mitigating the complication of a large lattice-mismatch between Ge-rich SiGe and Si wafers. As a result, we show a significant enhancement of the crystal quality of the heterostructure, as well as a drastic improvement in the disorder properties of the two-dimensional hole gas (2DHG) that it supports.

6.2. STRUCTURAL AND MORPHOLOGICAL CHARACTERIZATION

Schematics in Figs. 6.1(a) and (b) compare heterostructures on a Ge wafer with our control reverse-graded heterostructures on a Si wafer,[23] the same that supported a four qubit quantum processor and a 16 quantum dot crossbar array.[5, 6] The 100 mm Ge wafers are prepared for epitaxy by an *ex-situ* HF-dip etch followed by *in-situ* bake at 800 °C. The heterostructure is grown in a high-throughput reduced-pressure chemical vapor deposition tool from high-purity germane and dichlorosilane. The SiGe SRB is ~2.5 μm thick and obtained by forward step grading of the Si content ($1-x = 0.07, 0.13, 0.17$).

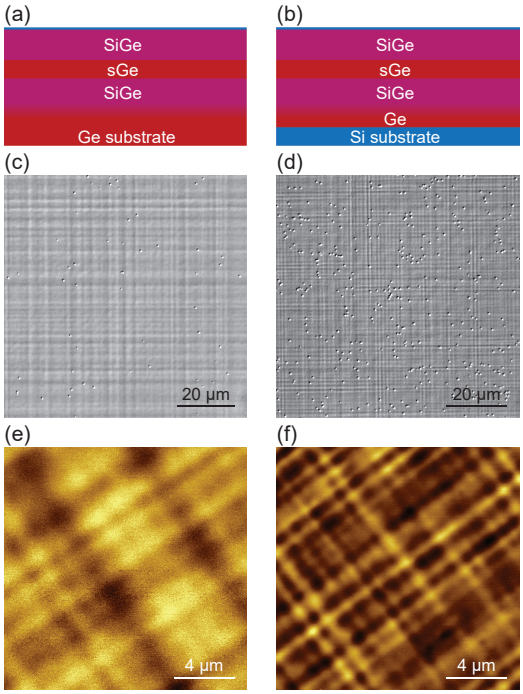

Figure 6.1: (a) Schematic of a Ge/SiGe heterostructure on a Ge wafer and (b) on a Si wafer. The strained Ge (sGe) quantum wells are grown with the same lattice parameter to SiGe strain-relaxed buffers (SRB). (c) and (d) Comparative optical microscope images of the heterostructures in (a) and (b) after threading dislocation decoration. The images are aligned to the ⟨110⟩ crystallographic axes. (e) and (f) Comparative atomic force microscopy images of the heterostructures in (a) and (b). The images were taken with an alignemnt of about 45 degrees to the ⟨110⟩ crystallographic axes.

This approach mirrors the common approach in Si/SiGe heterostructures where the Ge content is forward-graded starting from a Si wafer. Like our previous heterostructures,[21] the SiGe SRB is deposited at 800 °C and the growth temperature is reduced to 500 °C for the final 200 nm of SiGe below the quantum well and for all the layers above to achieve sharp quantum well interfaces. Importantly, by growing on Ge wafers we avoid the overtensile strain arising from the difference in the thermal expansion coefficients between Ge epilayers and Si substrates.[20] Consequently, to achieve an in-plane strain (ϵ) in the Ge quantum well similar to our previous heterostructures,[21, 23] here we increase the final Ge content x in the $Si_{1-x}Ge_x$ SRB to 0.83 (the supplementary material) compared to 0.8 in Refs. [21, 23]). The thickness of the Ge quantum well (16 nm) and of the SiGe barrier on top (55 nm) are nominally the same compared to Ref. [23] for a meaningful comparison of the electrical transport properties.

Figure 6.1(c) and (d) show comparative images by Nomarski microscopy of the heterostructures on a Ge and on a Si wafer after decorating the threading dislocations by *in-situ* HCl vapor etching.[24] We quantify the TDD by counting the number of decorated threading dislocations from multiple images taken across the wafer. Changing substrate

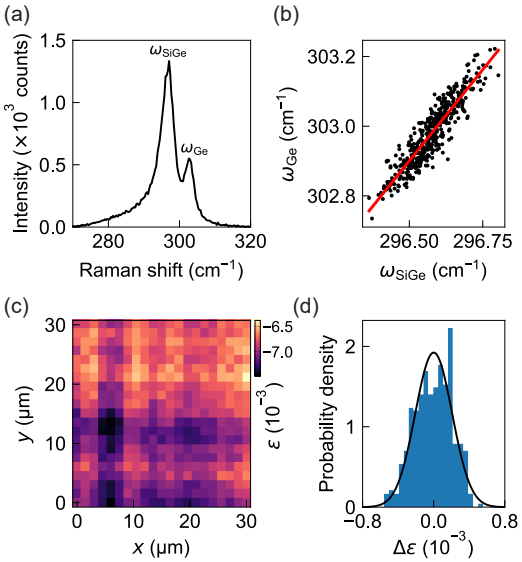

Figure 6.2: (a) Typical intensity spectra as a function of the Raman shift for a Ge/SiGe heterostructure on a Ge wafer. The positions of the Raman peaks from the Ge-Ge vibration modes in the strained Ge quantum well and in the SiGe layer are marked as ω_{Ge} and ω_{SiGe}, respectively. (b) Distribution of Raman peak positions of the Ge-Ge modes obtained by analyzing Raman spectra over an area of 30×30 μm^2 and linear fit (red). (c) Raman strain map, corresponding to the ω_{Ge} Raman shifts in (b). The map is aligned to the $\langle 110 \rangle$ crystallographic axes. (d) Strain fluctuations from the Raman map in (c) and normal distribution fit (black). Counts are normalized such that the area under the curve integrates to one.

from Si to Ge improves the TDD almost an order of magnitude, from $(5.3 \pm 0.3) \times 10^6$ cm^{-2} to $(6 \pm 1) \times 10^5$ cm^{-2}. Consequently the average TD separation ($1/\sqrt{\mathrm{TDD}}$) becomes much longer, from ~ 4.3 μm to ~ 13 μm. Comparative atomic-force microscopy images in Figs. 6.1(e) and (f) show the typical cross hatch pattern arising from the strain-releasing misfit dislocation network within the SiGe SRB on Ge and Si wafers, respectively. The root mean square surface roughness of both heterostructures is similar at ~1.5 nm. However, the heterostructure grown on a Ge wafer shows cross-hatch undulations with a longer wavelength and weaker high-frequency components of the Fourier spectrum (the supplementary material). This observation supports the intuition that the Ge-rich SiGe SRB has a less dense network of misfit dislocations when grown on a Ge wafer, as the lattice mismatch with the substrate is smaller compared to when it is grown on a Si wafer.

We further characterize the heterostructure on the Ge wafer by scanning Raman spectroscopy over an area of 30×30 μm^2, much larger than the length scale of the cross-hatch pattern features. In particular, we determined the in-plane strain in the quantum well ϵ and analyzed the origin and bandwidth of its fluctuations. The representative spectrum in Fig. 6.2(a) was obtained with a 633 nm red laser and shows two clear Raman peaks originating from the Ge-Ge vibration modes in the strained Ge quantum well (ω_{Ge}) and in the SiGe layer (ω_{SiGe}). The distribution of these Raman shifts in Fig. 6.2(b) shows a strong correlation, with a slope $\Delta\omega_{\mathrm{Ge}}/\Delta\omega_{\mathrm{SiGe}} = 1.05 \pm 0.02$. Comparing to predictions by Eq. 5 in Ref. [25], we argue that the distribution of the Raman shift in the Ge quantum well

is mainly driven by strain fluctuations in the SiGe SRB (expected $\Delta\omega_{Ge}/\Delta\omega_{SiGe} \sim 0.83$), rather than compositional fluctuations ($\Delta\omega_{Ge}/\Delta\omega_{SiGe} \sim 0.25$). Figure 6.2(c) shows the Raman strain map of the Ge quantum well calculated using $\epsilon = (\omega_{Ge} - \omega_0)/b^{Ge}$, where $\omega_0 = 299.9$ cm^{-1} is the Raman shift for bulk Ge and $b^{Ge} = -440$ cm^{-1} is the Ge phonon strain shift coefficient.[26] We identify signatures of the cross-hatch pattern, with regions featuring higher and lower strain around a mean strain value $\bar{\epsilon} = (-6.9 \pm 0.2) \times 10^{-3}$. This is similar to the compressive strain measured in our Ge quantum wells on a Si wafer,[21] validating our heterostructure design and comparative analysis. The statistics of the lateral strain map are shown in Fig. 6.2d. The strain fluctuations $\Delta\epsilon$ around the average $\bar{\epsilon}$ follow a normal distribution with a standard deviation of 2×10^{-4}. The bandwidth of the strain fluctuations is reduced when compared to the strain fluctuations from the heterostructure on a Si wafer,[22] pointing to a more uniform strain landscape.

The structural characterization highlights the improvement in crystal quality when growing a Ge-rich SRB on a Ge wafer instead of a Si wafer. Next, we show how a better and more uniform crystalline environment improves the disorder properties of the 2DHG. We fabricate six Hall-bar shaped heterostructure field effect transistors (H-FETs) on a 2×2 cm^2 coupon from the center of the 100 mm wafer with a similar process as in Ref. [23] We accumulate a 2DHG inside the Ge quantum well by applying a negative DC gate voltage (V_g) to the top gate of the H-FETs and we increase the density p in the 2DHG above the percolation density (p_p) by making V_g more negative. We use standard four-probe low-frequency lock-in techniques for mobility-density and magnetotransport characterization of all devices in a dilution refrigerator equipped with a cryo-multiplexer[27] ($T = 70$ mK measured at the mixing chamber).

6.3. CLASSICAL AND QUANTUM TRANSPORT

Figure 6.3(a) shows the density-dependent mobility curve (solid line), obtained by averaging over the six H-FETs, together with the standard deviation (shaded region). We observe a tight distribution over the entire density range, indicating a very uniform disorder potential landscape. The mobility increases steeply with increasing density, due to increasing screening of the remote impurity charges, most likely at the semiconductor-dielectric interface. At higher densities ($p > 5 \times 10^{10}$ cm^{-2}), the mobility increases less rapidly, signaling the relevance of scattering from impurities within or in the proximity of the quantum well.[28] We observe a maximum mobility μ_{max} in the range of $3.3-3.6 \times 10^6$ cm^2/Vs over the six investigated H-FETS (Fig. 6.3(a), inset), from which we extract an average $\mu_{max} = (3.4 \pm 0.1) \times 10^6$ cm^2/Vs at a saturation density $p_{sat} = (1.65 \pm 0.02) \times 10^{11}$cm^{-2}, corresponding to a long mean free path of 23 µm. Figure 6.3b shows the longitudinal conductivity σ_{xx} as a function of density p for a representative H-FET. We extract the percolation density p_p from fitting to percolation theory,[29] $\sigma_{xx} \propto (p - p_p)^{1.31}$. The inset shows p_p for the six H-FETs, from which we extract an average percolation density $p_p = (1.22 \pm 0.03) \times 10^{10}$ cm^{-2}.

Compared to our control heterostructures on a Si wafer supporting qubits,[23, 5] the maximum mobility is more than 15 times larger and the percolation density is more than 1.5 times smaller. We speculate that this significant improvement, throughout the whole density range, is associated with the suppression of short-range scattering from dislocations within the quantum well. Furthermore, the mobility has not yet saturated in-

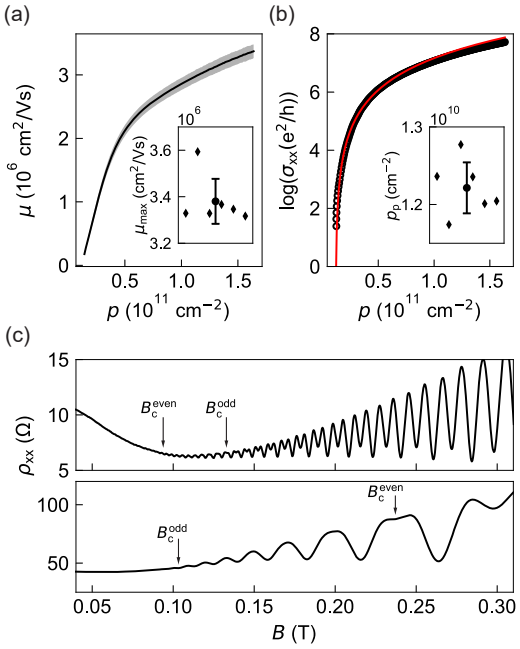

Figure 6.3: (a) Mobility μ mean (blue) and standard deviation (shaded) as a function of density p obtained from measurements at $T = 70$ mK of six Hall bar devices from the same wafer. The inset shows the maximum mobility $\mu_{\max}$ from all the devices and average value ± standard deviation (black). (b) Conductivity σ_{xx} as a function of p (circles) for one device and fit to the percolation theory in the low density regime (solid red line). The inset shows the percolation density p_p from all the devices and average value ± standard deviation (black). (c) Longitudinal resistivity ρ_{xx} as a function of perpendicular magnetic field B measured at a density of 1.5×10^{11} cm^{-2} (upper panel) and 6×10^{10} cm^{-2} (lower panel). B_c^{even} and B_c^{odd} indicate the critical magnetic fields for resolving even and odd filling factors, corresponding to the cyclotron and the spin gap, respectively.

dicating that it is still limited by long-range scattering from impurities at the dielectric interface, leaving room for further improvement. In fact, our maximum mobility, reproducible across multiple devices, is less than the value $\mu = 4.3 \times 10^6$ cm^2/Vs measured on a single H-FET in Ge/SiGe grown on a Si wafer,[30] likely because the dielectric interface in our samples is much closer to the channel (55 nm compared to 100 nm in Ref. [30]).

The low level of disorder is confirmed by high-quality magnetotransport characterization observed in all devices. Figure 6.3(c) shows representative magneto-resistivity curves from an H-FET at fixed densities of 1.5×10^{11} cm^{-2} (upper panel) and 6×10^{10} cm^{-2} (lower panel). The measurements were performed by keeping V_g constant and sweeping the perpendicular magnetic field B. For each longitudinal resistivity (ρ_{xx}) curve we extract the pair of critical magnetic fields for resolving the cyclotron and the spin gap, $\{B_c^{even}, B_c^{odd}\}$, corresponding, respectively, to even and odd filling factors $\nu = hp/eB$ in the Shubnikov –de Haas oscillations minima. Due to the very small Landau level broadening at high density, the cyclotron gap (see upper panel of Fig. 6.3(c)) is resolved already at very low critical fields and the spin gap only a few oscillations later, $\{B_c^{even}, B_c^{odd}\} = \{0.08, 0.13\}$ T. However, at low density the order is reversed and the spin gap is resolved

earlier than the cyclotron gap, $\{B_c^{even}, B_c^{odd}\} = \{0.24, 0.095\}$ T (see lower panel of Fig. 6.3(c)). This is typical to 2DHGs in Ge/SiGe and occurs when the spin gap is more than half of the cyclotron gap, due to the increased perpendicular g-factors of holes at low density.[31, 32, 30]

The combination of these two aspects, the very low level of disorder and the increasingly large spin gap at low density, makes the canonical methods[33, 34] for extracting the effective mass m^* and single-particle lifetime τ_q not straightforward throughout the investigated density range and will be pursued in a further study. However, we may still estimate the quantum mobility $\mu_q = e\tau_q/m^*$ without making assumptions on m^* and τ_q using the expression $\mu_q = (1 + \sqrt{B_c^{odd}/B_c^{even}})/2B_c^{odd}$ (the supplementary material). With this analysis, we obtain a maximum quantum mobility in the range of $7.7-9.1\times10^4$ cm^2/Vs over the six investigated H-FETS (the supplemental material), from which we extract an average maximum $\mu_q = (8.4\pm0.5)\times10^4$ cm^2/Vs at saturation density. This value should be considered as a conservative estimate of μ_q, as the onset of Shubnikov –de Haas oscillations in our high-quality samples might be limited by small density inhomogeneities at low magnetic field.[35] The maximum μ_q is over three times larger than that of our control heterostructures on a Si wafer,[23, 5] and approximately two times larger compared to the heterostructures on a Si wafer in Ref. [30] These results highlight the significantly improved short-range scattering in 2DHGs when the Ge-rich SiGe SRB is grown on a Ge substrate, setting a benchmark for holes in group IV semiconductors.

6.4. DISCUSSION

In summary, we challenged the mainstream approach to deposit Ge/SiGe heterostructures on Si wafers and instead, we started epitaxy on a Ge wafer. We demonstrate a more uniform crystalline environment with fewer dislocations and in-plane strain fluctuations compared to control heterostructures supporting a four-qubit quantum processors. Future investigations using X-ray diffraction spectroscopy to map the complete strain tensor[22] could provide insights into the local strain modifications and fluctuation caused by nanostructured metallic gates. The disorder properties of the 2DHG are also greatly improved, with reproducible ultra-high mobility, very low percolation density, and high quantum mobility. Considering these heterostructures on Ge wafers as a proof of principle, the electrical transport metrics are likely to further improve by routine optimization of the heterostructure design and chemical vapor deposition process. We anticipate immediate benefit of using these heterostructures for improved uniformity and yield in large quantum dot arrays. Future studies on charge noise and qubit performance may also provide insight in possible improved quantum coherence. Furthermore, it would be of significant interest to explore whether suppressing the dislocation network in the SiGe SRB could improve the performance of superconducting microwave resonators integrated atop the heterostructure, towards the development of hybrid superconductor-semiconductor architectures.

6.5. SUPPLEMENTARY INFORMATION

6.5.1. SECONDARY IONS MASS SPECTROSCOPY

Secondary ion mass spectroscopy (SIMS) was carried out to determine the chemical composition of the Ge/SiGe heterostructure on the Ge substrate. Supplementary Fig. 6.4 overlays the Ge (red), Si (blue), O (green), and C (yellow) signals. The data confirms the chemical composition $x = 0.83$ of the $Si_{1-x}Ge_x$ buffer and barrier surrounding the Ge quantum well. The oxygen and carbon concentrations far from the surface are below the detection limit. The rising O and C signals near the surface are routine in SIMS and should be considered an artifact of the measurement.

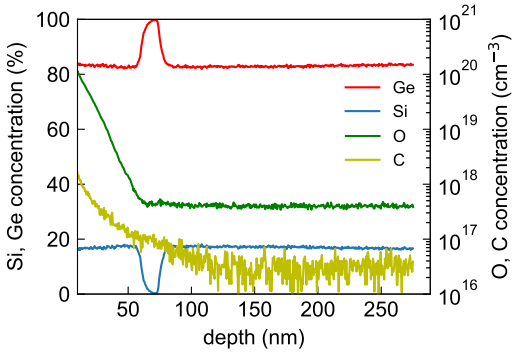

Figure 6.4: Secondary ions mass spectroscopy of Ge/SiGe heterostructures on a Ge wafer, showing Si (blue), Ge (red), O (green), C (yellow) concentration depth profiles

6.5.2. ATOMIC FORCE MICROSCOPY

We analysed the cross-hatch patterns shown in Figs. 1(e) and (f) in the main text by performing a 2D Fourier transform using Gwyddion.[36] The results are shown in supplementary Figs. 6.5(a) and (b) for the heterostructure grown on a Ge wafer and Si wafer, respectively. A comparison of the two images shows that the dominant frequencies are spaced closer together in the 2D Fourier transform of the heterostructure on a Ge substrate than those in the heterostructure on the Si substrate. This confirms that using a Ge wafer as a substrate results in a longer wavelength of the cross-hatch pattern compared to when a Si wafer is used, a consequence of the reduced misfit dislocation network present in this heterostructure.

6.5.3. QUANTUM MOBILITY

In these Ge/SiGe quantum wells on Ge wafers, the combination of the very low level of disorder and the increasingly large spin gap makes an estimate of the effective g-factor g^* and effective mass m^* challenging from the analysis of the thermal activation of the resistivity minima in the Shubnikov -de Haas oscillations corresponding to the cyclotron and spin gap. The same applies to the standard analysis[33] for extracting the single-particle lifetime τ_q, which measures the time for which a momentum eigenstate can be defined even in the presence of scattering,[37] and the associated quantum mobil-

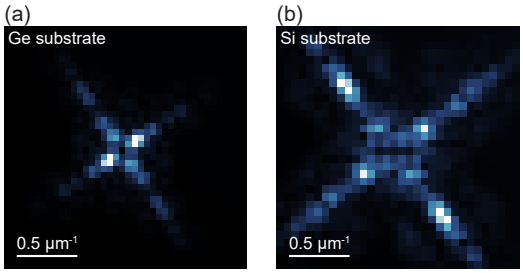

Figure 6.5: (a) 2D Fourier transform of AFM image in Fig. 1(e) in the main text for heterostructures on a Ge wafer. (b) 2D Fourier transform of AFM image in Fig. 1(f) in the main text for heterostructures on a Si wafer.

ity $\mu_q = e\tau_q/m^*$. However, just like the classical mobility is typically measured without knowing the effective mass m^* or the scattering time τ_t, we may also estimate the quantum mobility without a direct measurement of m^* and τ_q. Assuming that Landau levels have a Gaussian broadening $\Gamma = \hbar/2\tau_q$[37] that increases as $\sqrt{B}$, where B is the perpendicular magnetic field, Refs. [21, 30] show that:

$$g^* = \frac{2m_e}{m^*} \frac{\sqrt{B_c^{\text{even}}}}{\sqrt{B_c^{\text{even}}} + \sqrt{B_c^{\text{odd}}}} \tag{6.1}$$

where B_c^{even} and B_c^{odd} are the critical magnetic fields for resolving the cyclotron and the spin gap, corresponding, respectively, to even and odd filling factors $\nu = hp/eB$ in the Shubnikov–de Haas oscillations minima of the magnetoresistivity. Evaluating the level broadening at $B = B_c^{\text{odd}}$ yields:

$$\Gamma = g^* \mu_B B_c^{\text{odd}} \tag{6.2}$$

where the Bohr magneton $\mu_B = e\hbar/2m_e$. Expressing the level broadening in terms of quantum mobility yields:

$$\Gamma = e\hbar/2m^*\mu_q. \tag{6.3}$$

By inserting $g*$ from Eq. 6.1 and Γ from Eq. 6.3 into Eq. 6.2, we obtain an expression for quantum mobility that is independent of m^* and $g*$:

$$\mu_q = \frac{1 + \sqrt{B_c^{\text{odd}}/B_c^{\text{even}}}}{2B_c^{\text{odd}}}. \tag{6.4}$$

We apply this analysis to the magnetoresistivity curves at saturation density for all six heterostructures field effect transistors and show in Supplementary Fig. 6.6 the obtained quantum mobility values and the average with standard deviation (black).

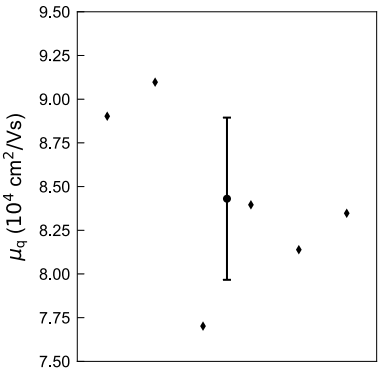

Figure 6.6: Quantum mobility for Ge/SiGe on Ge substrates measured at saturation density for all the six heterostructure field effect transistors.

BIBLIOGRAPHY

[1] G. Scappucci, C. Kloeffel, F. A. Zwanenburg, D. Loss, M. Myronov, J.-J. Zhang, S. De Franceschi, G. Katsaros, and M. Veldhorst. "The germanium quantum information route". en. In: *Nature Reviews Materials* 6.10 (Oct. 2021), pp. 926–943. ISSN: 2058-8437.

[2] N. W. Hendrickx, W. I. L. Lawrie, L. Petit, A. Sammak, G. Scappucci, and M. Veldhorst. "A single-hole spin qubit". en. In: *Nature Communications* 11.1 (July 2020), p. 3478. ISSN: 2041-1723.

[3] D. Jirovec, A. Hofmann, A. Ballabio, P. M. Mutter, G. Tavani, M. Botifoll, A. Crippa, J. Kukucka, O. Sagi, F. Martins, J. Saez-Mollejo, I. Prieto, M. Borovkov, J. Arbiol, D. Chrastina, G. Isella, and G. Katsaros. "A singlet-triplet hole spin qubit in planar Ge". en. In: *Nature Materials* 20.8 (Aug. 2021), pp. 1106–1112. ISSN: 1476-4660.

[4] C.-A. Wang, C. Déprez, H. Tidjani, W. I. L. Lawrie, N. W. Hendrickx, A. Sammak, G. Scappucci, and M. Veldhorst. "Probing resonating valence bonds on a programmable germanium quantum simulator". In: *Preprint at https://arxiv.org/abs/2208.11505* (Aug. 2022).

[5] N. W. Hendrickx, W. I. L. Lawrie, M. Russ, F. van Riggelen, S. L. de Snoo, R. N. Schouten, A. Sammak, G. Scappucci, and M. Veldhorst. "A four-qubit germanium quantum processor". en. In: *Nature* 591.7851 (Mar. 2021), pp. 580–585. ISSN: 1476-4687.

[6] F. Borsoi, N. W. Hendrickx, V. John, S. Motz, F. van Riggelen, A. Sammak, S. L. de Snoo, G. Scappucci, and M. Veldhorst. "Shared control of a 16 semiconductor quantum dot crossbar array". In: *Preprint at https://arxiv.org/abs/2209.06609* (Sept. 2022).

[7] A. Tosato, V. Levajac, J.-Y. Wang, C. J. Boor, F. Borsoi, M. Botifoll, C. N. Borja, S. Martí-Sánchez, J. Arbiol, A. Sammak, M. Veldhorst, and G. Scappucci. "Hard superconducting gap in germanium". en. In: *Communications Materials* 4.1 (Apr. 2023), p. 23. ISSN: 2662-4443.

[8] M.-S. Choi, C. Bruder, and D. Loss. "Spin-dependent Josephson current through double quantum dots and measurement of entangled electron states". In: *Physical Review B* 62.20 (Nov. 2000), pp. 13569–13572.

[9] M. Leijnse and K. Flensberg. "Coupling Spin Qubits via Superconductors". In: *Physical Review Letters* 111.6 (Aug. 2013), p. 060501.

[10] W. I. L. Lawrie, M. Russ, F. van Riggelen, N. W. Hendrickx, S. L. de Snoo, A. Sammak, G. Scappucci, and M. Veldhorst. "Simultaneous driving of semiconductor spin qubits at the fault-tolerant threshold". In: *Preprint at https://arxiv.org/abs/2109.07837* (2021).

[11] F. van Riggelen, W. I. L. Lawrie, M. Russ, N. W. Hendrickx, A. Sammak, M. Rispler, B. M. Terhal, G. Scappucci, and M. Veldhorst. “Phase flip code with semiconductor spin qubits”. en. In: *npj Quantum Information* 8.1 (Oct. 2022), p. 124. ISSN: 2056-6387.

[12] K. Itoh, W. L. Hansen, E. E. Haller, J. W. Farmer, V. I. Ozhogin, A. Rudnev, and A. Tikhomirov. “High purity isotopically enriched 70-Ge and 74-Ge single crystals: Isotope separation, growth, and properties”. In: *J. Mater. Res.* 8.6 (June 1993), pp. 1341–1347. ISSN: 2044-5326, 0884-2914.

[13] S. Bosco and D. Loss. “Fully Tunable Hyperfine Interactions of Hole Spin Qubits in Si and Ge Quantum Dots”. In: *Physical Review Letters* 127.19 (Nov. 2021), p. 190501.

[14] S. Bosco, B. Hetényi, and D. Loss. “Hole Spin Qubits in Si FinFETs With Fully Tunable Spin-Orbit Coupling and Sweet Spots for Charge Noise”. In: *PRX Quantum* 2.1 (Mar. 2021), p. 010348.

[15] O. Malkoc, P. Stano, and D. Loss. “Charge-Noise-Induced Dephasing in Silicon Hole-Spin Qubits”. In: *Physical Review Letters* 129.24 (Dec. 2022), p. 247701.

[16] L. A. Terrazos, E. Marcellina, Z. Wang, S. N. Coppersmith, M. Friesen, A. R. Hamilton, X. Hu, B. Koiller, A. L. Saraiva, D. Culcer, and R. B. Capaz. “Theory of hole-spin qubits in strained germanium quantum dots”. In: *Physical Review B* 103.12 (Mar. 2021), p. 125201.

[17] J. C. Abadillo-Uriel, E. A. Rodríguez-Mena, B. Martinez, and Y.-M. Niquet. “Hole-spin driving by strain-induced spin-orbit interactions”. In: *Physical Review Letters* 131.9 (2023), p. 097002.

[18] B. Paquelet Wuetz, D. Degli Esposti, A.-M. J. Zwerver, S. V. Amitonov, M. Botifoll, J. Arbiol, A. Sammak, L. M. K. Vandersypen, M. Russ, and G. Scappucci. “Reducing charge noise in quantum dots by using thin silicon quantum wells”. en. In: *Nature Communications* 14.1 (Mar. 2023), p. 1385. ISSN: 2041-1723.

[19] G. Isella, D. Chrastina, B. Rössner, T. Hackbarth, H.-J. Herzog, U. König, and H. Von Känel. “Low-energy plasma-enhanced chemical vapor deposition for strained Si and Ge heterostructures and devices”. en. In: *Solid-State Electronics* 48.8 (Aug. 2004), pp. 1317–1323. ISSN: 00381101.

[20] V. A. Shah, A. Dobbie, M. Myronov, D. J. F. Fulgoni, L. J. Nash, and D. R. Leadley. “Reverse graded relaxed buffers for high Ge content SiGe virtual substrates”. In: *Appl. Phys. Lett.* 93.19 (Nov. 2008), p. 192103. ISSN: 0003-6951.

[21] A. Sammak, D. Sabbagh, N. W. Hendrickx, M. Lodari, B. P. Wuetz, A. Tosato, L. Yeoh, M. Bollani, M. Virgilio, M. A. Schubert, P. Zaumseil, G. Capellini, M. Veldhorst, and G. Scappucci. “Shallow and Undoped Germanium Quantum Wells: A Playground for Spin and Hybrid Quantum Technology”. en. In: *Advanced Functional Materials* 29.14 (2019), p. 1807613. ISSN: 1616-3028.

[22] C. Corley-Wiciak, C. Richter, M. H. Zoellner, I. Zaitsev, C. L. Manganelli, E. Zatterin, T. U. Schülli, A. A. Corley-Wiciak, J. Katzer, F. Reichmann, W. M. Klesse, N. W. Hendrickx, A. Sammak, M. Veldhorst, G. Scappucci, M. Virgilio, and G. Capellini. "Nanoscale Mapping of the 3D Strain Tensor in a Germanium Quantum Well Hosting a Functional Spin Qubit Device". en. In: *ACS Applied Materials & Interfaces* 15.2 (Jan. 2023), pp. 3119–3130. ISSN: 1944-8244, 1944-8252.

[23] M. Lodari, N. W. Hendrickx, W. I. L. Lawrie, T.-K. Hsiao, L. M. K. Vandersypen, A. Sammak, M. Veldhorst, and G. Scappucci. "Low percolation density and charge noise with holes in germanium". en. In: *Materials for Quantum Technology* 1.1 (Jan. 2021), p. 011002. ISSN: 2633-4356.

[24] Y. Bogumilowicz, J. M. Hartmann, R. Truche, Y. Campidelli, G. Rolland, and T. Billon. "Chemical vapour etching of Si, SiGe and Ge with HCl; applications to the formation of thin relaxed SiGe buffers and to the revelation of threading dislocations". In: *Semiconductor Science and Technology* 20.2 (Feb. 2005), pp. 127–134. ISSN: 0268-1242, 1361-6641.

[25] K. Kutsukake, N. Usami, T. Ujihara, K. Fujiwara, G. Sazaki, and K. Nakajima. "On the origin of strain fluctuation in strained-Si grown on SiGe-on-insulator and SiGe virtual substrates". en. In: *Applied Physics Letters* 85.8 (Aug. 2004), pp. 1335–1337. ISSN: 0003-6951, 1077-3118.

[26] F. Pezzoli, E. Bonera, E. Grilli, M. Guzzi, S. Sanguinetti, D. Chrastina, G. Isella, H. Von Känel, E. Wintersberger, J. Stangl, and G. Bauer. "Phonon strain shift coefficients in Si1-xGex alloys". en. In: *Journal of Applied Physics* 103.9 (May 2008), p. 093521. ISSN: 0021-8979, 1089-7550.

[27] B. Paquelet Wuetz, P. L. Bavdaz, L. A. Yeoh, R. Schouten, H. van der Does, M. Tiggelman, D. Sabbagh, A. Sammak, C. G. Almudever, F. Sebastiano, J. S. Clarke, M. Veldhorst, and G. Scappucci. "Multiplexed quantum transport using commercial off-the-shelf CMOS at sub-kelvin temperatures". en. In: *npj Quantum Information* 6.1 (May 2020), p. 43. ISSN: 2056-6387.

[28] D. Monroe. "Comparison of mobility-limiting mechanisms in high-mobility Si1-xGex heterostructures". In: *Journal of Vacuum Science & Technology B: Microelectronics and Nanometer Structures* 11.4 (July 1993), p. 1731. ISSN: 0734211X.

[29] L. A. Tracy, E. H. Hwang, K. Eng, G. A. Ten Eyck, E. P. Nordberg, K. Childs, M. S. Carroll, M. P. Lilly, and S. Das Sarma. "Observation of percolation-induced two-dimensional metal-insulator transition in a Si MOSFET". In: *Physical Review B* 79.23 (June 2009), p. 235307.

[30] M. Myronov, J. Kycia, P. Waldron, W. Jiang, P. Barrios, A. Bogan, P. Coleridge, and S. Studenikin. "Holes Outperform Electrons in Group IV Semiconductor Materials". en. In: *Small Science* 3.4 (Apr. 2023), p. 2200094. ISSN: 2688-4046, 2688-4046.

[31] T. M. Lu, L. A. Tracy, D. Laroche, S.-H. Huang, Y. Chuang, Y.-H. Su, J.-Y. Li, and C. W. Liu. "Density-controlled quantum Hall ferromagnetic transition in a two-dimensional hole system". en. In: *Scientific Reports* 7.1 (June 2017), p. 2468. ISSN: 2045-2322.

[32] M. Lodari, A. Tosato, D. Sabbagh, M. A. Schubert, G. Capellini, A. Sammak, M. Veldhorst, and G. Scappucci. “Light effective hole mass in undoped Ge/SiGe quantum wells”. In: *Physical Review B* 100.4 (July 2019), p. 041304.

[33] P. T. Coleridge. “Small-angle scattering in two-dimensional electron gases”. In: *Physical Review B* 44.8 (Aug. 1991), pp. 3793–3801.

[34] P. T. Coleridge, M. Hayne, P. Zawadzki, and A. S. Sachrajda. “Effective masses in high-mobility 2D electron gas structures”. en. In: *Surface Science* 361-362 (July 1996), pp. 560–563. ISSN: 0039-6028.

[35] Q. Qian, J. Nakamura, S. Fallahi, G. C. Gardner, J. D. Watson, S. Lüscher, J. A. Folk, G. A. Csáthy, and M. J. Manfra. “Quantum lifetime in ultrahigh quality GaAs quantum wells: Relationship to Δ 5 / 2 and impact of density fluctuations”. en. In: *Physical Review B* 96.3 (July 2017), p. 035309. ISSN: 2469-9950, 2469-9969.

[36] D. Nečas and P. Klapetek. “Gwyddion: an open-source software for SPM data analysis”. In: *Open Physics* 10.1 (Jan. 2012). ISSN: 2391-5471.

[37] S. Das Sarma and F. Stern. “Single-particle relaxation time versus scattering time in an impure electron gas”. en. In: *Physical Review B* 32.12 (Dec. 1985), pp. 8442–8444. ISSN: 0163-1829.

7

A HIGH-MOBILITY HOLE BILAYER IN A GERMANIUM DOUBLE QUANTUM WELL

Thanks to the low disorder and the fine control achieved in the growth of Ge/SiGe heterostructures offer the opportunity to confine multiple layers of charge carriers in the out of plane direction. This offers interesting avenues both for scaling spin qubit systems and for exploring new physics. In this work we design, fabricate, and study a hole bilayer in a strained germanium double quantum well. Magnetotransport characterisation of double quantum well field-effect transistors as a function of gate voltage reveals the population of two hole channels with a high combined mobility of $3.34 \times 10^5\,\mathrm{cm^2\,V^{-1}\,s^{-1}}$ *and a low percolation density of* $2.38 \times 10^{10}\,\mathrm{cm^{-2}}$*. We resolve the individual population of the channels from the interference patterns of the Landau fan diagram. At a density of* $2.0 \times 10^{11}\,\mathrm{cm^{-2}}$ *the system is in resonance and we observe an anti-crossing of the first two bilayer subbands characterized by a symmetric-antisymmetric gap of* $\sim 0.69\,\mathrm{meV}$*, in agreement with Schrödinger-Poisson simulations.*

This work was originally published as :
A. Tosato, B. Ferrari, A. Sammak, A. R. Hamilton, M. Veldhorst, M. Virgilio, G. Scappucci, A High-Mobility Hole Bilayer in a Germanium Double Quantum Well. Advanced Quantum Technologies, 5(5), 2100167 (2022).

7.1. INTRODUCTION

The development of high-quality undoped Ge/SiGe quantum wells [1, 2] has established planar Ge as a front-runner material platform en route to a large-scale spin-qubit quantum processor [3]. In only three years, key milestones have been demonstrated, such as stable and quiet quantum dots [4, 2] , single hole qubits [5] with long relaxation times [6], singlet-triplet qubits [7], fast two-qubit logic [8], universal operation on a 2×2 qubit array [9], and simultaneous qubit driving at the fault-tolerant threshold [10]. Exploiting the third dimension by integrating two (or more) quantum wells in the same heterostructure could provide extra degrees of freedom for designing an entire new class of quantum device architectures with tailored electronic properties. For example, quantum devices patterned in multiple layers may provide increased qubit connectivity for high performance quantum circuits. In these devices, the wavefunction of quantum-confined holes may be shifted or delocalized in between quantum wells, providing a larger parameter space for effective mass, g-factor, and spin-orbit coupling tuning [11], and enabling low-power electric dipole spin resonance (EDSR) [12]. These are relevant parameters for advanced spin-qubit control [3]. Furthermore, bilayers with high-mobility at low density may provide a suitable test bed for exploration of exotic phenomena such as exciton condensation in the quantum Hall regime [13] and counterflow superconductivity in solid state devices at accessible temperatures [14].

Here we demonstrate hole bilayers in planar Ge double quantum wells with high mobility at low density, a first prerequisite for exploring any of these exciting avenues. Through careful design of the heterostructure and because of the low disorder in both quantum wells, we are able to study in detail the quantum transport properties of the system in the tunnel coupled regime and observe the signature of a symmetric-antisymmetric gap when we tune the density in the quantum wells to be the same.

7.2. HETEROSTRUCTURE DESIGN

Figure 7.1a shows a schematic of the heterostructure, along with a cross section of the double quantum well by transmission electron microscopy. The Ge/SiGe bilayer was grown on a 100 mm Si(001) substrate in a high-throughput reduced-pressure chemical vapor deposition reactor [1]. The 16 nm bottom quantum well and the 8 nm top quantum well are separated by a thin 3 nm $Si_{0.2}Ge_{0.8}$ barrier. The bilayer is grown on a strain-relaxed $Si_{0.2}Ge_{0.8}$ buffer layer obtained by reverse grading and is separated from the gate-stack by a 66 nm $Si_{0.2}Ge_{0.8}$ barrier and a thin sacrificial Si cap[1]. The quantum wells are compressively strained, the strain lifts the heavy hole (HH) - light holes (LH) degeneracy, with HH being the lowest energy band for holes.

The asymmetric design of the bilayer—the top quantum well being narrower than the bottom quantum well—allows both wells in the undoped heterostructure to be populated by applying a negative voltage to the top gate only [15]. We illustrate this capability in the three panels of Fig. 7.1b, which report the results of Schrödinger-Poisson (SP) simulations of our bilayer for increasing negative gate voltages. Each panel shows the HH-band-edge, the total hole density and the wavefunction amplitude for the first Ψ_1 and second Ψ_2 subband of the bilayer system, as a function of the spatial coordinate z. At small gate voltages ($V = V_0$, left panel), only the first subband is populated and its

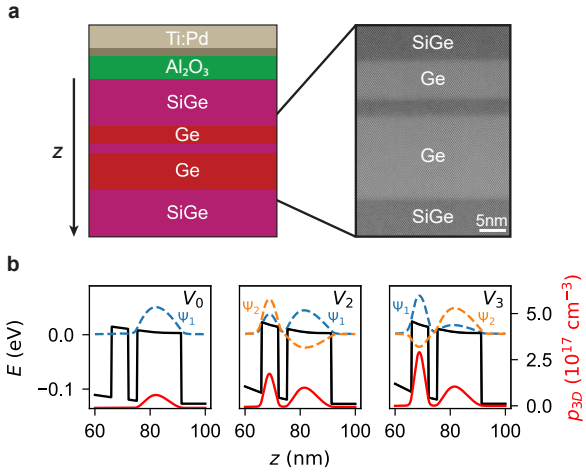

Figure 7.1: **a** Schematic of the Ge/SiGe heterostructure with the gate stack and cross section of the double quantum well by transmission electron microscopy. The bottom Ge quantum well (16 nm thick), and the top well (7 nm thick) are separated by a thin SiGe barrier (3 nm thick). **b** From left to right at increasing negative gate voltage (V_0, V_2, and V_3), each panel shows the heavy-holes band edge (black solid line), the wavefunction of the subbands above the Fermi energy (colored dashed lines), and the total density $p_{3D} = p_1|\Psi_1|^2 + p_2|\Psi_2|^2$ (red solid line) vs. bilayer depth (z). Here Ψ_1, Ψ_2 are the wavefunction amplitudes and p_1, p_2 the densities of the first and second subband. The Fermi energy is set as the reference energy at 0 eV.

wave function Ψ_1 is localized in the bottom well. At larger gate voltages occupation of the second subband becomes favourable with its wavefunction Ψ_2 initially localized in the top well. Then, the energy of the second subband increases with gate voltage until it anticrosses the energy level of the first subband at the resonance point. The central panel ($V = V_2$) shows the system at resonance. In this regime, the wavefunction of the first and second energy states are delocalized across both wells giving rise to the symmetric Ψ_1 and antisymmetric Ψ_2 states characteristic of a tunnel-coupled double quantum well system. The energy separation between the symmetric and antisymmetric states reaches its minimum (Δ_{SAS}) at resonance. Upon further increasing the gate voltage ($V = V_3$ right panel), the wavefunction of the symmetric state shifts towards the top well and the total carrier density of the top quantum well increases while the one of the bottom quantum well remains unchanged.

7.3. MAGNETOTRANSPORT MEASUREMENTS

We fabricated Hall-bar shaped heterostructure field effect transistors (H-FETs) featuring platinum-germanosilicide ohmic contacts [1] to the bilayer and performed measurements in a ^{3}He dilution refrigerator with base temperature of 50 mK and equipped with a 12 T magnet. Standard voltage-bias four-probe lock-in technique at a frequency of 17 Hz was used for magnetotransport characterization as described in ref. [1]. We measure the longitudinal ρ_{xx} and transverse ρ_{xy} components of the resistivity tensor and via tensor inversion calculate the longitudinal σ_{xx} and transverse σ_{xy} conductivity.

The three panels of Fig. 7.2a show the zero-field longitudinal conductivity σ_{xx}, the

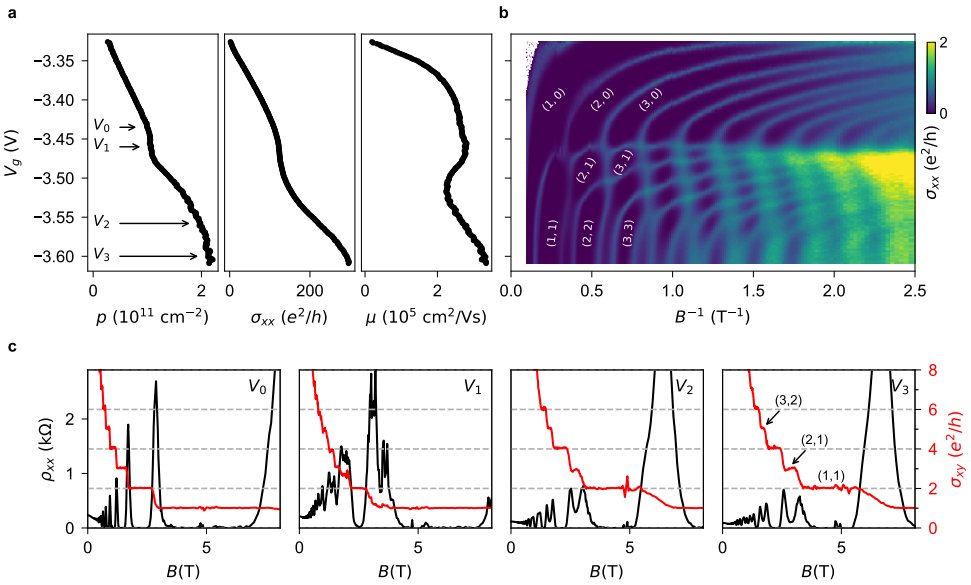

Figure 7.2: **a** From left to right: gate voltage (V_g) dependence of the hole bilayer Hall density p, conductivity σ_{xx} at zero magnetic field , and mobility μ. The bilayer behaviour at $V_g = V_0$, V_1, V_2, and V_3 is further described in the main text. **b** Colour map of the conductivity σ_{xx} as a function of V_g (same range as in **a**) and the inverse magnetic field B^{-1}. Dark regions correspond to filled Landau levels with vanishing σ_{xx} and correspondingly quantized σ_{xy}. In brackets the filling factor (ν_{sbb1},ν_{sbb2}) for the first and second subbands where $\nu = 0$ indicates an empty subband. **c** From left to right: ρ_{xx} (black) and σ_{xy} (red) as a function of magnetic field B at $V_g = V_0$, V_1, V_2, and V_3. These line cuts are obtained from the magnetotransport measurement in **b**. σ_{xy} shows plateaus at integer values of the total filling factor ($\nu_{sbb1} + \nu_{sbb2}$)

bilayer density p and the carrier mobility μ as a function of gate voltage V_g. At turn-on, only the bottom quantum well is populated. Mobility, density, and conductivity increase monotonically as the gate voltage is swept more negative up to a value $V_0 = -3.45$ V. In particular the Hall density increases linearly, consistent with a parallel-plate capacitor model of an H-FET with a single quantum well [16]. We estimate a percolation density $p_p = 2.38 \times 10^{10}\,\mathrm{cm}^{-2}$ by fitting the conductivity to percolation theory $\sigma_{xx} \sim (p - p_p)^{1.31}$ in the low density regime [17]. For $V_0 \leq V_g \leq V_1$ both the Hall density and conductivity deviate from the linear behaviour expected from SP simulations and flatten out. This observation signals that holes start populating the second subband; These holes are localized in the top quantum well, thereby screening the electric field at the bottom well. However, carriers in the top quantum well do not contribute to transport as their density is still below the percolation density. A further increase in negative gate voltage triggers transport in the top quantum well and for $V_1 \leq V_g \leq V_2$ we observe a transitory decrease in combined mobility due to inter-layer scattering [18, 19, 20]. For $V_g \geq V_2$ the combined mobility recovers its original monotonic increasing behaviour and saturates at $V_g = V_3$, reaching a maximum value $\mu = 3.34 \times 10^5\,\mathrm{cm}^2\mathrm{V}^{-1}\mathrm{s}^{-1}$ at bilayer density $p = 2.21 \times 10^{11}\,\mathrm{cm}^{-2}$. The carrier saturation at large negative gate voltages is due to tunneling of holes from the Ge quantum wells into localized states at the SiGe/Al_2@O_3

interface [16].

To elucidate the quantum transport properties of the bilayer we show in the right panel of Fig 7.2a a colour map of σ_{xx} as a function of V_g and the inverse magnetic field B^{-1}. Dark regions correspond to filled Landau levels (LLs) with vanishing σ_{xx} and correspondingly quantized σ_{xy}. Bright lines correspond to sharp peaks in σ_{xx} at half-filled LLs. Line cuts of ρ_{xx} and σ_{xy} at $V_g = V_0$, V_1, V_2, and V_3, are reported in Fig 7.2b as a function of magnetic field. For $V_g \leq V_0$, the conductivity color map reveals a LL fan diagram typical of a single subband 2DHG, with Zeeman splitting resolved at $B^{-1} < 2.5\ \mathrm{T}^{-1}$. This is highlighted in line cuts at $V = V_0$: ρ_{xx} shows clean Shubnikov–de Haas (SdH) oscillations that vanish when σ_{xy} develops flat conductance plateaus at integer multiples of e^2/h.

For $V_0 \leq V_g \leq V_1$, the population of the second subband becomes favourable, charge starts accumulating in the top quantum well effectively screening the electric field in the bottom well. Although we observe the conductance peaks associated to the first subband saturating with gate voltage due to this screening effect, the fan diagram associated to the second subband appears only at $V_g = V_1$, in agreement with the observations in Fig. 7.2a, when the density in the second subband overcomes the percolation threshold and contributes to transport. Correspondingly, the line cuts for ρ_{xx} and σ_{xy} at $V_g = V_1$ show a complex pattern resulting from the parallel transport of two channels with different density and mobility.

The hole bilayer reaches the resonance point at $V_g = V_2$, corresponding to a bilayer density of $2.0 \times 10^{11}\ \mathrm{cm}^{-2}$. At this point the wavefunction of the first and second subband are fully delocalized across both wells and we observe in the fan diagram the anticrossing of the σ_{xx} peaks arising from the first subband with the corresponding peaks arising from the second subband. The anticrossing is better resolved at high magnetic field, where the LLs energy separation is large compared to the disorder-induced LLs broadening. The line cuts at resonance show a very distinct feature. A dip develops in ρ_{xx} in correspondence of the quantum Hall plateaus in σ_{xy} at odd filling factors 3, 5 and 7. This observation is a clear signature of the anticrossing of symmetric-antisymmetric subbands at the resonance point in a tunnel coupled bilayer system [21]. If the two quantum wells were not tunnel coupled, at resonance we would observe plateaus in σ_{xy} only at even filling factors and a doubling of the ρ_{xx} peaks height, arising from the measurement of two independent hole gases in parallel.

Finally, as the negative gate voltage is further increased beyond resonance, the energy separation between the symmetric and antisymmetric gap increases; the symmetric subband rises in energy (and thus hole density) and the antisymmetric state remains relatively unchanged due to electric field screening effect. The line cuts at $V_g = V_3$ show a larger ρ_{xx} peak separation in correspondence to larger odd Hall conductance plateaus. At $V_g \approx -3.61\,\mathrm{V}$ the bilayer system reaches its saturation as the triangular quantum well at the interface between the SiGe barrier and the dielectric starts populating, screening the electric field in both quantum wells from further increases in V_g.

A closer inspection of the fan diagram and line cuts reveals two interesting features of quantum transport in the bilayer. The first observation is about the development of the σ_{xx} peaks of the first subband in the color map. We note for $V_1 \leq V_g \leq V_2$ that an increase in negative V_g induces a shift of the peaks towards larger inverse magnetic field,

implying that the charge in the first subband decreases as V_g is swept further negative. We ascribe this behaviour to the negative compressibility of the second subband [21]. When the charge density is still relatively low in the second subband, the first and second subbands are localized in the bottom and top quantum well, respectively. Making V_g more negative must increase the total density. The negative compressibility of the low density gas hole in the top quantum well causes the density in the bottom quantum well to decrease immediately after the top well is populated, explaining why the σ_{xx} peaks move to higher B^{-1} (lower B) in the region $V_1 \leq V_g \leq V_2$ [22, 23].

The second observation is about the emergence at resonance ($V_g = V_2$) of a quantum Hall state plateau at $\sigma_{xy} = 1e^2/h$. This dissipationless state could be ascribed either to the full occupation of the symmetric state while the antisymmetric one remains empty, or it could arise from a fractional quantum hall state. At such high magnetic fields (above 7 T), the intra-layer Coulomb energy $E_{intra} = e^2/\epsilon l_B$ (134 meV at 8 T) is much bigger than the tunneling energy Δ_{SAS}, as shown below, and the ratio of intra- to interlayer Coulomb energy $d/l_B = 0.76$ in our bilayer is less than two, suggesting that at resonance, the quantum Hall state at total $\nu = 1$ stems from spontaneous interlayer phase coherence [24]. Here, d is the distance between the centres of the two wells.

7.4. SCHRÖDINGER-POISSON SIMULATION AND SYMMETRIC-ANTISYMMETRIC GAP

The accurate measurement of the LL fan diagram allows to compare in Fig. 7.3 the experimental density of the first and second subband to simulations [1]. We calculate the experimental subband density p_1 and p_2 using the quantum Hall relationship $p = \nu Be/h$ and tracking in Fig 7.2b the B position of the σ_{xx} peaks corresponding to the half filled LL with $\nu = 1.5$ [2]. We observe that the simulated subband population ($p_{1,sim}$, $p_{2,sim}$) matches well the experimental densities ($p_{1,exp}$, $p_{2,exp}$) in the ranges $V_g \leq V_0$ and $V_g \geq V_2$. SP calculations only include the Hartree contribution to many body effects, and so do not reproduce the negative compressibility effects observed in the range $V_1 \leq V_g \leq V_2$; we therefore expect a discrepancy between simulations and experimental data in this region. Furthermore, in the range between V_0 and V_1, we ascribe the deviation of the measured Hall density p from the simulated bilayer density $p_{tot,sim}$, to the population of the second subband when its density is still below the percolation threshold and effectively does not contribute to transport.

Around resonance ($V_g = V_2$) we observe the avoided-crossing of the simulated and experimental densities of the first and second subband. From the subband population difference at resonance $\Delta p_{SAS} = p_1 - p_2$ we calculate the experimental energy gap between the symmetric and antisymmetric subbands by dividing Δp_{SAS} by the spin-resolved 2D density of states $m^*/2\pi\hbar^2$. We obtain $\Delta_{SAS} \sim 0.69$ meV, which is in agreement with simulations.

In summary, we have designed, fabricated, and measured a hole bilayer in strained

[1] We performed iterative self-consistent SP simulations of this Ge/SiGe bilayer system. We set in the model the thicknesses of SiGe spacer above the bilayer and Al_2O_3, to match the saturation density and capacitance respectively, of the measured device.

[2] Using the peaks of the half filled LL with $\nu = 2.5$ yields a very similar density.

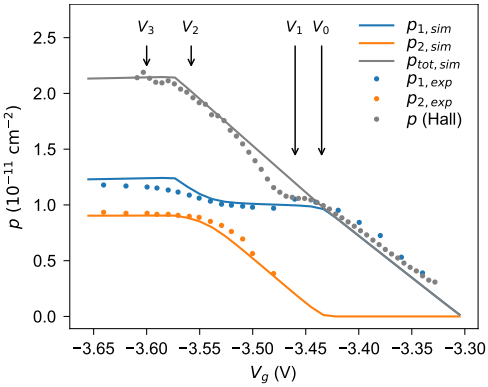

Figure 7.3: Comparison of the experimental and Schrödinger-Poisson simulated densities in the bilayer system as a function of gate voltage (V_g). The blue and orange solid lines are the simulated density for the first and second subband, respectively. The gray solid line is the simulated total density in the bilayer. The blue and orange dotted lines are the density of the first and second subband, as computed from the position of the Shubnikov-de Haas conductance peaks in Fig. 7.2b. The dotted gray line is the bilayer Hall density reported in Fig. 7.2a.

Ge double quantum wells. The bilayer has high-mobility, low percolation density, and a large symmetric-antisymmetric energy gap at resonance in agreement with simulations. Taken together, these results open up a plethora of exciting new possibilities for the Ge quantum information route, ranging from Ge quantum devices and circuits with increased connectivity to the exploration in this new platform of rich physics associated with quantum Hall effects in bilayers.

Data sets supporting the findings of this study are available at
https://doi.org/10.4121/17209091

BIBLIOGRAPHY

[1] A. Sammak, D. Sabbagh, N. W. Hendrickx, M. Lodari, B. Paquelet Wuetz, A. Tosato, L. Yeoh, M. Bollani, M. Virgilio, M. A. Schubert, P. Zaumseil, G. Capellini, M. Veldhorst, and G. Scappucci. "Shallow and Undoped Germanium Quantum Wells: A Playground for Spin and Hybrid Quantum Technology". In: *Advanced Functional Materials* 29.14 (2019), p. 1807613. ISSN: 1616301X.

[2] M. Lodari, N. W. Hendrickx, W. I. L. Lawrie, T.-K. Hsiao, L. M. K. Vandersypen, A. Sammak, M. Veldhorst, and G. Scappucci. "Low percolation density and charge noise with holes in germanium". In: *Materials for Quantum Technology* 1.1 (2021), p. 011002. ISSN: 2331-8422.

[3] G. Scappucci, C. Kloeffel, F. A. Zwanenburg, D. Loss, M. Myronov, J. J. Zhang, S. De Franceschi, G. Katsaros, and M. Veldhorst. "The germanium quantum information route". In: *Nature Reviews Materials* 6.10 (Dec. 2020), pp. 926–943. ISSN: 20588437.

[4] N. W. Hendrickx, D. P. Franke, A. Sammak, M. Kouwenhoven, D. Sabbagh, L. Yeoh, R. Li, M. L. Tagliaferri, M. Virgilio, G. Capellini, G. Scappucci, and M. Veldhorst. "Gate-controlled quantum dots and superconductivity in planar germanium". In: *Nature Communications* 9.1 (Dec. 2018), p. 2835. ISSN: 20411723.

[5] N. W. Hendrickx, W. I. Lawrie, L. Petit, A. Sammak, G. Scappucci, and M. Veldhorst. "A single-hole spin qubit". In: *Nature Communications* 11.1 (2020), p. 3478. ISSN: 20411723.

[6] W. I. Lawrie, H. G. Eenink, N. W. Hendrickx, J. M. Boter, L. Petit, S. V. Amitonov, M. Lodari, B. Paquelet Wuetz, C. Volk, S. G. Philips, G. Droulers, N. Kalhor, F. Van Riggelen, D. Brousse, A. Sammak, L. M. Vandersypen, G. Scappucci, and M. Veldhorst. "Quantum dot arrays in silicon and germanium". In: *Applied Physics Letters* 116.8 (2020), p. 80501. ISSN: 00036951.

[7] D. Jirovec, A. Hofmann, A. Ballabio, P. M. Mutter, G. Tavani, M. Botifoll, A. Crippa, J. Kukucka, O. Sagi, F. Martins, J. Saez-Mollejo, I. Prieto, M. Borovkov, J. Arbiol, D. Chrastina, G. Isella, and G. Katsaros. "A singlet-triplet hole spin qubit in planar Ge". In: *Nature Materials* 20.8 (June 2021), pp. 1106–1112. ISSN: 14764660.

[8] N. W. Hendrickx, D. P. Franke, A. Sammak, G. Scappucci, and M. Veldhorst. "Fast two-qubit logic with holes in germanium". In: *Nature* 577.7791 (2020), pp. 487–491. ISSN: 14764687.

[9] N. W. Hendrickx, W. I. Lawrie, M. Russ, F. van Riggelen, S. L. de Snoo, R. N. Schouten, A. Sammak, G. Scappucci, and M. Veldhorst. "A four-qubit germanium quantum processor". In: *Nature* 591.7851 (2021), pp. 580–585. ISSN: 14764687.

[10] W. I. L. Lawrie, M. Russ, F. van Riggelen, N. W. Hendrickx, S. L. de Snoo, A. Sammak, G. Scappucci, and M. Veldhorst. “Simultaneous driving of semiconductor spin qubits at the fault-tolerant threshold”. In: *Preprint at https://arxiv.org/abs/2109.07837* (2021).

[11] G. Burkard, G. Seelig, and D. Loss. “Spin interactions and switching in vertically tunnel-coupled quantum dots”. In: *Physical Review B - Condensed Matter and Materials Physics* 62.4 (2000), pp. 2581–2592. ISSN: 01631829.

[12] X. Croot, X. Mi, S. Putz, M. Benito, F. Borjans, G. Burkard, and J. R. Petta. “Flopping-mode electric dipole spin resonance”. In: *Physical Review Research* 2.1 (2020), 012006(R). ISSN: 26431564.

[13] J. P. Eisenstein and A. H. MacDonald. “Bose-Einstein condensation of excitons in bilayer electron systems”. In: *Nature* 432.7018 (Dec. 2004), pp. 691–694. ISSN: 00280836.

[14] J. J. Su and A. H. MacDonald. “How to make a bilayer exciton condensate flow”. In: *Nature Physics* 4.10 (2008), pp. 799–802. ISSN: 17452481.

[15] D. Laroche, S. H. Huang, E. Nielsen, C. W. Liu, J. Y. Li, and T. M. Lu. “Magnetotransport of an electron bilayer system in an undoped Si/SiGe double-quantum-well heterostructure”. In: *Applied Physics Letters* 106.14 (2015), p. 143503. ISSN: 00036951.

[16] J.-Y. Li, T.-M. Lu, Y.-H. Su, Y. Chuang, and C.-Y. Liu. “Effects of surface tunneling of two-dimensional hole gases in undoped Ge/GeSi heterostructures”. In: *Physical Review Materials* 1.4 (2017), p. 044601.

[17] L. A. Tracy, E. H. Hwang, K. Eng, G. A. Ten Eyck, E. P. Nordberg, K. Childs, M. S. Carroll, M. P. Lilly, and S. Das Sarma. “Observation of percolation-induced two-dimensional metal-insulator transition in a Si MOSFET”. In: *Physical Review B* 79.23 (2009), p. 235307. ISSN: 10980121.

[18] R. Fletcher, E. Zaremba, M. D’Iorio, C. T. Foxon, and J. J. Harris. “Evidence of a mobility edge in the second subband of an Al0.33Ga0.67As-GaAs heterojunction”. In: *Physical Review B* 38.11 (1988), pp. 7866–7869. ISSN: 01631829.

[19] A. R. Hamilton, E. H. Linfield, M. J. Kelly, D. A. Ritchie, G. A. Jones, and M. Pepper. “Transition from one- to two-subband occupancy in the 2DEG of back-gated modulation-doped GaAs-AlxGa1-xAs heterostructures”. In: *Physical Review B* 51.24 (1995), pp. 17600–17604. ISSN: 01631829.

[20] H. L. Störmer, A. C. Gossard, and W. Wiegmann. “Observation of intersubband scattering in a 2-dimensional electron system”. In: *Solid State Communications* 41.10 (Mar. 1982), pp. 707–709. ISSN: 00381098.

[21] A. R. Hamilton, M. Y. Simmons, F. M. Bolton, N. K. Patel, I. S. Millard, J. T. Nicholls, D. A. Ritchie, and M. Pepper. “Fractional quantum Hall effect in bilayer two-dimensional hole-gas systems”. In: *Physical Review B* 54 (1996), R5259.

[22] J. P. Eisenstein, L. N. Pfeiffer, and K. W. West. “Negative compressibility of interacting two-dimensional electron and quasiparticle gases”. In: *Physical Review Letters* 68.5 (1992), pp. 674–677. ISSN: 00319007.

[23] I. S. Millard, N. K. Patel, M. Y. Simmons, E. H. Linfield, D. A. Ritchie, G. A. Jones, and M. Pepper. “Compressibility studies of double electron and double hole gas systems”. In: *Applied Physics Letters* 68 (1995), p. 3323. ISSN: 00036951.

[24] K. Yang, K. Moon, L. Belkhir, H. Mori, S. Girvin, A. MacDonald, and L. Zheng. “Spontaneous interlayer coherence in double-layer quantum Hall systems: Symmetry-breaking interactions, in-plane fields, and phase solitons”. In: *Physical Review B - Condensed Matter and Materials Physics* 54.16 (1996), pp. 11644–11658. ISSN: 1550235X.

8

A VERTICAL GATE-DEFINED DOUBLE QUANTUM DOT IN A STRAINED GERMANIUM DOUBLE QUANTUM WELL

Gate-defined quantum dots in silicon-germanium heterostructures have become a compelling platform for quantum computation and simulation. Thus far, developments have been limited to quantum dots defined in a single plane. Here, we propose to advance beyond planar systems by exploiting heterostructures with multiple quantum wells. We demonstrate the operation of a gate-defined double quantum dot in a strained germanium double quantum well, where both quantum dots are tunnel coupled to both reservoirs and parallel transport occurs. We analyze the capacitive coupling to nearby gates and find both quantum dots to be accumulated under the central plunger gate. We extract their position and size, from which we conclude that the double quantum dots are vertically stacked in the two quantum wells. We discuss challenges and opportunities of multilayer devices, and outline some potential applications in quantum computing and quantum simulation.

This work was originally published as:
H. Tidjani*, A. Tosato*, A. Ivlev, C. Déprez, S. Oosterhout, L. Stehouwer, A. Sammak, G. Scappucci, M. Veldhorst, Vertical gate-defined double quantum dot in a strained germanium double quantum well. Physical Review Applied 20.5 (2023)

INTRODUCTION

Semiconductor heterostructures composed of silicon and germanium have become the leading material platform for building quantum dot qubits [1, 2, 3]. Developments in their fabrication and operation have enabled demonstrations of high-fidelity single and two-qubit logic, multi-qubit operation, and rudimentary quantum error correction [4, 5, 6, 7, 2, 1, 8, 9]. Efforts in scaling quantum dots have led to the operation of a cross-bar array comprising 16 quantum dots [10], and long-range quantum links may enable interconnecting modules of quantum dot arrays [11, 12, 13, 14]. These developments in gate-defined quantum dots have been restricted to quantum dots defined in a single plane, yet the versatile nature of silicon-germanium heterostructures allows for further exploration. In particular, structures with multiple quantum wells can be grown, and double quantum wells of germanium [15] and silicon [16, 17] have been realized. An open question is thus whether multi-layer heterostructures can become a relevant platform for quantum information. Here, we motivate potential applications and experimentally explore quantum dots in stacked quantum wells.

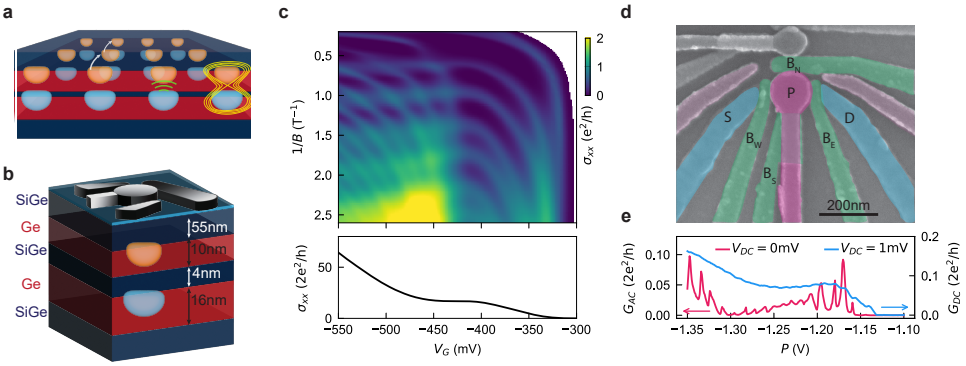

Figure 8.1: **Gate defined vertical double quantum dot in a bilayer heterostructure. a** Vision of a larger bilayer device, with different use-cases depicted, such as shuttling (white), sensing (green) and vertical 2-qubit gates (yellow). **b** Schematic of the heterostructure and gate stack. The light blue layer in between the gates and SiGe layer indicates the aluminum oxide layer. **c** Colour map of the conductivity σ_{xx} as a function of gate voltage V_G and the inverse magnetic field $1/B$. Dark regions correspond to filled Landau levels with vanishing σ_{xx} and correspondingly quantized σ_{xy}. Lower Panel: linecut at $B = 0$ T showing the zero field conductance trace. Density and mobility for the bilayer system are presented in appendix 8.1. **d** False coloured SEM image of a nearly identical device to the one used in this work. Quantum dots are defined under the plunger gate P (pink) and measured in transport using the ohmic contacts source (S) and drain (D) (blue). The coupling between the quantum dot and ohmics is tuned by B_E and B_W (green). The potential landscape is further shaped by the gates B_N and B_S (green). The experiments presented in this work are performed on a section of a larger device (see Appendix 8.2). **e** Conductance trace as a function of the plunger gate voltage across S-D at V_{DC}=1 mV (blue line), and differential conductance trace (pink) at V_{DC}=0 mV and V_{AC} = 17 µV, $f_{\text{lock-in}}$ = 70 Hz.

Heterostructures with parallel quantum wells may support integration of important functionalities for spin qubit based quantum processors, as depicted in Fig.8.1a. Precise control over the growth of individual layers allows for the engineering of inter and intralayer properties. When charges residing in separate quantum wells are capacitively coupled, but have little to no tunnel coupling, charge sensors could be integrated into

separate layers from the qubits they sense. In an intermediate regime where tunnel coupling is in the order of one to a few tens of gigahertz, coherent spin shuttling between the wells could be realized [18]. Consequently, one layer may serve as a quantum link for qubits defined in the other layer, for example by offering shuttling lanes that connect remote qubits [19, 14]. In this regime, the second layer can also host dedicated ancilla qubits that aid in spin-to-charge conversion for initialization and readout. Tunnel-coupled quantum wells may also be used to develop novel qubit implementations such as vertical singlet-triplet qubits or flopping mode spin qubits [20]. Moreover, the thickness and atomic composition of each quantum well may be tuned to optimize g-tensors [21] and spin-orbit interactions [22], in order to provide dedicated functionality. In addition, double quantum wells engineered to provide different g-tensors could be used to execute quantum gates on spin qubits by shuttling the qubit between quantum dots defined in the two quantum wells [23, 18]. This would enable qubit control with baseband pulses, diminishing the need for high-power microwave electronics.

Quantum dots in multiple quantum wells may also present new opportunities for analog quantum simulation. While planar two-dimensional quantum dot arrays may be used to simulate correlated physics such as the resonating valence bond [24], quantum dots in a double quantum well may simulate even more exotic systems. For example, exciton condensation may be induced by the Coulomb interaction when the quantum dot occupation in one layer is almost filled and in the other almost empty, creating an effective electron and hole layer. Such a gate-defined quantum dot system may provide more control over individual parameters when studying excitons, when compared to quantum transport implementations [25, 26, 27, 28]. Quantum dots in multi-layer structures comprised of three or more quantum wells could also be envisioned. The confinement of quantum dots in three layers potentially supports artificial superconductivity. Attractive Coulomb interaction in quantum dot systems has been observed in planar systems [29, 30] and integration of such interactions into a trilayer system may provide a route toward tunable and controllable superconducting condensation.

These motivations warrant the study of quantum dots defined in multilayer heterostructures. However, there are also many challenges in the design and operation that need to be understood and overcome. We take a first step and demonstrate a gate-defined vertical double quantum dot in a strained germanium double quantum well heterostructure. Through quantum transport measurements, we obtain charge stability diagrams consistent with two quantum dots coupled in parallel. We characterise the capacitive interaction of the quantum dots to the surrounding gates and determine their location. The size of one of the quantum dots is estimated through bias-spectroscopy. Together, these findings point toward the formation of a double quantum dot vertically aligned under the same plunger gate.

8.1. RESULTS

An undoped and compressively-strained Ge/SiGe double quantum well heterostructure is epitaxially grown on a 100 mm Si(100) substrate. A 55 nm thick $Si_{0.2}Ge_{0.8}$ spacer separates the bilayer system from the gate stack. The top and bottom quantum wells in the bilayer are 10 nm and 16 nm thick respectively, and are separated by a 4 nm $Si_{0.2}Ge_{0.8}$ barrier (Fig. 8.1b). We perform magnetotransport characterization of a Hall-bar shaped

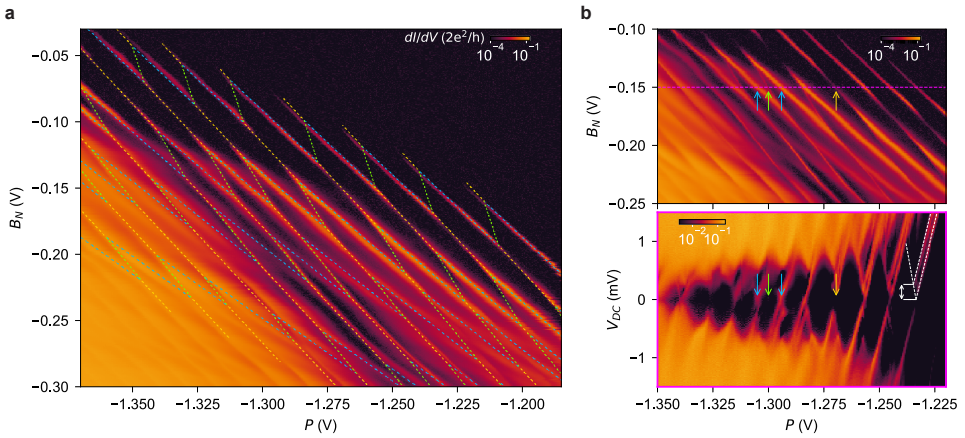

Figure 8.2: **Charge stability diagram of the vertical double quantum dot. a** By sweeping the gates P vs B_N, a honeycomb pattern emerges as the gates induce transport resonances. The dashed coloured lines overlain on the data correspond to the electrochemical simulation of the double-quantum dot system, detailed in Appendix 8.4. **b** Upper panel: A zoom-in of the data presented in panel a with coloured arrows corresponding to different transitions. Lower panel: Bias spectroscopy across a line-cut of panel b top (magenta) at $B_N = -0.15$V, the coloured arrows correspond to the transitions highlighted in the top panel. Measurement of the orbital energy for the first Coulomb diamond is indicated by the white lines and is extracted to be approximately 260 µeV.All measurements in this figure are acquired with a lock-in amplifier, with a typical frequency of 70 Hz, and amplitude of 17 μV.

heterostructure field effect transistor to infer the energy spectrum of the hole bilayer. The conductance map in Fig. 8.1c reveals the emergence of two sets of Landau levels typical of such a bilayer system [15, 31]. At $V_G \approx -320$ mV the longitudinal conductivity σ_{xx} shows the first set of quantized Landau levels, corresponding to the subband localized in the bottom well. At $V_G \approx -400$ mV the conductance curve at zero-magnetic-field (Fig. 8.1c bottom panel) deviates from a linear increase and flattens out as the sub-band localized in the top well starts being populated. This originates from the electric field screening caused by the accumulation of charge carriers in the top well, while its density is still below the percolation threshold and transport is only available through the bottom well [15]. For more negative voltages, the carriers in the top well start contributing to transport and conductance increases. This confirms that this heterostructure is compatible with the accumulation of a bilayer 2D hole gas.

We then fabricate gates to electrostatically define quantum dots in this bilayer system (see Methods). A 3D schematic depicting the heterostructure and gate stack, and a scanning electron microscopy (SEM) image of a nominally identical device are respectively shown in Fig. 8.1b,d. The gate geometry is similar to quantum dot devices with a single quantum well [2]. The central plunger gate P is negatively biased to accumulate holes beneath it, while the barrier gates B_W and B_E are used primarily to tune the tunnel barrier to the ohmic contacts (S and D). The gates B_N and B_S further shape the potential landscape without significantly affecting the tunnel barrier to the ohmics. We measure the transport through the device with DC and low-frequency lock-in techniques (see Methods).

At high source-drain DC bias (V_{DC} = 1 mV, Fig. 8.1e blue line) the conductance trace starts to increase as P is lowered and a transport channel opens. After a first increase, the conductance plateaus at $P = -1.2$ V, before showing a second increase in conductance indicating the opening of a second transport channel. We study this same phenomenon at low bias V_{DC} =0 mV and measure the differential conductance using a lock-in amplifier. The differential conductance trace I_{AC}/V_{AC} (pink line) reveals the emergence of Coulomb peaks, which begin at -1.14 V. Interestingly, the Coulomb peaks show a decrease in amplitude between -1.2 V and -1.3 V, after which the amplitude increases again. We speculate that this decrease in amplitude is caused by an increased tunnel coupling to a second parallel quantum dot which may not contribute to transport itself yet. If this second quantum dot has lower conductance, an increased wavefunction amplitude in this second quantum dot would reduce the Coulomb peak height [32]. This wavefunction delocalization across two tunnel-coupled quantum wells has also been predicted by Schrödinger-Poisson simulations [15]. At lower voltages, the second quantum dot also starts contributing to transport, and Coulomb peaks re-emerge. While the intermediate voltage gives rise to a complex gate voltage dependence, the observation of a double turn-on suggests the presence of a second quantum dot.

To further investigate the quantum dots in this bilayer system, we map the charge stability diagram as a function of the gate voltages applied on B_N and P, shown in Fig. 8.2a,b. A distinct honeycomb pattern emerges, indicating the presence of a double quantum dot system [33]. This is confirmed by an overlayed electrochemical simulation of a double quantum dot coupled in parallel, which reproduces the location of the charge transitions (see Appendix 8.4 for details of the model). In the region between $P = -1.32$ Vand $P = -1.25$ V we observe transport at every edge of this honeycomb, corresponding to the interdot charge transition and the two reservoir to quantum dot transitions.

To distinguish the inter-dot transitions from the reservoir transitions in the charge stability diagram of Fig. 8.2a,b, we measure the differential conductance as a function of V_{DC} and P. The bottom panel of Fig. 8.2b shows a set of Coulomb diamonds taken in the regime where $B_N = -0.15$ V (magenta line-cut shown in the top panel). The transition lines that fall on this line-cut corresponding to a signal at $V_{\mathrm{DC}} = 0$ mV in the lower panel are indicated by the four coloured arrows. The transition lines indicated by the blue and orange arrows correspond to the edges of the Coulomb diamonds, and are attributed to quantum dot-reservoir transitions. In contrast, the transition line indicated by the green arrow lies in the middle of a Coulomb diamond, and a conductance peak is barely visible. This is the expected behaviour for an interdot transition, where transport is only possible through co-tunneling processes, such as elastic co-tunneling [34], resulting in a faint conductance signal, only when the two quantum dots are in resonance. The unusual negative slope of the interdot transition is a result from both B_N and P predominantly coupling to the same quantum dot, corresponding to the orange transitions (see Appendix 8.3). With the four identified transition lines as a reference, we map each transition line in the charge stability diagram using the hexagonal pattern and slopes of the lines.

The presence of the two reservoir transition lines (blue and orange) indicates that both quantum dots are connected in parallel to the ohmic contacts. At the interdot transition line (green) series transport may occur. Since a simulated double quantum dot

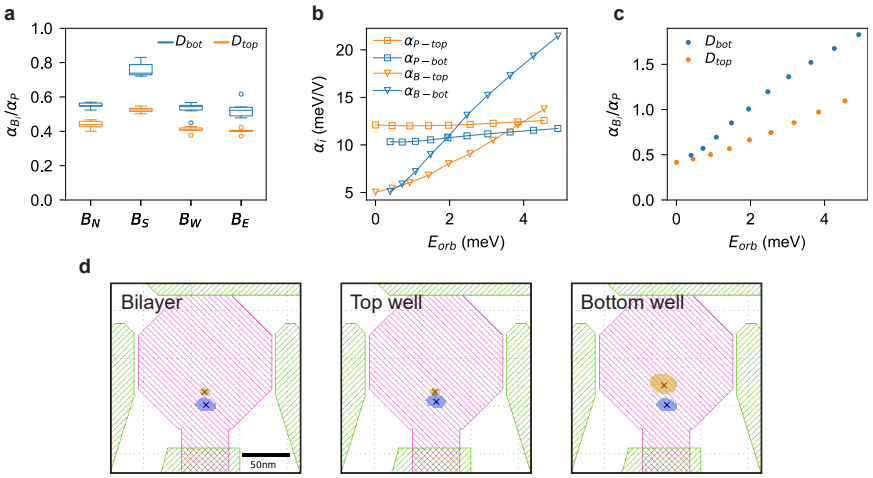

Figure 8.3: **Measured and simulated lever arm ratios of the surrounding gates to the quantum dots, and the triangulation of their centre points. a** Boxplot of the lever arm ratios ($\alpha_{B_i,D_i}/\alpha_{P,D_i}$) of each barrier gate B_i to the plunger gate P for the top and bottom quantum dot (D_i). These couplings are extracted from the slopes of different reservoir transitions in the charge stability diagrams as a function of B_i and P (see Appendix 8.4). The spread in $\alpha_{B_i,D_i}/\alpha_{P,D_i}$ for different occupations is small compared to the difference in $\alpha_{B_i,D_i}/\alpha_{P,D_i}$ between the two quantum dots, ensuring that the average value of $\alpha_{B_i,D_i}/\alpha_{P,D_i}$ for a quantum dot across a range of different occupations is a meaningful metric for assessing the positioning of the quantum dots with respect to the surrounding gates. **b** Simulated lever arms for the plunger gate P and barrier gate B to the top and bottom quantum dot calculated from the 2D Schrödinger-Poisson simulation described in Appendix 8.5. **c** Simulated lever arm ratios $\alpha_{B_i,D_i}/\alpha_{P,D_i}$ for the first 20 orbital states, plotted against the orbital energy (E_{orb}), with data extracted from the Schrödinger-Poisson simulation. **d** Triangulation of the position of the quantum dots by comparing the lever arm ratios in **a** with capacitive simulation (Appendix 8.6). The cross indicates the centre point of each quantum dot, and the coloured area represents the 1σ standard deviation of this value. In the 'Bilayer' panel the quantum dots are simulated one at a time in separate wells, with the orange quantum dot and blue quantum dot placed in the top and bottom well respectively. In the 'Top Well' and 'Bottom Well' panels, the quantum dots are simulated one at a time in the same layer.

system fits our data well, we consider the formation of a triple quantum dot improbable. Such a triple quantum dot would produce pentagonal or heptagonal features [35] which we do not observe. We further exclude the possibility of a triple quantum dot as that would require at least two of the three quantum dots to be located in the same quantum well, and as a result have distinct lever arms to the surrounding gates, which we elaborate on further in the upcoming paragraphs. We observe just two distinct reservoir transitions, and we argue in the following paragraphs that these must correspond to vertically stacked quantum dots.

The behaviour of this bilayer quantum dot system outside of the explored parameter regimes may have different characteristics. Above $P = -1.2$V, we expect there are two quantum dots, with one or both of them contributing to transport. Below $P = -1.35$V, the system allows for multiple scenarios. The increased quantum dot size with occupancy may cause delocalization across the two quantum wells. High charge occupation may also result in a decreased charging energy and high coupling to the ohmics, which can give rise to a constant current, potentially observed in the bottom left region of Fig.

2a, if a dot opens to a channel. Additionally, a high top gate voltage may result in wavefunction localization in the top quantum well, resulting in only the top quantum dot contributing to transport.

Unlike a typical double-quantum dot charge stability diagram [33] where each quantum dot predominantly responds to its own dedicated plunger gate, transition lines in this diagram have very similar slopes, indicating that the gates have similar lever arm ratios α_{B_N}/α_P to both quantum dots. This observation is consistent with vertically stacked quantum dots of similar shape, as the lever arm ratio primarily depends on the in-plane position of the quantum dots. Crucially, we are still able to populate both quantum dots, which is not trivial for a vertically coupled double quantum dot due to possible screening by the top well (see Appendix 8.3). In this device, this is aided by a higher charging energy of the top dot resulting from increased confinement. On the other hand, the reduced confinement increases the size of the bottom quantum dot and hence its lever arm to surrounding gates.

Next, we extract the position of both quantum dots using the measured capacitive coupling to surrounding gates. We map the charge stability diagram as a function of B_i ($i = N, W, S, E$) and P (see Appendix Fig.8.5) and based on the slopes of the reservoir transitions we find that both quantum dots have comparable lever arms to all surrounding gates (Fig. 8.3a). A first observation is that both quantum dots are most strongly coupled to the plunger gate, giving a first indication that they are located underneath it. Importantly, we find that all barrier gates have a similar capacitive coupling to the quantum dots. The symmetry of this coupling suggests there are no spurious quantum dots, with the observed quantum dots both being located underneath the plunger gate. Additionally, we find that one quantum dot has a higher lever arm ratio $\alpha_{B_i,D_i}/\alpha_{P,D_i}$ to all barrier gates. This is consistent with a stacked double quantum dot, where the top quantum dot is expected to be smaller, causing a reduction of the coupling o the barrier gates,

To further support the conclusion of having created a vertical double quantum dot, we estimate the position of both quantum dots using an electrostatic finite element method (FEM) simulation in Ansys Q3D [36], in which the heterostructure, gate layers and insulating layers are included (details can be found in Appendix 8.6). The quantum dots are simulated individually in both layers, to analyze all their possible locations (Fig.8.3d). Each quantum dot is modelled as a metallic disk as thick as the quantum well it is located in. The radius and position of this simulated metallic quantum dot are varied to analyze the effect on the capacitance. The geometric capacitance between each metallic quantum dot D and each gate G is determined and assumed to be directly proportional to the lever arm $\alpha_{G,D}$. By comparing the simulated capacitance with the measured lever arm ratio $\alpha_{B_i,D}/\alpha_{P,D}$, the position of a single quantum dot within either quantum well is triangulated. The predicted centre-centre distance between the quantum dots has an upper bound of 30 nm (Fig. 8.3d), regardless of which well the quantum dots are simulated in. This close proximity prohibits the coexistence of both quantum dots in the same layer without coalescing, suggesting that the quantum dots must be located in different quantum wells. We account for a 1σ error in the position, as indicated by the coloured area in Fig. 8.3d, which is based on the spread of the lever arm ratios that are extracted from each charge-stability diagram.

We estimate the size of one quantum dot from the orbital energy $E_{orb} = 260\,\mu$eV ex-

tracted from Fig.8.2b (lower panel, white lines). Assuming a harmonic in-plane potential $V_{xy} = \frac{1}{2}m^*\omega^2(x^2+y^2)$, where $\hbar\omega = E_{orb}$ and $m^* = 0.055m_e$, this gives a quantum dot diameter of about $d = \sqrt{\hbar/(\omega m^*)} = 137\,\text{nm}$, comparable to the plunger gate size of 150 nm. Based on the size approximation of this quantum dot and their mutual proximity, we conclude that the quantum dots cannot coexist in a single layer without coalescing. Overall, the measured lever arm ratios, together with the results from the FEM simulation and the estimates of the quantum dot size from the Coulomb diamonds, provide strong arguments for the quantum dots being vertically stacked under the plunger gate.

To identify in which quantum well each quantum dots resides, we perform a 2D Schrödinger-Poisson simulation (Fig. 8.3 b,c). We calculate the capacitive coupling between the plunger gate P and a barrier gate B for consecutive orbital fillings of the top and bottom quantum dot to deduce the lever arms (Fig. 8.3b). While the lever arm of the plunger gate to the top and bottom quantum dot (α_{P-top} and α_{P-bot}) remains approximately constant with increasing orbital number, the barrier gate lever arm to both quantum dots varies significantly with the orbital number. This originates from an increase in the wavefunction spread for consecutive orbitals, increasing the overlap and consequently the coupling to the barrier gate. Fig. 8.3c shows the corresponding lever arm ratio of the quantum dots formed in the top quantum dot (D_{top}) and bottom quantum dot (D_{bot}) for different orbitals. Panel c shows that for all simulated orbitals the bottom quantum dot has a relatively larger lever arm to the barrier gates. Comparing this to the measured lever arms ratios in Fig. 8.3a we conclude that D_{top} (orange transitions in Fig. 8.2) corresponds to a quantum dot located in the upper quantum well and D_{bot} (blue transitions in Fig. 8.2a) to a quantum dot located in the bottom quantum well. This interpretation is confirmed by the position and slope of the interdot transitions in the charge stability diagrams. As the plunger gate voltage becomes more negative, attracting holes to the gate, a hole tunnels from D_{bot} to D_{top} across the interdot transition. We thereore conclude that D_{top} is localized in the top well.

8

8.2. DISCUSSION AND OUTLOOK

In this work we demonstrate a double quantum dot defined in a double quantum well heterostructure. A single gate can be used to simultaneously populate quantum dots in two wells, whilst the charge occupation can be tuned using one of the surrounding gates. From the double quantum dot charge stability diagrams obtained from mapping P vs B_i , we extract the lever arm ratios of the quantum dots to the surrounding gates and confirm that neither quantum dot couples strongly to a particular barrier gate, excluding the possibility of a spurious dot. By comparing the lever arm ratios to an electrostatic FEM simulation we triangulate the in-plane position of the quantum dots and find their centre point at approximately the same in-plane position. If the quantum dots were to be in the same quantum well, we would expect a much larger coupling than observed, and effectively a merged quantum dot. Furthermore, the estimated quantum dot diameter $D_{bot} = 135$ nm suggests that a double quantum dot can only exist by occupying both quantum wells. Based on these findings we conclude the realisation of a vertically coupled double quantum dot in a double quantum well.

Operating many quantum dots, and specifically many vertical double quantum dots, is

certainly not an easy task. However, we can envision that a set of plunger gates, barrier gates, and gates at the corners in a 2D array could jointly provide a virtual gate space to control the charge occupation in the quantum dots, as well as the lateral tunnel coupling between the quantum dots. In doing so, vertically coupled quantum dots may provide new means for scaling, coupling, and addressing semiconductor quantum dot qubits.

8.3. ACKNOWLEDGEMENTS

We acknowledge useful discussions with members of the Veldhorst, Scappucci and Vandersypen groups. We thank S. G. J. Philips and S. De Snoo for the development of the software stack used to acquire data in this experiment.

8.4. DATA AVAILABILITY

The raw data and analysis supporting the findings of this study are openly available in a Zenodo repository: https://zenodo.org/record/8316529.

8.5. FUNDING

We acknowledge support through an NWO ENW grant and an ERC Starting Grant QUIST (850641).

8.6. COMPETING INTERESTS

The authors declare there are no competing interests.

8.7. METHODS

The device is fabricated on a Si_xGe_{1-x}/Ge/Si_xGe_{1-x}/Ge/Si_xGe_{1-x} heterostructure, where $x = 0.2$, grown by reduced pressure chemical vapour deposition. The virtual substrate on which the heterostructure is grown consists of a silicon substrate, upon which there is a 1.6 µm relaxed Ge layer; a 1 µm graded Si_xGe_{1-x} layer, with a final Ge composition of x = 0.2. On top of the SiGe virtual substrate, the bilayer system comprises a 16 nm thick bottom Ge quantum well, a 4 nm thick SiGe barrier, a 10 nm thick top Ge quantum well, and a final 55 nm thick SiGe spacer. At the top of the stack, a sacrificial Si cap is grown to provide a native SiOx layer. We define ohmic contacts using electron beam lithography and remove the Si cap in the exposed area using a buffered oxide etch. We then evaporate a 30 nm platinum layer and contact the quantum wells using a 10-minute rapid thermal anneal at 400°C, forming platinum germanosilicides. The ohmic layer is isolated using a 7 nm layer of Al_2O_3 grown by atomic layer deposition. Electrostatic gates used to define the quantum dots are patterned in two layers (3/17 nm and 3/37 nm of Ti/Pd.) and are separated by a 5 nm layer of Al_2O_3.

Devices are screened in 4 K liquid helium. Experiments reported in this paper are carried out in a Bluefors LD400 dilution refrigerator with a base temperature of 10 mK. The electrical properties of the quantum dots are investigated through two terminal AC and DC measurements. We apply a tunable DC bias V_{DC} across the source (S) and drain (D), and measure the resulting current with a Keysight digitizer and from this we calculate

the conductance $G_{DC} = I_{DC}/V_{DC}$. To measure differential conductance we use a lock-in technique and apply a sinusoidal bias with frequency 70 Hz and amplitude V_{AC} =17 µV from which we can calculate the differential conductance $G_{AC} = dI/dV = I_{AC}/V_{AC}$. When we acquire with the digitizer, the amplitude of the lock-in input signal is reduced to $V_{AC} = 0.04\,\mu$V.

8.1. MAGNETOTRANSPORT

Figure 8.1a shows the magnetotransport characterization of a Hall-bar shaped device. In the voltage range between −250 mV and −400 mV, only the bottom quantum well is occupied, and the density shows a linear dependence on gate voltage while the mobility and conductivity increase monotonically. The fan diagram in Fig. 8.1b shows the typical pattern of single channel transport. Below −400 mV population of the top well becomes energetically favourable, but its density remains below the percolation density until $V_G = -430$ mV, where it starts contributing to transport. Any further increase in the electric field in the bottom well is screened by the charge added to the top well, leaving the bottom well density unchanged. Within the voltage region where the density in the bottom well remains constant and the holes added to the top well are not mobile, the bilayer density measured from the Hall effect plateaus, as does the conductivity and mobility. Beyond this region for $V_G < -430$ mV, the top quantum well is above the percolation threshold, charges are mobile and contribute to transport, resulting in a second set of Landau levels. While the bilayer density and conductivity increase with increasing negative voltages, the mobility curve drops before reestablishing its increasing trend. We ascribe this temporary drop in mobility to interlayer scattering [15].

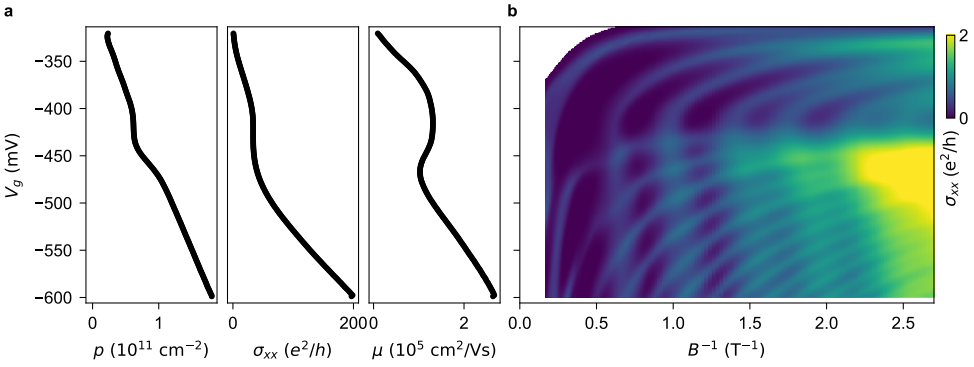

Figure 8.1: **Magnetotransport characterisation of the hole bilayer measured using a Hall-bar shaped field effect transistor. a** From left to right: gate voltage (V_g) dependence of the hole bilayer Hall density p, conductivity σ_{xx} at zero magnetic field, and mobility μ. **b** Colour map of the conductivity σ_{xx} as a function of V_g and the inverse magnetic field B^{-1}. Dark regions correspond to filled Landau levels with vanishing σ_{xx} and correspondingly quantized σ_{xy}.

8.2. FULL DEVICE

Figure 2 shows a false-coloured SEM of the whole device, of which only the left most gates were used in this experiment.

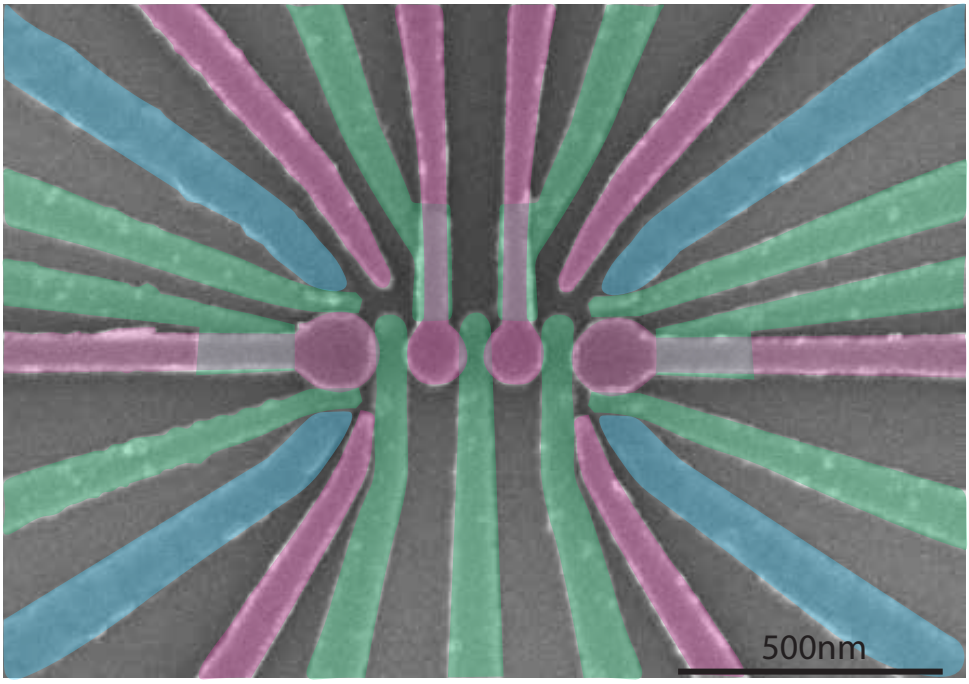

Figure 8.2: **A false-coloured SEM of a device similar to the one used in this experiment**. The experiments are conducted in quantum transport through the left quantum dot (purple) which is coupled to the ohmics (blue) and controlled via barrier gates (green).

8.3. DOUBLE QUANTUM DOT CHARGE STABILITY DIAGRAMS FOR DIFFERENT SYSTEM PARAMETERS

The features of a double quantum dot charge stability diagram strongly depend on the capacitive coupling between the gates and the quantum dots, as well as between the quantum dots themselves. These parameters are expected to be significantly different in a vertically coupled double quantum dot compared to more typical planar quantum dots. It is therefore instructive to qualitatively analyse the charge stability diagram of a double dot system that better describes a vertically coupled double quantum dot. This should aid the reader in interpreting the experimentally obtained charge stability diagrams in this paper.

In any double quantum dot system, a particular gate G can only subsequently load a quantum dot D_i if a voltage on G can offset the electrostatic energy arising from the loading of any other quantum dot. In particular, for G to load quantum dots D_1 or D_2

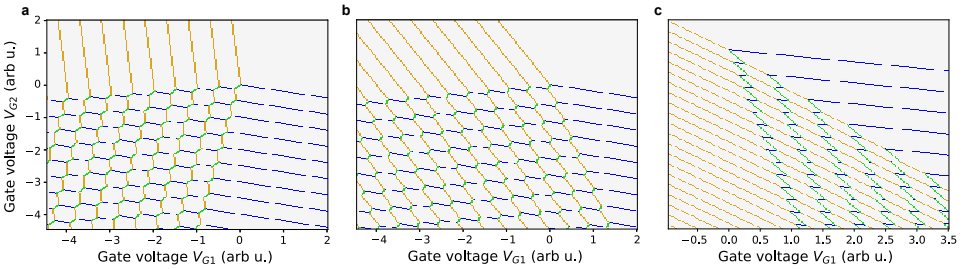

Figure 8.3: **Charge stability diagram dependence on different system parameters.** In each charge stability diagram G_1 satisfies (violates) inequality 8.1 (8.2). The charge carriers are assumed to be holes. **a** Regime where D_1 is not loaded via G_2 due to charge occupation in D_2, as inequality 1 is violated. **b** Regime where G_2 satisfies both inequalities. **c** Here G_2 violates inequality 8.2 while satisfying inequality 8.1.

while the other one is occupied, the system has to respectively satisfy the following inequalities:

$$\frac{E_{C2}}{\alpha_{2,G}} > \frac{E_{Cm}}{\alpha_{1,G}} \tag{8.1}$$

$$\frac{E_{C1}}{\alpha_{1,G}} > \frac{E_{Cm}}{\alpha_{2,G}} \tag{8.2}$$

Here $\alpha_{1(2),G}$ is the lever arm between the gate G and $D_{1(2)}$, and $E_{C1(2)}$, the charging energy of $D_{1(2)}$, and E_{Cm} the electrostatic coupling energy [33]. If inequality 8.1 (8.2) is violated, then quantum dot D_1 (D_2) can not be occupied due screening from D_2 (D_1).

In planar double quantum dots, each quantum dot is predominantly coupled to a single plunger gate, which in return couples relatively weakly to the other quantum dot. That is, plunger gate G_1 couples predominantly to D_1 such that $\alpha_{1,G_1}/\alpha_{2,G_1} > 1$, and inequality 8.1 is satisfied, since $E_{Cm} < E_{C2}$. The same holds for D_2 and the corresponding plunger gate. Figures 8.3**a** and **b** display examples of typical planar double quantum dots hosting holes.

For a vertically coupled double quantum dot, the situation may be different. The lever arm between all gates and the bottom quantum dot can become smaller than to the top quantum dot, and the electrostatic coupling energy E_{Cm} is large due to the close proximity of the wavefunctions. Hence the loading of the top quantum dot might prevent the bottom quantum dot from being loaded, screening the bottom quantum dot. Denoting D_2 as the bottom quantum dot, it is no longer trivial that there is a gate G for which the second inequality is satisfied. Such a situation is depicted in figure 8.3**c**. Once D_1 becomes occupied an increasingly negative voltage on either gate will deplete D_2 instead of loading more holes onto it, making it more challenging to find the desired charge occupation within the operating window of the device.

To ensure loading of the bottom quantum dot, it is therefore crucial to maximise $\alpha_{2,G}/\alpha_{1,G}$ for some gate G. In our experiment this is achieved by having more in-plane confinement of the top quantum dot, due to the close proximity to the top gates. Less

in-plane confinement allows the bottom quantum dot to be more coupled to the surrounding barrier gates. Moreover, the stronger in-plane and out-of-plane confinement of the top quantum dot (D_1) increases the charging energy E_{C1} making condition 8.2 more easily satisfied. We note that in a realistic system, where the lever arms and charging energies are not constant, there could be a transition from one regime to another.

For vertically coupled quantum dots, the interdot transition also might have the opposite slope compared to that of a typical planar double quantum dot. In general for any double quantum dot system controlled by gates G_1 and G_2 an interdot transition occurs along a line in the voltage space (V_{G1}, V_{G2}) for which:

$$\alpha_{1,1}\Delta V_{G1} + \alpha_{1,2}\Delta V_{G2} = \alpha_{2,1}\Delta V_{G1} + \alpha_{2,2}\Delta V_{G2}$$

where $\alpha_{D,G}$ is the lever arm between dot D and gate G, and ΔV_G denotes a change in the voltage of gate G. The slope of this line is hence given by

$$\frac{\Delta V_{G2}}{\Delta V_{G1}} = \frac{\alpha_{21} - \alpha_{11}}{\alpha_{12} - \alpha_{22}}$$

For planar double quantum dots the plunger gates couple predominantly to different dots, such that $\alpha_{11} > \alpha_{21}$ and $\alpha_{22} > \alpha_{12}$. Planar double quantum dots will thus have a positive slope $\frac{\Delta V_{G2}}{\Delta V_{G1}} > 0$ for the interdot transition (Fig. 8.4a). However, for a vertical double quantum dot both gates generally couple predominantly to the same dot. This will lead to a negatively sloped interdot transition $\frac{\Delta V_{G2}}{\Delta V_{G1}} < 0$. In our measurements we observe the situation in Fig. 8.4c, suggesting that both gates in our charge-stability diagrams are dominantly coupled to the same quantum dot located in the upper quantum well. This also suggests that loading of the bottom dot is only possible due to the large charging energy of the top quantum dot, compared to the mutual electrostatic interaction.

8.4. COMPARISON BETWEEN MEASURED CHARGE STABILITY DIAGRAMS AND ELECTROCHEMICAL SIMULATION

In order extract the lever arm ratios of both quantum dots as described in the main text, charge stability diagrams (CSD) were measured by varying the plunger gate P voltage together with the voltage of surrounding barrier gates (Fig. 8.5). The inter-dot transitions in these measurements are less pronounced compared to figure 8.2 of the main text, which is attributed to a change in the tunnel coupling due to a different voltage regime. In this appendix, we compare these measurements with classical electrochemical simulations of a double quantum dot system [33].
The charge carriers in the simulation are holes, and gates couple to both quantum dots through the occupation-dependent lever arm matrix α. Hence the electrochemical po-

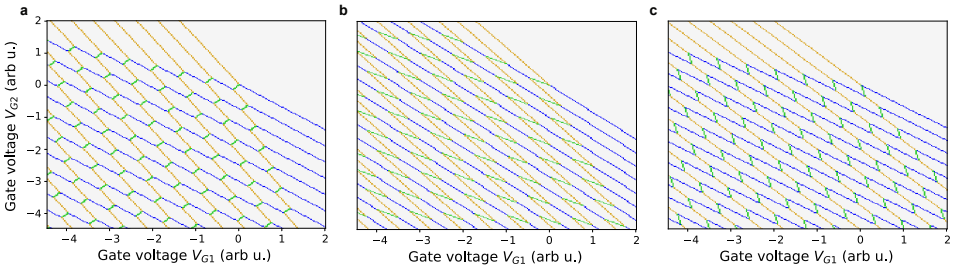

Figure 8.4: **Charge stability diagrams with different interdot slopes.** The interdot slope (depicted in green) depends on the ratio between the lever arms. We denote D_1 (D_2) as the quantum dots with the steep (shallow) reservoir transition line. A positive interdot slope as in **a** is observed whenever each gate couples predominantly to different quantum dots. If both gates couple stronger to D_2 than to D_1 the situation in **b** is observed. If both gates couple more to D_1 than to D_2 we observe the situation in **c**, as is the case in our experiments. We note that in a real system the different gate arrangements corresponding to **a**-**c** may also lead to a variation in charging voltage, which has not been highlighted in these simulations.

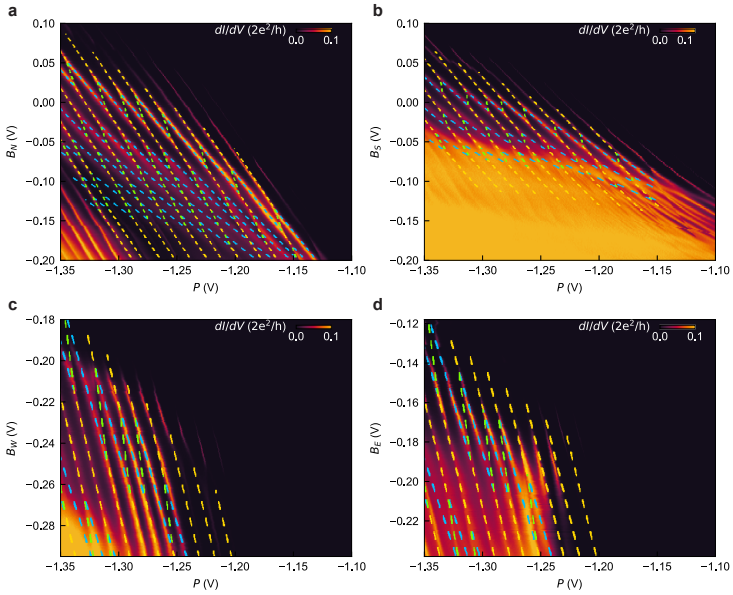

Figure 8.5: **Charge stability diagrams as a function of the Plunger gate P, and barrier gates $\mathbf{B_N}, \mathbf{B_S}, \mathbf{B_W}, \mathbf{B_E}$, with electrochemical simulation overlain.** Comparison between transport data and the double quantum dot simulation defined by equation 8.3. The data is measured with lock-in techniques. Subfigures **a-d** give the differential conduction through the system as a function of the voltages on the plunger gate P against the voltage applied on respectively B_N, B_S, B_W and B_E. These plots share a common gate reference at $\mathbf{V_{ref}} = [P = -1.217\text{V}, B_N = 0\text{V}, B_S = 0\text{V}, B_W = -0.237\text{V}, B_E = -0.178\text{V}]$. The simulation has been limited to the double-quantum dot region. Data without the simulation is found in Fig. 8.6. The code used to produce the simulated transition lines can be found on Zenodo via the link provided in the main manuscript.

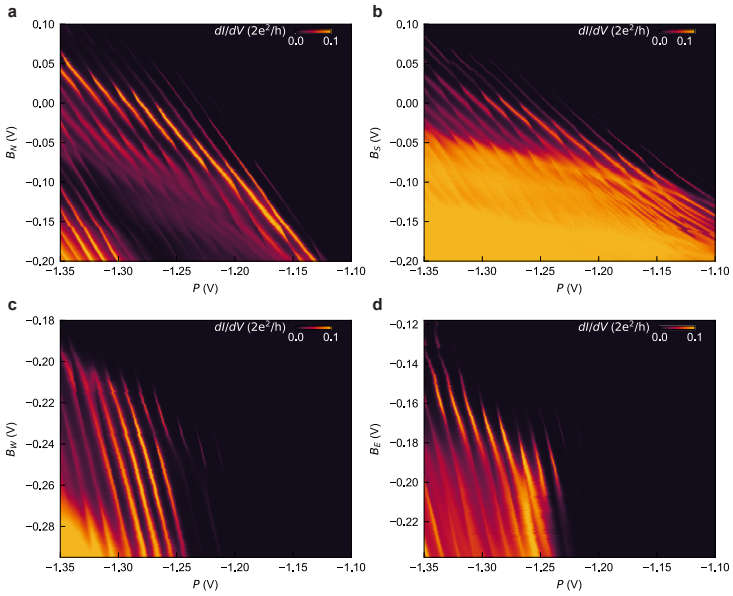

Figure 8.6: **Charge stability diagrams as a function of the Plunger gate P, and barrier gates B_N, B_S, B_W, B_E, without electrochemical simulation overlain.**

tential μ of the quantum dots is given by:

$$\begin{aligned}\mu_1(N_1,N_2,\mathbf{V}) &= \Sigma_{n_1=1}^{N_1} E_{C1}(n_1) \\ &\quad + \Sigma_{n_2=1}^{N_2} E_{Cm}(N_1,n_2) \\ &\quad + \alpha_1(N_1,N_2,\mathbf{V})\mathbf{V} \\ \mu_2(N_1,N_2,\mathbf{V}) &= \Sigma_{n_2=1}^{N_2} E_{C2}(n_2) \\ &\quad + \Sigma_{n_1=1}^{N_1} E_{Cm}(n_1,N_2) \\ &\quad + \alpha_2(N_1,N_2,\mathbf{V})\mathbf{V}\end{aligned} \tag{8.3}$$

$N_{1(2)}$ denotes the occupation of the top (bottom) quantum dot. $E_{C1(2)}(N_{1(2)})$ and $E_{Cm}(N_1,N_2)$ are the occupation-dependent charging energies of the top (bottom) quantum dot and the electrostatic inter-dot coupling energy respectively. $\mathbf{V}$ is the vector denoting the gate voltages. The coupling between the gates and the top (bottom) quantum dot is given by two row matrices $\alpha_{1(2)}$, with purely positive entries. These lever arms are generally taken to be occupation- and voltage-dependent. Since the charging energy is poorly defined for level-dependent lever-arms, these are defined at an (arbitrary) fixed reference voltage $\mathbf{V_{ref}}$:

$$\begin{aligned}E_{C1(2)}(N_{1(2)}) \equiv \mu_{1(2)}(N_{1(2)},N_{2(1)},\mathbf{V_{ref}}) \\ - \mu_{1(2)}(N_{1(2)}-1,N_{2(1)},\mathbf{V_{ref}})\end{aligned} \tag{8.4}$$

fixing $\mu(0,0,\mathbf{V_{ref}}) = 0$. The charging energies and the inter-dot capacitive energies are consistent across simulations in figure 8.5. To reduce the free parameters further the

coupling matrix α is simplified. $\alpha_1(V_P)$ and $\alpha_2(N_2, V_P)$ are dependent on the plunger gate voltage V_P instead of on all the gate voltages, with the latter also depending on the occupation of the bottom quantum dot. With these assumptions, the data matches a charge stability diagram of a double quantum dot as seen in Figure 8.5 and Figure 8.2 of the main text. The used parameters can be found in full on Zenodo using the link provided in the main text. This match suggests that the system indeed consists of a double quantum dot, with no additional dot interacting with it in a meaningful way. The latter would namely result in additional (triangular, pentagonal or heptagonal) features that we do not observe.

To achieve the observed match, the lever arms between the gates and the bottom quantum dot need a significant dependency on the occupation of the bottom quantum dot. This is not as pronounced for the top quantum dot, which is expected from the stronger in-plane confinement. Any additional charges on the top quantum dot will have a larger impact on its size and thus on the coupling to the barrier gates.

We note that the plunger gate voltage has a significant effect on the lever arm of B_S, as seen by the curvature of the transition lines in Figure 8.6b. This suggests that the plunger gate significantly changes the capacitive coupling between B_S and the quantum dots, which would occur if the quantum dots are close to B_S. This is consistent with the estimated positions of the quantum dots that are presented in the main text.

Small discrepancies between the data and the electrochemical simulation are attributed to the limited parameters of the model, like the neglected dependence on the top quantum dot occupation and the exclusion of tunnel-coupling. Moreover for increasingly negative voltages on B_N and B_S the system is generally poorly described by a double quantum dot as seen in Figure 8.5a,b. For lower voltages on B_N (and P) the overall transport first decreases, which we attribute to the same phenomenon which leads to the decrease in the Coulomb peak amplitude in Figure 8.1c (lower panel). namely a larger tunnel-coupling between the top and bottom layer. This increased tunnel coupling could change the interaction between the quantum dots and the leads. At even lower voltages B_N and P a single-dot charge stability diagram emerges corresponding to loading of the top quantum dot, which corresponds to either the merging of the top and bottom quantum dot, or the screening of the bottom quantum dot by the top layer. For the latter case, the possibility of this transition is described in appendix 8.3. For lower voltages on B_S we observe a large background current (Fig. 8.5b). This background current seems to emerge as the resonances of one of the quantum dots become poorly defined and closely spaced. We propose that a conductive channel is formed under B_S through one of the layers of the quantum well. Despite these discrepancies, the good match between the data and this relatively simple model strongly supports that the system in question consists of a double quantum dot without any additional quantum dots.

The code and the parameters used to perform the simulation can be found in full on Zenodo using the link provided in the main text. Here the parameters to fit the charge stability diagram in Figure 8.2 of the main text are also found.

8.5. SCHRÖDINGER-POISSON SIMULATION

We perform 2D Schrödinger-Poisson simulation with Nextnano [37]. Figure 8.7a shows the heavy-hole (HH) band edge for the heterostructure ($z > 0$) where the top edges of the

quantum wells are positioned at z=55 nm and z=69 nm. For $z < 0$ the gate stack is visible. This comprises of a plunger gate, two barrier gates and a layer of Al_2O_3. Fig. 8.7b shows the wavefunction amplitude for the first 20 2D orbitals for which we calculated the lever arm. The potential applied to the plunger and the barriers is −1.15 V and −0.25 V respectively.

We estimate the tunnel coupling between the two quantum wells by solving the Schrödinger equation for this system and extracting the symmetric-antisymmetric gap between the first two energy states, from which we obtain $t_c^{QW} = 16$ GHz. Assuming a harmonic confinement potential in the in-plane direction and the dot centre in the same axis, the single-hole dot-dot tunnel coupling can then be obtained from the radius of the two dots (r_{top} and r_{bottom}) $t_c^{QD} = t_c^{QW}(2r_1r_2)/(r_1^2 + r_2^2)$, with r the Bohr radius. From these assumptions, the upper bound on the estimated dot-dot tunnel coupling for the case of equally sized quantum dots is $t_c^{QD} = t_c^{QW} = 16$ GHz.

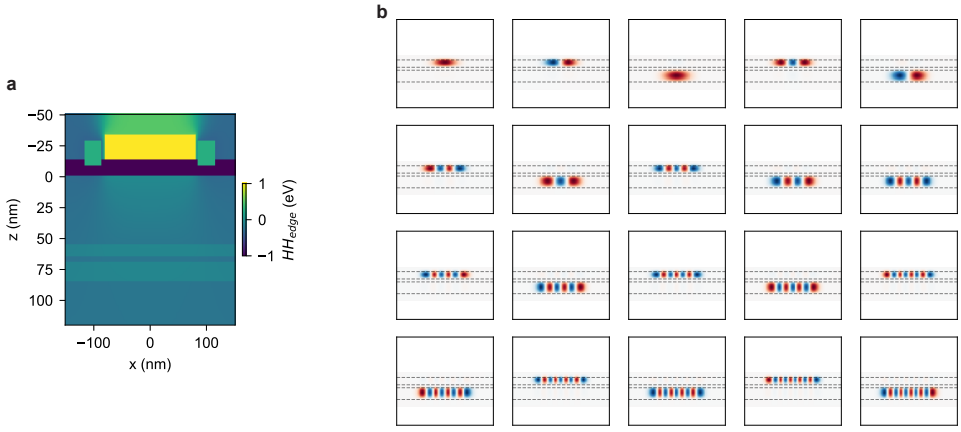

Figure 8.7: **Results of the 2D Schrödinger-Poisson simulations. a** Heavy hole band edge as a function of x and z coordinates for the bilayer heterostructure which also comprises the gate stack for $z < 0$, where z is the growth direction. **b** Colour map of the wavefunction amplitude for the first 20 energy levels ordered from left to right, top to bottom.

8.6. FINITE ELEMENTS SIMULATIONS OF CAPACITANCE

To get an indication of the position of the quantum dots based on the lever arms, a finite element simulation with Ansys Q3D [36] is performed, to extract the geometric capacitance between a gate and quantum dot. These simulated geometric capacitances are converted to lever arm ratios by dividing the absolute quantum dot-barrier gate capacitance by the quantum dot-plunger gate capacitance. The simulated lever arm ratios are then compared to those obtained from the charge-stability diagrams, and the position at which these best match each other is determined (see Fig. 8.8). This is simulated for the quantum dot being positioned in either the top or the bottom well. The heterostructure has been modelled up to 500 nm in-plane around the plunger gate, and up to a depth of 125 nm below the bottom quantum well. The reservoirs underneath the ohmic gates

are excluded in this simulation. While these gates may affect the electrostatic coupling of the other gates to the quantum dot, their symmetric positioning will partly compensate for their impact on the quantum dot location. The dielectric material permittivities used in the simulation are found in table 8.1. The metallic gates have been simulated as uniform perfect conductors.

To emulate a quantum dot a circular, perfectly conducting, uniform disk is placed in either quantum well. This allows us to estimate the geometric capacitance between the quantum dot and the surrounding gates. Each quantum dot is simulated with different disk radii. We note that the wavefunction density of the quantum dot is not taken into account here, and non-circular shapes are not investigated.

Table 8.1: **Relative dielectric permittivity used in the Ansys simulation.** For the properties of $Si_{0.2}Ge_{0.8}$ a linear approximation based on the atomic concentration is used.

Material	ϵ_r
Al_2O_3 [38]	5.9
Ge [39]	15.8
$Si_{0.2}Ge_{0.8}$ [39]	15.0
SiO_2 [40]	3.9

To determine how well the simulations fit the experimental data, we determine the Euclidean distance $\Delta = \sqrt{\sum_{B_i}(\tilde{\alpha}_{B_i,\text{meas}} - \tilde{\alpha}_{B_i,\text{sim}})^2}$, where $\tilde{\alpha}_{B_i,\text{meas(sim)}}$ is the measured (simulated) lever arm ratio α_{B_i}/α_P and the sum is taken over the barrier gates B_N, B_S, B_E and B_W. This Δ is the cost-metric from which we estimate the position (and approximate radius) of the quantum dot.

For each analysed quantum dot and quantum well, there is a particular position and radius at which Δ is minimised (see Fig. 8.8). These are considered to be the most probable locations and radii of that particular quantum dot in the quantum well.

To achieve the minimal Δ, the quantum dots are both predicted to have a radius of about 30 nm and are positioned closer than that to each other (Fig. 8.9). The radius determined here is lower than expected from the plunger gate size, with the discrepancy arising from the approximation of the quantum dot as a uniform disk. From their proximity we conclude that the quantum dots are likely to be in two separate wells. Δ is minimised for D_{top} whenever it is located in the top well, and for D_{bot} when it is in the bottom well. This is consistent with the allocation made in the main text.

Future improvements on this method would consider the electrostatic potential arising from the gates, the strain of the system and the effects of the disorder. Moreover, the interplay between multiple quantum dots spread across the wells can be taken into account in the future, as we stress that currently just a single quantum dot is simulated at a time. A self-consistent 3D Schrödinger-Poisson approach could make this possible.

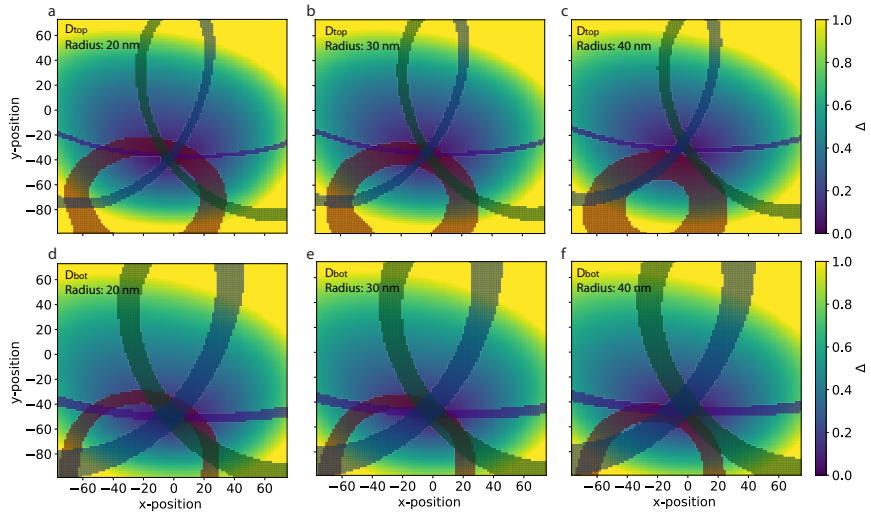

Figure 8.8: **Triangulation of the quantum dots.** Within the red, purple, green and blue contours, the simulated lever arm to the respective gate is within the standard deviation of the empirically extracted values. For D_{top} these are $\tilde{\alpha}_{B_N,\text{meas}} = 0.44 \pm 0.02, \tilde{\alpha}_{B_S,\text{meas}} = 0.53 \pm 0.02, \tilde{\alpha}_{B_W,\text{meas}} = 0.41 \pm 0.02, \tilde{\alpha}_{B_E,\text{meas}} = 0.40 \pm 0.02$ respectively. For D_{bot} these are $\tilde{\alpha}_{B_N,\text{meas}} = 0.55 \pm 0.01, \tilde{\alpha}_{B_S,\text{meas}} = 0.76 \pm 0.04, \tilde{\alpha}_{B_W,\text{meas}} = 0.53 \pm 0.04, \tilde{\alpha}_{B_E,\text{meas}} = 0.53 \pm 0.05$ respectively. The measurement and simulation agree best at the position for which Δ is minimal. The origin is defined at the centre of the plunger gate. Subfigures **a-c** show the results for D_{top}, simulated in the top quantum well for radii of a 20, 30 and 40 nm. Similarly subfigures **d-e** show the results for D_{bot}, as it is simulated in the bottom quantum well for radii of a 20, 30 and 40 nm. For both quantum dots other radii and simulation within the other quantum well result in a higher minimal Δ.

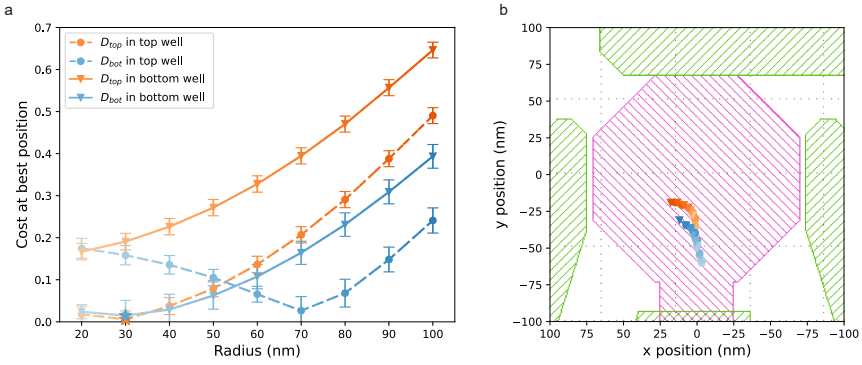

Figure 8.9: **Simulated quantum dot radius and position. a** The Δ corresponding to the most likely quantum dot position for a given quantum dot radius. The simulation and experiments have been compared for either quantum dot in both wells. Quantum dot 1 (2) corresponds to the orange (blue) transitions in the Fig. 8.2 of the main text. For each quantum dot, the most likely radius is 30 nm. Error bars are based on the standard deviation in the slopes extracted from the raw data in 8.5. **b** The expected position for each radius of the two quantum dots in either the bottom or the top well. For all radii, the quantum dots are close to one another. The darker colours correspond to the larger radii as depicted in **a**.

BIBLIOGRAPHY

[1] S. G. J. Philips, M. T. Mądzik, S. V. Amitonov, S. L. de Snoo, M. Russ, N. Kalhor, C. Volk, W. I. L. Lawrie, D. Brousse, L. Tryputen, B. P. Wuetz, A. Sammak, M. Veldhorst, G. Scappucci, and L. M. K. Vandersypen. "Universal control of a six-qubit quantum processor in silicon". In: *Nature* 609 (7929 Sept. 2022), pp. 919–924. ISSN: 0028-0836.

[2] N. W. Hendrickx, W. I. L. Lawrie, M. Russ, F. van Riggelen, S. L. de Snoo, R. N. Schouten, A. Sammak, G. Scappucci, and M. Veldhorst. "A four-qubit germanium quantum processor". In: *Nature* 591 (7851 Mar. 2021), pp. 580–585. ISSN: 0028-0836.

[3] P. Stano and D. Loss. "Review of performance metrics of spin qubits in gated semiconducting nanostructures". In: *Nature Reviews Physics* 4 (2021), pp. 672–688.

[4] J. Yoneda, K. Takeda, T. Otsuka, T. Nakajima, M. R. Delbecq, G. Allison, T. Honda, T. Kodera, S. Oda, Y. Hoshi, N. Usami, K. M. Itoh, and S. Tarucha. "A quantum-dot spin qubit with coherence limited by charge noise and fidelity higher than 99.9%". In: *Nature Nanotechnology* 13.2 (Feb. 2018), pp. 102–106. ISSN: 1748-3395.

[5] W. I. L. Lawrie, M. Rimbach-Russ, F. van Riggelen, N. W. Hendrickx, S. L. de Snoo, A. Sammak, G. Scappucci, J. Helsen, and M. Veldhorst. "Simultaneous single-qubit driving of semiconductor spin qubits at the fault-tolerant threshold". In: *Nature Communications* 14 (1 June 2023), p. 3617. ISSN: 2041-1723.

[6] X. Xue, M. Russ, N. Samkharadze, B. Undseth, A. Sammak, G. Scappucci, and L. M. K. Vandersypen. "Quantum logic with spin qubits crossing the surface code threshold". In: *Nature* 601 (7893 Jan. 2022), pp. 343–347. ISSN: 0028-0836.

[7] A. Noiri, K. Takeda, T. Nakajima, T. Kobayashi, A. Sammak, G. Scappucci, and S. Tarucha. "Fast universal quantum gate above the fault-tolerance threshold in silicon". In: *Nature* 601.7893 (Jan. 2022), pp. 338–342. ISSN: 1476-4687.

[8] K. Takeda, A. Noiri, T. Nakajima, T. Kobayashi, and S. Tarucha. "Quantum error correction with silicon spin qubits". In: *Nature* 608 (7924 Aug. 2022), pp. 682–686. ISSN: 0028-0836.

[9] F. van Riggelen, W. I. L. Lawrie, M. Russ, N. W. Hendrickx, A. Sammak, M. Rispler, B. M. Terhal, G. Scappucci, and M. Veldhorst. "Phase flip code with semiconductor spin qubits". In: *npj Quantum Information* 8 (1 Oct. 2022), p. 124. ISSN: 2056-6387.

[10] F. Borsoi, N. W. Hendrickx, V. John, M. Meyer, S. Motz, F. van Riggelen, A. Sammak, S. L. de Snoo, G. Scappucci, and M. Veldhorst. "Shared control of a 16 semiconductor quantum dot crossbar array". In: *Nature Nanotechnology* (Aug. 2023). ISSN: 1748-3387.

[11] L. M. K. Vandersypen, H. Bluhm, J. S. Clarke, A. S. Dzurak, R. Ishihara, A. Morello, D. J. Reilly, L. R. Schreiber, and M. Veldhorst. "Interfacing spin qubits in quantum dots and donors—hot, dense, and coherent". In: *npj Quantum Information* 3.1 (Sept. 2017), p. 34. ISSN: 2056-6387.

[12] Z. Wang, M. Feng, S. Serrano, W. Gilbert, R. C. C. Leon, T. Tanttu, P. Mai, D. Liang, J. Y. Huang, Y. Su, W. H. Lim, F. E. Hudson, C. C. Escott, A. Morello, C. H. Yang, A. S. Dzurak, A. Saraiva, and A. Laucht. "Jellybean Quantum Dots in Silicon for Qubit Coupling and On-Chip Quantum Chemistry". In: *Advanced Materials* n/a.n/a (2023), p. 2208557.

[13] F. Borjans, X. G. Croot, X. Mi, M. J. Gullans, and J. R. Petta. "Resonant microwave-mediated interactions between distant electron spins". In: *Nature* 577.7789 (Jan. 2020), pp. 195–198. ISSN: 1476-4687.

[14] J. Yoneda, W. Huang, M. Feng, C. H. Yang, K. W. Chan, T. Tanttu, W. Gilbert, R. C. C. Leon, F. E. Hudson, K. M. Itoh, A. Morello, S. D. Bartlett, A. Laucht, A. Saraiva, and A. S. Dzurak. "Coherent spin qubit transport in silicon". In: *Nature Communications* 12.1 (July 2021), p. 4114. ISSN: 2041-1723.

[15] A. Tosato, B. Ferrari, A. Sammak, A. R. Hamilton, M. Veldhorst, M. Virgilio, and G. Scappucci. "A High-Mobility Hole Bilayer in a Germanium Double Quantum Well". In: *Advanced Quantum Technologies* 5 (5 May 2022), p. 2100167. ISSN: 2511-9044.

[16] D. Laroche, S.-H. Huang, E. Nielsen, C. W. Liu, J.-Y. Li, and T. M. Lu. "Magnetotransport of an electron bilayer system in an undoped Si/SiGe double-quantum-well heterostructure". In: *Applied Physics Letters* 106.14 (Apr. 2015). 143503. ISSN: 0003-6951. eprint: https://pubs.aip.org/aip/apl/article-pdf/doi/10.1063/1.4917296/13050894/143503_1_online.pdf.

[17] M. G. Borselli, R. S. Ross, A. A. Kiselev, E. T. Croke, K. S. Holabird, P. W. Deelman, L. D. Warren, I. Alvarado-Rodriguez, I. Milosavljevic, F. C. Ku, W. S. Wong, A. E. Schmitz, M. Sokolich, M. F. Gyure, and A. T. Hunter. "Measurement of valley splitting in high-symmetry Si/SiGe quantum dots". In: *Applied Physics Letters* 98.12 (Mar. 2011), p. 123118. ISSN: 0003-6951. eprint: https://pubs.aip.org/aip/apl/article-pdf/doi/10.1063/1.3569717/14446901/123118_1_online.pdf.

[18] F. van Riggelen-Doelman, C.-A. Wang, S. L. de Snoo, W. I. L. Lawrie, N. W. Hendrickx, M. Rimbach-Russ, A. Sammak, G. Scappucci, C. Déprez, and M. Veldhorst. *Coherent spin qubit shuttling through germanium quantum dots*. 2023. arXiv: 2308.02406 [cond-mat.mes-hall].

[19] T. Fujita, T. A. Baart, C. Reichl, W. Wegscheider, and L. M. K. Vandersypen. "Coherent shuttle of electron-spin states". In: *npj Quantum Information* 3.1 (June 2017), p. 22. ISSN: 2056-6387.

[20] P. M. Mutter and G. Burkard. "Natural heavy-hole flopping mode qubit in germanium". In: *Physical Review Research* 3 (1 Feb. 2021), p. 13194. ISSN: 2643-1564.

[21] H. Malissa, D. Gruber, D. Pachinger, F. Schäffler, W. Jantsch, and Z. Wilamowski. "Design and fabrication of a SiGe double quantum well structure for g-factor tuning". In: *Superlattices and Microstructures* 39 (5 May 2006), pp. 414–420. ISSN: 07496036.

[22] G. Scappucci, C. Kloeffel, F. A. Zwanenburg, D. Loss, M. Myronov, J. J. Zhang, S. De Franceschi, G. Katsaros, and M. Veldhorst. "The germanium quantum information route". In: *Nature Reviews Materials* 6.10 (Dec. 2020), pp. 926–943. ISSN: 20588437.

[23] R. Vrijen, E. Yablonovitch, K. Wang, H. W. Jiang, A. Balandin, V. Roychowdhury, T. Mor, and D. DiVincenzo. "Electron-spin-resonance transistors for quantum computing in silicon-germanium heterostructures". In: *Physical Review A* 62 (1 June 2000), p. 012306. ISSN: 1050-2947.

[24] C.-A. Wang, C. Déprez, H. Tidjani, W. I. L. Lawrie, N. W. Hendrickx, A. Sammak, G. Scappucci, and M. Veldhorst. "Probing resonating valence bonds on a programmable germanium quantum simulator". In: *npj Quantum Information* 9 (1 June 2023), p. 58. ISSN: 2056-6387.

[25] S. Conti, S. Saberi-Pouya, A. Perali, M. Virgilio, F. M. Peeters, A. R. Hamilton, G. Scappucci, and D. Neilson. "Electron–hole superfluidity in strained Si/Ge type II heterojunctions". en. In: *npj Quantum Materials* 6.1 (2021), p. 41. ISSN: 2397-4648.

[26] D. Nandi, A. D. K. Finck, J. P. Eisenstein, L. N. Pfeiffer, and K. W. West. "Exciton condensation and perfect Coulomb drag". In: *Nature* 488 (7412 Aug. 2012), pp. 481–484. ISSN: 0028-0836.

[27] R. Wang, T. Sedrakyan, B. Wang, D. Lingjie, and D. Rui-Rui. "Excitonic topological order in imbalanced electron–hole bilayers". In: *Nature* 619 (2023), pp. 57–62.

[28] D. Buterakos and S. D. Sarma. *Magnetic Phases of Bilayer Quantum-Dot Hubbard Model Plaquettes*. 2023. arXiv: 2308.04504 [cond-mat.mes-hall].

[29] A. Hamo, A. Benyamini, I. Shapir, I. Khivrich, J. Waissman, K. Kaasbjerg, Y. Oreg, F. von Oppen, and S. Ilani. "Electron attraction mediated by Coulomb repulsion". In: *Nature* 535 (7612 July 2016), pp. 395–400. ISSN: 0028-0836.

[30] C. Hong, G. Yoo, J. Park, M.-K. Cho, Y. Chung, H.-S. Sim, D. Kim, H. Choi, V. Umansky, and D. Mahalu. "Attractive Coulomb interactions in a triple quantum dot". In: *Phys. Rev. B* 97 (24 June 2018), p. 241115.

[31] A. R. Hamilton, E. H. Linfield, M. J. Kelly, D. A. Ritchie, G. A. Jones, and M. Pepper. "Transition from one- to two-subband occupancy in the 2DEG of back-gated modulation-doped GaAs-AlxGa1-xAs heterostructures". In: *Physical Review B* 51.24 (1995), pp. 17600–17604. ISSN: 01631829.

[32] D. Y. Baines, T. Meunier, D. Mailly, A. D. Wieck, C. Bäuerle, L. Saminadayar, P. S. Cornaglia, G. Usaj, C. A. Balseiro, and D. Feinberg. "Transport through side-coupled double quantum dots: From weak to strong interdot coupling". In: *Phys. Rev. B* 85 (19 May 2012), p. 195117.

[33] W. G. van der Wiel, S. De Franceschi, J. M. Elzerman, T. Fujisawa, S. Tarucha, and L. P. Kouwenhoven. "Electron transport through double quantum dots". In: *Rev. Mod. Phys.* 75 (1 Dec. 2002), pp. 1–22.

[34] S. D. Franceschi, S. Sasaki, J. M. Elzerman, W. G. van der Wiel, S. Tarucha, and L. P. Kouwenhoven. “Electron Cotunneling in a Semiconductor Quantum Dot”. In: *Physical Review Letters* 86 (5 Jan. 2001), pp. 878–881. ISSN: 0031-9007.

[35] D. Schröer, A. D. Greentree, L. Gaudreau, K. Eberl, L. C. L. Hollenberg, J. P. Kotthaus, and S. Ludwig. “Electrostatically defined serial triple quantum dot charged with few electrons”. In: *Phys. Rev. B* 76 (7 Aug. 2007), p. 075306.

[36] *Ansys® Electronics Desktop, Release 22.2*. 2022.

[37] S. Birner, T. Zibold, T. Andlauer, T. Kubis, M. Sabathil, A. Trellakis, and P. Vogl. “nextnano: General Purpose 3-D Simulations”. In: *IEEE Transactions on Electron Devices* 54.9 (2007), pp. 2137–2142.

[38] M. Groner, J. Elam, F. Fabreguette, and S. George. “Electrical characterization of thin Al2O3 films grown by atomic layer deposition on silicon and various metal substrates”. In: *Thin Solid Films* 413.1 (2002), pp. 186–197. ISSN: 0040-6090.

[39] W. C. Dunlap and R. L. Watters. “Direct Measurement of the Dielectric Constants of Silicon and Germanium”. In: *Phys. Rev.* 92 (6 Dec. 1953), pp. 1396–1397.

[40] S. M. Sze. *Physics of Semiconductor Devices*. New York: Wiley, 1981.

9

HARD SUPERCONDUCTING GAP IN GERMANIUM

The co-integration of spin, superconducting, and topological systems is emerging as an exciting pathway for scalable and high-fidelity quantum information technology. High-mobility planar germanium is a front-runner semiconductor for building quantum processors with spin-qubits, but progress with hybrid superconductor-semiconductor devices is hindered by the difficulty in obtaining a superconducting hard gap, that is, a gap free of subgap states. Here, we address this challenge by developing a low-disorder, oxide-free interface between high-mobility planar germanium and a germanosilicide parent superconductor. This superconducting contact is formed by the thermally-activated solid phase reaction between a metal, platinum, and the Ge/SiGe semiconductor heterostructure. Electrical characterization reveals near-unity transparency in Josephson junctions and, importantly, a hard induced superconducting gap in quantum point contacts. Furthermore, we demonstrate phase control of a Josephson junction and study transport in a gated two-dimensional superconductor-semiconductor array towards scalable architectures. These results expand the quantum technology toolbox in germanium and provide new avenues for exploring monolithic superconductor-semiconductor quantum circuits towards scalable quantum information processing.

This work was originally published as:
A. Tosato, V. Levajac, J.Y. Wang, C.J. Boor, F. Borsoi, M. Botifoll, C.N. Borja, S. Martí-Sánchez, J. Arbiol, A. Sammak, M. Veldhorst, Hard superconducting gap in germanium. Communications Materials, 4(1), 23 (2023).

9.1. INTRODUCTION

The intimate coupling between superconductors and semiconductors in hybrid devices is at the heart of exciting pursuits, including topological qubits with Majorana zero modes [1, 2], superconducting (Andreev) spin qubits [3], and gate-tunable superconducting qubits [4]. Combining hybrid devices with high-fidelity semiconductor spin qubits in a single material platform may resolve key challenges for scalable quantum information processing. In particular, quantum information transfer between spin and topological qubits [5, 6, 7, 8] may enable a universal gate set for topological quantum computation and, conversely, superconductors may be used to coherently couple spin qubits at a distance via crossed Andreev reflection [5, 9] or topologically protected links [10].

The use of epitaxial superconducting Al to induce a hard superconducting gap in III-V semiconductors [11, 12] stimulated great progress with hybrid devices, leading to experimental reports of topological superconductivity in planar Josephson junctions [13] and in electrostatically defined quasi-1D wires [14], the demonstration of Andreev spin qubits [3], and the realization of a minimal Kitaev chain in coupled quantum dots [15]. However, spin qubits in III-V semiconductors suffer from the hyperfine interactions with the nuclear spin bath [16] that severely deteriorate their quantum coherence [17] and challenges their integration with hybrid devices.

On the other hand, spin qubits with quantum dots in Ge [18, 19, 20, 21] can achieve long quantum coherence due to the suppressed hyperfine interaction [22] and the possibility of isotopic purification into a nuclear spin-free material [23]. Thanks to the light effective mass [24] and high mobility exceeding one million cm^2/Vs [25], holes in planar Ge/SiGe heterostructures have advanced semiconductors spin qubits to the universal operation on a 2×2 qubit array [26], and the shared control of a 16 semiconductor quantum dot crossbar array [27]. Moreover, the ability of holes to make contacts with low Schottky barrier heights to metals [28], including superconductors, makes Ge a promising candidate for hybrid devices. Initial work used superconducting Al to contact Ge either via thermal diffusion [29, 30, 31] or by deposition on the sidewalls of etched mesas [32, 33]. However, the key demonstration of a superconducting gap in Ge free of subgap quasiparticle states is lacking, challenged by the difficulty of contacting uniformly a buried quantum well (QW) with a superconductor, whilst maintaining the low disorder at the superconductor-semiconductor interface and in the semiconductor channel.

Here we address these challenges and demonstrate a hard superconducting gap in Ge. We contact the quantum well with a superconducting germanosilicide (PtSiGe), similar to the silicidation process used by the microelectronics industry for low resistance contacts [34]. The superconductor is formed uniformly within the heterostructure and reaches the buried quantum well via a controlled thermally-activated solid phase reaction between the metal (Pt) and the semiconductor stack (Ge/SiGe). This process is simple, robust, and does not require specialised vacuum conditions or etching because the superconductor-semiconductor interface is buried into the pure semiconducting heterostructure and consequently remains pristine. This represents a conceptually different approach compared to the subtractive nanofabrication processes commonly used for hybrid devices, since our additive process does not deteriorate the active area of the semiconductor. As a result, we demonstrate a suite of reproducible Ge hybrid devices

with low disorder and excellent superconducting properties.

9.2. MATERIAL PROPERTIES

Our approach to superconductor-semiconductor hybrid devices in Ge is illustrated in Fig. 1a. We use an undoped and compressively-strained Ge quantum well, grown by chemical vapor deposition on a Si(001) wafer [35] and separated from the surface by a SiGe barrier (Methods). This heterostructure supports a two-dimensional hole gas (2DHG) with high mobility ($\sim 6\times10^5$ cm^2/Vs), long transport scattering time τ (~ 30 ps), and long mean free path ($\sim 7\mu$m) (Supplementary Fig. 1) and hosts high-performance spin-qubits [20]. Crucial for the reliable search of topological superconductivity [36] and for scaling to large spin-qubit architectures [37], the disorder in our buried Ge quantum wells is characterised by an energy level broadening $\hbar/2\tau$ of ~ 0.01 meV, which is more than one order of magnitude smaller than in the other material systems exhibiting a hard superconducting gap (Supplementary Table 1).

As shown by the schematics in Fig. 1a, we obtain PtSiGe contacts to the quantum well by room-temperature evaporation of a Pt supply layer, metal lift-off, and rapid thermal process at 400 °C (Methods). This low-temperature process preserves the structural integrity of the quantum well grown at 500 °C, whilst activating the solid phase reaction driving Pt into the heterostructure and Ge and Si into the Pt (Supplementary Fig. 3). As a result, low-resistivity germanosilicide phases are formed [38, 39] and under these process conditions the obtained PtSiGe films are superconducting with a $T_c \approx 0.5$ K and an in-plane critical field of $B_{c\parallel} \approx 400$ mT (Supplementary Fig. 2). Finally, we use patterned electrostatic gates, insulated by dielectric films in between, to accumulate charge carriers in the quantum well and to shape the electrostatic confinement potential of the hybrid superconductor-semiconductor devices (Methods). This approach to hybrid devices is different compared to the conventional process with 1D nanowires, where an epitaxial superconductor proximitizes the semiconductor region underneath. Because we do not perform any etch during the nanofabrication of hybrid devices, the low-disorder landscape that determines the 2DHG high mobility is likely to be preserved when further dimensional confinement is achieved by means of electrostatic gates. By contrast, for processes where etching of the superconductor is required, the fabrication of hybrid devices yields to mobility degradation [40].

The morphological, structural, and chemical properties of the hybrid devices are inferred by aberration corrected high-angle annular dark-field scanning transmission electron microscopy (HAADF-STEM) and electron energy-loss spectroscopy (EELS). Fig. 1b shows a HAADF-STEM image of a cross-section of a superconductor-normal-superconductor quantum point contact (SNS-QPC) taken off-center to visualise the two gate layers (Fig 2a shows a top view of the device). We observe a uniform quantum well of high-crystalline quality, with sharp interfaces to the adjacent SiGe and absence of extended defects. As a result of the annealing, Pt diffuses predominantly vertically through the SiGe spacer reaching the quantum well. The sharp lateral interfaces between the two PtSiGe contacts and the QW in between set the length of the channel populated by holes via the top-gates. The PtSiGe film presents poly-crystalline domains with a crystal size up to 50×50 nm and orthorhombic phase (PBNM, space group number 62) [41]. This is inferred from the power spectra or fast Fourier transforms (FFTs) taken from the two PtSiGe domains

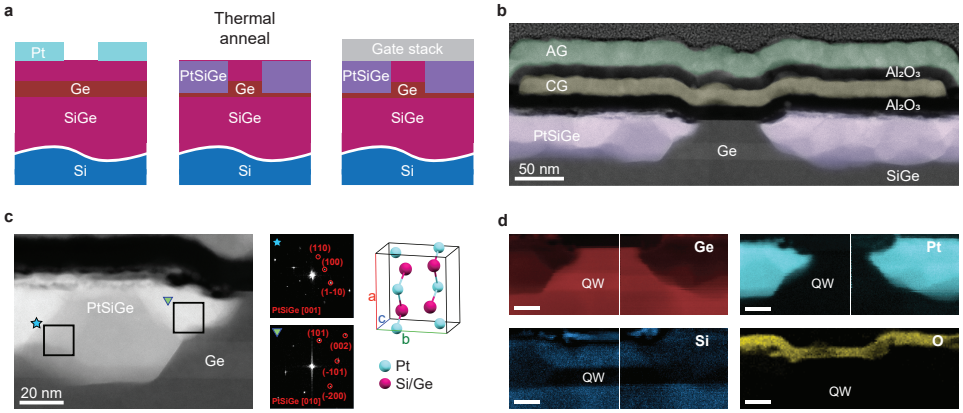

Figure 9.1: **Material properties of superconductor-semiconductor Ge devices.** **a**) Schematics of the fabrication process for a superconductor-normal-superconductor quantum point contact (SNS-QPC). First, platinum is deposited on the heterostructure, then thermal annealing at 400 °C drives Pt in the heterostructure to form PtSiGe, finally two gate layers are deposited, insulated by Al_2O_3. **b**) False-color high angle annular dark field scanning transmission electron microscopy (HAADF STEM) image of a cross-section of a SNS-QPC. The PtSiGe contacts are violet, the Ti/Pd constriction gate (CG) operated in depletion mode is yellow, the Ti/Pd accumulation gate (AG), used to populate the quantum well, is green. A scanning electron microscopy top view image of this device is shown in Fig. 2. **c**) Atomic resolution HAADF STEM image of the Ge/PtSiGe interface along with the indexed fast Fourier transforms (FFTs) of the two regions (black squares) within the PtSiGe contacts and a schematics of the PtSiGe orthorhombic unit cell. The corresponding ternary lattice parameters $T = a_T, b_T, c_T$ that define the dimensions of the unit cell can be calculated, in a first approximation, by Vegard's law: $T_{PtSi_{1-x}Ge_x} = x\, B_{PtGe} + (1-x)\, B_{PtSi}$ where $B = a_B, b_B, c_B$ are the lattice parameters of the binary compounds PtSi and PtGe, and x is the relative content of Ge with respect to Si. **d**) Electron energy-loss spectroscopy (EELS) composition maps showing the Pt, Ge, Si and O signals for the central area of the TEM lamella of panel b, the scale-bar indicates 50 nm. The PtGeSi stoichiometry is extracted by quantitative EELS analysis and reported in Supplementary Fig. 4.

interfacing with the QW from the left contact, shown in Fig. 1c along with a schematic view of the unit cell of such phase. More detailed studies by high-resolution plane TEM are required to assess the junction uniformity in the direction parallel to the junction and whether this would impact Majorana experiments. The analysis of EELS elemental concentration profiles across the Ge QW→PtSiGe heterointerface (Supplementary Fig. 4) reveals that the threefold PtSiGe stoichiometry is Ge-rich, with relative composition in the range between $Pt_{0.1}Si_{0.2}Ge_{0.7}$ and $Pt_{0.1}Si_{0.05}Ge_{0.85}$ depending locally on the analysed grain. The EELS compositional maps in Fig. 1d show the elemental distribution of Ge, Si, Pt, Al, and O, at the key regions of the device. We observe Pt well confined to the two contacts areas, which also appear Ge-rich. Crucially, O is detected only in the Al_2O_3 dielectric layer below the gates, pointing to a high-purity quantum well and a pristine superconductor-semiconductor interface.

9.3. HIGHLY TRANSPARENT JOSEPHSON JUNCTION

We perform low-frequency four-terminal current and voltage bias measurements (Methods) on the SNS-QPC device shown in Fig. 2a to infer the properties of the superconductor-

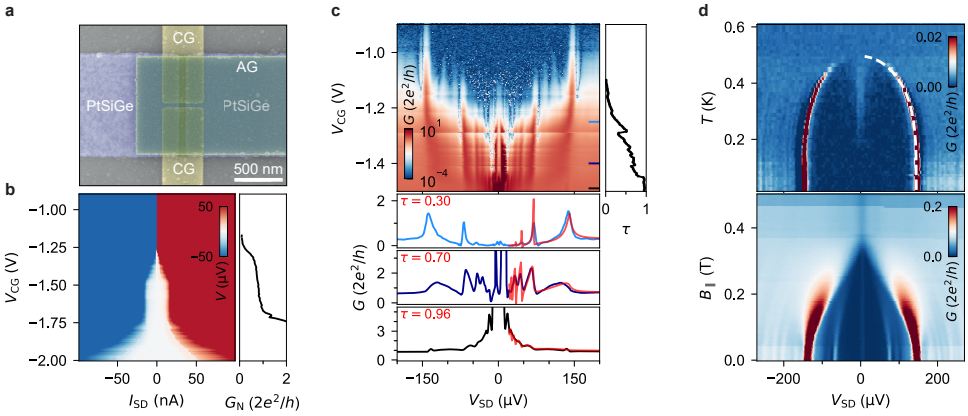

Figure 9.2: **Highly-transparent Josephson junctions.** **a**) False-color scanning electron microscope image of the SNS device. The PtSiGe contacts are violet, the constriction gates (CG) are yellow and the accumulation gate (AG) is green. The channel length between the two superconducting leads is 70 nm and the channel width between the constriction gates is 40 nm. The two constriction gates are separate by design but always shorted together during measurements. **b**) Color map of the voltage drop across the junction V *vs* source-drain current I_{SD} and constriction-gate voltage V_{CG} at zero magnetic field along with normal-state conductance (G_N) trace *vs* V_{CG}. G_N is calculated as the conductance average where the voltage drop across the device is in the range [500, 650] mV or -[650,500] mV, that is much higher than the estimated superconducting gap. **c**) Color map of G in units of $2e^2/h$ *vs* the source-drain voltage V_{SD} and V_{CG}. Bottom panel shows line-cuts of conductance at $V_{CG} = [-1.25, -1.4, -1.49]$ V, red lines are the fit with the coherent scattering model from which transparency τ is extracted. Right inset shows the evolution of the transparency, as extracted from the fitting of conductance curves to the coherent scattering model (Methods), with the constriction gate V_{CG}. **d**) Color map of G *vs* T and V_{SD} (top panel), and *vs* $B_\parallel$ and V_{SD} (bottom panel), where $B_\parallel$ is the in-plane magnetic field in the direction of transport and T the temperature. The color scale in panel (d) has been saturated to better infer the low conductance limit. The source-drain bias is applied between the PtSiGe contacts, and the voltage drop across the junction is measured with a standard 4-terminal setup. The accumulation voltage for measurements in b,c and d was set to −4.5 V, where the 2DHG is expected to reach saturation density (see Supplementary Fig. 1) of $\simeq 6 \times 10^{11}$ cm^{-2} [35]. Measurement presented in b, c and in panel d (bottom), are performed at 15 mK, corresponding to an electron temperature of ~ 25 mK.

semiconductor interface. Accumulation (AG, in green) and constriction (CG, in yellow) gates control transport within the 70 nm long channel between the two PtSiGe leads. We apply a large negative voltage to the accumulation gate to populate the quantum well with holes, and we then control the effective width of the channel by applying a more positive voltage to the constriction gates, thus depleting the underlying quantum well.

The current bias measurements (Fig. 2b) reveal a tunable supercurrent with a plateau when the constriction gate voltage V_{CG} is in the range $\approx [-1.75, -1.50]$ V. This is the same range where we observe the first conductance plateau in the normal-state conductance G_N (Fig. 2b, right inset), indicating that the switching current (I_{sw}) plateau observed in the color plot stems form the supercurrent discretization due to the discrete number of modes in the QPC [30, 42]. Supercurrent discretization up to the third conductance plateau is shown in Supplementary Fig. 5 (data are for a different SNS-QPC device with identical design to the one presented here). The discretization of the supercurrent at zero magnetic field, indicates that the quality of the 2DHG is preserved also upon the formation of the superconducting contacts. We use the switching current as a lower bound

for the critical current and we estimate an $I_{sw}R_N$ product of 51 µV, showing an improvement as compared to previous results obtained with pure Al contacts in Ge QWs [30, 32, 33], despite the Al T_c is higher than the PtSiGe T_c. The measured $I_{sw}R_N$ product is ~ 0.5 the theoretical I_cR_N product calculated for a ballistic short junction using the Ambegaokar–Baratoff formula $\pi\Delta^*/2e = 110\,\mu V$ with I_c being the critical current, Δ^* the induced superconducting gap and e the electron charge [43]. This discrepancy has been observed in previous works [44, 30] and is consistent with a premature switching due to thermal activation [45].

By operating the device in voltage-bias configuration and stepping the constriction gates, we observe in the conductance color plot the typical signature of multiple Andreev reflections (MARs) (Fig. 2c). When the applied voltage bias corresponds to an integer fraction of $2\Delta^*$, with Δ^* being the induced superconducting gap, we observe differential conductance dI/dV peaks (dips) in the tunneling (open) regime [46, 47]. We measure MARs up to the 5th order, suggesting that the coherence length ξ_N in the Ge QW is a few times larger than the junction length L, and setting a lower bound to the phase coherence length in the QW $l_\psi > 5L = 350\,nm$. These observations are consistent with the findings of ref. [33] where a similar Ge/SiGe heterostructure is used. Fitting the differential conductance with the coherent scattering model described in ref. [48] (and used in refs. [47, 44, 49]) reveals single channel transport with gate tunable transparency up to 96%. Such a high transparency confirms the high quality interface between the PtSiGe and the Ge QW. From the MARs fit we estimate an induced superconducting gap $\Delta^* = 70.6 \pm 0.9\,\mu eV$, which is about half compared to the $\Delta^* = 129\,\mu eV$ [14] and 150 µeV [50] for recent InAs-Al devices reporting topological superconductivity.

Further, we characterise the evolution of the induced superconducting gap with temperature and magnetic field. After setting the device in tunneling regime, where sharp coherence peaks are expected at $e|V_{SD}| = 2\Delta^*$ (Fig. 2d), we observe the induced superconducting gap closing with increasing temperature and magnetic field. By fitting the temperature dependence of the coherence peaks with the empirical formula from ref. [51] we obtain a critical temperature of 0.5 K. The peak close to zero bias emerging at $T > 0.2\,K$ can be explained in terms of thermally-activated quasiparticle current [49]. The in-plane magnetic field in the transport direction quenches the superconductivity at $B_{c\parallel} = 0.37\,T$. The same critical field is found for the in-plane direction perpendicular to the transport direction while for the out of plane direction $B_{c\perp} = 0.1\,T$ (Supplementary Fig. 6). This in-plane *vs* out-of-plane anisotropy is expected given the thin-film nature of the PtSiGe superconductor [45].

9.4. HARD INDUCED SUPERCONDUCTING GAP

To gain insights into the quality of the Ge/PtSiGe junction we characterise transport through the normal-superconductor quantum point contact (NS-QPC) device shown in Fig. 3a. Importantly, the methodology based on spectroscopy of NS devices alleviates the ambiguity of measuring the amount of quasiparticle states inside the gap with SNS junctions [31]. On the left side of the QPC there is a PtSiGe superconducting lead and on the right side a normal lead consisting of a 2DHG accumulated in the Ge QW. With the accumulation gate (AG) set at large negative voltages to populate the QW we apply a more positive voltage to the constriction gates (CG), creating a tunable barrier between

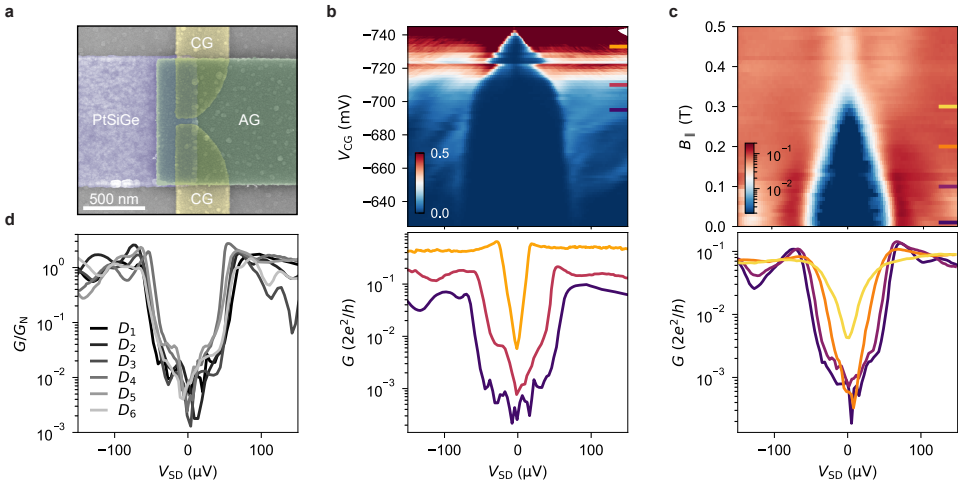

Figure 9.3: **Hard induced superconducting gap.** **a**) False-color SEM image of the normal-superconductor quantum point contact device (NS-QPC). The PtSiGe contact is violet, the constriction gate (CG) are yellow and the accumulation gate (AG) is green. The two constriction gates are separate by design but always shorted together during measurements. **b**) Color map of conductance G *vs* the source-drain voltage V_{SD} and constriction gate V_{CG}, along with line cuts in log-scale of G at the constriction gate voltages $V_{CG} = [-733, -710, -695]$ mV marked by the colored segment in the color-plot. **c**) Color map of G in units of $2e^2/h$ *vs* the in-plane magnetic field $B_\parallel$ perpendicular to the transport direction and constriction gate V_{CG}, along with line cuts in log-scale of G at the field strength $B_\parallel = [0.01, 0.1, 0.2, 0.3]$ T marked by the colored segment in the color-plot. **d**) Conductance traces normalised to the above-gap conductance (G/G_N) *vs* V_{SD} in tunneling regime for 6 different NS-QPC devices D_1-D_6 processed in the same fabrication run, device D_1 is the one reported in Fig 3 a-c, in the remaining devices the constriction gates separation varies (specifications of these devices are provided in Supplementary Fig. 8).

the superconducting and the normal region. In Fig. 3b we progressively decrease the barrier height (decreasing V_{CG}) going from the tunneling regime, where conductance is strongly suppressed, to a more open regime where conductance approaches the single conductance quantum G_0. Line-cuts of the conductance color map are presented in the bottom panel of Fig. 3c. In the tunneling regime, we observe a hard induced superconducting gap, characterised by a two orders of magnitude suppression of the in-gap conductance to the normal-state conductance, and the arising of coherence peaks at $e|V_{SD}| \approx \Delta^* = 70\,\mu$eV. Fig. 3b also shows that the induced superconducting gap varies with the constriction gate voltage. This observation brings confidence that we are measuring the induced superconducting gap rather than the parent gap [52]. A possible explanation is that, upon increasing the density in the semiconductor nearby the junction, the coupling to the parent superconductor might vary, as also observed in other hybrid nanostructures [53].

The evolution of the gap as a function of in-plane magnetic field ($B_\parallel$) shown in Fig. 3c confirms that the gap remains hard for finite magnetic fields up to 0.25 T, ultimately vanishing at $B_\parallel \approx 0.37$ T. The magnetic field evolution of the gap in all three directions matches the behaviour observed in the SNS-QPC (Supplementary Fig. 7).

Finally, Fig. 3d reports the conductance traces in tunneling regime for all the six

measured devices (an overview of the geometries of these devices and the respective measurements are available in the Supplementary Fig. 8, the conductance maps for all these devices are shown in Supplementary Fig. 9). For all devices we observe suppression of conductance equal or larger than two orders of magnitude. At a quantitative level, the conductance traces of Fig 3d are well fitted by the BTK theory [54] (Supplementary Fig. 9) consistent with a hard induced superconducting gap free of subgap states [44, 11]. This finding is the signature of a robust process that yields a reproducible high-quality superconductor-semiconductor interface, overcoming a long-standing challenge for hybrid superconductor-semiconductor quantum devices in Ge.

9.5. SUPERCONDUCTING QUANTUM INTERFERENCE DEVICES

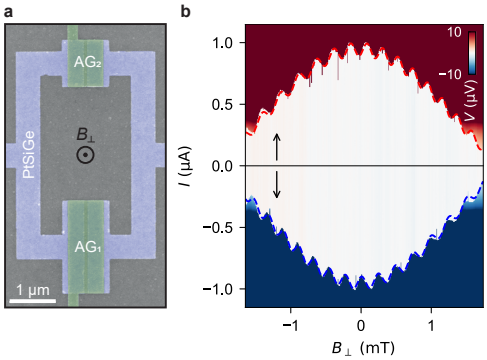

Figure 9.4: **Phase control of a Josephson junction in a SQUID. a**) False-color SEM image of the two JoFET SQUID device. The JoFETs have a channel length of 70 nm and a channel width of 1 μm and 2 μm respectively and can be independently controlled by gates AG_1 and AG_2. The geometric loop area of the SQUID is of 10 μm^2, calculated assuming a rectangle with sides positioned in the center of the PtSiGe loop cross-section. **b**) Color-plot of voltage drop (V) across the SQUID *vs* current (I) and out-of-plane magnetic field ($B_\perp$). Arrows represent the direction of the current (I) sweep. With the gate voltages set at $V_{AG1} = -3.5$ V and $V_{AG2} = -1.65$ V the superconducting phase drops mainly over the second junction. Upon sweeping the out-of-plane magnetic field $B_\perp$ we observe oscillations of the switching current. Red and blue dashed lines are the fit of the evolution of the critical current with magnetic field. The magnetic field is applied in the out of plane direction as depicted in panel (a).

We use the superconducting quantum interference device (SQUID) in Fig. 4a to demonstrate phase control across a Josephson junction, an important ingredient for achieving topological states at low magnetic field [55, 50, 56, 57]. The device is composed of two Josephson field-effect transistors (JoFETs) with a width of 2 μm and 1 μm for $JoFET_1$ and $JoFET_2$ respectively, and equal length of 70 nm. The critical current of the junctions I_{c1} and I_{c2} can be tuned independently by applying the accumulation gate voltages V_{AG1} and V_{AG2} to the corresponding gates. We investigate the oscillations of the SQUID switching current as a function of the out-of-plane-magnetic field penetrating the SQUID loop. Namely, we set V_{AG1} and V_{AG2}, such that both arms support supercurrent and $I_{c1} \gg I_{c2}$. This condition provides that the first junction is used as a reference junction and that the phase drop on it is flux independent, while the phase drop over the second junction is therefore modulated by the external flux through the loop. This

allows the measurement of the current-phase-relation (CPR) of the second junction. This is demonstrated in Fig. 4b where the shown SQUID oscillations are well fitted by the relation: $I_{c,SQUID} = I_{c1}(B_\perp A_1) + I_{c2}(B_\perp A_2)\sin\left(2\pi B_\perp A_{SQUID} - LI_{c1}(B_\perp A_1)/\Phi_0\right)$ where $I_{c1,2}(BA_{1,2})$ are the Fraunhofer dependencies of the critical current obtained from fitting the Fraunhofer pattern of each junction (Supplementary Fig. 10), $A_{1,2}$ are the junction areas, $B_\perp$ is the out-of-plane magnetic field and Φ_0 the flux quantum. From the fit of the data in Fig. 4b (red dashed-line) we extract the effective SQUID loop area $A_{SQUID} = 8.9\,\mu m^2$ (comparable to the $10\,\mu m^2$ SQUID geometric area) and the self-inductance $L = 1.65\,pH$. In order to confirm for the self-inductance effects, we also fit SQUID oscillations for the opposite direction of the current bias (blue dashed-line) and we get similar values for the effective loop area and self-inductance.

9.6. SCALABLE JUNCTIONS

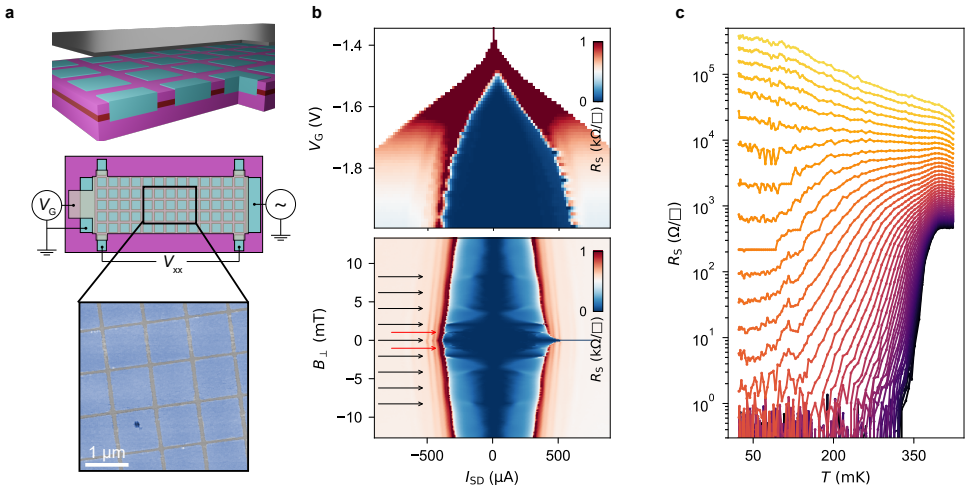

Figure 9.5: **A gated 2D superconductor-semiconductor array.** **a**) 3D and top view schematics of an array of 51 × 10 PtSiGe islands. The inset shows an atomic force microscopy image of the PtSiGe islands of the array. The PtSiGe islands are 930 × 930 nm wide and the separation between neighbouring islands is of 70 nm. **b**) Top panel shows a color map of sheet resistance (R_S) *vs* accumulation gate voltage V_G and source-drain current I_{SD}. Bottom panels shows a color map of sheet resistance *vs* out of plane magnetic field B and source-drain current I_{SD}. The measurement is taken at gate voltage $V_G = -1.99\,V$, where we expect carriers in the quantum well to approach a saturation density value of about 6×10^{11} cm^{-2} and have a mean free path (~ 7μm) much longer than the separation between between neighbouring islands. Black arrows denote the magnetic field corresponding to one flux quantum Φ_0 per unit cell of the array. Red arrows correspond to one-half flux per unit cell. **c**) Sheet resistance as a function of temperature for gate voltages ranging from −2 V to −1.55 V. Yellow curves correspond to small negative gates, and purple curves to large negative gates.

As a first step towards monolithic superconductor-semiconductor quantum circuits in two dimensions, we fabricate and study transport in a macroscopic hybrid device comprising a large array of 510 PtSiGe islands (Fig. 5a) and a global top gate. Each pair of neighbouring islands forms a Josephson junction whose transparency can be tuned by the global accumulation gate. The top panel of Fig. 5b shows a current bias measurement

of the junctions array resistance. As the accumulation gate becomes more negative, all the junctions are proximitized and a supercurrent flows through the device. Remarkably, as the source-drain current approaches the junctions critical current the whole array simultaneously switches from superconducting to resistive regime, as shown from the sharp resistance step (Fig. 5b top).

With this device we also study the evolution of the switching current in a small perpendicular magnetic field. In the bottom panel of Fig. 5b we observe Fraunhofer-like interference, along with the fingerprint of flux commensurability effects associated with the periodicity of the array. At integer numbers of flux quantum per unit area of the periodic array $f = B_\perp / B_0$, where $B_0 = \Phi_0 / A$ with A the junction area and Φ_0 the flux quanta, we observe switching current peaks at $\pm 1f$, $2f$, $3f$, $4f$ and $5f$, denoted by a black arrow in the plot. We also notice this effect at fractional values of f, most notably at $f/2$ (red arrow). Flux commensurability effects, due to the pinning and interference of vortices in Josephson junctions arrays, have been previously reported [58, 59].

The observation of simultaneous switching of super-current and of the Fraunhofer pattern with flux commensurability effects, suggests that all islands effective areas are similar and that the supercurrent through the various junctions is comparable, meaning that all junctions respond synchronously to the applied gate voltage. This is further supported by the observation of sharp switching of super-current and the Fraunhofer pattern of a 1D array of superconducting islands presented in Supplementary Fig. 11.

Finally we present in Fig. 5b the sheet resistance as a function of temperature for different gate voltages. As the gate voltage becomes more negative, the coupling between neighbouring superconducting islands increases and the system transitions from an insulating to a superconducting regime. At low gate voltage the resistance increases with decreasing temperature (yellow curves) indicating the insulating state, while at high gates the resistance drops to zero (purple curves) owing to the global superconducting state. At intermediate gate voltages ($-1.95\,\mathrm{V} \leq V_G \leq -1.93\,\mathrm{V}$, orange curves) there is a transition where the resistance shows a weak temperature dependence. It will be interesting to study this regime in detail, in light of the recent claims of an anomalous metallic state between the superconducting and the insulating phases [59].

9.7. DISCUSSION

In conclusion, we have developed superconducting germanosilicides for contacting Ge quantum wells, which has resulted in excellent superconducting properties imparted to the high-mobility 2DHG. We induced a hard superconducting gap in Ge, a large advancement compared to previous work on Ge hybrid superconductor-semiconductor devices [30, 32, 33, 31]. We were able to observe a hard gap with 100% yield across all the six measured devices, pointing to a robust and reproducible fabrication process. Next to this central result, we further demonstrate phase control across a Josephson junction and take advantage of the planar geometry to scale these devices in 2D arrays.

While we focused on the poly-crystalline superconducting PtSiGe compound, we anticipate two strategies to further increase the size of the induced superconducting gap, which sets a relevant energy scale for hybrid devices. Firstly, following the approach in ref. [33] a superconducting layer with a larger gap, such as Al or Nb, may be deposited on top of the superconducting PtSiGe. Secondly, other ternary superconducting ger-

manosilicides with a higher critical temperature may be explored, starting from the deposition and thermal anneal of other platinoid metals such as Rh and Ir [60].

Based on our findings, we foresee the following use cases for superconductor-semiconductor hybrids in high mobility planar Ge. Although a hard gap is necessary but not sufficient on its own for achieving a topologically protected system, this work positions planar Ge as a promising platform to explore Majorana bound states in phased-biased Josephson junctions [61, 62, 13]. Calculations with experimentally realistic material parameters [57] show that accessing the topological phase is feasible by careful design of Ge planar Josephson junctions geometries that relaxes magnetic field and spin-orbit constrains. More advanced future experiments should build on our current results to fully assess the readiness of Ge for Majorana bound states experiments, such as increasing the induced superconducting gap and measuring it by non local spectroscopy in multi-terminal devices and demonstrate the two-electron charging effect in hybrid Ge/PtSiGe islands, a pre-requisite for their use in topological quantum computation.

Crucially, the realization of a hard superconducting gap positions planar Ge as a unique material platform to pursue the coherent coupling of high fidelity spin qubits using crossed Andreev reflection to enable two-qubit gates over micrometer distances [5, 9]. Remote coupling of spin qubits in Ge may also be achieved by coupling spin qubits via superconducting quantum dots [5, 6], potentially offering a topological protection[10]. Coupling on an even longer distance may be obtained via superconducting resonators [63]. In such a scenario, a capacitive interaction may suffice, but connecting the resonator to a superconducting ohmic, such as PtSiGe, could result in a larger lever arm and therefore boost the coupling, while a direct tunnel coupling would give further directions to explore. The ability to couple qubits over different length scales is highly relevant and a critical component in network-based quantum computing [37].

Furthermore, the demonstration of a hard gap in Ge motivates the investigation of alternative spin qubits systems, such as Andreev spin qubits (ASQ) [64, 65], that may be coupled with gatemons [66] or superconductors [67]. Similar to semiconductor spin qubits, the use of isotopically purified Ge [23] may overcome the strong decoherence from the nuclear environment currently limiting progress with ASQs in III-V materials [3, 66].

All together, these findings represent a major step in the Ge quantum information route, aiming to co-integrate spin, superconducting, and topological systems for scalable and high-fidelity quantum information processing on a silicon wafer.

9.8. METHODS

Ge/SiGe heterostructure growth. The Ge/SiGe heterostructure of this study is grown on a 100-mm n-type Si(001) substrate using an Epsilon 2000 (ASMI) reduced pressure chemical vapor deposition reactor. The layer sequence comprises a $Si_{0.2}Ge_{0.8}$ virtual substrate obtained by reverse grading, a 16 nm thick Ge quantum well, a 22 nm-thick $Si_{0.2}Ge_{0.8}$ barrier, and a thin sacrificial Si cap [35]. Detailed electrical characterisation of heterostructure field effect transistors from these heterostructures are presented in ref. [35].

Device fabrication. The fabrication of the devices presented in this paper entails the following steps. Wet etching of the sacrificial Si-cap in buffer oxide etch for 10 s. Deposi-

tion of the Pt contacts via e-gun evaporation of 15 nm of Pt at pressure of 3×10^{-6} mbar at the rate of 0.5 Å/s. Rapid thermal anneal of Pt contacts at 400 °C for 15 minutes in a halogen lamps heated chamber in argon atmosphere. Atomic layer deposition of 10 nm of Al_2O_3 at 300 °C. Deposition of the first gate layer via e-gun evaporation of 3 nm of Ti and 17 nm of Pd. For the devices with a second gate layer the last two steps are repeated, 27 nm of Pd are deposited for the second gate layer to guarantee film continuity where overlapping with first gate layer.

Transport measurements. Electrical transport measurements of the SNS-QPC, NS-QPC, SQUID devices are carried out in a dry dilution refrigerators at a base temperature of 15 mK, corresponding to an electron temperature of ≈25 mK measured with a metallic N–S tunnel junction thermometer. This refrigerator is equipped with a 3-axis vector magnet. Measurements of the junctions array are carried out in a wet dilution refrigerator with base temperature of 50 mK and z-axis magnet.

Measurements are performed using a standard 4-terminals low-frequency lock-in technique at the frequency of 17 Hz. Voltage bias measurements are performed with an excitation voltage $V_{AC} < 4\,\mu V$. By measuring in a four-terminal setup, additional data processing to subtract series resistances of various circuit components is avoided. For the measurements in Fig. 2b, c, d and Fig. 5b the (maximum) gate voltage is tuned to be just below the threshold for hysteresis, caused by trapped charges in the surface states at the semiconductor/dielectric. In these electrostatic conditions the valence band edge at the semiconductor/dielectric interface and the Fermi level align and the density in the buried channel is expected to approach a saturation density of about 6×10^{11} cm^{-2} [35].

Simulations and fitting of MARs. The experimentally measured conductance $G_{exp}(V)$ of an SNS junction is assumed to be superposition of N single-mode contributions [47]:

$$G_{theory}(V) \sum_{i=1}^{M} N_i G^{(\tau_i,\Delta)}(V) \tag{9.1}$$

where $G^{(\tau_i,\Delta)}$ is the simulated conductance for the N_i modes with transparency τ_i. We allow for M different transparencies, but all N_i modes have the same superconducting gap Δ. The simulations of conductance were implemented in Python using a modified version of the code presented in ref. [68].

The theoretically computed conductance $G_{theory}(V)$ is fitted to $G_{exp}(V)$ using a nonlinear least-squares procedure: $\chi = \int [G_{exp}(V) - G_{theory}(V)]^2 dV$ is minimised for the fitting parameters Δ, N_i, τ_i with $i \in 1, ..., M$. The fitting is performed for increasing M, provided that all N_i and τ_i are nonzero. We note that we assume a coherent 1D system. When the MAR contribution is significant, this assumption leads to an overestimation of the sharpness and amplitude of the peaks. Nonetheless, overall we find a good agreement between the data and the model.

9.9. SUPPLEMENTARY INFORMATION

9.9.1. TWO-DIMENSIONAL HOLE GAS PROPERTIES

Figure 9.6 illustrates the mobility-density and density-gate curves, for a Hall-bar shaped heterostructure field-effect transistor fabricated on the same 22 nm deep Ge/SiGe heterostructure used for all devices in this work. The maximum mobility of 615×10^3 cm^2/Vs

is reached at the density of 5.5×10^{11} cm^{-2}, corresponding to an elastic transport scattering time $\tau = 31$ ps, calculated using $m^* = 0.09$ [24] and a mean free path of 7.4 µm. The density vs gate curve deviates from the expected linear behaviour due to tunneling of charges from the quantum well to the the trap states at the oxide interface, partly screening the electric field in the quantum well. The density and mobility reach saturation when the states at the triangular well in the SiGe barrier at the oxide interface start to populate and thus screen the electric field in the QW.

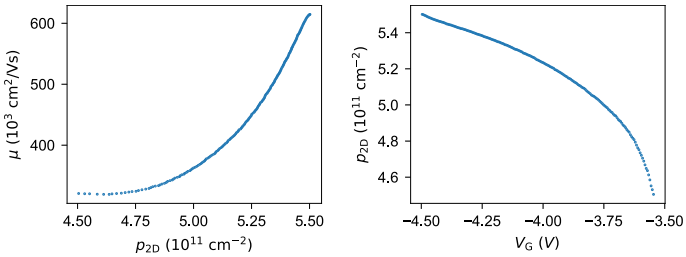

Figure 9.6: **2DHG transport properties.** Mobility μ vs 2D-carrier density p_{2D} (left panel) and 2D-carrier density vs accumulation gate V_G.

9.9.2. PTSIGE PROPERTIES

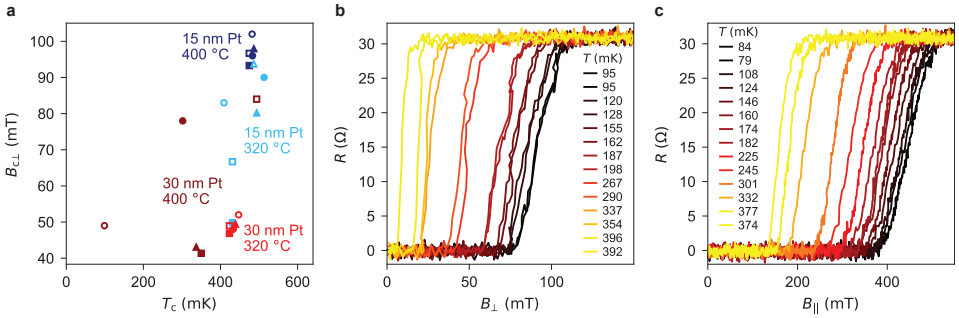

Figure 9.7: **PtSiGe film characterization. a**) Critical perpendicular magnetic field $B_{c\perp}$ and critical temperature T_c of a PtSiGe film deposited and anneled in a 22 nm deep Ge/SiGe QW for different process conditions. The colours of the markers indicate the thickness of the deposited platinum layer (that covers the whole surface of a 3 × 3 mm Ge/SiGe heterostructure) and the anneal temperature. The filled (open) markers correspond to an anneal time of 15 (30) minutes. The marker's shape signifies the used atomic layer deposition (ALD) of Al_2O_3 process: no ALD (circles), ALD with 60 min pre-heating at 300 °C (squares), or ALD with 15 min pre-heating (triangles). In both ALD processes, 10 nm of Al_2O_3 was deposited. **b, c**) Analysis of the critical temperature and fields of a 3 µm wide PtSiGe strip (15 nm Pt has been annealed for 15 minutes at 400 °C). Resistance R versus perpendicular magnetic field ($B_\perp$) and parallel magnetic field ($B_\parallel$) for various temperatures T. These measurements were performed in a 4-probe configuration with standard low frequency lock-in technique in a wet dilution refrigerator with electron temperature of 100 mK.

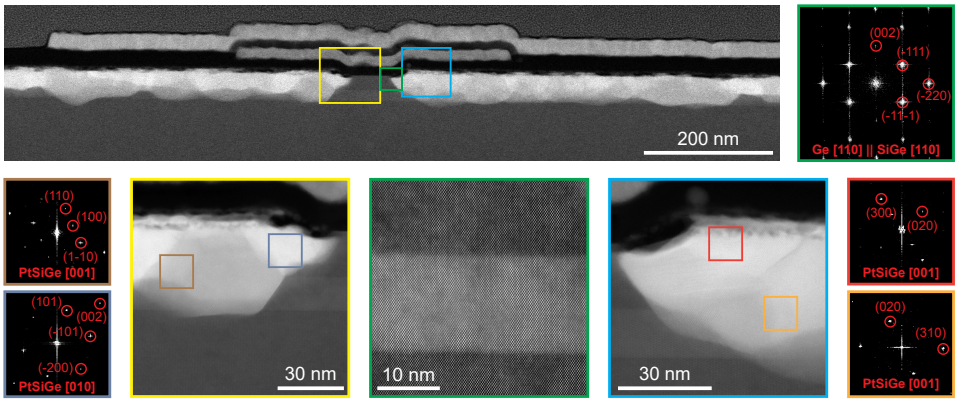

Figure 9.8: **Structural details of the PtSiGe poly-cristalline phase.** High-angle annular dark field scanning transmission electron microscopy (HAADF STEM) and crystallographic information of the SNS-QPC device. The yellow and blue insets show atomic-resolution images of both the left and right contacts highlighting the sharp interfaces between the QW and the PtSiGe film. The atomic-resolution micrograph in the center (green) displays the high quality of the Ge QW interfaces with diamond-structure (FD3-MS, space group number 227). The local contrast variations observed here are attributed to uneven thickness distribution of the lamella due to the focused ion beam (FIB) sample preparation. The fast Fourier transform (FFT) on the top right (green) indicates that the (002) planes in the QW grow epitaxially following the [001] axis. In addition, no dislocations were identified. The insets on the bottom left and right show the power spectra that identify the orthorhombic phase (PBNM, space group number 62) of the PtSiGe film.

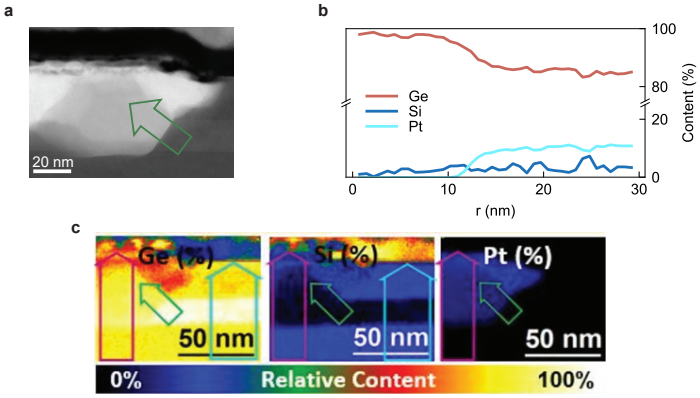

Figure 9.9: **PtSiGe stoichiometry.** Electron energy-loss spectroscopy (EELS) quantitative compositional map of the region indicated from the white arrow in the HAADF STEM image (a) of the Ge/PtSiGe interface of the SNS-QPC. The threefold PtSiGe stoichiometry presented in panel (b) is Ge-rich, with relative composition in the range between $Pt_{0.1}Ge_{0.7}Si_{0.2}$ and $Pt_{0.1}Ge_{0.85}Si_{0.05}$ depending locally on the analysed grain. Panel (c) shows the quantitative EELS compositional maps for Ge Si and Pt. The averaged signal in the region along the green arrows is shown in panel (b).

9.9.3. SNS-QPC MEASUREMENTS

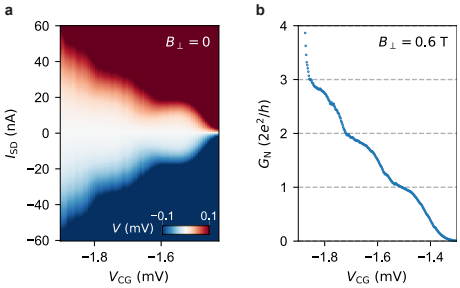

Figure 9.10: **Supercurrent discretization.** **a**) Voltage drop V across an SNS-QPC device as a function of the source drain current I_{SD} and constriction gate voltage V_{CG}. Discrete plateaus in the switching current can be observed, indicating a discrete number of modes in the QPC. **b**) Normal-state differential conductance G versus V_{CG} taken at out-of-plane magnetic field $B_\perp = 0.6$ T, showing plateaus at quantized value of conductance. The plateaus in the two plots are slightly shifted with respect to each other due to the hysteretic behaviour of the device.

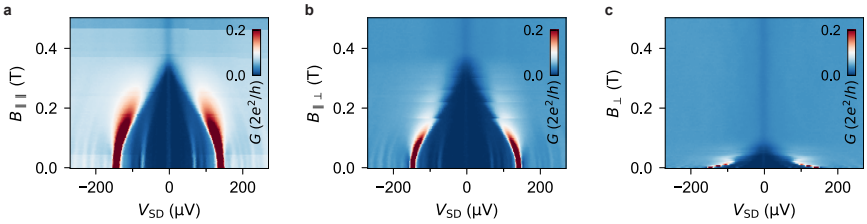

Figure 9.11: **SNS-QPC, evolution of the superconducting gap with magnetic field.** Color map of conductance G in units of $2e^2/h$ vs source-drain bias V_{SD} and magnetic field B for the SNS-QPC. From left to right the magnetic field direction is: in-plane parallel to transport ($B_\parallel$), in-plane perpendicular to transport ($B_{\parallel\perp}$), out of plane ($B_\perp$). The device is tuned in the tunneling regime to show the evolution of the induced superconducting gap with the strength of the magnetic field.

9.9.4. NS-QPC MEASUREMENTS

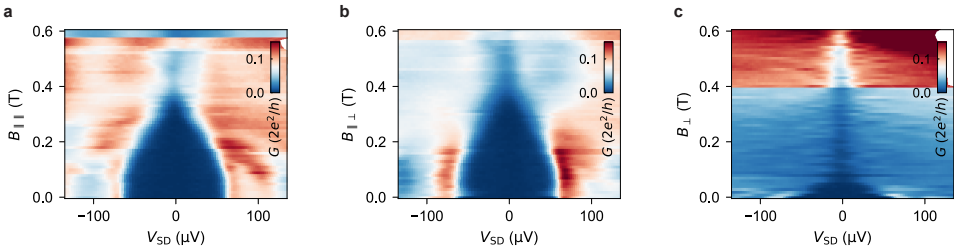

Figure 9.12: **NS-QPC, evolution of the induced superconducting gap with magnetic field.** Color map of conductance G in units of $2e^2/h$ vs source-drain bias V_{SD} and magnetic field B for the NS-QPC. From left to right the magnetic field direction is: in-plane parallel to transport ($B_{\parallel\parallel}$), in-plane perpendicular to transport ($B_{\parallel\perp}$), out of plane ($B_{\perp}$). The device is tuned in the tunneling regime to show the evolution of the induced superconducting gap with the strength of the magnetic field.

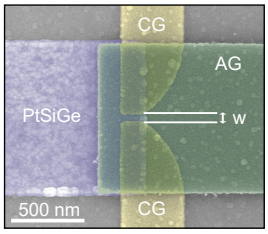

Device	*Constriction width (nm)*
1	25
2	25
3	50
4	50
5	50
6	75

Figure 9.13: **NS-QPCs devices specifications.** False-color SEM image of a normal-superconductor quantum point contact device (NS-QPC). The PtSiGe contact is violet, the constriction gates (CG) are yellow and the accumulation gate (AG) is green. The constriction width (w) between the two CGs is varied across the 6 measured devices and is reported in the table. The 6 devices were fabricated in the same fabrication run.

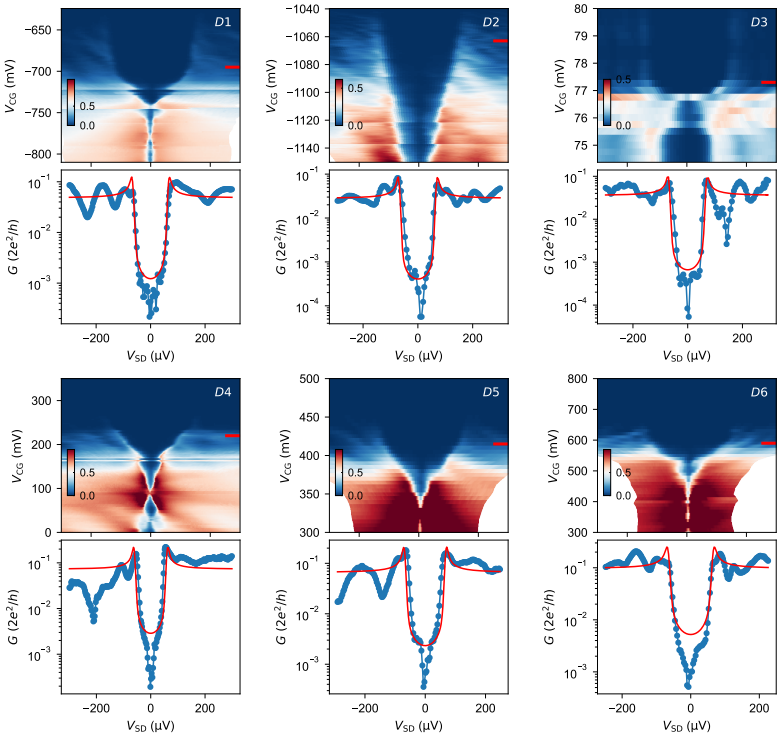

Figure 9.14: **Conductance maps of 6 NS-QPC devices.** Color map of G in units of $2e^2/h$ vs. the source-drain voltage V_{SD} and constriction gate V_{CG}, for the 6 NS-QPC devices presented in the main text, along with the conductance line-cuts presented in Fig. 3d main text. The red segment in the color maps indicates the V_{CG} of each linecut. Fits of the conductance linecuts to the BTK model [54] (red lines) are consistent with a hard induced superconducting gap. Variation on the V_{CG} operational window can be ascribed both to the different constriction gate size and to the accumulation gate voltage used for the specific measurement. The different evolution of G as a function of V_{CG} can also be related to the different accumulation gate voltages.

9.9.5. SQUID MEASUREMENTS

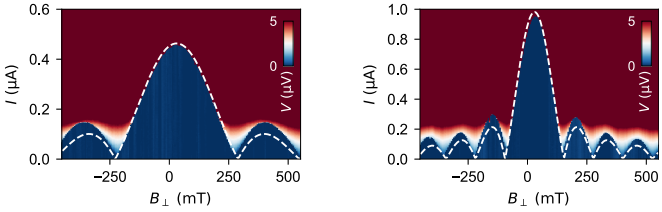

Figure 9.15: **JoFETs Fraunhofer pattern for the SQUID device.** Fraunhofer pattern of the small junction ($JoFET_2$, left panel) and large junction ($JoFET_1$, right panel) of the SQUID device. White dashed line represents the fitting of the switching current to the theoretical Fraunhofer formula.

We measured the Fraunhofer pattern for each junction of the SQUID device independently by measuring the dependence of its critical current on the out-of-plane mag-

netic field while the gate voltage of the measured junction is set to −3.5 V and the other junction is pinched-off. By fitting the obtained dependencies $I_{c1,2}(\Phi_{1,2})$ as $I_{c1,2}(BA_{1,2}) = I_{c01,2}\sin(\pi BA_{1,2}/\Phi_0)/(\pi BA_{1,2}/\Phi_0)$, where B is the out-of-plane magnetic field and Φ_0 is superconducting flux quantum, we obtain from the fits the areas of the two junctions to be $A_1 = 1\,\mathrm{um}^2$ and $A_2 = 0.48\,\mathrm{um}^2$. Note that the ratio $A_1/A_2 \sim 2$, as designed and shown in Fig. 4a, while the values for both areas are smaller than the geometrical areas in the design due to the flux focusing effects.

9.9.6. 1D ARRAY

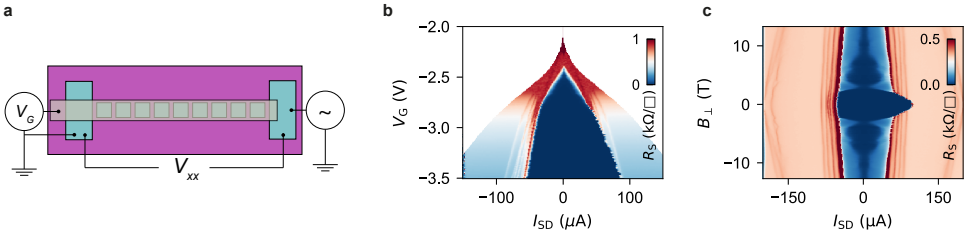

Figure 9.16: **1D PtSiGe superconducting array. a**) Top view schematics of an array of 51 × 1 PtSiGe islands on a Ge/SiGe heterostructure. The PtSiGe islands are 930 × 930 nm wide and the separation between the PtSiGe islands is of 70 nm. **b**) Color map of the sheet resistance (R_S) vs accumulation gate voltage V_G and source-drain current I_{SD}. Increasing the negative voltage of the accumulation gate the array becomes superconducting (R_S goes to zero) when the source-drain current is below the switching current. **c**) Color map of the sheet resistance vs out-of-plane magnetic field $B_\perp$ and source-drain current I_{SD}. The switching current shows the typical Fraunhofer pattern expected for a single Josephson junction. Compared to the 2D PtSiGe array this device does not present any signature of commensurability effects in the switching current, as expected for a linear array.

9.9.7. KEY METRICS

Semiconductor	Superconductor	μ ($\times 10^3$ cm^2/Vs)	$\hbar/2\tau$ (μeV)	Δ^* (μeV)	l_{SO} (nm)	g^*	T_1 (ms)	T_2^* (ns)	1Q gate fidelity (%)
Ge/SiGe, 2D	PtSiGe	615	10	70	76	0.76-15	32	833	99.99
InSb, nw	Al	44	940	250	100	26-51	na	8	na
InAs, nw	Al	25	890	270	60	8	0.001	8	na
	Pb			1250					
InAs, 2D	Al	60	370	190	45	10	na	na	na
InSbAs, 2D	Al	28	1200	220	60	55	na	na	na

Table 9.1: Comparison of key metrics for building quantum information processing devices based on topological or spin-qubit systems. We consider only systems where a hard hap is assessed via NS spectroscopy, the most reliable measurement for verifying the absence of subgap states. From left to right, columns indicate: the semiconductor system and whether it is a planar heterostructures (2D) or a nanowire (nw); the superconductor material used to proximitize the semiconductor; maximum carrier mobility (μ), typically Hall mobility in 2D systems and estimated field effect mobility in nanowires; the disorder quantified by the transport level broadening ($\hbar/2\tau$, where τ is the elastic scattering time)[36]; maximum induced superconducting gap (Δ^*); spin-orbit length (l_{SO}); g-factor (g^*), the range can be large when the g-factor is strongly anisotropic; longest relaxation time (T_1) measured in a spin qubit, longest dephasing time (T_2^*) measured in a spin-qubit; largest measured 1 qubit gate fidelity (1Q gate fidelity). The metrics reported in this table are reported from the references below as following. Ge/SiGe, 2D: μ from this work; $\hbar/2\tau$ calculated using $m^* = 0.09$ [24]; Ge/SiGe-PtSiGe Δ^* from this work; $l_{SO} = 76$ nm (corresponding to a spin-orbit energy of 2.2 meV) follows from the cubic Rashba coefficient α_3 reported in ref. [69] at a density of 6.1×10^{11} cm^{-2}, for which we assume an effective mass of 0.09 [35]; g^* [70]; T_1 [71]; T_2^* [20]; 1Q gate fidelity [72]. InSb, nw: μ [73]; $\hbar/2\tau$ calculated using $m^* = 0.014$ [74]; InSb-Al Δ^* [75]; l_{SO} [76]; g^* [77]; T_2^* [78].; 1Q gate fidelity. InAs nw: μ [79]; $\hbar/2\tau$ calculated using $m^* = 0.0026$ [74]; InAs-Pb Δ^* [80]; InAs-Al Δ^* [81]; l_{SO} [82]; g^* [79]; T_1 [83]; T_2^* [84]. InAs 2D: μ [85], $\hbar/2\tau$ calculated using $m^* = 0.026$ [74], InAs-Al Δ^* [12], l_{SO} [40, 12], g^* [12]. InSbAs 2D: μ [86], $\hbar/2\tau$ calculated using $m^* = 0.018$ [86], Δ^* [86], l_{SO} [86], g^* [86].

In Supplementary Table 9.1 we present a comparison of key metrics for material systems for hybrid superconductor-semiconductor applications. Given that in this paper the main focus is on applications that require the presence of a hard gap, we limit the table only to semiconductor-superconductor material systems with a hard gap assessed via NS spectroscopy, which is a reliable measurement for verifying the absence of subgap states.

On the first half of Supplementary Table 9.1 we present the typical values for different platforms for (peak) mobility (μ), disorder quantified by the transport level broadening ($\hbar/2\tau$, where τ is the elastic scattering time), size of induced superconducting gap (Δ^*), spin orbit length (l_{SO}) and g-factor (g^*), important metrics for accessing the topological phase. On the second half of Supplementary Table 9.1 we illustrate the metrics that are significant for control and operation of spin qubits: relaxation time (T_1), dephasing time (T_2^*) and 1 qubit gate fidelity (1Q gate fidelity). For a comprehensive review of performance metrics of spin qubits in gated semiconducting nanostructures see ref. [17]. While III/V materials benefit from a larger induced superconducting gap and g-factor, planar Ge proximitized by PtSiGe stands out for the exceptionally low disorder (quantified by the high μ and low $\hbar/2\tau$), which is necessary for the emergence of topological Majorana zero modes [36]. In line with the remarks made in the introductory section, planar Ge also shows excellent spin qubit metrics. This comparison positions Ge/SiGe-PtGeSi as a compelling platform for topological devices, where small disorder is neces-

sary to preserve the topological gap ($\delta_\tau > \frac{\hbar}{2\tau}$, where δ_τ is the topological gap and and for hybrid devices, were we envision the coupling of spins via cross Andreev reflection mechanisms, Andreev spin qubits, and the co-integration of spins, topological, and superconducting qubits.

BIBLIOGRAPHY

[1] R. M. Lutchyn, E. P. Bakkers, L. P. Kouwenhoven, P. Krogstrup, C. M. Marcus, and Y. Oreg. "Majorana zero modes in superconductor-semiconductor heterostructures". In: *Nature Reviews Materials* 3.5 (May 2018), pp. 52–68. ISSN: 20588437.

[2] K. Flensberg, F. von Oppen, and A. Stern. "Engineered platforms for topological superconductivity and Majorana zero modes". en. In: *Nature Reviews Materials* 6.10 (Oct. 2021), pp. 944–958. ISSN: 2058-8437.

[3] M. Hays, V. Fatemi, D. Bouman, J. Cerrillo, S. Diamond, K. Serniak, T. Connolly, P. Krogstrup, J. Nygård, A. Levy Yeyati, A. Geresdi, and M. H. Devoret. "Coherent manipulation of an Andreev spin qubit". en. In: *Science* 373.6553 (July 2021), pp. 430–433. ISSN: 0036-8075, 1095-9203.

[4] L. Casparis, M. R. Connolly, M. Kjaergaard, N. J. Pearson, A. Kringhøj, T. W. Larsen, F. Kuemmeth, T. Wang, C. Thomas, S. Gronin, G. C. Gardner, M. J. Manfra, C. M. Marcus, and K. D. Petersson. "Superconducting gatemon qubit based on a proximitized two-dimensional electron gas". In: *Nature Nanotechnology* 13.10 (2018), pp. 915–919. ISSN: 17483395.

[5] M.-S. Choi, C. Bruder, and D. Loss. "Spin-dependent Josephson current through double quantum dots and measurement of entangled electron states". In: *Physical Review B* 62.20 (Nov. 2000), pp. 13569–13572.

[6] M. Leijnse and K. Flensberg. "Quantum information transfer between topological and spin qubit systems". In: *Physical Review Letters* 107.21 (2011), p. 210502. ISSN: 00319007.

[7] M. Leijnse and K. Flensberg. "Hybrid topological-spin qubit systems for two-qubit-spin gates". In: *Physical Review B - Condensed Matter and Materials Physics* 86.10 (2012), p. 104511. ISSN: 10980121.

[8] S. Hoffman, C. Schrade, J. Klinovaja, and D. Loss. "Universal quantum computation with hybrid spin-Majorana qubits". In: *Physical Review B* 94.4 (July 2016), p. 045316.

[9] M. Leijnse and K. Flensberg. "Coupling spin qubits via superconductors". In: *Physical Review Letters* 111.6 (2013), p. 060501. ISSN: 00319007.

[10] A. Y. Kitaev. "Unpaired Majorana fermions in quantum wires". In: *Physics-Uspekhi* 44.10S (2001), pp. 131–136. ISSN: 1063-7869.

[11] W. Chang, S. M. Albrecht, T. S. Jespersen, F. Kuemmeth, P. Krogstrup, J. Nygård, and C. M. Marcus. "Hard gap in epitaxial semiconductor-superconductor nanowires". In: *Nature Nanotechnology* 10.3 (Mar. 2015), pp. 232–236. ISSN: 17483395.

[12] M. Kjaergaard, F. Nichele, H. J. Suominen, M. P. Nowak, M. Wimmer, A. R. Akhmerov, J. A. Folk, K. Flensberg, J. Shabani, C. J. Palmstrøm, and C. M. Marcus. "Quantized conductance doubling and hard gap in a two-dimensional semiconductor-superconductor heterostructure". In: *Nature Communications* 7 (2016), pp. 1–6. ISSN: 20411723.

[13] A. Fornieri, A. M. Whiticar, F. Setiawan, E. Portolés, A. C. C. Drachmann, A. Keselman, S. Gronin, C. Thomas, T. Wang, R. Kallaher, G. C. Gardner, E. Berg, M. J. Manfra, A. Stern, C. M. Marcus, and F. Nichele. "Evidence of topological superconductivity in planar Josephson junctions". en. In: *Nature* 569.7754 (May 2019), pp. 89–92. ISSN: 1476-4687.

[14] M. Aghaee, A. Akkala, Z. Alam, R. Ali, A. Alcaraz Ramirez, M. Andrzejczuk, A. E. Antipov, P. Aseev, M. Astafev, B. Bauer, et al. "InAs-Al hybrid devices passing the topological gap protocol". In: *Physical Review B* 107.24 (2023), p. 245423.

[15] T. Dvir, G. Wang, N. van Loo, C.-X. Liu, G. P. Mazur, A. Bordin, S. L. D. t. Haaf, J.-Y. Wang, D. van Driel, F. Zatelli, X. Li, F. K. Malinowski, S. Gazibegovic, G. Badawy, E. P. A. M. Bakkers, M. Wimmer, and L. P. Kouwenhoven. *Realization of a minimal Kitaev chain in coupled quantum dots*. arXiv:2206.08045 [cond-mat]. June 2022.

[16] Ł. Cywiński, W. M. Witzel, and S. Das Sarma. "Electron spin dephasing due to hyperfine interactions with a nuclear spin bath". In: *Physical Review Letters* 102.5 (2009), pp. 1–4. ISSN: 00319007.

[17] P. Stano and D. Loss. "Review of performance metrics of spin qubits in gated semiconducting nanostructures". en. In: *Nature Reviews Physics* 4.10 (Oct. 2022), pp. 672–688. ISSN: 2522-5820.

[18] G. Scappucci, C. Kloeffel, F. A. Zwanenburg, D. Loss, M. Myronov, J. J. Zhang, S. De Franceschi, G. Katsaros, and M. Veldhorst. "The germanium quantum information route". In: *Nature Reviews Materials* 6.10 (Dec. 2020), pp. 926–943. ISSN: 20588437.

[19] H. Watzinger, J. Kukučka, L. Vukušić, F. Gao, T. Wang, F. Schäffler, J. J. Zhang, and G. Katsaros. "A germanium hole spin qubit". In: *Nature Communications* 9.1 (Dec. 2018), pp. 1–6. ISSN: 20411723.

[20] N. W. Hendrickx, D. P. Franke, A. Sammak, G. Scappucci, and M. Veldhorst. "Fast two-qubit logic with holes in germanium". In: *Nature* 577.7791 (2020), pp. 487–491. ISSN: 14764687.

[21] D. Jirovec, A. Hofmann, A. Ballabio, P. M. Mutter, G. Tavani, M. Botifoll, A. Crippa, J. Kukucka, O. Sagi, F. Martins, J. Saez-Mollejo, I. Prieto, M. Borovkov, J. Arbiol, D. Chrastina, G. Isella, and G. Katsaros. "A singlet-triplet hole spin qubit in planar Ge". In: *Nature Materials* 20.8 (June 2021), pp. 1106–1112. ISSN: 14764660.

[22] J. H. Prechtel, A. V. Kuhlmann, J. Houel, A. Ludwig, S. R. Valentin, A. D. Wieck, and R. J. Warburton. "Decoupling a hole spin qubit from the nuclear spins". In: *Nature Materials* 15.9 (July 2016), pp. 981–986. ISSN: 14764660.

[23] K. M. Itoh and H. Watanabe. "Isotope engineering of silicon and diamond for quantum computing and sensing applications". In: *MRS Communications* 4.4 (Sept. 2014), pp. 143–157. ISSN: 21596867.

[24] M. Lodari, A. Tosato, D. Sabbagh, M. A. Schubert, G. Capellini, A. Sammak, M. Veldhorst, and G. Scappucci. "Light effective hole mass in undoped Ge/SiGe quantum wells". In: *Physical Review B* 100.4 (2019). ISSN: 24699969.

[25] M. Lodari, O. Kong, M. Rendell, A. Tosato, A. Sammak, M. Veldhorst, A. R. Hamilton, and G. Scappucci. "Lightly strained germanium quantum wells with hole mobility exceeding one million". In: *Applied Physics Letters* 120.12 (Mar. 2022), p. 122104. ISSN: 0003-6951.

[26] N. W. Hendrickx, W. I. Lawrie, M. Russ, F. van Riggelen, S. L. de Snoo, R. N. Schouten, A. Sammak, G. Scappucci, and M. Veldhorst. "A four-qubit germanium quantum processor". In: *Nature* 591.7851 (2021), pp. 580–585. ISSN: 14764687.

[27] F. Borsoi, N. W. Hendrickx, V. John, S. Motz, F. van Riggelen, A. Sammak, S. L. de Snoo, G. Scappucci, and M. Veldhorst. "Shared control of a 16 semiconductor quantum dot crossbar array". In: *Preprint at https://arxiv.org/abs/2209.06609* (Sept. 2022).

[28] A. Dimoulas, P. Tsipas, A. Sotiropoulos, and E. K. Evangelou. "Fermi-level pinning and charge neutrality level in germanium". In: *Applied Physics Letters* 89.25 (Dec. 2006), p. 252110. ISSN: 00036951.

[29] N. W. Hendrickx, D. P. Franke, A. Sammak, M. Kouwenhoven, D. Sabbagh, L. Yeoh, R. Li, M. L. Tagliaferri, M. Virgilio, G. Capellini, G. Scappucci, and M. Veldhorst. "Gate-controlled quantum dots and superconductivity in planar germanium". In: *Nature Communications* 9.1 (Dec. 2018), p. 2835. ISSN: 20411723.

[30] N. W. Hendrickx, M. L. Tagliaferri, M. Kouwenhoven, R. Li, D. P. Franke, A. Sammak, A. Brinkman, G. Scappucci, and M. Veldhorst. "Ballistic supercurrent discretization and micrometer-long Josephson coupling in germanium". In: *Physical Review B* 99.7 (2019), pp. 7–9. ISSN: 24699969.

[31] J. Ridderbos, M. Brauns, F. K. De Vries, J. Shen, A. Li, S. Kölling, M. A. Verheijen, A. Brinkman, W. G. Van Der Wiel, E. P. A. M. Bakkers, and F. A. Zwanenburg. "Hard Superconducting Gap and Diffusion-Induced Superconductors in Ge–Si Nanowires". en. In: *Nano Letters* 20.1 (Jan. 2020), pp. 122–130. ISSN: 1530-6984, 1530-6992.

[32] F. Vigneau, R. Mizokuchi, D. C. Zanuz, X. Huang, S. Tan, R. Maurand, S. Frolov, A. Sammak, G. Scappucci, F. Lefloch, and S. De Franceschi. "Germanium Quantum-Well Josephson Field-Effect Transistors and Interferometers". In: *Nano Letters* 19.2 (2019), pp. 1023–1027. ISSN: 15306992.

[33] K. Aggarwal, A. Hofmann, D. Jirovec, I. Prieto, A. Sammak, M. Botifoll, S. Martí-Sánchez, M. Veldhorst, J. Arbiol, G. Scappucci, J. Danon, and G. Katsaros. "Enhancement of proximity-induced superconductivity in a planar Ge hole gas". In: *Physical Review Research* 3.2 (2021), p. L022005. ISSN: 26431564.

[34] J. A. Kittl, K. Opsomer, C. Torregiani, C. Demeurisse, S. Mertens, D. P. Brunco, M. J. Van Dal, and A. Lauwers. "Silicides and germanides for nano-CMOS applications". In: *Materials Science and Engineering B* 154.1-3 (Dec. 2008), pp. 144–154. ISSN: 09215107.

[35] A. Sammak, D. Sabbagh, N. W. Hendrickx, M. Lodari, B. Paquelet Wuetz, A. Tosato, L. Yeoh, M. Bollani, M. Virgilio, M. A. Schubert, P. Zaumseil, G. Capellini, M. Veldhorst, and G. Scappucci. "Shallow and Undoped Germanium Quantum Wells: A Playground for Spin and Hybrid Quantum Technology". In: *Advanced Functional Materials* 29.14 (2019), p. 1807613. ISSN: 1616301X.

[36] S. Ahn, H. Pan, B. Woods, T. D. Stanescu, and S. D. Sarma. "Estimating disorder and its adverse effects in semiconductor Majorana nanowires". In: *Physical Review Materials* 5 (2021), p. 124602. ISSN: 24759953.

[37] L. M. K. Vandersypen, H. Bluhm, J. S. Clarke, A. S. Dzurak, R. Ishihara, A. Morello, D. J. Reilly, L. R. Schreiber, and M. Veldhorst. "Interfacing spin qubits in quantum dots and donors — hot , dense , and coherent". In: *npj Quantum Information* December 2016 (2017), pp. 1–10. ISSN: 2056-6387.

[38] S. Gaudet, C. Detavernier, A. J. Kellock, P. Desjardins, and C. Lavoie. "Thin film reaction of transition metals with germanium". In: *Journal of Vacuum Science & Technology A: Vacuum, Surfaces, and Films* 24.3 (2006), pp. 474–485. ISSN: 0734-2101.

[39] C. J. Raub, W. H. Zachariasen, T. H. Geballe, and B. T. Matthias. "Superconductivity of some new Pt-metal compounds". en. In: *Journal of Physics and Chemistry of Solids* 24.9 (Sept. 1963), pp. 1093–1100. ISSN: 0022-3697.

[40] J. Shabani, M. Kjaergaard, H. J. Suominen, Y. Kim, F. Nichele, K. Pakrouski, T. Stankevic, R. M. Lutchyn, P. Krogstrup, R. Feidenhans'L, S. Kraemer, C. Nayak, M. Troyer, C. M. Marcus, and C. J. Palmstrøm. "Two-dimensional epitaxial superconductor-semiconductor heterostructures: A platform for topological superconducting networks". In: *Physical Review B* 93.15 (2016), pp. 1–6. ISSN: 24699969.

[41] E. Alptekin, C. J. Kirkpatrick, V. Misra, and M. C. Ozturk. "Platinum germanosilicide contacts formed on strained and relaxed Si1-xGex layers". In: *IEEE Transactions on Electron Devices* 56.6 (2009), pp. 1220–1227. ISSN: 00189383.

[42] H. Irie, Y. Harada, H. Sugiyama, and T. Akazaki. "Josephson coupling through one-dimensional ballistic channel in semiconductor-superconductor hybrid quantum point contacts". In: *Physical Review B - Condensed Matter and Materials Physics* 89.16 (2014), pp. 1–6. ISSN: 1550235X.

[43] V. Ambegaokar and A. Baratoff. "Tunneling between superconductors". In: *Physical Review Letters* 10.11 (1963), p. 486.

[44] S. Heedt, M. Quintero-Pérez, F. Borsoi, A. Fursina, N. van Loo, G. P. Mazur, M. P. Nowak, M. Ammerlaan, K. Li, S. Korneychuk, J. Shen, M. A. Y. van de Poll, G. Badawy, S. Gazibegovic, N. de Jong, P. Aseev, K. van Hoogdalem, E. P. Bakkers, and L. P. Kouwenhoven. "Shadow-wall lithography of ballistic superconductor–semiconductor quantum devices". In: *Nature Communications* 12.1 (2021), pp. 1–9. ISSN: 20411723.

[45] M. Tinkham. *Introduction to superconductivity*. eng. 2nd ed. OCLC: 853663851. Mineola, N.Y.: Dover Publications, 2004. ISBN: 9781621985983.

[46] M. Octavio, M. Tinkham, G. E. Blonder, and T. M. Klapwijk. “Subharmonic energy-gap structure in superconducting constrictions”. In: *Physical Review B* 27.11 (1983), pp. 6739–6746. ISSN: 01631829.

[47] M. Kjaergaard, H. J. Suominen, M. P. Nowak, A. R. Akhmerov, J. Shabani, C. J. Palmstrøm, F. Nichele, and C. M. Marcus. “Transparent Semiconductor-Superconductor Interface and Induced Gap in an Epitaxial Heterostructure Josephson Junction”. In: *Physical Review Applied* 7.3 (2017), p. 034029. ISSN: 23317019.

[48] D. Averin and A. Bardas. “ac Josephson effect in a single quantum channel”. In: *Physical Review Letters* 75.9 (1995), pp. 1831–1834. ISSN: 00319007.

[49] F. Borsoi, G. P. Mazur, N. van Loo, M. P. Nowak, L. Bourdet, K. Li, S. Korneychuk, A. Fursina, J.-Y. Wang, V. Levajac, E. Memisevic, G. Badawy, S. Gazibegovic, K. van Hoogdalem, E. P. A. M. Bakkers, L. P. Kouwenhoven, S. Heedt, and M. Quintero-Pérez. “Single-Shot Fabrication of Semiconducting–Superconducting Nanowire Devices”. In: *Advanced Functional Materials* 31.34 (June 2021), p. 2102388. ISSN: 1616-301X.

[50] A. Fornieri, A. M. Whiticar, F. Setiawan, E. Portolés, A. C. Drachmann, A. Keselman, S. Gronin, C. Thomas, T. Wang, R. Kallaher, G. C. Gardner, E. Berg, M. J. Manfra, A. Stern, C. M. Marcus, and F. Nichele. “Evidence of topological superconductivity in planar Josephson junctions”. In: *Nature* 569.7754 (2019), pp. 89–92. ISSN: 14764687.

[51] H. A. Nilsson, P. Samuelsson, P. Caroff, and H. Q. Xu. “Supercurrent and Multiple Andreev Reflections in an InSb Nanowire Josephson Junction”. In: *Nano Lett* 12 (2012), p. 233.

[52] N. van Loo, G. P. Mazur, T. Dvir, G. Wang, R. C. Dekker, J.-Y. Wang, M. Lemang, C. Sfiligoj, A. Bordin, D. van Driel, G. Badawy, S. Gazibegovic, E. P. A. M. Bakkers, and L. P. Kouwenhoven. *Electrostatic control of the proximity effect in the bulk of semiconductor-superconductor hybrids*. arXiv:2211.06709 [cond-mat]. Nov. 2022.

[53] M. W. De Moor, J. D. Bommer, D. Xu, G. W. Winkler, A. E. Antipov, A. Bargerbos, G. Wang, N. V. Loo, R. L. Op Het Veld, S. Gazibegovic, D. Car, J. A. Logan, M. Pendharkar, J. S. Lee, E. P. M Bakkers, C. J. Palmstrom, R. M. Lutchyn, L. P. Kouwenhoven, and H. Zhang. “Electric field tunable superconductor-semiconductor coupling in Majorana nanowires”. In: *New Journal of Physics* 20.10 (Oct. 2018), p. 103049. ISSN: 13672630.

[54] G. E. Blonder, M. Tinkham, and T. M. Klapwijk. “Transition from metallic to tunneling regimes in superconducting microconstrictions: Excess current, charge imbalance, and supercurrent conversion”. In: *Physical Review B* 25.7 (1982), pp. 4515–4532. ISSN: 01631829.

[55] F. Pientka, A. Keselman, E. Berg, A. Yacoby, A. Stern, and B. I. Halperin. “Topological superconductivity in a planar Josephson junction”. In: *Physical Review X* 7.2 (2017), pp. 1–17. ISSN: 21603308.

[56] H. Ren, F. Pientka, S. Hart, A. T. Pierce, M. Kosowsky, L. Lunczer, R. Schlereth, B. Scharf, E. M. Hankiewicz, L. W. Molenkamp, B. I. Halperin, and A. Yacoby. "Topological superconductivity in a phase-controlled Josephson junction". In: *Nature* 569.7754 (Apr. 2019), pp. 93–98. ISSN: 14764687.

[57] M. Luethi, K. Laubscher, S. Bosco, D. Loss, and J. Klinovaja. *Planar Josephson junctions in germanium: Effect of cubic spin-orbit interaction.* arXiv:2209.12745 [cond-mat]. Sept. 2022.

[58] N. Poccia, T. I. Baturina, F. Coneri, C. G. Molenaar, X. R. Wang, G. Bianconi, A. Brinkman, H. Hilgenkamp, A. A. Golubov, and V. M. Vinokur. "Critical behavior at a dynamic vortex insulator-to-metal transition". In: *Science* 349.6253 (Sept. 2015), pp. 1202–1205. ISSN: 10959203.

[59] C. G. Bøttcher, F. Nichele, M. Kjaergaard, H. J. Suominen, J. Shabani, C. J. Palmstrøm, and C. M. Marcus. "Superconducting, insulating and anomalous metallic regimes in a gated two-dimensional semiconductor–superconductor array". In: *Nature Physics* 14.11 (2018), pp. 1138–1144. ISSN: 17452481.

[60] B. T. Matthias, T. H. Geballe, and V. B. Compton. "Superconductivity". en. In: *Reviews of Modern Physics* 35.1 (Jan. 1963), pp. 1–22. ISSN: 0034-6861.

[61] M. Hell, M. Leijnse, and K. Flensberg. "Two-Dimensional Platform for Networks of Majorana Bound States". In: *Physical Review Letters* 118.10 (Mar. 2017), p. 107701.

[62] F. Pientka, A. Keselman, E. Berg, A. Yacoby, A. Stern, and B. I. Halperin. "Topological Superconductivity in a Planar Josephson Junction". en. In: *Physical Review X* 7.2 (May 2017), p. 021032. ISSN: 2160-3308.

[63] G. Burkard, M. J. Gullans, X. Mi, and J. R. Petta. "Superconductor–semiconductor hybrid-circuit quantum electrodynamics". In: *Nature Reviews Physics* 2.3 (2020), pp. 129–140. ISSN: 25225820.

[64] N. M. Chtchelkatchev and Y. V. Nazarov. "Andreev Quantum Dots for Spin Manipulation". In: *Physical Review Letters* 90.22 (June 2003), p. 226806.

[65] C. Padurariu and Y. V. Nazarov. "Theoretical proposal for superconducting spin qubits". In: *Physical Review B* 81.14 (Apr. 2010), p. 144519.

[66] M. Pita-Vidal, A. Bargerbos, R. Žitko, L. J. Splitthoff, L. Grünhaupt, J. J. Wesdorp, Y. Liu, L. P. Kouwenhoven, R. Aguado, B. van Heck, A. Kou, and C. K. Andersen. *Direct manipulation of a superconducting spin qubit strongly coupled to a transmon qubit.* arXiv:2208.10094 [cond-mat, physics:quant-ph]. Aug. 2022.

[67] M. Spethmann, X.-P. Zhang, J. Klinovaja, and D. Loss. "Coupled superconducting spin qubits with spin-orbit interaction". In: *Physical Review B* 106.11 (Sept. 2022). arXiv:2205.03843 [cond-mat, physics:quant-ph], p. 115411. ISSN: 2469-9950, 2469-9969.

[68] M. P. Nowak, M. Wimmer, and A. R. Akhmerov. "Supercurrent carried by nonequilibrium quasiparticles in a multiterminal Josephson junction". In: *Physical Review B* 99.7 (2019), p. 075416. ISSN: 24699969.

[69] P. Del Vecchio, M. Lodari, A. Sammak, G. Scappucci, and O. Moutanabbir. "Vanishing Zeeman energy in a two-dimensional hole gas". In: *Physical Review B* 102.11 (2020), p. 115304. ISSN: 24699969.

[70] R. Mizokuchi, R. Maurand, F. Vigneau, M. Myronov, and S. De Franceschi. "Ballistic One-Dimensional Holes with Strong g-Factor Anisotropy in Germanium". In: *Nano Letters* 18.8 (2018), pp. 4861–4865. ISSN: 15306992.

[71] W. I. Lawrie, H. G. Eenink, N. W. Hendrickx, J. M. Boter, L. Petit, S. V. Amitonov, M. Lodari, B. Paquelet Wuetz, C. Volk, S. G. Philips, G. Droulers, N. Kalhor, F. Van Riggelen, D. Brousse, A. Sammak, L. M. Vandersypen, G. Scappucci, and M. Veldhorst. "Quantum dot arrays in silicon and germanium". In: *Applied Physics Letters* 116.8 (2020), p. 80501. ISSN: 00036951.

[72] W. I. L. Lawrie, M. Russ, F. van Riggelen, N. W. Hendrickx, S. L. de Snoo, A. Sammak, G. Scappucci, and M. Veldhorst. "Simultaneous driving of semiconductor spin qubits at the fault-tolerant threshold". In: *Preprint at https://arxiv.org/abs/2109.07837* (2021).

[73] G. Badawy, S. Gazibegovic, F. Borsoi, S. Heedt, C. A. Wang, S. Koelling, M. A. Verheijen, L. P. Kouwenhoven, and E. P. Bakkers. "High Mobility Stemless InSb Nanowires". In: *Nano Letters* 19.6 (June 2019), pp. 3575–3582. ISSN: 15306992.

[74] Y.-S. Kim, K. Hummer, and G. Kresse. "Accurate band structures and effective masses for InP, InAs, and InSb using hybrid functionals". In: *Physical Review B* 80.3 (2009), p. 035203.

[75] R. L. Op het Veld, D. Xu, V. Schaller, M. A. Verheijen, S. M. Peters, J. Jung, C. Tong, Q. Wang, M. W. de Moor, B. Hesselmann, K. Vermeulen, J. D. Bommer, J. Sue Lee, A. Sarikov, M. Pendharkar, A. Marzegalli, S. Koelling, L. P. Kouwenhoven, L. Miglio, C. J. Palmstrøm, H. Zhang, and E. P. Bakkers. "In-plane selective area InSb–Al nanowire quantum networks". In: *Communications Physics* 3.1 (Mar. 2020), pp. 1–7. ISSN: 23993650.

[76] I. Van Weperen, B. Tarasinski, D. Eeltink, V. S. Pribiag, S. R. Plissard, E. P. Bakkers, L. P. Kouwenhoven, and M. Wimmer. "Spin-orbit interaction in InSb nanowires". In: *Physical Review B - Condensed Matter and Materials Physics* 91.20 (2015), pp. 1–5. ISSN: 1550235X.

[77] F. Qu, J. Van Veen, F. K. De Vries, A. J. Beukman, M. Wimmer, W. Yi, A. A. Kiselev, B. M. Nguyen, M. Sokolich, M. J. Manfra, F. Nichele, C. M. Marcus, and L. P. Kouwenhoven. "Quantized Conductance and Large g-Factor Anisotropy in InSb Quantum Point Contacts". In: *Nano Letters* 16.12 (Dec. 2016), pp. 7509–7513. ISSN: 15306992.

[78] J. W. Van Den Berg, S. Nadj-Perge, V. S. Pribiag, S. R. Plissard, E. P. Bakkers, S. M. Frolov, and L. P. Kouwenhoven. "Fast spin-orbit qubit in an indium antimonide nanowire". In: *Physical Review Letters* 110.6 (2013). ISSN: 00319007.

[79] S. Heedt, W. Prost, J. Schubert, D. Grützmacher, and T. Schäpers. "Ballistic Transport and Exchange Interaction in InAs Nanowire Quantum Point Contacts". In: *Nano Letters* 16.5 (2016), pp. 3116–3123. ISSN: 15306992.

[80] T. Kanne, M. Marnauza, D. Olsteins, D. J. Carrad, J. E. Sestoft, J. de Bruijckere, L. Zeng, E. Johnson, E. Olsson, K. Grove-Rasmussen, and J. Nygård. "Epitaxial Pb on InAs nanowires for quantum devices". In: *Nature Nanotechnology* 16.7 (May 2021), pp. 776–781. ISSN: 17483395.

[81] M. T. Deng, S. Vaitiekenas, E. B. Hansen, J. Danon, M. Leijnse, K. Flensberg, J. Nygård, P. Krogstrup, and C. M. Marcus. "Majorana bound state in a coupled quantum-dot hybrid-nanowire system". In: *Science* 354.6319 (2016), pp. 1557–1562. ISSN: 10959203.

[82] D. Liang and X. P. Gao. "Strong tuning of rashba spin-orbit interaction in single InAs nanowires". In: *Nano Letters* 12.6 (2012), pp. 3263–3267. ISSN: 15306984.

[83] K. D. Petersson, L. W. McFaul, M. D. Schroer, M. Jung, J. M. Taylor, A. A. Houck, and J. R. Petta. "Circuit quantum electrodynamics with a spin qubit". In: *Nature* 490.7420 (Oct. 2012), pp. 380–383. ISSN: 00280836.

[84] S. Nadj-Perge, S. M. Frolov, E. P. Bakkers, and L. P. Kouwenhoven. "Spin-orbit qubit in a semiconductor nanowire". In: *Nature* 468.7327 (Dec. 2010), pp. 1084–1087. ISSN: 00280836.

[85] M. Aghaee et al. "InAs-Al Hybrid Devices Passing the Topological Gap Protocol". In: *Preprint at https://arxiv.org/pdf/2207.02472.pdf* (2021).

[86] C. M. Moehle, C. T. Ke, Q. Wang, C. Thomas, D. Xiao, S. Karwal, M. Lodari, V. Van De Kerkhof, R. Termaat, G. C. Gardner, G. Scappucci, M. J. Manfra, and S. Goswami. "InSbAs Two-Dimensional Electron Gases as a Platform for Topological Superconductivity". In: *Nano Letters* 21.23 (2021), pp. 9990–9996. ISSN: 15306992.

10

QARPET: A CROSSBAR CHIP FOR BENCHMARKING SEMICONDUCTOR SPIN QUBITS

Large-scale integration of semiconductor spin qubits into industrial quantum processors hinges on the ability to characterize the performance of quantum components at scale. While the semiconductor industry has addressed scalable testing for transistors using device matrix arrays, extending this approach to quantum dot spin qubits is challenged by their operation at sub-kelvin temperatures, in the presence of magnetic fields, and by the use of radio-frequency signals. Here, we present QARPET (Qubit-Array Research Platform for Engineering and Testing), a scalable architecture for characterizing spin qubits using a quantum dot crossbar array with sublinear scaling of interconnects. The crossbar features tightly pitched ($1\,\mu\mathrm{m}$*), individually addressable spin qubit tiles and is implemented in planar germanium, by fabricating a large device with the potential to host 1058 hole spin qubits. We focus our measurements on a patch of 40 tiles and demonstrate key device functionality at millikelvin temperature including unique tile addressability, threshold voltage and charge noise statistics, and characterisation of hole spin qubits and their coherence times in a single tile. These demonstrations pave the way for a new generation of quantum devices designed for the statistical characterisation of spin qubits and for developing automated routines for quantum dot tuning and spin qubit operation.*

This work was originally published on arxiv as: A. Tosato, A. Elsayed, F. Poggiali, L. Stehouwer, D. Costa, K. Hudson, D. Degli Esposti, G. Scappucci.

10.1. INTRODUCTION

The recent demonstration of spin qubits [1] manufactured in a modern semiconductor foundry [2] offers a promising avenue to address scalability challenges of quantum technology, by leveraging decades of technology development in the semiconductor industry. However, integrating millions of highly coherent spin qubits into a quantum processor still demands substantial industrial developments to advance material synthesis, fabrication processes, and control strategies [3, 4]. These developments depend critically on the ability to test quantum components at scale for yield and performance, under environmental conditions, such as cryogenic temperatures, that differ significantly from those in which current semiconductor technology operates.

Various approaches have been explored to streamline the cryogenic testing of quantum devices, including on-chip and off-chip multiplexers [5, 6, 7, 8, 9, 10, 11, 12, 13] to improve the limited input/output connectors in existing cryostats. Alternatively, a cryogenic 300 mm wafer prober has been employed to perform low-frequency measurements on a large number of quantum dots at 1.6 K [14], offering fast feedback to optimise CMOS-compatible fabrication processes of spin qubit devices. However, none of these approaches currently provides a scalable solution for statistical measurements of spin qubits, which typically require radio-frequency (RF) measurements at millikelvin temperatures in the presence of magnetic fields.

In this article, we introduce a scalable architecture for characterising spin qubits using a quantum dot crossbar array, named QARPET (Qubit-Array Research Platform for Engineering and Testing). The crossbar is based on arrayed, individually addressable, and tightly pitched spin qubit tiles, featuring a qubit density of $2 \times 10^6\,\mathrm{mm}^{-2}$ and sublinear scaling of interconnects. This architecture draws inspiration from device matrix arrays (DMAs) widely used in the semiconductor industry as test vehicles for assessing the matching properties of transistors[15, 16, 17, 18]. DMAs enable precise characterisation of transistor threshold voltage variability within a die by measuring a large number of individual transistors through shared lines. We implement QARPET in planar germanium quantum wells [19] and fabricate a large crossbar array device of 23×23 tiles, which offers the potential to test 1058 single hole spin qubits within a single cool-down. In this first implementation, we demonstrate the unique tile addressability and the capability to acquire spin qubit device metrics, such as threshold voltages and charge noise, by using RF reflectometry at millikelvin temperatures. These measurements are extended to a statistical analysis across 40 tiles, showcasing the scalability of the approach. Importantly, we demonstrate spin control within a tile by implementing singlet-triplet qubits, operated with baseband-only control signals, and Loss-DiVincenzo single-hole qubits, driven by electric dipole spin resonance (EDSR) and characterize their coherence time.

10.2. RESULTS

10.2.1. A SCALABLE SPIN QUBIT TILE IN A CROSSBAR ARRAY

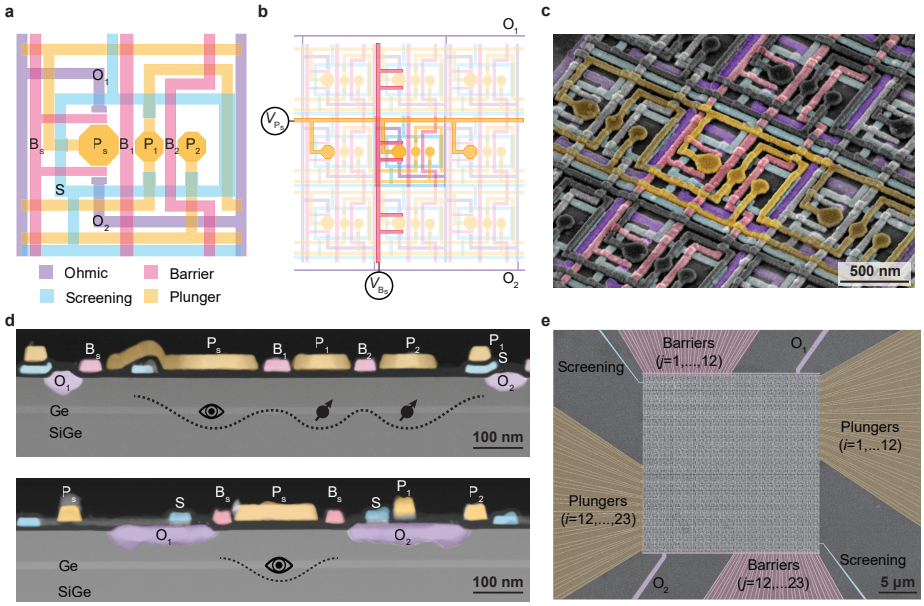

Figure 10.1: **Quantum dot spin-qubit crossbar**. **a,** Design of a scalable spin-qubit tile comprising a sensing dot and a double dot, with plunger gates (P_S, P_1, P_2), barrier gates (B_S, B_1, B_2), ohmic contacts (O_1, O_2), and a screening gate S. **b,** The tile layout, with meandering vertical plunger gates and horizontal barrier gates, allows for integration into a scalable device architecture. A single tile, e.g. the central tile in the illustrated 3×3 array, is selected for measurements by energizing the correspondent sensor plunger and barrier with gate bias V_{P_S} and V_{B_S} respectively. The reflectance measured between O_1 and O_2 will be proportional to the reflectance of the sensor in the central tile, allowing to be exclusively sensitive to the charges in the dots of the selected tile. **c,** False coloured scanning electron microscopy image highlighting a tile within a crossbar device comprising 23×23 tiles and fabricated on a Ge/SiGe heterostructure following the architecture in **a**,**b**. The colour scheme matches the schematics in panel **a**. The tile has a footprint of 1×1 µm^2, the circular plungers defining the sensor and the dots have a nominal diameter of 180 nm and 130 nm, respectively. The barriers B_1 and B_2 have a width of 60 nm and 50 nm, respectively. **d,** Transmission electron microscope images showing cross-sections of a tile within the crossbar. The top panel is along the horizontal axis of the tile, crossing the circular sensor and dot plungers. The bottom panel is along the vertical axis of the tile, crossing the sensor barriers and circular plunger. The multi-layer gate structure is fabricated on a buried 16 nm thick Ge/SiGe quantum well, positioned at 55 nm from the surface. The colour scheme and labels match the schematics in **a**. **e,** Scanning electron micrograph image showing the entire crossbar device extending over an area of 23×23 µm^2 and featuring 529 tiles arranged in a 23×23 array indexed by plunger rows i and barrier columns j. The gate electrodes and the ohmic contacts fan out at the periphery of the crossbar.

Figure 10.1a,b illustrates the design of a scalable spin qubit tile that can be arranged into an $n \times m$ crossbar array architecture. Plunger gates control the chemical potentials of the charge sensor (P_S) and of two quantum dots (P_1, P_2), while barrier gates adjust the coupling between the sensor and the ohmics (B_S), the sensor and the neighbouring dot (B_1), and between the dots (B_2). A global screening gate (S) shapes the surrounding potential landscape. Two ohmic electrodes (O_1, O_2) run vertically and merge at the edges

into a single pair of ohmic contacts for the entire crossbar, minimizing the off-chip resonators needed for RF-reflectometry. Rows of tiles share plunger gates, columns share barrier gates, and the meandering design of P_1 prevents overlaps, enabling P_s, P_1, and P_2 to be patterned in the same layer to simplify fabrication. Similarly to wordlines and bitlines in random-access memories [20, 21], a specific tile indexed (i, j) is activated and addressed by energising its P_s and B_s electrodes, which form a sensor dot sufficiently coupled to the ohmic contacts to provide a transport path. With sensor-based tile selectivity, dot plungers and barriers electrodes can be shorted across tiles, reducing the required control lines. An $n \times m$ crossbar hosting $2mn$ qubits needs only $(n + m + 7)$ lines: $(n + m)$ for B_s and P_s, seven for P_1, P_2, B_1, B_2, S, O_1, and O_2. Therefore, this architecture achieves sub-linear scaling of control lines with number of qubits, following Rent's rule with an exponent $p = 0.5$ [22, 23].

We implement this architecture in a low-disorder Ge/SiGe heterostructure on a Si wafer [24] (Methods), which was used in several spin qubit experiments [25, 26, 27, 28]. We fabricate a crossbar array of 23×23 spin qubit tiles, which can support up to 1058 individually addressable spin qubits, while requiring only 53 control lines. The fabrication process entails germanosilicide ohmic contacts to the germanium quantum well and a multi-layer gate-stack patterned by electron beam lithography and metal lift-off (Methods). The scanning electron microscope image in Fig. 10.1c provides detailed views of a tile within the crossbar. The tile footprint is 1 µm, achieved through a tightly knit fabric of nanoscale electrodes and yielding a high density of quantum dot qubits of 2×10^6 mm^{-2}. Furthermore, the tile footprint is comparable to the length scale of strain and compositional fluctuations of the heterostructure [29], making the device suitable for probing variations in quantum dot metrics arising from the underlying heterostructure.

The transmission electron microscope images from Fig. 10.1d show cross sections of a tile along the circular dot and sensor plungers direction (top panel) and, orthogonally, across the sensor plunger and barrier direction (bottom panel). These images illustrate the germanosilicide ohmic contacts to the buried germanium quantum well and the three layers of gates (screening, barriers, plungers) with dielectric in between. To electrostatically define charge sensors and quantum dots in the buried Ge quantum well, circular plunger gates are set to negative potential to accumulate holes, while barrier gates potentials are adjusted to tune the tunnel couplings between source and drain reservoirs and between the dots. The image of the entire crossbar in Fig 10.1e highlights the fanout of the nanoscale gate electrodes and ohmic contacts at the periphery of the crossbar. The realization of such QARPET chip demonstrates the viability of our approach to array dense spin-qubit tiles even without the strict process control available in an advanced semiconductor foundry.

10.2.2. CHARGE SENSOR ADDRESSABILITY AND SINGLE HOLE OCCUPANCY

We evaluate the functionality of the device at 100 mK, by measuring a subset of 40 tiles, arranged in five rows and eight columns (Methods and Supplementary Fig. 1). Tile selectivity is demonstrated using RF-reflectometry to measure sensor reflectance through the ohmic contacts, tuning the sensor of one tile at a time to a regime showing clear Coulomb blockade signatures in B_s versus P_s gate maps (Fig. 10.2a). A negative slope of the Coulomb peaks confirms that the measured reflectance corresponds to the targeted

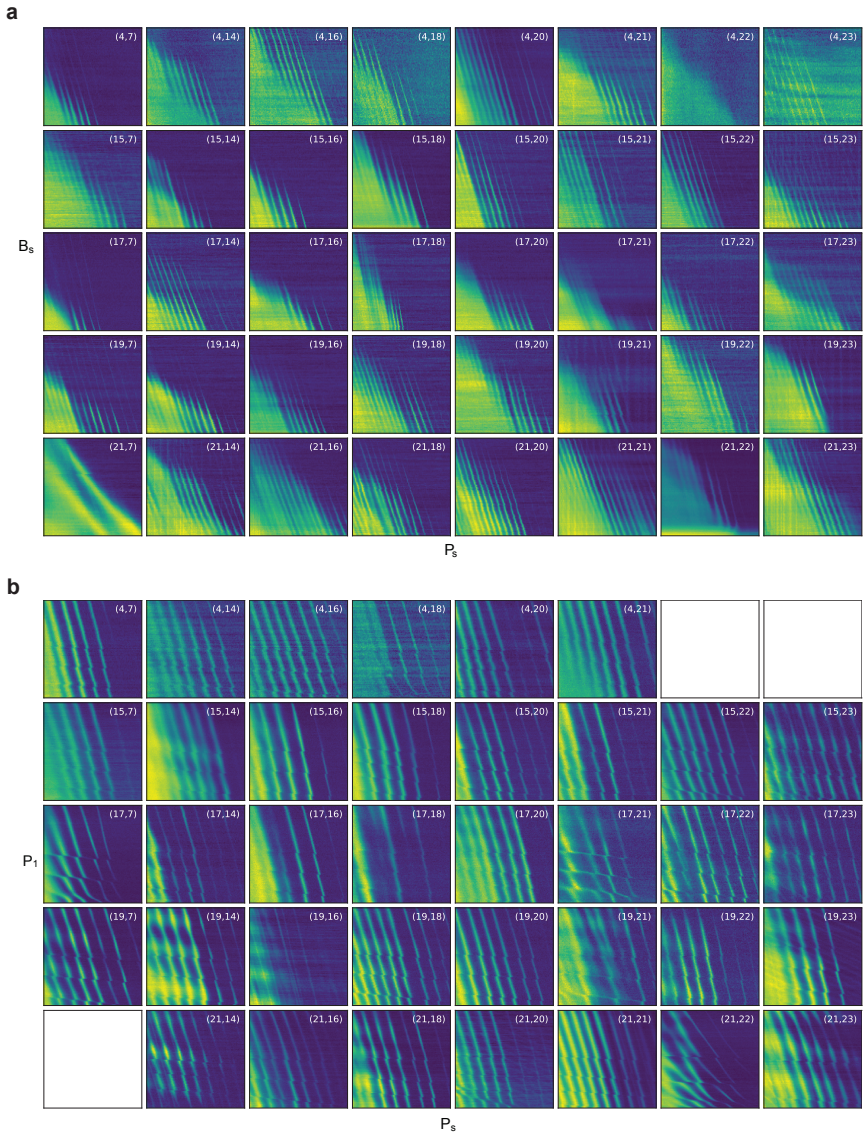

Figure 10.2: **Addressability and single hole quantum dot regime. a,** The sensor reflectance maps are measured on a QARPET device with RF reflectometry as a function of the sensor plunger (P_S) and the sensor barrier (B_S) for a subset of 40 tiles arranged in 5 rows and 8 columns of the device. The selectivity of each tile is confirmed by the observation that the sensor signal of all sensor-barrier maps presents Coulomb peaks with a negative slope. This indicates that the sensing dot is capacitively coupled to both the intended sensor plunger gate (P_S) and the sensor barrier gate (B_S). Furthermore, Coulomb blockade is observed in all tiles expect for two ([4,22] and [21,7]), indicating that the tile design is suitable for performing charge sensing. **b,** Sensor reflectance maps as a function of the sensor plunger (P_S) and the plunger of dot 1 (P_1) show charge occupation down to the last hole for the 37 tiles with a sensor that displays a clear Coulomb blockade signal.

tile. If the reflectance signal originated from another tile, vertical or horizontal Coulomb peak lines would appear. Vertical lines would indicate the signal comes from the sensor of a tile in the same row as the targeted tile, as the selected barrier gate would not affect its chemical potential, while horizontal lines would correspond to a sensor of a tile in the same column. We are able to tune the sensor of 38/40 tiles in Coulomb blockade, demonstrating single tile addressability in the dense array. These measurements also demonstrate the robustness of the RF-reflectometry approach in addressing hundreds of sensor dots connected in parallel, despite the increased parasitic capacitance.

Using charge sensing, we demonstrate quantum dots in the few-hole occupation regime, a typical condition for spin qubit operations. We focus on the occupation of the first dot (D_1) that can be directly loaded from the nearby sensing dot easing the operation. We sequentially tune D_1 to the few-hole regime in each tile by measuring charge stability diagrams of P_s versus P_1 (Fig. 10.2b) and adjusting voltages in real time, with all other gates grounded during tuning. Overall, we tune D_1 to the last hole in 37/40 tiles, with the first transition line approximately centred in each stability diagram. Only three dots failed achieving the last hole due to sensor issues, with tile (4,23) showing insufficient contrast in sensor Coulomb peaks and tiles (4,22) and (23,7) failing to reach Coulomb blockade.

10.2.3. ELECTROSTATIC VARIABILITY

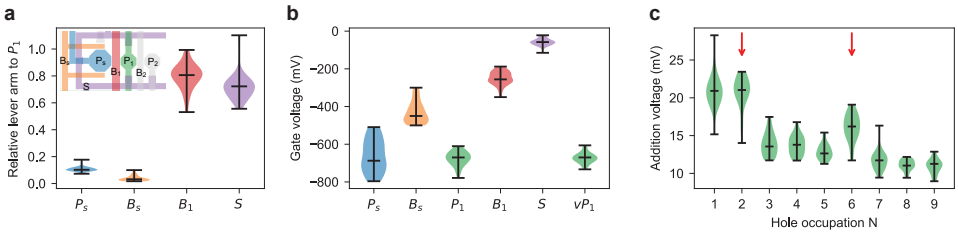

Figure 10.3: **Electrostatic variability. a,** By analysing statistical data over multiple tiles of a QARPET device such as in Fig.10.2 and Supplementary Figs 2–5, we obtain violin plots of the relative lever arm of all gates with respect to P_1. **b,** The violin plots show the distribution of voltages for the different gates whilst the last hole is reached in dot 1. We also report the values of virtual P_1 (vP_1), calculated by adding the contribution of each surrounding gate, weighted by the relative lever arm and normalized by the median value of P_1. While part of the variability of P_1 arises from the different voltages applied to the surrounding gates, vP_1 accounts for this and therefore results in a smaller variability. The variability in vP_1 can be used across different crossbar devices as a metric to benchmark, for example, improvements in the uniformity of the Ge/SiGe heterostructure. **c,** The violin plots show the distribution of the addition voltage for different hole occupations of dot 1. We observe on average a larger addition voltage for N=2 and 6 (red arrows), consistent with shell filling of circular hole quantum dots.

We investigate the electrostatic variability across the tiles by focusing on lever arms, single-hole voltages, and addition voltages related to D_1. The distributions of these metrics across different tiles reflect differences in dot shape and position, the uniformity of the semiconductor heterostructure and gate stack, and must be evaluated collectively to account for tile-specific tuning conditions.

Figure 10.3a shows the distributions of the lever arms of nearby gates (P_s, B_s, S, and

B_1) relative to D_1, divided by the lever arm of P_1 to D_1 (Methods and Supplementary Figs. 2–5) [30]. As expected from the tile design (Fig. 10.3a, inset), the chemical potential of D_1 is more influenced by the gates closest to the dot plunger (B_1 and S) and less by sensor gates (P_s and B_s) in spite of their larger dimensions. Figure 10.3b shows the distribution of voltages applied to gates within a tile for tuning D_1 to the single-hole regime. The distribution for the sensor gates has the largest standard deviation (σ_{P_s} = 86 mV, σ_{B_s} = 58 mV) compared to the other gates (e.g. σ_{P_1} = 38 mV, σ_{B_1} = 36 mV). This is expected given the manual tuning approach and the typically broad voltage range available for achieving sharp Coulomb peaks that can be used for sensing. Surprisingly, these standard deviations are smaller than what reported in industrially fabricated quantum dot devices in Si/SiGe heterostructures with highly optimized gate stacks [14], pointing to a very low level of disorder achieved with QARPET devices on Ge/SiGe heterostructures. To isolate the variability introduced by manual tuning, we calculate the virtual gate voltage vP_1 (proportional to the chemical potential of D_1, Methods) by summing the contributions of each gate weighted by its relative lever arm. We observe that the distribution width is reduced to σ_{vP_1} = 29 mV compared to σ_{P_1} = 38 mV.

In Fig. 10.3c we investigate the distribution of addition voltages across different tiles for different hole occupations. We observe on average a larger addition voltage for occupation with two and six holes (red arrows), consistent with shell filling of circular hole quantum dots [31] and absence of low-energy excited states in all the dots [32]. From the distribution, we note that the variability of addition voltage for each occupation is about 10% of its mean value, which gives an insight into the minimum expected variability of pulse amplitudes required for operating multiple qubits in a device. Comparing the median addition voltage for the first hole (~21 mV) to the distribution of P_1 voltages for the first charge transition (Fig. 10.3b), we estimate that applying the P_1 median voltage to different tiles would tune D_1 to single-hole occupation in 25% of the cases. This increases to 57% and 75% when targeting occupation up to three and five holes, respectively. Odd charge occupation different than the single-hole can be explored for robust and localized qubit control [33]. These insights provides a concrete benchmark for further materials and process optimization towards shared-control spin-qubit architectures [34].

10.2.4. CHARGE NOISE

We characterize the charge noise properties of the sensors in the multi-hole regime using the flank method [35, 24, 36, 37]. Figure 10.4a shows the obtained charge noise power spectral density S_ϵ as a function of frequency f (Methods), measured at the flank of three neighbouring Coulomb peaks (inset Fig. 10.4a) of charge occupation $(n-1)$, n, $(n+1)$ to build up statistics. We fit each spectrum with the function S_0/f^γ to obtain the charge noise $\sqrt{S_0}$ at 1 Hz (black arrow in Fig. 10.4a) and the spectral exponent γ, and iterate this protocol for all tiles under investigation (see Supplementary Figs. 6,7). The average γ is close to 1 and is not correlated to $\sqrt{S_0}$ (see Supplementary Fig. 8), suggesting that the observed $1/f$ trend results from an ensemble of two-level fluctuators with a wide range of activation energies [38, 39].

For each addressed tile (i, j), the heat map in Fig. 10.4b displays the charge noise $\sqrt{S_0}$ measured at the three subsequent charge occupations, with the specific charge oc-

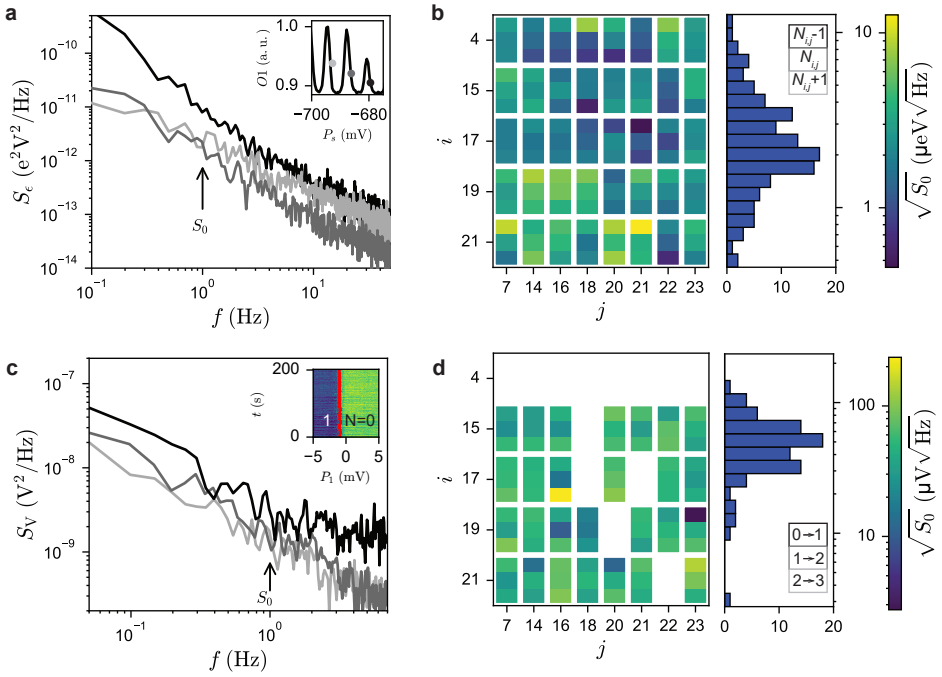

Figure 10.4: **Charge noise characterisation**. **a,** The power spectral densities S_ϵ from the three measured Coulomb flanks of the charge sensor in tile (4,16). The spectra are fitted to a S_0/f^γ dependence (Supplementary Fig.7). The inset shows the sensor reflectance at ohmic O_1 with respect to the sensor plunger P_s, showing three Coulomb peaks. with black, grey and light grey circles positioned at their flanks. **b,** Heat map of $\sqrt{S_0}$ from the 40 investigated tiles (row i, column j) within the QARPET device. Each tile in the heat map is partitioned in three to report $\sqrt{S_0}$ for increasing charge occupancy $N_{i,j}-1, N_{i,j}, N_{i,j}+1$, corresponding to measurements from subsequent Coulomb flanks. The accompanying histogram shows the overall distribution, made of the total 120 experimental $\sqrt{S_0}$ values. **c,** The voltage power spectral density of dot D_1 in tile (4,16) in the few hole regime calculated from tracking the transition voltages to charge occupancy $N = 1,2,3$ (Methods). The spectra are fitted to a S_0/f^γ dependence (Supplementary Fig.11). The inset shows a 200 s repeated loading of the first hole in D_1 by sweeping the plunger P_1. The red line shows the estimated position for the $N = 0$ to $N = 1$ charge state transition. The transition voltage is then converted to the spectral density (Methods) shown in the panel. **d,** Similar to **b**, the heat map of the few hole regime $\sqrt{S_0}$ corresponding to the physical location of each tile within the QARPET device. A faulty RF line prevents fast measurements of tiles in row 4. (Methods).

cupation affecting marginally the noise properties of the device (Supplementary Fig. 9). The overall distribution is shown in the accompanying histogram and is characterized by a spread over more than an order of magnitude, with a geometric mean of 2.4 ± 1.7 μeV/$\sqrt{\text{Hz}}$. This experimental mean matches closely the bootstrapped mean (Supplementary Fig. 10), indicating that our sample size is sufficiently large to provide confidence in the accuracy of the mean value. From the heat map, we identify a noisier device region in the bottom-left quadrant, $i \in \{19,21\}$, $j \in \{14,16\}$, as well as the best-performing tile, indexed (17,21), with an average charge noise S_0 of 0.7 ± 0.24 μeV/$\sqrt{\text{Hz}}$ and a minimum of 0.36 μeV/$\sqrt{\text{Hz}}$.

We complement the charge noise analysis by characterizing quantum dot D_1 un-

der P_1 in the few-hole regime, which is the typical regime of operation for qubits. Figure 10.4c shows the frequency dependence of the voltage spectral density for the first three hole transitions. Following the methodology in ref. [40], these spectra are evaluated from the transition voltages time traces (inset Fig. 10.4c) obtained by sweeping across the charge transition region over a fixed time. As in Fig. 10.4a, we fit each spectrum to S_0/f^{γ} to obtain the charge noise $\sqrt{S_0}$ at 1 Hz (black arrow in Fig. 10.4c) and the spectral exponent γ, and extend this protocol to all measurable tiles (Supplementary Fig 11). The resulting heat map in Fig. 10.4d displays the charge noise values $\sqrt{S_0}$ measured at the three subsequent charge transitions with the accompanying histogram showing the overall distribution. The distribution is characterized by a geometric mean value $\sqrt{S_0}$ of 52 ± 31 $\mu V/\sqrt{Hz}$. The charge noise average value does not change significantly with respect to hole filling, but rather the standard deviation decreases with increasing hole occupancy (Supplementary Fig. 9).

Our statistical characterisation enables a comparison with charge noise measurements in quantum dot devices using a higher-quality Ge/SiGe heterostructure grown on a Ge substrate [40]. We observe charge noise values an order of magnitude higher than in ref. [40] for both charge sensors (Supplementary Fig. 12) in the multi-hole regime and dots in the few-hole regime. These results support the understanding from ref. [40] that charge noise in Ge/SiGe heterostructures grown on Ge wafers may be lower than in those grown on Si wafers. Fabrication of QARPET devices on Ge/SiGe heterostructures grown on Ge wafers will improve statistical assessments of charge noise uniformity over larger areas.

10.2.5. QUBITS

Lastly, we focus on a single tile of a second QARPET device and demonstrate the ability to encode singlet-triplet (ST) and Loss-DiVincenzo (LD) spin qubits in the crossbar. Figure 10.5a shows the charge stability diagram of the double dot (D_1, D_2) obtained by sweeping the detuning ε_{12} and constant potential axes μ_{12}. For ST qubits, we define the detuning of the two dots ε_{12} to be zero at the centre of the (1,1) charge region and perform a spin funnel experiment. Starting from the (0,2) region, we pulse the system towards the (1,1) region at varying detuning ε_{12}, we let it evolve for 100 ns, and pulse back to the readout point (red dot in Fig. 10.5a). We do this for varying magnetic fields (B) to map the S-T_- anti-crossing as a function of B (dark blue line) [41], which confirms the ability to read out spins using the Pauli spin blockade (PSB) method.

Figure 10.5c,d demonstrate coherent ST_0 oscillations as a function of detuning, magnetic field, and evolution time. We initialize a singlet in the (0,2) configuration, diabatically pulse towards (1,1), let evolve for a time τ, and diabatically pulse to the readout point. This sequence is repeated for different τ, for different detuning (Fig. 10.5c) and different magnetic field (Fig. 10.5d). From fitting the oscillations as a function of magnetic field we estimate the g-factor difference $\Delta g = 0.073$ and the residual exchange at zero detuning $J(\varepsilon_{12} = 0) = 3.74$MHz (Supplementary Fig. 13).

We measure the electric dipole spin resonance (EDSR) spectra of the two single hole spin LD qubits Q_1 and Q_2 (Fig. 10.6a) by starting with a singlet in the (0,2) configuration, pulsing slowly towards the (1,1), applying a microwave (MW) pulse to plunger P_1 / P_2 (top/bottom panel) at frequency f, and pulsing to the readout point. A dark blue line is

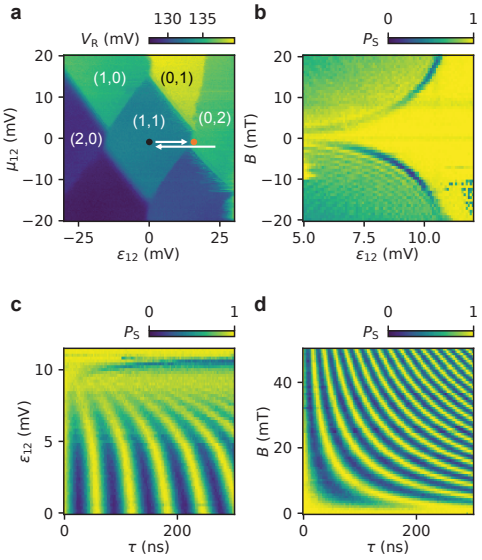

Figure 10.5: **Spin readout and singlet-triplet qubit. a,** Charge stability diagram of dot 1 and dot 2 measured on tile (19,14) from a second QARPET device. The red dot indicates the readout point inside the Pauli spin blockade window, the black dot the manipulation point, while the white arrows represent the pulse sequence from initialization to manipulation and readout. For the spin funnel observed in **b,** the system is initialized in a singlet, pulsed from the (0,2) region towards the (1,1) region in 1 µs at varying detuning ε_{12}, left evolving for 100 ns and pulsed to the readout point in 1 ns. **c** ST_0 oscillations as a function of detuning, at 20 mT the system is is initialized in a singlet, pulsing from the (0,2) region towards the (1,1) region in 1 ns, left evolving for varying time τ and pulsed to the readout point in 1 ns, this sequence is repeated for different detuning ε_{12}. **d** ST_0 oscillations as a function of magnetic field: the system is is initialized in a singlet, pulsed from the (0,2) to the manipulation point in 1 ns and left evolving for varying time τ and pulsed to the readout point in 1 ns. This sequence is repeated for different magnetic fields. By analysing the oscillation frequency as a function of magnetic field (Supplementary Fig.˙ 13) we extract the g-factor difference $\Delta g = 0.073$ and the residual exchange at zero detuning $J(\varepsilon_{12} = 0) = 3.74$MHz. In panels b, c, d the colour bar represents the singlet (high values) triplet (low values) probability.

visible where the MW driving frequency is at resonance with the qubit. At zero detuning, that is at the centre of the (1,1) region, the g-factors for the two qubits result in $g_1 = 0.30$ and $g_2 = 0.36$ (in line with the values reported for the same heterostructure in ref. [25] and with other works on Ge [42, 26]). The difference of these g-factors is also consistent with the $\Delta g = 0.073$ extracted from the ST qubit experiment in Fig. 10.5b.

After calibrating the $\pi/2$ qubit rotations we characterize the qubits' coherence in this system. We perform a Ramsey experiment (Fig. 10.6b) on both qubits at a magnetic field of 50 mT and extract coherence time T_2^* of 4.4 µs and 5.7 µs for Q_1 and Q_2 respectively. These coherence times are comparable to the best results measured in Ge at a similar magnetic field [27]. Further we perform a Hahn-echo experiment (Fig. 10.6c) and extract coherence times of 10.1 µs and 12.7 µs for Q_1 and Q_2 respectively, comparable with previous experiments [27] (note that in ref.[27] T_2^H of 32 µs is measured at at 20 mT where coherence is expected to be longer compared to our field of 50 mT). These results demonstrate that the qubit coherence properties are preserved in the QARPET architec-

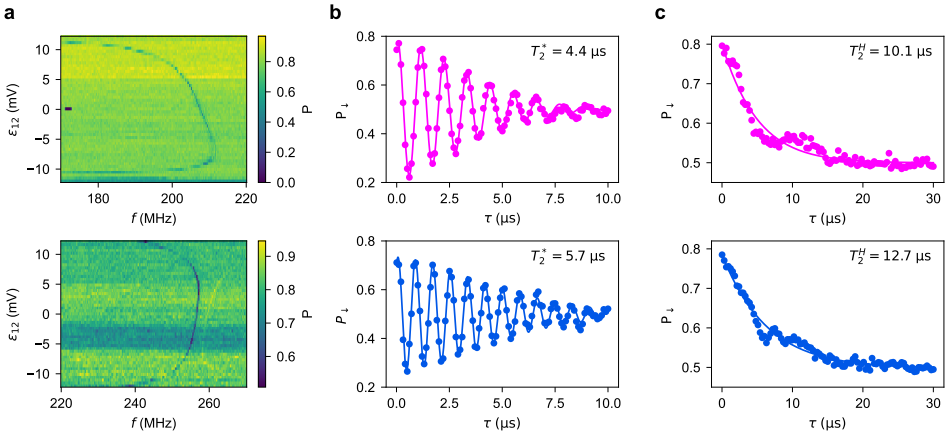

Figure 10.6: **Coherence of Loss-DiVincenzo hole spin-qubits. a,** EDSR spectra of qubits Q_1 and Q_2 as a function of detuning (ϵ_{12}). Starting from the (0,2) configuration, we pulse in 10 μs towards the (1,1) at varying detuning (ϵ_{12}), apply a microwave pulse with frequency f and pulse diabatically to the readout point. At zero detuning the g-factor of the two qubits are $g_1 = 0.36$ and $g_2 = 0.30$. A higher value in the colour bar represents a higher singlet probability. **b,** Ramsey experiment in which $\pi/2$ pulses are separated by time τ. Fitting of the results with $P = a\cos(2\pi\Delta f\tau + \phi)\exp\left(-(\tau/T_2^*)^{\alpha^*}\right)$, yields a T_2^* of 5.7 μs and 4.4 μs for Q_1 and Q_2 respectively. **c,** Hahn-echo experiment consisting of $\pi/2$, π, and $\pi/2$ pulses, separated by waiting time τ. Fitting the results with $P = a\exp\left(-\left(2\tau/T_2^H\right)^{\alpha^H}\right)$ yields a T_2^H of 12.7 μs and 10.1 μs for Q_1 and Q_2, respectively. Initialization is performed pulsing deep in the (0,2) and waiting for 100 μs for the system to relax into the singlet. All measurements are performed at a magnetic field of 50 mT, oriented parallel to the device.

ture, which further motivates the use of QARPET devices for statistical characterisation of qubit coherence and is encouraging for scaling quantum processors in dense Ge qubit arrays.

10.3. CONCLUSIONS

We have demonstrated key functionalities of the QARPET architecture at millikelvin temperature using RF reflectometry, including tile selectivity, single-hole quantum dots, singlet-triplet, and single-spin Loss-DiVincenzo qubits. We gathered statistics on single-hole and addition voltages, providing insights into the uniformity of gate-defined quantum confinement in our device architecture, relevant for hole-spin qubit operations [43, 44] and for developing shared-control spin qubit architectures [34]. The systematic exploration of charge noise showcases the power of the architecture as a measurement tool for statistical benchmarking and motivates further fabrication and characterisation of similar devices on improved heterostructures grown on germanium wafers. Together with the proof of principle demonstration of spin qubits with respectable quantum coherence, our results open the door to the statistical study of spin qubits within a single cooldown and across μm-scale length-scales, which are relevant for noisy intermediate scale quantum processors.

QARPET is a flexible platform with potential for further optimization in both design

and implementation. While the current design features two quantum dots per tile for charge and spin manipulation, this number could be extended to $q > 2$, requiring a linear increase in control lines ($n+m+2q+3$) to operate $q \times n \times m$ qubits, thereby maintaining a sublinear scaling of interconnects. The specific properties of the heterostructure, such as the SiGe barrier thickness, also influence the dimensions of the plunger and barrier gates, thereby setting the minimum tile footprint and determining the overall qubit density of the device.

Although demonstrated in a Ge/SiGe heterostructure, the QARPET architecture could be adapted to other accumulation-mode undoped heterostructures with appropriate design and process modifications. However, such adaptations may introduce additional challenges. For instance, implementing QARPET in Si/SiGe heterostructures would require narrower gates due to the the heavier electron mass compared to holes in strained Ge, as well as additional accumulation gate layers to connect charge sensors to remote doped reservoirs.

With hundreds of nominally identical quantum dot qubits integrated in a single die, we anticipate the use of QARPET as an ideal test-bed for training of automated routines for all phases of the device tuning, from quantum dot read out, to single-spin operation, also exploiting machine learning and artificial intelligence [45, 46]. On the other hand, implementing test vehicles like QARPET with advanced semiconductor manufacturing will reduce device variability stemming from the material stack and fabrication and accelerate the development-cycle of industrial spin qubits. Additionally, due to the dense pattern of multi-layer gates, QARPET-like devices may provide benchmarking of spin qubit performance in a practically relevant electrostatic environment, paving the way for the development of large-scale quantum processors.

10.4. METHODS

Ge/SiGe heterostructure growth. The Ge/SiGe heterostructure is grown on a 100-mm n-type Si(001) substrate using an Epsilon 2000 (ASMI) reduced pressure chemical vapor deposition reactor. The layer sequence comprises a $Si_{0.2}Ge_{0.8}$ virtual substrate obtained by reverse grading, a 16 nm thick Ge quantum well, a 55 nm-thick $Si_{0.2}Ge_{0.8}$ barrier, and a thin sacrificial Si cap. Further details and electrical characterisation of Hall-bar shaped heterostructure field effect transistors on this semiconductor stack are presented in ref. [24].

Device fabrication. The fabrication of QARPET devices entails the following steps: Electron beam lithography of the ohmic contacts layer; Wet etching of the sacrificial Si-cap in buffer oxide etch for 10 s; Deposition of the ohmic contacts via e-gun evaporation of 15 nm of Pt at pressure of 3×10^{-6} mbar at the rate of 3 nm/minute, followed by rapid thermal anneal at 400 C for 15 minutes in a halogen lamps heated chamber in argon atmosphere to form PtSiGe ohmic contacts [47]; Atomic layer deposition of 5 nm of Al_2O_3 at 300 C; Electron beam lithography and deposition of the first gate layer via e-gun evaporation of 3 nm of Ti and 17 nm of Pd; Lift-off in AR600-71 45 C with sonication at medium-high power for 1 hour, the patterned side of the chip facing downwards to avoid re-deposition of metal on the chip surface. For each subsequent gate layer the last two steps are repeated, increasing each time the deposited Pd thickness by 5 nm to guarantee film continuity where overlapping with the first gate layer. We perform AFM imaging

of the developed resist after each resist development and metal lift-off to monitor the fabrication process.

Measurements All measurements are performed in a Oxford wet dilution refrigerator with a base temperature of ≈ 100 mK. Using battery-powered voltage sources, dc-voltages are applied to the gates. The DC voltages on gates are combined with an AC voltage from a Qblox arbitrary waveform generator (AWG) by a bias-tee with a cut-off frequency of 3 Hz. The AC-voltage used for pulses and RF driving is generated by an AWG . We studied two devices. Measurements and corresponding analysis reported in Figs. 2-4 and Supplementary Figs. 1-12. are from QARPET device 1. The inter-dot barrier B_2 was leaky, preventing double-dot studies on this specific device and the RF line connected to for $i = 4$ was faulty, preventing on this row to perform fast 2D maps of P_1 vs other gates. In QARPET device 2 we focused on a single tile with measurements and corresponding analysis reported in Figs 5,6 and Supplementary Fig. 13.

Relative lever arm calculation The relative lever arms to D_1 with respect to P_1 in Figure 10.3a are derived from the slopes of the transition lines in the reflectance maps of all P_1-to-surrounding-gates pairs [30] for all the tiles where it was measurable (Supplementary Figs. 2–5). The slope of the transition lines in these gate-P_1 maps allows to extract the lever arm of gate g_i to D_1 relative to the lever arm of P_1 to D_1 ($\alpha_{g_i,D_1}/\alpha_{P_1,D_1}$) [30]. The variability of the relative lever arms across different spin qubit tiles arises form differences in the shape and position of dot D_1, which depends on the electrostatic potential surrounding the dot and reflects the variability in semiconductor stack and gate-stack uniformity, as well as differences in electrostatic tuning of the tile. The virtual gate voltage v$P1$ is calculated as u$P_1 \cdot$ median(P_1)/median(uP_1) where u$P_1 = \sum g_i \alpha_{g_i,D_1}/\alpha_{P_1,D_1}$ with g_i comprising P_s, B_s, B_1, P_1 and S.

Flank method for charge noise characterisation of the quantum dots in the multi-hole regime We characterize charge noise of the sensors using the flank method, measured via RF reflectometry. The process begins by tuning the surrounding gates until the reflected signal exceeds the baseline by at least 10 mV, marking the turn-on of the device. A multi-hole quantum dot is then defined beneath P_s by gradually lowering the barrier gates surrounding P_s until a spectrum of Coulomb peaks is observed without any background signal. Next, we record the reflected signal on the right flank of the first three Coulomb peaks, where the slope ($|dI/dV_{sd}|$) of the peaks is steepest. The signal is sampled at a rate of 1 kHz for a duration of 100 seconds using a Qblox digitizer. To compute the current power spectral density S_I, the 100-second current trace is divided into ten 10-second segments. The power spectral densities for each segment are calculated and averaged to yield S_I. For each Coulomb peak analysed, we convert S_I into the charge noise power spectral density (S_ϵ) using:

$$S_\epsilon = \frac{\alpha^2 S_I}{|dI/dV_{sd}|^2} \tag{10.1}$$

where α is the lever arm extracted from the analysis of the Coulomb diamonds (Supplementary Figs 6). Finally, the spectral densities are fitted to a $1/f^\gamma$ model, and the value of the spectral density at 1 Hz (S_0) and exponent (γ) are extracted and reported.

Charge transition method for charge noise characterisation of quantum dots in the few-hole regime We begin by tuning P_1 to the last-hole, as described previously.

To probe electrostatic fluctuations in the quantum dot, we repeatedly sweep across the charge transition point over a period of 200 s at a rate of 300 Hz. Transition voltages are extracted by performing a sigmoid fit to each sweep repetition [40]. From the transition voltage data, we calculate the voltage spectral density and fit the results to a $1/f^{\gamma}$ dependence, reporting the noise value at 1 Hz and the spectral exponent. Because we use the sensor to monitor the transition voltage, the measurements include noise contributions from both P_s and P_1. However, we find that the spectral density of the sensor is an order of magnitude lower than the spectral densities measured for P_1. This confirms that the observed traces are dominated by charge noise from the quantum dot under P_1 [40].

SUPPLEMENTARY INFORMATION

Supplementary Figs. 1–13.

ACKNOWLEDGEMENTS

We are grateful to Francesco Borsoi, Pablo Cova Fariña, Hanifa Tidjani, Stephan Philips, and Daniel Jirovec for fruitful discussions. We acknowledge support by the European Union through the IGNITE project with grant agreement No. 101069515 and the QLSI project with grant agreement No. 951852. This work was supported by the Netherlands Organisation for Scientific Research (NWO/OCW), via the Open Competition Domain Science - M program. This research was sponsored in part by the Army Research Office (ARO) under Awards No. W911NF-23-1-0110. The views, conclusions, and recommendations contained in this document are those of the authors and are not necessarily endorsed nor should they be interpreted as representing the official policies, either expressed or implied, of the Army Research Office (ARO) or the U.S. Government. The U.S. Government is authorized to reproduce and distribute reprints for Government purposes notwithstanding any copyright notation herein. This research was sponsored in part by The Netherlands Ministry of Defence under Awards No. QuBits R23/009. The views, conclusions, and recommendations contained in this document are those of the authors and are not necessarily endorsed nor should they be interpreted as representing the official policies, either expressed or implied, of The Netherlands Ministry of Defence. The Netherlands Ministry of Defence is authorized to reproduce and distribute reprints for Government purposes notwithstanding any copyright notation herein.

DECLARATIONS

- G.S. and A.T. are inventors on a patent application (International Application No. PCT/NL2024/050325) submitted by Delft University of Technology related to the QARPET architecture. G.S. is founding advisor of Groove Quantum BV and declares equity interests.

- The datasets supporting the findings of this study are openly available at https://zenodo.org/records/15089359.

- A.T. designed and fabricated the devices on heterostructures provided by L.E.A.S, with contributions from D.C. to packaging, from K.H. to device inspection, and

from D.D.E for process development. A.T. assembled the setup and fridge, performed quantum dot and qubit measurements, and analysed the corresponding data. A.E. and F.P. performed noise measurements, analysed with help from L.E.A.S. and D.D.E. A.T., A.E., and G.S. wrote the manuscript with input from all authors. G.S. and A.T. conceived the project, supervised by G.S.

10.5. SUPPLEMENTARY INFORMATION

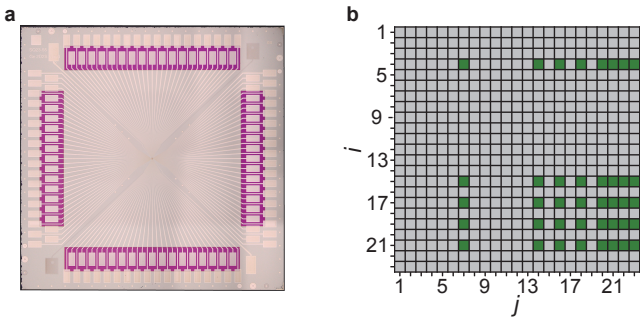

Supplementary Fig. 10.1: **a)** Optical image of chip with a QARPET device. **b)** Schematics of the 23 × 23 tiles of QARPET device 1 with highlighted in blue the 40 tiles that were bonded with measurements and corresponding analysis reported in Figs. 2-4 and Supplementary Figs.2-12. The RF line connected to P_1 for $i = 4$ was faulty, preventing fast measurements of dot 1 on this row, and the inter-dot barrier B_2 was leaky, preventing double-dot studies on this specific device.

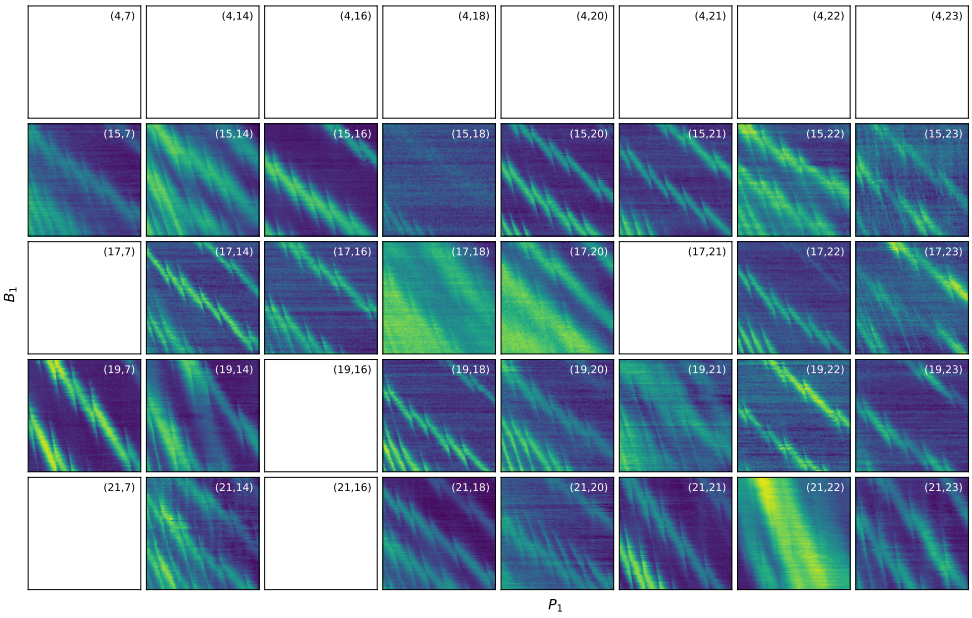

Supplementary Fig. 10.2: Reflectance maps of B_1 (y-axis) vs P_1 (x-axis) used to determine the relative lever arm values presented in Fig. 3a. The slope of the transitions is used to determine the relative lever arm to D_1 $\alpha_{B_1,D_1}/\alpha_{P_1,D_1}$. Measurement on row 4 were not performed as the RF line connected to P_1 for $i = 4$ was faulty therefore preventing efficient measurements on those tiles. The remaining missing maps were not measured because the voltage range would violate the constraints sets for the device. The same considerations apply to the reflectance maps in Supplementary Figs. 3–5

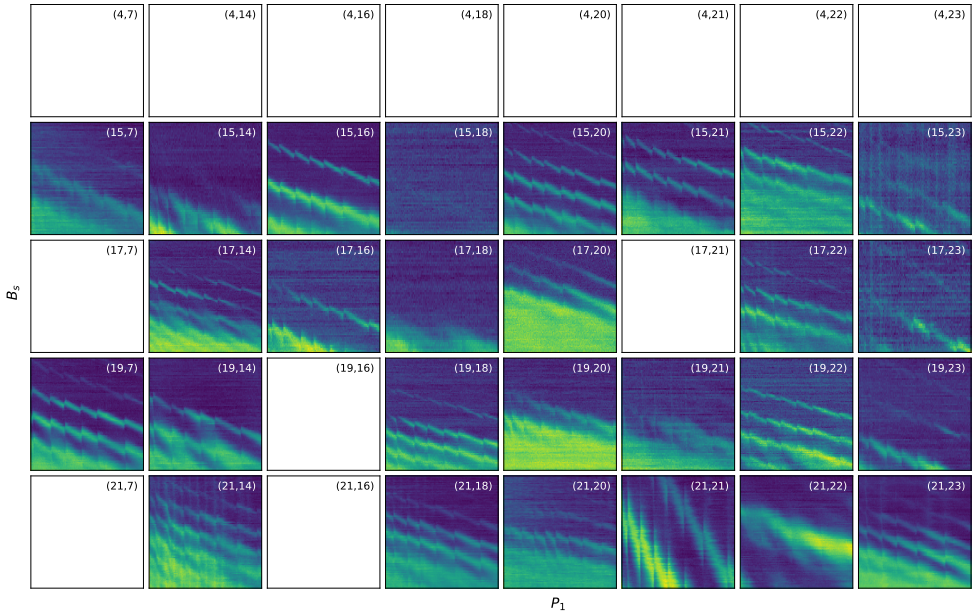

Supplementary Fig. 10.3: Reflectance maps of B_s (y-axis) vs P_1 (x-axis) used to determine the relative lever arm values presented in Fig. 3a. The slope of the transitions is used to determine the relative lever arm to D_1 $\alpha_{B_s,D_1}/\alpha_{P_1,D_1}$.

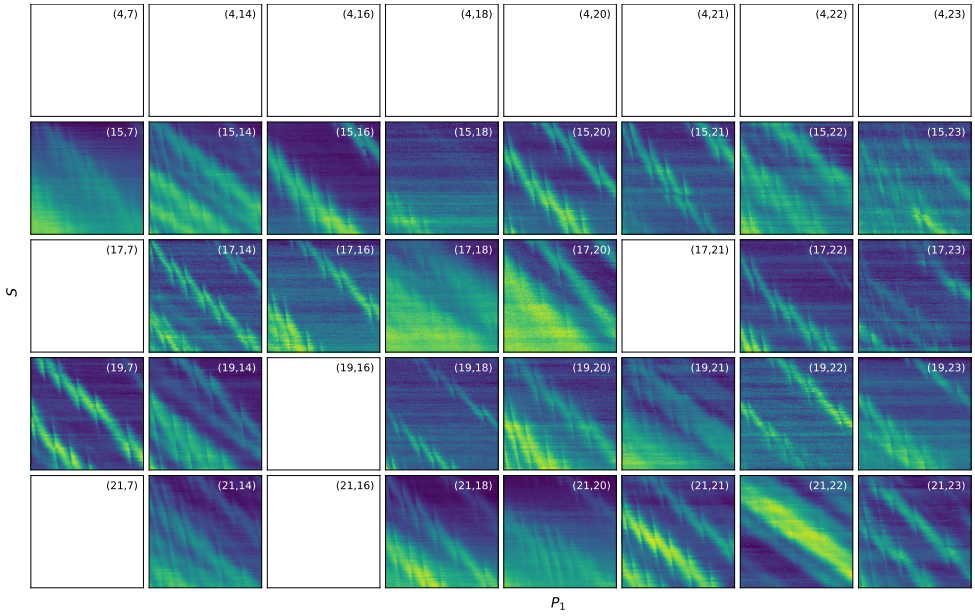

Supplementary Fig. 10.4: Reflectance maps of S (y-axis) vs P_1 (x-axis) used to determine the relative lever arm values presented in Fig. 3a. The slope of the transitions is used to determine the relative lever arm to D_1 $\alpha_{B_s,D_1}/\alpha_{P_1,D_1}$.

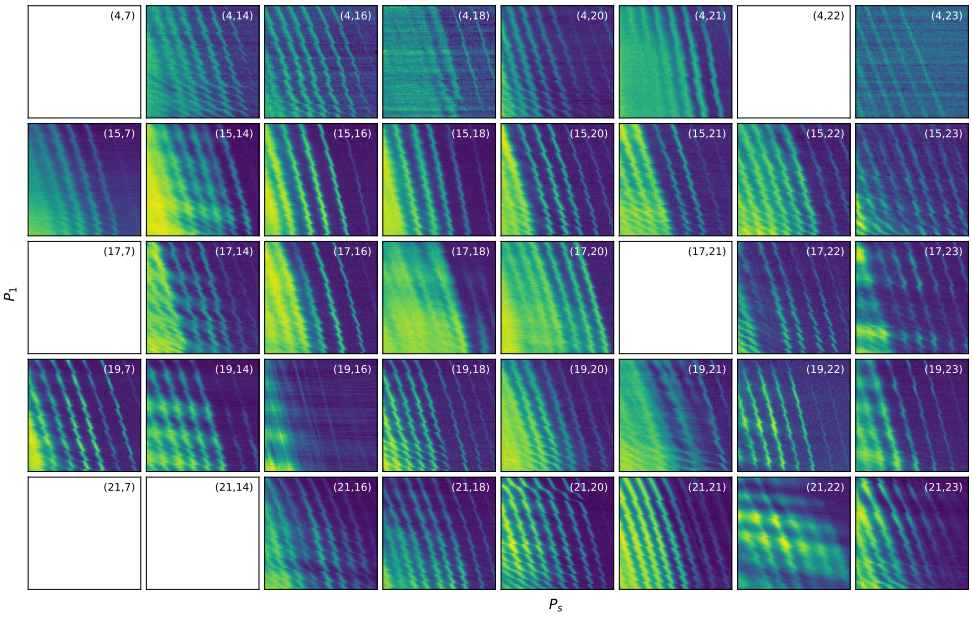

Supplementary Fig. 10.5: Reflectance maps of P_1 (y-axis) vs P_s (x-axis) used to determine the charging voltages presented in Fig. 3c. The first transition line at the top corresponds to the last hole transition.

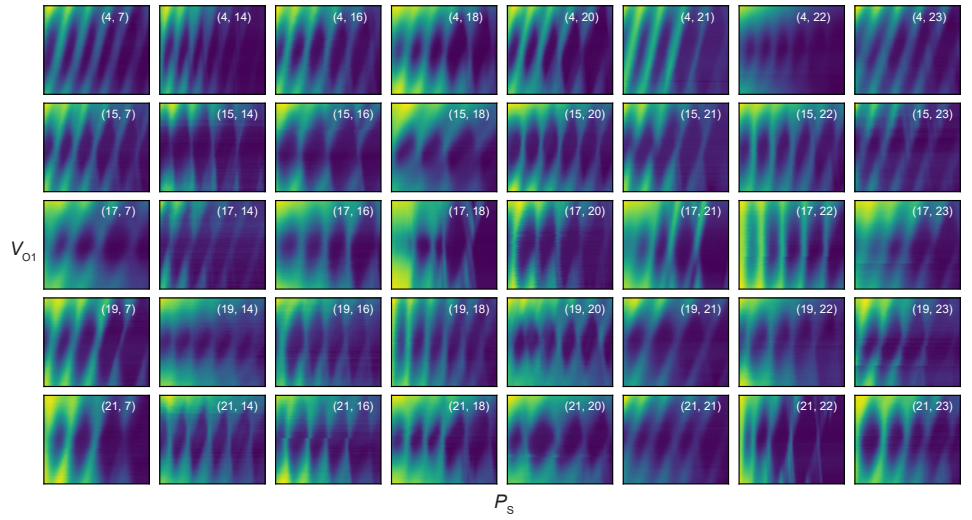

Supplementary Fig. 10.6: The reflectance measured as a function of sensor plunger (P_s) and voltage applied to ohmic contact (O_1) showing Coulomb diamonds for individual tiles.

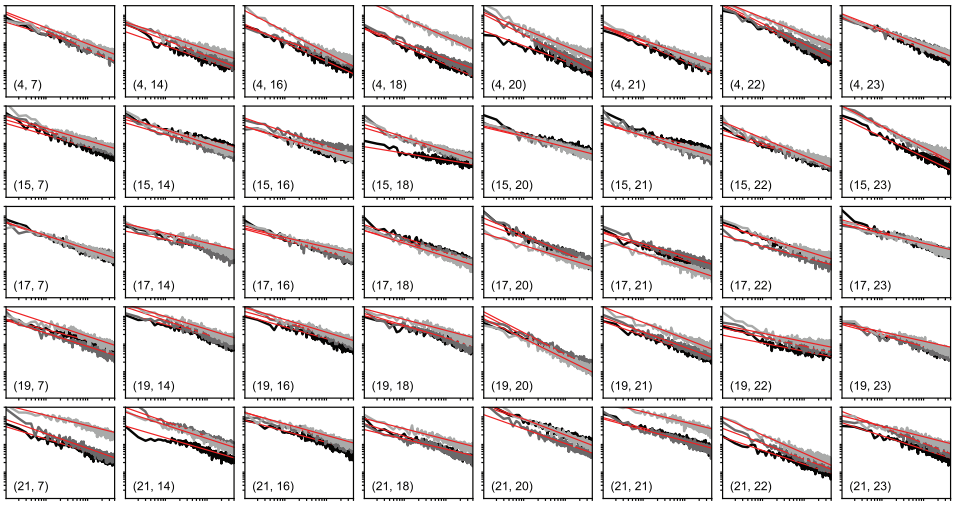

Supplementary Fig. 10.7: The power spectral densities S_ϵ from the three measured coulomb flanks of the sensor dot in each of the 40 investigated tiles. The spectral densities are individually fit to a $1/f^\gamma$ and both S_0 and γ are extracted.

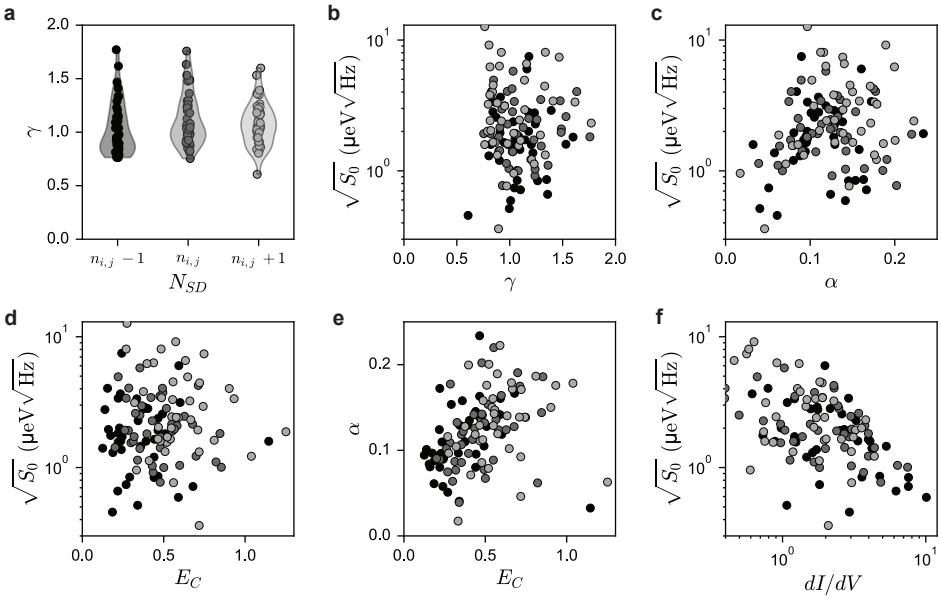

Supplementary Fig. 10.8: **a** Violin plots of the charge noise exponent γ obtained from fitting the power spectral densities, showing that most values cluster around ~ 1 **b** Scatter plot of γ versus $\sqrt{S_0}$, revealing no apparent correlation between the two metrics, supporting a $1/f$ noise behaviour consistent with a log-uniform frequency distribution of TLFs. **c, d** Scatter plots of the lever arm (α) and the charging energy (E_C) versus $\sqrt{S_0}$, respectively, both showing no significant correlation. **e** Scatter plot of E_C versus α, demonstrating a positive correlation, confirming that the quantum dot size influences the lever arm. Together with **c** and **d**, this suggests that dot size does not impact the magnitude of charge noise. **f** Scatter plot of the Coulomb peak slope versus $\sqrt{S_0}$, revealing a negative correlation, indicating that sharper peaks correspond to lower charge noise.

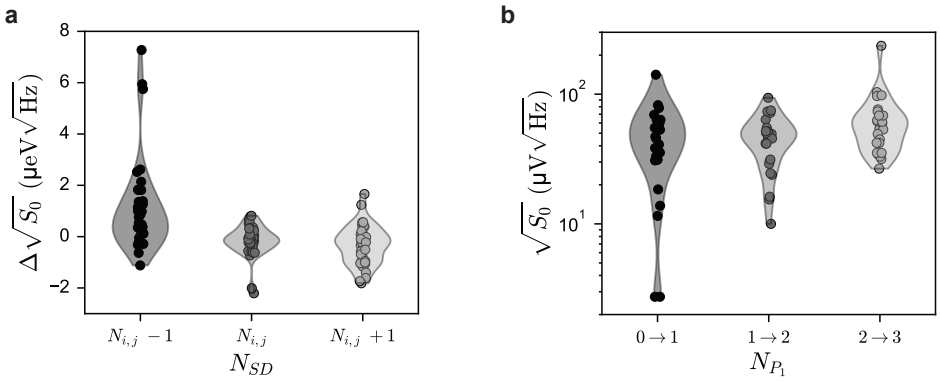

Supplementary Fig. 10.9: Violin plots for three consecutive hole occupancies in each tile reporting the distributions of the charge noise variations ($\Delta\sqrt{S_0}$) with respect to the average charge noise in each tile . With the exception of a few outliers, such as tile (21,21), the median value of $\Delta\sqrt{S_0}$) fluctuates around zero, suggesting that in the multi-hole regime the specific charge occupation affects marginally the noise properties of the device. **b,** The violin plots of the charge noise measurements for 27 tiles across each charge occupation transition in D_1. The average charge noise does not depend significantly on hole filling, however, we observe a decrease in the standard deviation of the charge noise distribution with increasing hole occupation, indicating that higher hole occupations lead to more predictable average charge noise.

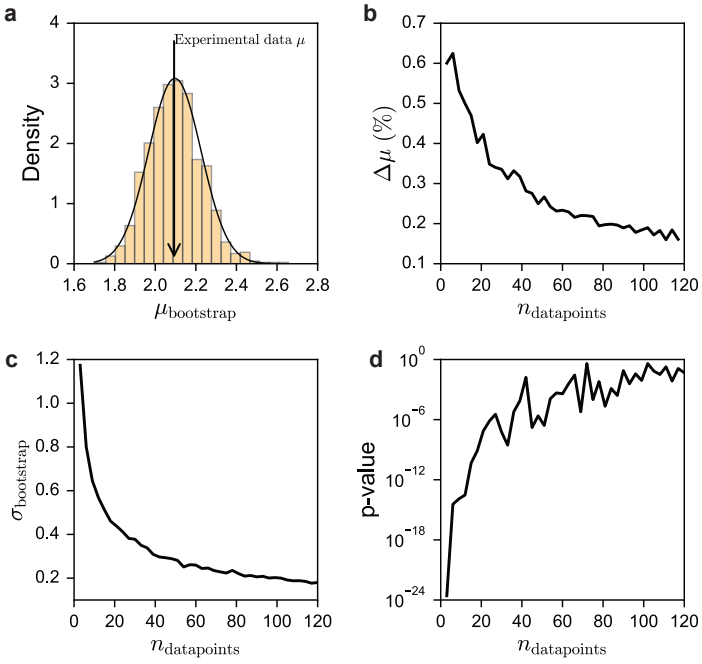

Supplementary Fig. 10.10: Histogram of bootstrapped means with the experimental mean from Fig. 4b indicated by a black arrow. The close agreement between the experimental and bootstrapped means (within 0.2%) suggests that the experimental sample size (120 data points from 40 tiles) is sufficiently large to ensure an accurate estimation of the mean value. **b,** Difference between the bootstrapped and experimental means as a function of the experimental sample size. While the difference remains small throughout, it stabilizes at approximately 60 data points (20 tiles), indicating a sufficient sample size. **c,** Standard deviation of the bootstrapped means as a function of sample size, which similarly converges around 60 data points, reinforcing the reliability of the experimental sample size. **d,** p-value from a Shapiro-Wilk test as a function of sample size. This test assesses whether the dataset follows a normal distribution, which suggests that multiple independent random variables contribute additively to the measured quantity. High p-values (> 0.001) indicate greater normality, which is achieved at approximately 20 tiles. Collectively, these results confirm that QARPET provides a sufficiently large dataset to accurately characterize charge noise.

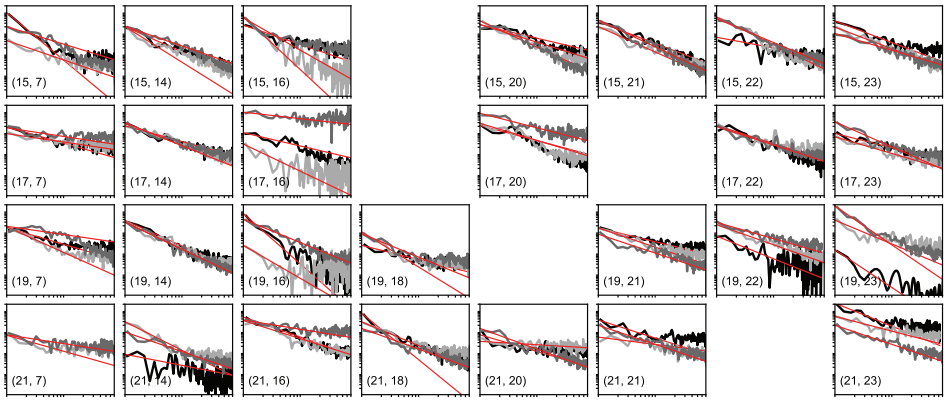

Supplementary Fig. 10.11: The voltage spectral densities S_ϵ from the three measured charge transitions of D_1 in each of the 27 investigated tiles. The spectral densities are individually fit to a $1/f^\gamma$ and both S_0 and γ are extracted.

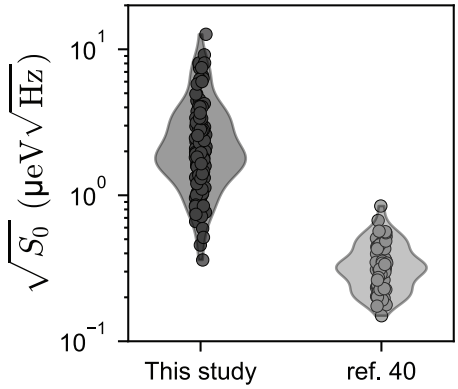

Supplementary Fig. 10.12: Violin plots of $\sqrt{S_0}$ at 1 Hz comparing the sensor noise of this study with those reported in Ref. 40 (main text), highlighting the significant differences in charge noise values between the two datasets.

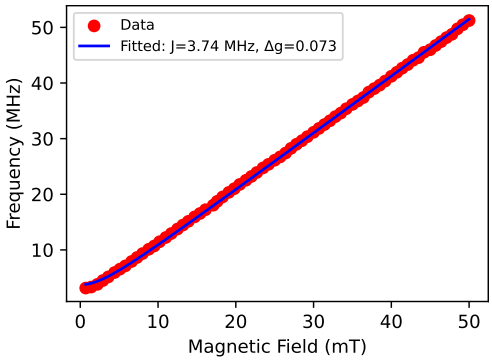

Supplementary Fig. 10.13: Frequency of the ST-oscillations in Fig. 5d at different magnetic fields. For each magnetic field we extract the frequency of the oscillations (fitting with a sine function) and the resulting points are fitted to $f = \frac{1}{h}\sqrt{J^2 + (\Delta g \mu_B B)^2}$ from which we extract the g-factor difference $\Delta g = 0.073$ and the residual exchange at zero detuning $J(\Delta e_{12} = 0) = 3.74$MHz. Measurements are from QARPET device 2.

BIBLIOGRAPHY

[1] G. Burkard, T. D. Ladd, A. Pan, J. M. Nichol, and J. R. Petta. “Semiconductor spin qubits”. In: *Reviews of Modern Physics* 95.2 (2023), p. 025003.

[2] A. Zwerver, T. Krähenmann, T. Watson, L. Lampert, H. C. George, R. Pillarisetty, S. Bojarski, P. Amin, S. Amitonov, J. Boter, et al. “Qubits made by advanced semiconductor manufacturing”. In: *Nature Electronics* 5.3 (2022), pp. 184–190.

[3] N. P. De Leon, K. M. Itoh, D. Kim, K. K. Mehta, T. E. Northup, H. Paik, B. S. Palmer, N. Samarth, S. Sangtawesin, and D. W. Steuerman. “Materials challenges and opportunities for quantum computing hardware”. en. In: *Science* 372.6539 (Apr. 2021), eabb2823. ISSN: 0036-8075, 1095-9203.

[4] A. Saraiva, W. H. Lim, C. H. Yang, C. C. Escott, A. Laucht, and A. S. Dzurak. “Materials for Silicon Quantum Dots and their Impact on Electron Spin Qubits”. en. In: *Advanced Functional Materials* 32.3 (Jan. 2022), p. 2105488. ISSN: 1616-301X, 1616-3028.

[5] D. R. Ward, D. E. Savage, M. G. Lagally, S. N. Coppersmith, and M. A. Eriksson. “Integration of on-chip field-effect transistor switches with dopantless Si/SiGe quantum dots for high-throughput testing”. In: *Appl. Phys. Lett.* 102.21 (May 2013), p. 213107. ISSN: 0003-6951.

[6] H. Al-Taie, L. W. Smith, B. Xu, P. See, J. P. Griffiths, H. E. Beere, G. a. C. Jones, D. A. Ritchie, M. J. Kelly, and C. G. Smith. “Cryogenic on-chip multiplexer for the study of quantum transport in 256 split-gate devices”. In: *Appl. Phys. Lett.* 102.24 (June 2013), p. 243102. ISSN: 0003-6951.

[7] R. K. Puddy, L. W. Smith, H. Al-Taie, C. H. Chong, I. Farrer, J. P. Griffiths, D. A. Ritchie, M. J. Kelly, M. Pepper, and C. G. Smith. “Multiplexed charge-locking device for large arrays of quantum devices”. In: *Appl. Phys. Lett.* 107.14 (Oct. 2015), p. 143501. ISSN: 0003-6951.

[8] S. Schaal, A. Rossi, V. N. Ciriano-Tejel, T.-Y. Yang, S. Barraud, J. J. L. Morton, and M. F. Gonzalez-Zalba. “A CMOS dynamic random access architecture for radio-frequency readout of quantum devices”. en. In: *Nature Electronics* 2.6 (June 2019), pp. 236–242. ISSN: 2520-1131.

[9] B. Paquelet Wuetz, P. L. Bavdaz, L. A. Yeoh, R. Schouten, H. van der Does, M. Tiggelman, D. Sabbagh, A. Sammak, C. G. Almudever, F. Sebastiano, J. S. Clarke, M. Veldhorst, and G. Scappucci. “Multiplexed quantum transport using commercial off-the-shelf CMOS at sub-kelvin temperatures”. en. In: *npj Quantum Information* 6.1 (May 2020), p. 43. ISSN: 2056-6387.

[10] S. Pauka, K. Das, J. Hornibrook, G. Gardner, M. Manfra, M. Cassidy, and D. Reilly. “Characterizing Quantum Devices at Scale with Custom Cryo-CMOS”. en. In: *Physical Review Applied* 13.5 (May 2020), p. 054072. ISSN: 2331-7019.

[11] A. Ruffino, T.-Y. Yang, J. Michniewicz, Y. Peng, E. Charbon, and M. F. Gonzalez-Zalba. “A cryo-CMOS chip that integrates silicon quantum dots and multiplexed dispersive readout electronics”. en. In: *Nature Electronics* 5.1 (Dec. 2021), pp. 53–59. ISSN: 2520-1131.

[12] P. L. Bavdaz, H. G. J. Eenink, J. Van Staveren, M. Lodari, C. G. Almudever, J. S. Clarke, F. Sebasatiano, M. Veldhorst, and G. Scappucci. “A quantum dot crossbar with sublinear scaling of interconnects at cryogenic temperature”. en. In: *npj Quantum Information* 8.1 (July 2022), p. 86. ISSN: 2056-6387.

[13] E. J. Thomas, V. N. Ciriano-Tejel, D. F. Wise, D. Prete, M. d. Kruijf, D. J. Ibberson, G. M. Noah, A. Gomez-Saiz, M. F. Gonzalez-Zalba, M. A. I. Johnson, and J. J. L. Morton. “Rapid cryogenic characterization of 1,024 integrated silicon quantum dot devices”. en. In: *Nature Electronics* (Jan. 2025), pp. 1–9. ISSN: 2520-1131.

[14] S. Neyens, O. K. Zietz, T. F. Watson, F. Luthi, A. Nethwewala, H. C. George, E. Henry, M. Islam, A. J. Wagner, F. Borjans, E. J. Connors, J. Corrigan, M. J. Curry, D. Keith, R. Kotlyar, L. F. Lampert, M. T. Madzik, K. Millard, F. A. Mohiyaddin, S. Pellerano, R. Pillarisetty, M. Ramsey, R. Savytskyy, S. Schaal, G. Zheng, J. Ziegler, N. C. Bishop, S. Bojarski, J. Roberts, and J. S. Clarke. “Probing single electrons across 300-mm spin qubit wafers”. In: *Nature* 629.8010 (May 2024), pp. 80–85. ISSN: 14764687.

[15] M. Pelgrom, A. Duinmaijer, and A. Welbers. “Matching properties of MOS transistors”. en. In: *IEEE Journal of Solid-State Circuits* 24.5 (Oct. 1989), pp. 1433–1439. ISSN: 0018-9200.

[16] S. Ohkawa, M. Aoki, and H. Masuda. “Analysis and characterization of device variations in an LSI chip using an integrated device matrix array”. In: *International Conference on Microelectronic Test Structures, 2003.* Mar. 2003, pp. 3–75.

[17] T. Tsunomura, A. Nishida, and T. Hiramoto. “Analysis of NMOS and PMOS Difference in V_T Variation With Large-Scale DMA-TEG”. In: *IEEE Transactions on Electron Devices* 56.9 (Sept. 2009), pp. 2073–2080. ISSN: 1557-9646.

[18] T. Mizutani, A. Kumar, and T. Hiramoto. “Measuring threshold voltage variability of 10G transistors”. In: *2011 International Electron Devices Meeting.* ISSN: 2156-017X. Dec. 2011, pp. 25.2.1–25.2.4.

[19] G. Scappucci, C. Kloeffel, F. A. Zwanenburg, D. Loss, M. Myronov, J.-J. Zhang, S. De Franceschi, G. Katsaros, and M. Veldhorst. “The germanium quantum information route”. en. In: *Nature Reviews Materials* 6.10 (Oct. 2021), pp. 926–943. ISSN: 2058-8437.

[20] M. Veldhorst, H. G. J. Eenink, C. H. Yang, and A. S. Dzurak. “Silicon CMOS architecture for a spin-based quantum computer”. en. In: *Nature Communications* 8.1 (Dec. 2017). ISSN: 2041-1723.

[21] R. Li, L. Petit, D. P. Franke, J. P. Dehollain, J. Helsen, M. Steudtner, N. K. Thomas, Z. R. Yoscovits, K. J. Singh, S. Wehner, L. M. K. Vandersypen, J. S. Clarke, and M. Veldhorst. “A crossbar network for silicon quantum dot qubits”. en. In: *Science Advances* 4.7 (July 2018), eaar3960. ISSN: 2375-2548.

[22] B. Landman and R. Russo. “On a Pin Versus Block Relationship For Partitions of Logic Graphs”. In: *IEEE Transactions on Computers* C-20.12 (Dec. 1971), pp. 1469–1479. ISSN: 0018-9340.

[23] D. P. Franke, J. S. Clarke, L. M. Vandersypen, and M. Veldhorst. “Rent’s rule and extensibility in quantum computing”. In: *Microprocessors and Microsystems* 67 (June 2019), pp. 1–7. ISSN: 01419331.

[24] M. Lodari, N. W. Hendrickx, W. I. L. Lawrie, T.-K. Hsiao, L. M. K. Vandersypen, A. Sammak, M. Veldhorst, and G. Scappucci. “Low percolation density and charge noise with holes in germanium”. en. In: *Materials for Quantum Technology* 1.1 (Jan. 2021), p. 011002. ISSN: 2633-4356.

[25] N. W. Hendrickx, W. I. L. Lawrie, L. Petit, A. Sammak, G. Scappucci, and M. Veldhorst. “A single-hole spin qubit”. en. In: *Nature Communications* 11.1 (July 2020), p. 3478. ISSN: 2041-1723.

[26] N. Hendrickx, L. Massai, M. Mergenthaler, F. Schupp, S. Paredes, S. Bedell, G. Salis, and A. Fuhrer. “Sweet-spot operation of a germanium hole spin qubit with highly anisotropic noise sensitivity”. In: *Nature Materials* 23 (2024), p. 920.

[27] C.-A. Wang, V. John, H. Tidjani, C. X. Yu, A. S. Ivlev, C. Déprez, F. van Riggelen-Doelman, B. D. Woods, N. W. Hendrickx, W. I. L. Lawrie, L. E. A. Stehouwer, S. D. Oosterhout, A. Sammak, M. Friesen, G. Scappucci, S. L. de Snoo, M. Rimbach-Russ, F. Borsoi, and M. Veldhorst. “Operating semiconductor quantum processors with hopping spins”. In: *Science* 385.6707 (2024), pp. 447–452. eprint: https://www.science.org/doi/pdf/10.1126/science.ado5915.

[28] X. Zhang, E. Morozova, M. Rimbach-Russ, D. Jirovec, T.-K. Hsiao, P. C. Fariña, C.-A. Wang, S. D. Oosterhout, A. Sammak, G. Scappucci, M. Veldhorst, and L. M. K. Vandersypen. “Universal control of four singlet–triplet qubits”. en. In: *Nature Nanotechnology* (Oct. 2024). ISSN: 1748-3387, 1748-3395.

[29] L. E. A. Stehouwer, A. Tosato, D. Degli Esposti, D. Costa, M. Veldhorst, A. Sammak, and G. Scappucci. “Germanium wafers for strained quantum wells with low disorder”. In: *Applied Physics Letters* 123.9 (Aug. 2023), p. 092101. ISSN: 0003-6951.

[30] H. Tidjani, A. Tosato, A. Ivlev, C. Déprez, S. Oosterhout, L. Stehouwer, A. Sammak, G. Scappucci, and M. Veldhorst. “Vertical gate-defined double quantum dot in a strained germanium double quantum well”. In: *Physical Review Applied* 20.5 (Nov. 2023), p. 054035. ISSN: 2331-7019.

[31] F. Van Riggelen, N. W. Hendrickx, W. I. Lawrie, M. Russ, A. Sammak, G. Scappucci, and M. Veldhorst. “A two-dimensional array of single-hole quantum dots”. In: *Applied Physics Letters* 118.4 (Jan. 2021). ISSN: 00036951.

[32] W. H. Lim, C. H. Yang, F. A. Zwanenburg, and A. S. Dzurak. “Spin filling of valley–orbit states in a silicon quantum dot”. In: *Nanotechnology* 22.33 (Aug. 2011), p. 335704. ISSN: 0957-4484, 1361-6528.

[33] V. John, C. X. Yu, B. v. Straaten, E. A. Rodríguez-Mena, M. Rodríguez, S. Oosterhout, L. E. A. Stehouwer, G. Scappucci, S. Bosco, M. Rimbach-Russ, Y.-M. Niquet, F. Borsoi, and M. Veldhorst. *A two-dimensional 10-qubit array in germanium with robust and localised qubit control.* arXiv:2412.16044. Feb. 2025.

[34] F. Borsoi, N. W. Hendrickx, V. John, M. Meyer, S. Motz, F. van Riggelen, A. Sammak, S. L. de Snoo, G. Scappucci, and M. Veldhorst. "Shared control of a 16 semiconductor quantum dot crossbar array". en. In: *Nature Nanotechnology* 19.1 (Jan. 2024), pp. 21–27. ISSN: 1748-3395.

[35] E. J. Connors, J. Nelson, H. Qiao, L. F. Edge, and J. M. Nichol. "Low-frequency charge noise in Si/SiGe quantum dots". In: *Physical Review B* 100.16 (2019), p. 165305.

[36] B. Paquelet Wuetz, D. Degli Esposti, A.-M. J. Zwerver, S. V. Amitonov, M. Botifoll, J. Arbiol, A. Sammak, L. M. K. Vandersypen, M. Russ, and G. Scappucci. "Reducing charge noise in quantum dots by using thin silicon quantum wells". en. In: *Nature Communications* 14.1 (Mar. 2023), p. 1385. ISSN: 2041-1723.

[37] L. Massai, B. Hetényi, M. Mergenthaler, F. J. Schupp, L. Sommer, S. Paredes, S. W. Bedell, P. Harvey-Collard, G. Salis, A. Fuhrer, and N. W. Hendrickx. "Impact of interface traps on charge noise and low-density transport properties in Ge/SiGe heterostructures". en. In: *Communications Materials* 5.1 (Aug. 2024), p. 151. ISSN: 2662-4443.

[38] E. Paladino, Y. Galperin, G. Falci, and B. Altshuler. "1/f noise: Implications for solid-state quantum information". In: *Reviews of Modern Physics* 86.2 (2014), p. 361.

[39] A. Elsayed, M. Shehata, C. Godfrin, S. Kubicek, S. Massar, Y. Canvel, J. Jussot, G. Simion, M. Mongillo, D. Wan, B. Govoreanu, I. P. Radu, R. Li, P. Van Dorpe, and K. De Greve. "Low charge noise quantum dots with industrial CMOS manufacturing". In: *npj Quantum Information* 10.1 (July 2024), p. 70. ISSN: 2056-6387.

[40] L. E. A. Stehouwer, C. X. Yu, B. v. Straaten, A. Tosato, V. John, D. D. Esposti, A. Elsayed, D. Costa, S. D. Oosterhout, N. W. Hendrickx, M. Veldhorst, F. Borsoi, and G. Scappucci. *Exploiting epitaxial strained germanium for scaling low noise spin qubits at the micron-scale.* arXiv:2411.11526. Feb. 2025.

[41] D. Jirovec, A. Hofmann, A. Ballabio, P. M. Mutter, G. Tavani, M. Botifoll, A. Crippa, J. Kukucka, O. Sagi, F. Martins, J. Saez-Mollejo, I. Prieto, M. Borovkov, J. Arbiol, D. Chrastina, G. Isella, and G. Katsaros. "A singlet-triplet hole spin qubit in planar Ge". en. In: *Nature Materials* 20.8 (Aug. 2021), pp. 1106–1112. ISSN: 1476-4660.

[42] D. Jirovec, P. M. Mutter, A. Hofmann, A. Crippa, M. Rychetsky, D. L. Craig, J. Kukucka, F. Martins, A. Ballabio, N. Ares, D. Chrastina, G. Isella, G. Burkard, and G. Katsaros. "Dynamics of Hole Singlet-Triplet Qubits with Large g-Factor Differences". In: *Physical Review Letters* 128.12 (Mar. 2022), p. 126803.

[43] S. Bosco, M. Benito, C. Adelsberger, and D. Loss. "Squeezed hole spin qubits in Ge quantum dots with ultrafast gates at low power". In: *Physical Review B* 104.11 (2021), pp. 1–6. ISSN: 24699969.

[44] O. Malkoc, P. Stano, and D. Loss. “Optimal geometry of lateral GaAs and Si/SiGe quantum dots for electrical control of spin qubits”. In: *Physical Review B* 93.23 (June 2016). ISSN: 24699969.

[45] J. P. Zwolak, J. M. Taylor, R. W. Andrews, J. Benson, G. W. Bryant, D. Buterakos, A. Chatterjee, S. Das Sarma, M. A. Eriksson, E. Greplová, M. J. Gullans, F. Hader, T. J. Kovach, P. S. Mundada, M. Ramsey, T. Rasmussen, B. Severin, A. Sigillito, B. Undseth, and B. Weber. “Data needs and challenges for quantum dot devices automation”. en. In: *npj Quantum Information* 10.1 (Oct. 2024), pp. 1–8. ISSN: 2056-6387.

[46] Y. Alexeev, M. H. Farag, T. L. Patti, M. E. Wolf, N. Ares, A. Aspuru-Guzik, S. C. Benjamin, Z. Cai, Z. Chandani, F. Fedele, N. Harrigan, J.-S. Kim, E. Kyoseva, J. G. Lietz, T. Lubowe, A. McCaskey, R. G. Melko, K. Nakaji, A. Peruzzo, S. Stanwyck, N. M. Tubman, H. Wang, and T. Costa. *Artificial Intelligence for Quantum Computing*. arXiv:2411.09131. Nov. 2024.

[47] A. Tosato, V. Levajac, J.-Y. Wang, C. J. Boor, F. Borsoi, M. Botifoll, C. N. Borja, S. Martí-Sánchez, J. Arbiol, A. Sammak, M. Veldhorst, and G. Scappucci. “Hard superconducting gap in germanium”. en. In: *Communications Materials* 4.1 (Apr. 2023), p. 23. ISSN: 2662-4443.

11

Conclusions and Outlook

The development of semiconductor spin qubits has made remarkable progress in recent years, with demonstrations of high-fidelity operations and increasingly larger devices. Throughout this thesis, we have explored different aspects of materials engineering and device architectures to advance the germanium quantum computing platform. In this chapter, we discuss the challenges ahead and outline promising directions for future research.

11.1. CONCLUSIONS

When I began my PhD, the field of germanium quantum computing was in its infancy. The first germanium quantum dots had just been demonstrated, and while the material's theoretical advantages were understood, numerous practical challenges stood between these early demonstrations and the realization of scalable quantum processors. My research addressed several of these challenges, advancing germanium's viability as a platform for quantum computation.

A lesson learned throughout my PhD journey has been recognizing the value of both systematic engineering approaches and exploring radically new ideas that, at the time of experimental design, might have appeared to be audacious experimental leaps. The work presented in this thesis is the result of both approaches.

To confirm the theoretical predictions of holes' low effective mass in planar Ge, we experimentally investigated the effective mass and its density dependence. In Chapter 4 we show that holes in germanium quantum wells can achieve effective masses as low as $0.05 m_e$, the lightest for any planar spin qubit platform. This light effective mass directly translates to larger quantum dots and more forgiving fabrication tolerances, addressing one of the key challenges in scaling quantum dot arrays.

Germanium quantum wells were for long exclusively grown on silicon wafers, accepting the inevitable lattice mismatch and resulting defects as a necessary compromise. The prevailing wisdom was to manage strain through complex buffer layers. Our work in Chapter 6 challenged this paradigm by demonstrating that growing directly on germanium wafers could reduce threading dislocation density by nearly an order of magnitude improved electrical properties and reduced charge noise. While 300mm Ge wafers are not currently used in semiconductor foundries, germanium quantum technology may emerge as the compelling application that drives their widespread industrial adoption.

An example of successful systematic engineering has been the realization of a hard superconducting gap in germanium (Chapter 9). We addressed what was one of the obstacles to hybrid quantum devices in planar germanium. While superconducting contacts to germanium had been demonstrated before my work, they lacked the demonstration of a hard gap, limiting their utility for topological qubits or coherent qubit coupling schemes. The development of the PtSiGe process, using a thermally activated solid-phase reaction to form superconducting contacts, provided a reproducible method to achieve high quality semi-superconductor contact with absence of in-gap states. This changed germanium's prospects as a platform for hybrid quantum devices.

Prior to my PhD, quantum dot research for spin qubits operated primarily within two-dimensional architectures. We recognized the potential of three-dimensional integration to enhance connectivity and expand functionality, and expanded our designs in the third dimension. By showing that we could maintain high mobility and low disorder in double quantum wells (Chapter 7), and then successfully operate vertically stacked quantum dots (Chapter 8), we created new possibilities for three-dimensional qubit architectures. This work made me appreciate how theoretical simulations, in this case Schrödinger-Poisson, serve as an invaluable guide for designing complex experiments and predicting device behavior.

The QARPET architecture (Chapter 10) is an example of what we initially considered an audacious experimental leap. It represents a paradigm shift in how we approach

quantum device testing. For several years, spin qubit characterization at mK temperature was limited to individual devices or small arrays, making statistical analysis impractical. By demonstrating that 1058 potential qubits could be controlled with just 54 lines, and showing that individual tiles could be addressed and operated as spin qubits, we created a platform for the systematic study of device variability, yield and qubit performance. This capability is essential as the field transitions from hero devices to statistical process control.

I consider my work on bilayers, hybrid devices, and QARPET to represent my most meaningful contribution to the field. It has been particularly rewarding to see these efforts stimulate the community to build upon our findings and conduct further research in these areas.

11.2. OUTLOOK

11.2.1. MATERIALS IMPROVEMENTS FOR BETTER QUBITS

The quality of semiconductor heterostructures remains a fundamental aspect for advancing quantum computation with spin qubits. Qubits in germanium have been measured only on a few handful of heterostructures and the path to the optimal material system is still a long one. The demonstration of high-mobility hole gases in lightly-strained germanium in Chapter 5 highlights the importance of optimizing the trade-off between strain and defect minimization. Strain, directly impact qubit performance by determining the spin-orbit coupling and g-factor and future investigations should focus on systematic studies of quantum wells with varying strain profiles to identify optimal configurations, balancing band structure control, g-factor, spin-orbit coupling strength, and defect density.

A critical aspect determining the quality of heterostructures is the role of the strain-relaxed buffer layers and the substrate choice. While heterostructures for quantum devices have traditionally been grown on silicon wafers, this requires complex strain-relaxed buffers to accommodate the large lattice mismatch between silicon and germanium-rich layers. The resulting misfit dislocation network propagates through the quantum well as threading dislocations and drives significant local strain fluctuations, potentially limiting qubit performance. In chapter 6 we show that direct growth on germanium wafers can dramatically improve crystalline quality, significantly reducing threading dislocation density and providing a more uniform strain landscape. The reproducible high mobility and very low percolation density, combined with the recent charge noise measurements and coherence measurements [1] demonstrate that this approach provides a better starting material for spin qubit devices. Looking ahead, the buffer layer challenge might be eliminated entirely by growing tensile-strained SiGe barriers directly on (unstrained) germanium [2], similar to approaches used in III-V semiconductors, where the carrier gas is confined at a single buried heterojunction interface. This could provide an even more uniform environment for Ge spin qubits by removing the need for complex strain relaxation processes.

Background impurities present another critical challenge, particularly oxygen incorporation during growth, which degrades the potential landscape making it harder to form quantum dots where intended. Growth optimization should focus on reducing

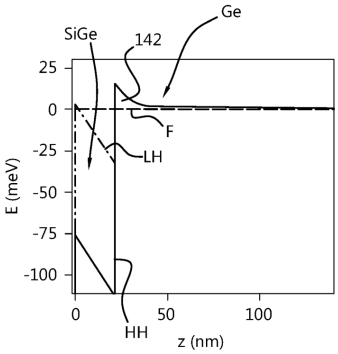

Supplementary Fig. 11.1: Heavy-hole (HH) and Light-hole (LH) band edges calculated with a Schrödinger-Poisson simulation of a Ge/SiGe heterojunction as proposed in patent [2]. The growth direction is from left to right, the heterostructure is composed by a Ge substrate and a strained SiGe barrier. Negatively biasing the heterostructure with a top gate, HH and LH states become available at the Ge/SiGe interface.

impurity either by changing the growth conditions or by reducing the impurities in the growth chamber.

Interface engineering, both at quantum well boundaries and semiconductor-dielectric interfaces, remains crucial for realizing high-performance quantum devices in germanium. New oxide deposition methods and surface preparation techniques should be explored to improve interface quality and mitigate charge noise. The semiconductor-dielectric interface is particularly critical as it directly impacts qubit coherence through charge noise.

The positioning of quantum wells within the heterostructure also deserves attention, deeper quantum wells could reduce the impact of interface traps at the oxide interface while maintaining adequate electrostatic control. In addition, the SiGe barrier, whose purpose has been traditionally only to separate the quantum well from the oxide, could be further engineered to reduce the tunneling of charge from the quantum well to the oxide interface and increase the saturation density [3].

Isotopic enrichment of both Si and Ge will reduce decoherence from hyperfine interactions. The development of growth processes compatible with isotopically enriched materials which maintain the current levels of material quality will be essential.

11.2.2. FUTURE PROSPECTS FOR HYBRID DEVICES

The development of a hard-gap superconducting germanosilicides (PtSiGe) contact to the high mobility 2D hole gas in germanium, presented in Chapter 9, opens interesting new pathways for hybrid quantum devices.

A key opportunity lies in exploring Majorana bound states in phase-biased Josephson junctions [4]. While achieving a hard gap is necessary but not sufficient for topological protection, the demonstrated high-quality interfaces and reproducible fabrication provide a strong foundation. Future experiments should focus on increasing the induced superconducting gap, which could be achieved through two main approaches. First, a

superconducting layer with a larger gap, such as Al or Nb, could be deposited on top of the PtSiGe. Alternatively, other ternary superconducting germanosilicides with higher critical temperatures could be explored, particularly those based on platinoid metals like Rh and Ir. These advances would need to be complemented by non-local spectroscopy measurements in multi-terminal devices and demonstrations of two-electron charging effects in hybrid Ge/PtSiGe islands.

Perhaps most importantly for spin-qubit applications, the realization of a hard superconducting gap positions germanium as a unique platform for coherent coupling of high-fidelity spin qubits over long distances. Crossed Andreev reflection could enable two-qubit gates spanning micrometer distances, while coupling via superconducting quantum dots might offer additional control options and potential topological protection. Even longer-range coupling could be achieved through integration with superconducting resonators, with the PtSiGe contacts potentially providing a large coupling strength thanks to their proximity to the quantum dots. It is encouraging in this direction that recent experiments at IBM and University of Copenhagen have replicated the the PtGeSi process, demonstrating both Andreev bound state spectroscopy in planar Josephson junctions [5] and controllable proximitization of quantum dots in Ge/SiGe heterostructures [6].

Furthermore, the demonstration of a hard gap motivates investigation of alternative qubit systems, such as Andreev spin qubits. Combined with germanium's ability to be isotopically purified, this could overcome the decoherence limitations currently seen in III-V implementations of such qubits.

11.2.3. SCALING QUBIT TESTING

The challenge of scaling up goes beyond increasing qubit numbers. Understanding device variability and yield, developing robust control strategies, and establishing efficient testing protocols are equally important. QARPET-like architectures can provide a powerful platform for addressing these challenges, enabling the collection of statistical data which is crucial as the field moves toward industrial-scale quantum processors.

Key aspects of scaling that will be relevant to investigate in future research using QARPET-like platforms, include systematic studies of device variability, crosstalk effects, and coherence properties. Future experiments measuring quantum dot formation characteristics, tunnel coupling ranges, and spin-orbit coupling strengths across hundreds of nominally identical devices will enable meaningful statistical analysis of process variations and provide crucial insights into the uniformity of the material stack and fabrication processes. The dense packing of quantum dots in large arrays offers opportunities to investigate crosstalk and electrostatic interactions, which are important for maintaining high-fidelity control. Additionally, measurements of coherence times across multiple devices could reveal spatial correlations in noise sources and inform the development of strategies for coherence protection in larger systems. Such statistical studies will be essential for understanding and overcoming the challenges of scaling quantum dot arrays to the sizes required for practical quantum computation.

The development of algorithms for automatic quantum dot formation and gate virtualization (to compensate for cross-capacitance) will become essential as system sizes grow. Machine learning approaches could prove particularly valuable for handling the

high-dimensional parameter space of large arrays, with QARPET-like architectures providing ideal testbeds for developing and validating such algorithms through multiple iterations on different tiles.

11.2.4. THREE-DIMENSIONAL QUANTUM DOTS INTEGRATION

The demonstration of quantum dots in double quantum wells presented in chapter 8 opens new possibilities for architectures with three-dimensional integration of quantum dots. Building on the results presented in this thesis, recent advances demonstrated the ability to tune a device with two neighboring vertically coupled double dots in a Ge bilayer heterostructure to the (1,1,1,1) charge state [7]. The vertical coupling between quantum dots provides an additional degree of freedom for designing spin qubit devices with enhanced connectivity and functionality. Future research should systematically investigate the parameter space for g-tensor and spin-orbit coupling tuning in multi-layer systems. Quantum wells with different strain profiles or compositions could be engineered to create differences in parameters like g-factor between layers. This could enable novel ways of implementing quantum operations, for example, shuttling qubits between quantum dots in different wells with distinct g-factors could allow qubit control using only baseband pulses, potentially reducing the need for high-power microwave electronics. Precise control of charge occupation on vertically stacked dots could enable vertical Pauli spin-blockade readout, potentially allowing integration of readout ancilla qubits directly above or below data qubits. The capability to shift or delocalize wavefunctions between quantum wells could enable low-power electric dipole spin resonance and advanced spin-qubit control schemes. Important to realizing most of these possibilities however, will be the development of reliable methods for controlling vertical tunnel coupling.

The vertical separation between wells provides also opportunities for new device architectures. For example, when charges in separate wells are capacitively coupled but have minimal tunnel coupling, charge sensors could be integrated into separate layers from the qubits they sense. In regimes with tunnel coupling in the gigahertz range, coherent spin shuttling between wells could be realized, enabling one layer to serve as quantum links connecting remote qubits in another layer.

Our work has also stimulated theoretical investigations into the rich physics these systems can exhibit. Recent theoretical work has shown that bilayer arrangements of four quantum dots per layer can display complex magnetic ground states, providing new opportunities for exploring fundamental condensed matter phenomena in these devices particularly interesting in the context of spin-qubit-based analog quantum simulations [8].

BIBLIOGRAPHY

[1] L. E. Stehouwer, C. X. Yu, B. van Straaten, A. Tosato, V. John, D. D. Esposti, A. Elsayed, D. Costa, S. D. Oosterhout, N. W. Hendrickx, et al. "Exploiting epitaxial strained germanium for scaling low noise spin qubits at the micron-scale". In: *arXiv preprint arXiv:2411.11526* (2024).

[2] G. Scappucci, M. Russ, A. Sammak, L. Stehouwer, and A. Tosato. *Method for manufacturing a single heterojunction semiconductor device and such a single heterojunction semiconductor device*. English. Patent. H01L. 2024.

[3] A. Tosato and G. Scappucci. "Buried-channel semiconductor heterostructures with enhanced band offset". Patent NL2031791B1. D. U. of Technology. Filed with the Netherlands Patent Office. 2022.

[4] M. Luethi, K. Laubscher, S. Bosco, D. Loss, and J. Klinovaja. "Planar Josephson junctions in germanium: Effect of cubic spin-orbit interaction". In: *Physical Review B* 107.3 (2023), p. 035435.

[5] M. Hinderling, S. Ten Kate, M. Coraiola, D. Haxell, M. Stiefel, M. Mergenthaler, S. Paredes, S. Bedell, D. Sabonis, and F. Nichele. "Direct microwave spectroscopy of andreev bound states in planar Ge josephson junctions". In: *PRX Quantum* 5.3 (2024), p. 030357.

[6] L. Lakic, W. I. Lawrie, D. van Driel, L. E. Stehouwer, M. Veldhorst, G. Scappucci, F. Kuemmeth, and A. Chatterjee. "A proximitized quantum dot in germanium". In: *arXiv preprint arXiv:2405.02013* (2024).

[7] A. S. Ivlev, H. Tidjani, S. D. Oosterhout, A. Sammak, G. Scappucci, and M. Veldhorst. "Coupled vertical double quantum dots at single-hole occupancy". In: *Applied Physics Letters* 125.2 (2024).

[8] D. Buterakos and S. D. Sarma. *Magnetic Phases of Bilayer Quantum-Dot Hubbard Model Plaquettes*. 2023. arXiv: 2308.04504 [cond-mat.mes-hall].

SUMMARY

Quantum computers could solve certain problems exponentially faster than classical computers. Among the various physical implementations being explored, spin qubits in semiconductor quantum dots have emerged as a promising platform due to their potential scalability and compatibility with existing semiconductor manufacturing. Within semiconductor platforms, germanium has recently gained significant attention due to its strong spin-orbit coupling, absence of valley states, and compatibility with industrial processes.

In this thesis, we explore several aspects key to advance germanium-based quantum computing technology. The work focuses on improving the material quality and understanding fundamental properties, developing new device architectures, and enabling hybrid superconductor-semiconductor systems.

We begin by investigating the effective mass of holes in strained germanium quantum wells and its dependence on carrier density, confirming theoretical predictions of a remarkably light effective mass in compressively strained germanium. We then investigate the properties of a lightly-strained germanium quantum wells which can achieve hole mobility exceeding 1×10^6 cm^2/Vs while maintaining a remarkably low percolation density. Further, we achieve a major materials breakthrough by growing germanium quantum wells directly on germanium wafers, rather than the traditional silicon substrates. This novel approach reduces threading dislocation density of nearly an order of magnitude, resulting in mobility consistently exceeding 3×10^6 cm^2/Vs.

Building on our understanding of single quantum wells, we develop and characterize germanium double quantum well systems. Through magnetotransport measurements, we demonstrate the formation of a high-mobility hole bilayer and study the coupling between the two layers. Leveraging this bilayer platform, we demonstrate the first vertical gate-defined double quantum dot in a strained germanium double quantum well, opening possibilities for three-dimensional quantum circuits.

We further expand the germanium planar platform and create hybrid semiconductor-superconductor systems by developing high-quality superconducting contacts to germanium. Using a germanosilicide process formed through thermal reaction between platinum and the semiconductor, we achieve the first demonstration of a hard superconducting gap in germanium. This breakthrough enables the integration of quantum dots with superconducting elements for hybrid quantum devices.

Finally, we present a qubit-array research platform for engineering and testing (QARPET). In a significant step toward testing scalability, we present a crossbar array approach for statistical testing of spin qubit tiles, each composed of one sensor and two quantum dots. The device with over 1000 potential spin qubits, achieves a quantum dot density of 2 million per mm^2 while requiring minimal control lines and a single cooldown. This development represents a significant advance for characterizing quantum devices at scale.

The results presented in this thesis establish planar germanium as a versatile platform for quantum devices, offering high-quality materials, novel three-dimensional architectures, and integration with superconductors. Altogether, these developments provide a foundation for scaling up the complexity of quantum devices.

SAMENVATTING

Quantumcomputers zouden bepaalde problemen exponentieel sneller kunnen oplossen dan klassieke computers. Onder de verschillende fysieke implementaties die worden onderzocht, zijn spinqubits in halfgeleider-quantumdots naar voren gekomen als een veelbelovend platform vanwege hun potentiële schaalbaarheid en compatibiliteit met bestaande halfgeleiderproductie. Binnen halfgeleiderplatforms heeft germanium onlangs aanzienlijke aandacht gekregen vanwege de sterke spin-baan-koppeling, de afwezigheid van valleitoestanden en de compatibiliteit met industriële processen.

In dit proefschrift onderzoeken we verschillende aspecten die cruciaal zijn voor de vooruitgang van germanium-gebaseerde kwantumcomputingtechnologie. Het werk richt zich op het verbeteren van de materiaalkwaliteit en het begrijpen van fundamentele eigenschappen, het ontwikkelen van nieuwe apparaatarchitecturen en het mogelijk maken van hybride supergeleider-halfgeleidersystemen.

We beginnen met het onderzoeken van de effectieve massa van gaten in gespannen germanium-quantumputten en de afhankelijkheid daarvan van de ladingsdichtheid, waarbij we theoretische voorspellingen bevestigen van een opmerkelijk lichte effectieve massa in samengedrukt germanium. Vervolgens onderzoeken we de eigenschappen van licht-gespannen germanium-quantumputten die een gatmobiliteit kunnen bereiken van meer dan 1×10^6 cm^2/Vs, terwijl ze een opmerkelijk lage percolatiedichtheid behouden. Verder bereiken we een grote doorbraak in materiaalkunde door germanium-quantumputten rechtstreeks te laten groeien op germaniumwafers in plaats van op de traditionele siliciumsubstraten. Deze nieuwe aanpak vermindert de dichtheid van dislocaties met bijna een orde van grootte, wat resulteert in een mobiliteit die consequent hoger is dan 3×10^6 cm^2/Vs.

Voortbouwend op ons begrip van enkele quantumputten, ontwikkelen en karakteriseren we germanium dubbele quantumputsystemen. Door middel van magnetotransportmetingen tonen we de vorming van een hoog-mobiel gaten-bilayer aan en bestuderen we de koppeling tussen de twee lagen. Gebruikmakend van dit bilayerplatform demonstreren we de eerste verticaal poort-gedefinieerde dubbele quantumdot in een gespannen germanium dubbele quantumput, waarmee de weg wordt vrijgemaakt voor driedimensionale kwantumcircuits.

We breiden het germanium-planarplatform verder uit en creëren hybride halfgeleider-supergeleidersystemen door hoogwaardige supergeleidende contacten met germanium te ontwikkelen. Door gebruik te maken van een germanosilicideproces, gevormd door thermische reactie tussen platina en het halfgeleidermateriaal, realiseren we de eerste demonstratie van een harde supergeleidende kloof in germanium. Deze doorbraak maakt de integratie mogelijk van quantumdots met supergeleidende elementen voor hybride kwantumapparaten.

Ten slotte presenteren we een qubit-array-onderzoeksplatform voor engineering en testen (QARPET). In een belangrijke stap richting het testen van schaalbaarheid presen-

teren we een crossbar-arraybenadering voor statistisch testen van spinqubit-tegels, elk bestaande uit één sensor en twee quantumdots. Het apparaat, met meer dan 1000 potentiële spinqubits, bereikt een quantumdot-dichtheid van 2 miljoen per mm^2, terwijl het minimale controlijnen en slechts één afkoeling vereist. Deze ontwikkeling vertegenwoordigt een belangrijke vooruitgang in het karakteriseren van kwantumapparaten op schaal.

De resultaten die in dit proefschrift worden gepresenteerd, vestigen planar germanium als een veelzijdig platform voor kwantumapparaten, met hoogwaardige materialen, nieuwe driedimensionale architecturen en integratie met supergeleiders. Al met al vormen deze ontwikkelingen een fundament voor het opschalen van de complexiteit van kwantumapparaten.

ACKNOWLEDGEMENTS

Research is often a collaborative effort, and my PhD was certainly no exception. It has been a privilege to work in such a supportive environment, and I am deeply grateful for the guidance, inspiration, and encouragement I received from so many people at QuTech.

Thank you **Giordano** for the trust, guidance, freedom, and support you provided throughout my PhD. You were at once a supervisor, a teammate, and a friend. I greatly appreciated your ability to listen, your willingness to take risks and support unconventional projects, your enthusiasm for new results, and the remarkable speed with which you reviewed anything we sent you. Over the years you always managed to build a wonderful team, one that not only produces excellent research but is also great to work with.

Brian, you were the first to take me under your wing, showing me around the lab with care and patience. I truly enjoyed our endless fridge-refilling conversations, which ranged across countless topics. I also value the trust between us, and I am grateful that after all these years we still keep in touch and continue to have inspiring conversations.

Mario, you had the difficult task of teaching me the art of fabrication, certainly no easy challenge. I am grateful for the patience you showed me.

Davide, your presence in the lab has been essential. You have a big heart, always ready to help anyone in need, and you took care of everything that needed to be done. I often thought your efforts went unnoticed, but your presence truly made a difference.

Pablo and **Hanifa**, when you joined QuTech you brought with you a breath of fresh air. We shared so many meaningful moments both at QuTech and outside, on land and at sea. Without you my PhD journey would not have been the same, and I am so grateful for our friendship!

Sergey thank you for the incredible support you've given me in the cleanroom. Even with your busy schedule, you always found the time to offer advice, training, and hands-on help. You've been an invaluable resource for spin-qubit fabrication, and a nice office mate as well.

Vukan and **Ji-Yin**, it was wonderful working with you, and I learned a great deal from both of you.

Federico and **Asser**, it was a pleasure to work with you and to hand over the QARPET project, which I am excited to see continue in your hands.

Karina, thank you for taking a stunning SEM of the QARPET device, and for bringing nice vibes to the office.

Desa, **Luka**, and **Lucas**, it was a joy to have you on the team. Thank you for the scientific discussions and for the many fun moments we shared.

Francesco, thank you for always being available to discuss and patiently answer my questions.

Will, although we did not spend much time together, you were a bright presence at QuTech.

Stephan, although the bulk of our work together is outside this PhD, you still left a significant mark on my research. Thank you for building the software infrastructure that enabled my experiments as well as those of many others, and also for the scientific discussions and your practical help on the QARPET project.

The quality and availability of the **technical staff** is one of the things that makes QuTech unique. I am very grateful for the immense help I received from all the technicians, whose support made a real difference in our research.

Thanks also to everyone else I interacted with during this period at QuTech, and in particular to **Daniel**, **Brennan**, **Uri**, and **Irene**, who made our workplace a little bit more special.

Bibi, thank you for being by my side during my PhD.

Mamma e **papà**, grazie per la fiducia e il supporto. Grazie a mio fratello **Tommaso** per avermi spronato e consigliato ad intraprendere un PhD, e a mio fratello **Giulio** per i bei weekend trascorsi insieme qui in Olanda. Giulio, passo il testimone a te che sei prossimo a laurearti!

‘

CURRICULUM VITÆ

Alberto TOSATO

17-12-1993	Born in Padova, Italy.

EDUCATION

2012-2015	B.Sc. Chemical and Materials Engineering	
	University of Padova, Italy	
2016-2019	M.Sc. Material Science	
	Augsburg University, Germany	
2019-2024	PhD Physics	
	Thesis:	Quantum-engineered germanium for spin-based quantum computing
	Promotor:	Dr. Giordano Scappucci
	Promotor:	Dr. Menno Veldhorst

LIST OF PUBLICATIONS

JOURNAL PAPERS AND PREPRINTS

11. **A. Tosato**, A. Elsayed, F. Poggiali, L. Stehouwer, D. Costa, K. Hudson, D. Degli Esposti, G. Scappucci. "QARPET: A Crossbar Chip for Benchmarking Semiconductor Spin Qubits". In: arXiv preprint arXiv:arXiv:2504.05460 (2025).

10. L. E. Stehouwer, C. X. Yu, B. van Straaten, **A. Tosato**, V. John, D. D. Esposti, A. El- sayed, D. Costa, S. D. Oosterhout, N. W. Hendrickx, et al. "Exploiting epitaxial strained germanium for scaling low noise spin qubits at the micron-scale". In: arXiv preprint arXiv:2411.11526 (2024).

9. H. Tidjani*, **A. Tosato***, A. Ivlev, C. Déprez, S. Oosterhout, L. Stehouwer, A. Sammak, G. Scappucci, and M. Veldhorst. "Vertical gate-defined double quantum dot in a strained germanium double quantum well". In: Physical Review Applied 20.5 (Nov. 2023), p. 054035. ISSN: 2331-7019.

8. L. E. Stehouwer, **A. Tosato**, D. Degli Esposti, D. Costa, M. Veldhorst, A. Sammak, and G. Scappucci. "Germanium wafers for strained quantum wells with low disor- der". In: Applied Physics Letters 123.9 (2023).

7. **A. Tosato**, V. Levajac, J. Y. Wang, C. J. Boor, F. Borsoi, M. Botifoll, C. N. Borja, S. Martí-Sánchez, J. Arbiol, A. Sammak, M. Veldhorst, and G. Scappucci. "Hard su- perconducting gap in germanium". In: Communications Materials 4.1 (2023). ISSN: 26624443.

6. **A. Tosato**, B. Ferrari, A. Sammak, A. R. Hamilton, M. Veldhorst, M. Virgilio, and G. Scappucci. "A High-Mobility Hole Bilayer in a Germanium Double Quantum Well". In: Advanced Quantum Technologies 5 (5 May 2022), p. 2100167. ISSN: 2511- 9044.

5. M. Lodari, O. Kong, M. Rendell, **A. Tosato**, A. Sammak, M. Veldhorst, A. R. Hamil- ton, and G. Scappucci. "Lightly strained germanium quantum wells with hole mo- bility exceeding one million". In: Applied Physics Letters 120.12 (Mar. 2022), p. 122104. ISSN: 0003-6951.

4. B. P. Wuetz, M. P. Losert, **A. Tosato**, M. Lodari, P. L. Bavdaz, L. Stehouwer, P. Amin, J. S. Clarke, S. N. Coppersmith, A. Sammak, et al. "Effect of quantum hall edge strips on valley splitting in silicon quantum wells". In: Physical review letters 125.18 (2020), p. 186801.

3. M. Lodari, **A. Tosato**, D. Sabbagh, M. A. Schubert, G. Capellini, A. Sammak, M. Veld- horst, and G. Scappucci. "Light effective hole mass in undoped Ge/SiGe quantum wells". In: Physical Review B 100.4 (July 2019), p. 041304.

2. A. Sammak, D. Sabbagh, N. W. Hendrickx, M. Lodari, B. P. Wuetz, **A. Tosato**, L. Yeoh, M. Bollani, M. Virgilio, M. A. Schubert, P. Zaumseil, G. Capellini, M. Veldhorst, and G. Scappucci. "Shallow and Undoped Germanium Quantum Wells: A Playground for Spin and Hybrid Quantum Technology". en. In: Advanced Functional Materials 29.14 (2019), p. 1807613. ISSN: 1616-3028.

* These authors contributed equally

1. G. H. Ahmed, M. R. Parida, **A. Tosato**, L. G. AbdulHalim, A. Usman, Q. A. Alsu- lami, B. Murali, E. Alarousu, O. M. Bakr, and O. F. Mohammed. “The impact of elec- trostatic interactions on ultrafast charge transfer at Ag 29 nanoclusters–fullerene and CdTe quantum dots–fullerene interfaces”. In: Journal of Materials Chemistry C 4.14 (2016), pp. 2894–2900.

PUBLISHED PATENTS

3. **A. Tosato** and G. Scappucci. “Buried-channel semiconductor heterostructures with enhanced band offset”. Patent NL2031791B1. D. U. of Technology. Filed with the Netherlands Patent Office. 2022.

2. G. Scappucci, **A. Tosato**, F. Russ Maximilian, A. Sammak, E. A. Stehouwer Lucas. “Method for manufacturing a single heterojunction semiconductor device and such a single heterojunction semiconductor device”. Patent NL2034508B1. TNO and D. U. of Technology. Filed with the Netherlands Patent Office, application filed on 2023-04-05, granted on 2024-10-14. 2024.

1. **A. Tosato** and G. Scappucci. “Quantum dot structure unit cell, quantum dot system and method of manufacturing the same”. Patent NL2035150A. D. U. of Technology. Filed with the Netherlands Patent Office. 2023.